UNIVERSITÀ DI TRENTO

UNIVERSITÀ DEGLI STUDI DI BARI ALDO MORO

Doctorate of National Interest

on

Space Science and Technology

Multi-wavelength and multi-messenger observation of blazars' jets

Chiara Bartolini

Supervisor
Prof. Francesco Giordano

Dipartimento di Fisica "M. Merlin" dell'Università e del Politecnico di Bari
Istituto Nazionale di Fisica Nucleare, Sezione di Bari

Co-Supervisor
Prof. Elisabetta Bissaldi

Dipartimento di Fisica "M. Merlin" dell'Università e del Politecnico di Bari
Istituto Nazionale di Fisica Nucleare, Sezione di Bari

January 8, 2026

Abstract

Relativistic jets in Active Galactic Nuclei (AGN) are among the most powerful sources of radiation in the Universe. The radiation spans the entire electromagnetic spectrum, from radio wavelengths to γ-rays. Active Galactic Nuclei are divided into different categories, and the one this thesis will focus on is blazars. Blazars are radio-loud galaxies whose jet is aligned with the line of sight. Hence, the observed emission is strongly beamed and amplified due to relativistic Doppler effects. Moreover, their Spectral Energy Distribution (SED) is entirely dominated by non-thermal jet emission. Blazar's SEDs are characterized by two humps: the first one is due to synchrotron radiation from relativistic electrons accelerated in the jet, while the second hump has more than one explanation. The first one is that the particle population in the jet is dominated by electrons and positrons that are being accelerated. This is the leptonic scenario. The second one is that protons and ions are accelerated in the jets. The acceleration of hadrons involves the production of neutrinos. For this reason, blazars are considered a possible origin for astrophysical neutrinos. Hence, the second peak of the SED can be attributed to both hadrons and leptons. Because of these two interpretations, the study of the multi-wavelength emission of blazars, the modeling of their broad-band SED, and the detection of neutrinos are still fundamental pieces to understand particle acceleration in blazars' jets. This thesis aims to explore the acceleration of leptons and hadrons in blazars' jets, employing data from various facilities, several data analysis techniques, different statistical approaches, and distinct physically motivated spectral model simulations.

Chapter 1 presents the different messengers of the Universe and introduces the basic properties of AGN and blazars, which are the main focus of this thesis.

Chapter 2 shows the state of the art of the instruments, facilities, and the techniques to detect radiation from very high energy γ-rays to the radio band and neutrinos. For each instrument whose data are employed in this thesis, the corresponding data analysis methodology is summarized.

Chapter 3 presents the 15-year multi-wavelength analysis of the Flat Spectrum Radio Quasar (FSRQ) OP 313. This chapter investigates the intense flaring activity exhibited by this source between November 2023 and March 2024, from γ-rays to radio frequencies. In particular, the attention is mainly focused on the *Fermi* Large Area Telescope (LAT) γ-ray and radio Very Long Baseline Array (VLBA) data analysis to explore the intrinsic relationship between high-energy emission and jet kinematics in the blazar's jet, and on the SED modeling considering only leptons being accelerated. One important focus is the behavior of the new radio 43 GHz components found in OP 313's jet to determine the time of ejection with good accuracy and see if there is a correlation between the ejection time and the γ-ray flaring activity.

Chapter 4 shows a sensitivity study for the Cherenkov Telescope Array Observatory (CTAO) experiment. In particular, four configurations of CTAO were compared to explore which of them has the best performance during the observation of flaring activity from a

sample of eight FSRQs. For each FSRQ, the highest *Fermi*-LAT γ-ray flare was considered. The simulations aim to quantify the ability of various CTAO configurations to detect flares and constrain spectral parameters. Then, the simulations assess whether adding CTAO data to the *Fermi*-LAT ones can help to discriminate between different spectral models linked to the leptonic distribution in the jet and the curvature of the SEDs.

Chapter 5 finally considers blazars' jets as the origin of the neutrinos observed by IceCube. In particular, it focuses on IcuCube real-time alerts, and on the *Fermi*-Large Area Telescope analysis to identify possible γ-ray activity from known and new sources. With the increase in the number of real-time alerts, a growing sample of γ-ray sources that are coincident with neutrinos is emerging. Most of them are caused by large positional uncertainties in the arrival directions of the neutrinos. Therefore, detailed multi-wavelength studies are necessary to select possible source candidates.

A brief summary with the main results is shown in Chapter 6.

Contents

Chapter 1

Introduction

1.1 The messengers of the Universe

The Universe is filled with numerous types of messengers that provide unique insights into cosmic events, enabling the scientific community to have a comprehensive understanding of the Universe's physical processes and the nature of celestial phenomena [252]. Multi-messenger astronomy studies different astronomical sources using photons, neutrinos, cosmic rays, and gravitational waves.

1.1.1 Cosmic rays

Cosmic Rays (CRs) are high-energy particles originating in astrophysical environments and traveling at relativistic speeds. They are mainly protons ($\sim 85\%$), alpha particles ($\sim 12\%$), heavier nuclei ($\sim 2\%$), and electrons ($< 1\%$), spanning several orders of magnitude in energy. The discovery of CRs is attributed to Victor Hess in 1912. After several balloon flights with different instruments on board, he concluded that the increase in the ionisation rate with altitude was caused by radiation coming from space. For this discovery, Hess was awarded the Nobel Prize in 1936.

Since then, several experiments have been conducted to enhance the characterization of these particles and improve the understanding of their origin. Figure 1.1 shows the differential flux (flux of particles reaching Earth per unit time, unit surface, unit energy, and unit solid angle) of CRs over energy. The energy of charged CRs ranges from tens of MeV to over 10^{20} eV [50]. The striking features of the CRs spectrum are the steepening called "knee" at 10^{15} eV, where the spectral index changes from ~ 2.7 to ~ 3, "second knee" at 10^{17} eV, where it changes to ~ 3.3, and the "ankle" at 10^{19} eV where it changes to ~ 2.5 [83, 85, 172]. Up to 10^{15} eV, the flux of CR is high enough to allow the scientific community to measure them directly using space-based detectors or balloon missions [126]. Above that flux, the CR are measured indirectly using large ground-based detectors to have better statistics. These detectors measure the secondary particles generated in the atmospheric air showers initiated by CR coming from space. When CRs enter the Earth's atmosphere, they collide with the nucleons of the atmospheric nuclei and produce a cascade of secondary particles called "extensive air shower".

One of the main efforts of the study of CRs is the identification of their sources. The general picture adopted nowadays is that CRs with energies below the "knee" are principally of Galactic origin, while those with energies above $\sim 10^{18}$ eV have an extragalactic origin [50, 200]. Supernova Remnants (SNRs) have been considered the most promising candidates to accelerate Galactic CRs, since they provide the required energy budget

and host strong shock waves capable of accelerating particles via diffusive shock acceleration (see Section A.1.3 for more details). However, whether SNRs alone can account for the entire Galactic CR population up to the knee remains unclear. Results from the H.E.S.S. Galactic Plane Survey have revealed a rich population of extended TeV sources, suggesting that multiple classes of Galactic accelerators may contribute to the CR flux [163]. Recently, Galactic pevatrons were discovered. The LHAASO experiment detected PeV-energy γ-rays, demonstrating that some Galactic sources are capable of accelerating particles to energies close to 1 PeV [66, 67, 330]. These observations illustrate a more complex origin of Galactic CRs, where SNRs may play a leading role but are likely not the only contributors.

The last category of CRs is called *Ultra High Energy Cosmic Rays* (UHECRs). The extragalactic origin arises because the gyroradius of the proton population above 10^{18} eV starts to exceed the size of the Milky Way, so CRs can travel outside the galaxy. Hence, the galactic CR flux decreases, allowing the extragalactic flux to dominate. This means that low-energy CRs are significantly influenced by galactic magnetic fields, which can alter their trajectories, causing them to be deflected or trapped, while UHECRs are not. UHECRs are believed to be accelerated in Active Galactic Nuclei (AGN), radio galaxies, Gamma-Ray Bursts (GRBs), or in other powerful astrophysical systems. Above 5 $\times 10^{19}$ eV, the energy of CRs lies above the threshold for photo-pion production through the interaction with the Cosmic Microwave Background (CMB) (see Section 1.2.8 for more details on how photo-pion production works). The effect of this process on the spectrum is a cutoff called Greisen-Zatsepin-Kuzmin (GZK) cutoff [e.g. 160, 318, 333].

1.1.2 Photons

Till a few decades ago, our knowledge of the Universe was mainly based on observations of the electromagnetic radiation within a wide range of wavelengths. Photons have been crucial in astronomy, allowing scientists to gather information about distant stars and galaxies. Most of the electromagnetic radiation is blocked by the atmosphere, as shown by Figure 1.2. Hence, to observe them, we require space observatories or some form of indirect detection.

Photons can be emitted by several non-thermal processes, which are key to interpreting the spectra of high-energy astrophysical sources:

- Bremsstrahlung: when a charged particle is close to an atomic nucleus, the Coulomb field deflects it and a photon is produced.
- Synchrotron radiation: when charged particles are spiraling around magnetic field lines, their trajectory is deflected, and photons are produced.
- Inverse-Compton: photons are scattered at higher energies by relativistic electrons. This process is the main channel in which γ-rays are produced.
- Pair annihilation: when a particle annihilates with its antiparticle, a γ-ray photon is produced.
- Neutral pion decay: neutral pions, which are produced during proton-proton or proton-photon interactions, decay into two γ-ray photons.

These processes explain the observed spectrum for a large variety of astrophysical objects over a wide energy range, from radio to γ-ray energies.

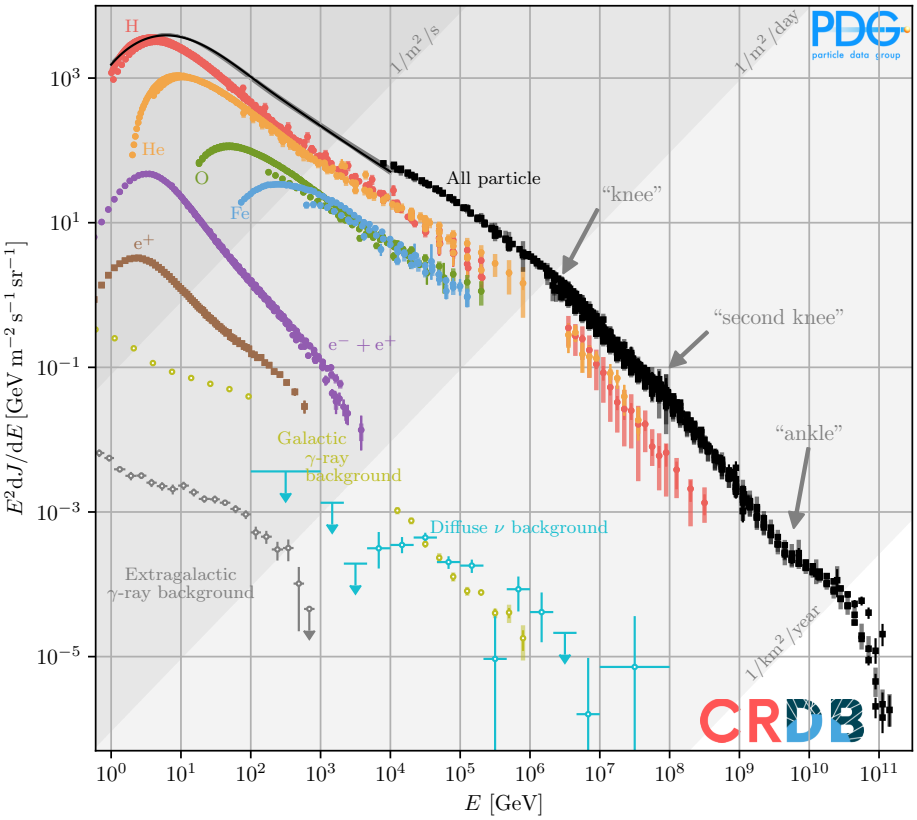

Figure 1.1: All-particle spectrum of CRs. The data for the charged CRs have been extracted from the Cosmic Ray Database (CRDB) [232]. Below 10^4 GeV, the all-particle spectrum is the sum of the most important nuclear species. The diffuse γ-ray fluxes have been extracted from [15, 17, 210], measurements of the diffuse neutrino background are from [247].

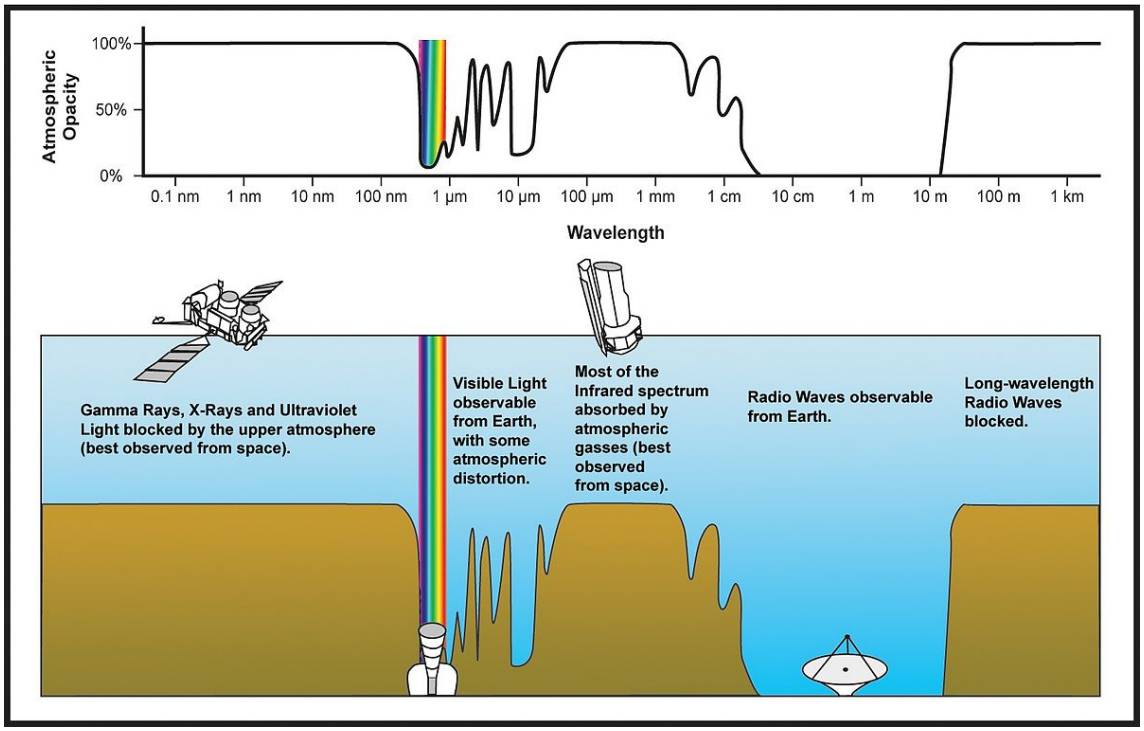

Figure 1.2: In the upper part, the atmosphere opacity as a function of the wavelength is presented, which is represented as the percentage of electromagnetic radiation that does not reach the Earth's surface. Space experiments are used to detect it. Credit: NASA.

In the context of cosmic-ray (CR) origin studies, γ-ray photons are the ideal messengers. They are produced in the radiative processes listed above that involve CRs in the source, where they are accelerated and are not deflected by the magnetic fields during their travel around the Universe. As a result, γ-rays point back directly to their sources, providing crucial spatial information about cosmic accelerators. However, they can be absorbed during their interaction with the CMB and the Extragalatic Background Light (EBL). The effect of the absorption of the γ-rays increases with increasing energy and increasing distance from us and the source where they are produced, as shown in Figure 1.3.

1.1.3 Neutrinos

Another abundant messenger in the Universe is the neutrino. Neutrinos are electrically neutral and interact only via the weak nuclear force, making them extremely elusive and capable of traveling vast cosmological distances without interacting. They are considered the definitive indicators of cosmic-ray acceleration, akin to γ-ray photons, due to their exclusive generation through hadronic interactions. However, unlike photons, neutrinos are not absorbed by interacting with matter, allowing them to reach Earth from the most remote and obscured regions of the Universe.

Using neutrino telescopes, we can study neutrinos of different flavors: the electronic neutrino, ν_e, the muonic neutrino, ν_μ, and the tauonic neutrino, ν_τ. All neutrino flavors undergo the mechanism of neutrino oscillations, which is a quantum mechanical phenomenon in which a neutrino changes its type as it propagates through space.

Finally, Figure 1.1 presents in light blue the diffuse neutrino background, which is composed of cosmological neutrinos produced when the Universe was hot and young surrounding us [291].

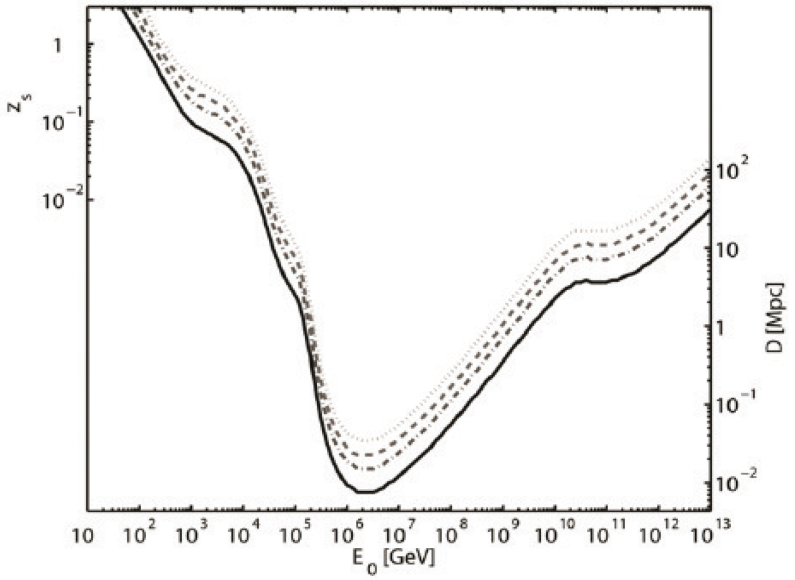

Figure 1.3: Source redshifts z_s at which the optical depth takes fixed values as a function of the observed photon energy E_0. The scale on the right side shows the distance in Mpc for nearby sources. The curves from bottom to top correspond to a photon survival probability of $e^{\tau(E_0,z_s)}$, where $\tau(E_0, z_s)$ is the optical depth, is: $e^{-1} \simeq 0.37$, $e^{-2} \simeq 0.14$, $e^{-3} \simeq 0.05$ and $e^{-4.6} \simeq 0.01$. For $D < 8\,\text{kpc}$, the photon survival probability is larger than 0.37 for any value of E_0. This plot is courtesy of [94].

1.1.4 Gravitational Waves

Gravitational waves are ripples in the fabric of spacetime, generated by some of the most energetic and cataclysmic events in the Universe, such as the mergers of black holes and neutron stars. These spacetime distortions, predicted by Einstein's general theory of relativity, propagate outward from their source at the speed of light [291]. Unlike electromagnetic radiation, gravitational waves originate from coherent, large-scale motions of massive bodies, making them a unique probe of relativistic astrophysical systems.

The first detection of a gravitational wave happened on 14 September 2015, when the Laser Interferometer Gravitational-Wave Observatory (LIGO) observed the signal from the merger of two black holes [84]. A second signal was detected on 17 August 2017, when the coalescence of two neutron stars was observed not only via gravitational waves [6], but also through a short Gamma-Ray Burst (GRB) detected by observatories across the entire Earth [5]. The combination of gravitational and electromagnetic observations is a powerful tool to study astrophysical phenomena.

Gravitational waves are the most recent addition to the list of astrophysical messengers, providing a new context to the high-energy Universe.

1.1.5 Acceleration sites

The acceleration of CRs at astrophysical sites can occur through two distinct mechanisms: *diffusive shock acceleration*, based on the Fermi mechanism (see Section A.1.3), and acceleration in a very high electric field generated by rapidly rotating compact magnetized objects. Hence, to reach energies above 1 EeV, large acceleration regions and/or highly relativistic shock waves are necessary [209].

[169] identified the potential acceleration sites of UHECRs using a relation between

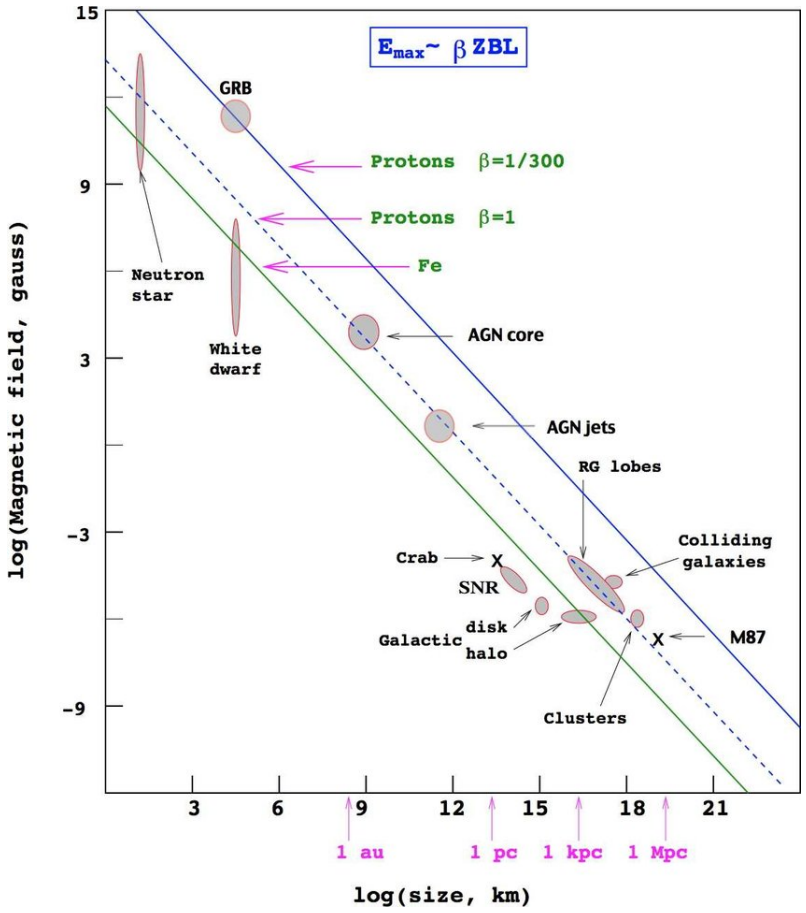

Figure 1.4: Hillas plot for candidate acceleration sites, relating their size R and magnetic field strength B. To accelerate a given particle species above 100 EeV, objects must lie above the corresponding lines. The green line corresponds to the condition for B, R to accelerate iron at 10^{20} eV. The blue line corresponds to the condition for B, R to accelerate a proton at 10^{20} eV with $\beta = 1/300$, while the dashed blue line represents the same condition but with $\beta = 1$. Courtesy of [209].

the maximum energy of a particle of charge Ze, the source size R, and its magnetic field strength B:

$$E_{max} = \beta \mathrm{Z}e \left(\frac{B}{1\mu\mathrm{G}}\right)\left(\frac{R}{1\mathrm{kpc}}\right) \mathrm{EeV} \tag{1.1}$$

where β is the velocity of the accelerating shock wave or the efficiency of the accelerator. Figure 1.4, which is the Hillas plot, shows this relation. The sources listed in the plot are both of Galactic and Extragalactic origin. The Galactic sources are:

- Neutron stars, in particular, young millisecond magnetars, easily fulfill the Hillas condition, and prove to be good candidates. Magnetars are neutron stars with extremely strong surface dipole fields of order 10^{15} G [200];
- SNRs are efficient accelerators of protons and electrons through *diffusive shock acceleration* (see Section A.1.3) and can reach energies up to the "knee" consistent with their size ($R \sim 10\,\mathrm{pc}$) and magnetic fields ($B \sim 10^{-5} - 10^{-4}\,\mathrm{G}$). A full description of these sources is shown in Section A.

The extragalactic ones are:

- AGN, which are the main focus of this thesis (see Section 1.2), satisfy the Hillas condition. AGN jets are a fraction of a parsec long with a magnetic field of the order of a few Gauss. Using these parameters, it is possible to accelerate particles until a few $\sim$ EeV. An AGN core with a magnetic field 10^3 G and a size of a few 10^{-5} parsec can reach about the same energy.
- The explosion of a GRB leads to the formation of multiple shock regions, which are acceleration zones for UHECRs. The value of the magnetic field at these shocks is estimated to be of order $B \sim 10^6$ G at a distance $R \sim 10^{12}$ cm from the center [200], leading to acceleration of particles up to $\sim 10^{20}$ eV.

1.2 Active Galactic Nuclei

AGN are among the most powerful steady sources of radiation in the Universe. They are galaxies that host a supermassive black hole ($M > 10^6 M_\odot$) in their center, which accretes matter and converts gravitational potential energy into radiation. This radiation spans the entire electromagnetic spectrum, from radio wavelengths to γ-rays, with bolometric luminosities from 10^{42}erg/s up to 10^{49}erg/s [327]. Only 1% of the galaxies in the Universe host an AGN.

A brief overview of the main elements that characterize AGN, the physics invoked to explain the observed phenomena, is presented in the following paragraphs. A more complete reading on the subject is [257]. Figure 1.5 shows a schematic representation of an AGN and the AGN unification scheme, which would be discussed as well.

1.2.1 Central engine of an AGN

The compactness and the large luminosity of AGN led to the conclusion that their fueling mechanism could be based on the conversion of gravitational energy into radiation, through accretion of large amounts of material onto a massive, compact central object [e.g. 278]. Nowadays, the scientific community agrees that the central object is a Super Massive Black Hole (SMBH). Black holes are massive objects that exhibit strong gravitational effects from which no information can escape, since the escape velocity exceeds the speed of light

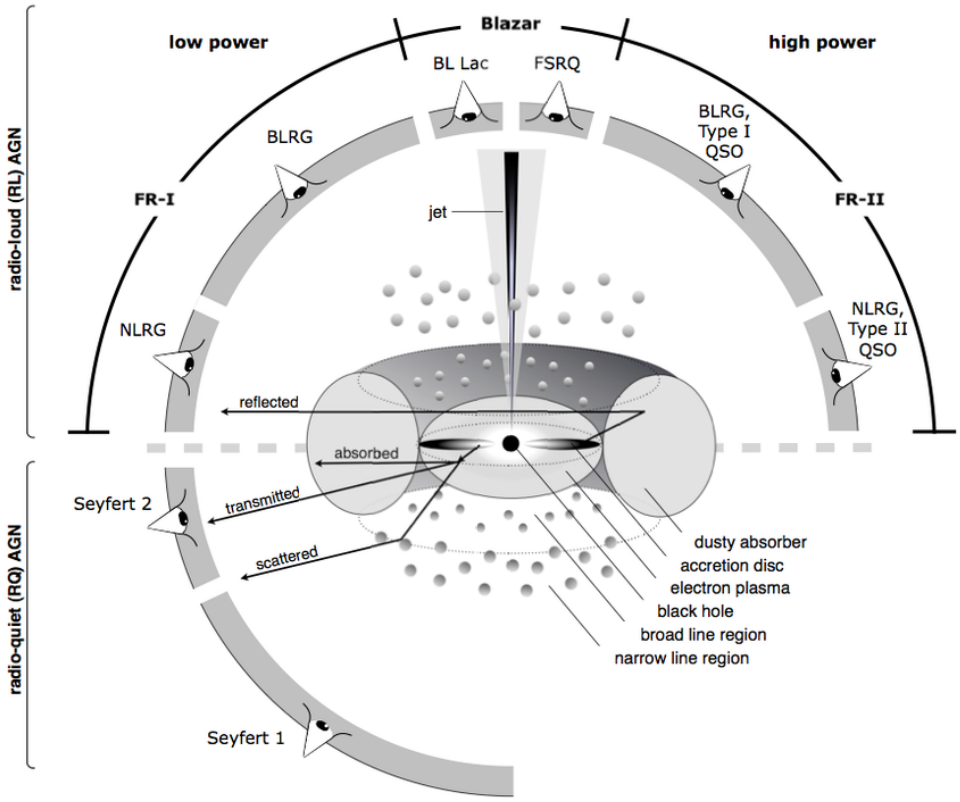

Figure 1.5: AGN unification scheme from [42].

in vacuum. The boundary over which events cannot affect an outside observer is called the *event horizon*. Usually, the *event horizon* is equivalent to the *Schwarzschild radius*, which is given by:

$$R_S = \frac{2GM_{BH}}{c^2} \tag{1.2}$$

where G is the gravitational constant, M_{BH} is the black hole mass, and c is the speed of light.

There is a theoretical upper limit for the luminosity of gravitationally bound systems: the Eddington limit L_{Edd} [276]. This limit is the point at which the outward radiation pressure on electrons due to Thomson scattering balances the gravitational pull of the accreting central object on protons. Assuming spherical symmetry and ionized hydrogen gas, the balance occurs when:

$$\frac{L_{Edd}\sigma_T}{4\pi r^2 c} = \frac{GM_{BH}m_p}{r^2} \tag{1.3}$$

where m_p is the proton mass, M_{BH} is the mass of the central black hole, and σ_T is the Thomson cross section. The Eddington luminosity is given by:

$$L_{Edd} = \frac{4\pi GM_{BH}m_p c}{\sigma_T} \approx 1.26 \times 10^{38} \left(\frac{M_{BH}}{M_\odot}\right) \text{erg s}^{-1} \tag{1.4}$$

This defines the maximum steady luminosity due to accretion under spherical symmetry.

1.2.2 Accretion disk

Assuming a radiative efficiency η (typically ~ 0.1 for thin disk accretion), we can relate the luminosity to the mass accretion rate $\dot{M}$:

$$L = \eta \dot{M} c^2 \tag{1.5}$$

The corresponding Eddington accretion rate is:

$$\dot{M}_{Edd} = \frac{L_{Edd}}{\eta c^2} \tag{1.6}$$

This provides an upper limit on the accretion rate assuming steady, radiatively efficient accretion.

Since the physical state of the material that accretes on the SMBH depends on the accretion rate, it can take the form of a geometrically thin, optically thick rotating disk of gas [285], when $\dot{M}/\dot{M}_{Edd} \gtrsim 0.01$, or a geometrically thick, optically thin, spherically-symmetric disk of gas [e.g. 43], called Advection Dominated Accretion Flow (ADAF), when $\dot{M}/\dot{M}_{Edd} \lesssim 0.01$. This last category of disks is characterized by a very low particle density, leading to inefficient cooling of the flow. This will cause the material to be heated by viscous friction up to 10^9 K. The emission spectrum of a disc with an ADAF configuration is dominated by non-thermal emission by electrons from radio to X-ray energies. Nevertheless, an ADAF disk does not contribute much to the overall emission observed from the system, due to its lower radiative efficiency.

Figure 1.6 shows the Spectral Energy Distribution (SED) of AGN. The presence of an efficient disk is well recognizable in the optical-UV band, and it is known as *Big Blue Bump*, which is the blue dashed line in Figure 1.6.

1.2.3 Hot corona

From X-ray observations, in the inner region of every AGN, a corona of low-density, high-temperature gas resides above the accretion disk, with $T = 10^6 - 10^7$ K. The photons from the accretion disk are scattered, through Inverse Compton, by the high-energy electrons in the corona. These scattered photons represent the hard X-ray emission in light blue in Figure 1.6 with a power-law shape [164]. Part of these scattered photons are absorbed by the accretion disk and give rise to the fluorescent Kα lines. The most prominent one is the iron line at 6.4 keV, which is the dashed green line in Figure 1.6.

1.2.4 Broad Line Region and Narrow Line Region

The optical spectrum of AGN is characterized by strong excitation and emission lines. They are emitted by the gas orbiting around the black hole and are excited through photoionisation by the continuum emission from the accretion disk and the corona. Photoionisation is the process by which an atom or molecule absorbs a high-energy photon, typically from ultraviolet or X-ray radiation, and loses one or more electrons. In the context of AGN, the intense radiation from the accretion disk ionizes the surrounding gas, which then re-emits energy as characteristic emission lines when electrons recombine or transition to lower energy levels. It is established that these lines are of two kinds [196]: broad lines due to a Doppler broadening due to orbital speeds of $10^3 - 10^4\,\mathrm{kms}^{-1}$ and narrow lines with a smaller Doppler broadening due to orbital speeds of $\sim 10^2\,\mathrm{kms}^{-1}$. To explain these two categories, two distinct spatially separated regions are taken into account: the Broad Line Region (BLR) and the Narrow Line Region (NLR) [262]. The

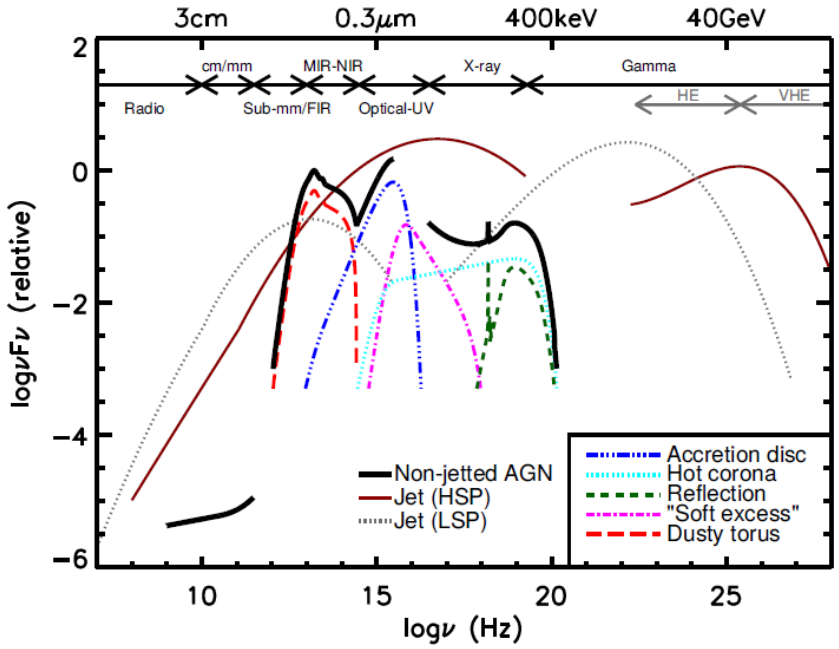

Figure 1.6: Typical SED of different kinds of AGN, from [257]. The black curve depicts the SED of a non-jetted AGN. The black solid curve represents the total emission, and the various coloured curves, shifted down, represent the individual components. The red dotted line is the SED of a BL Lac object, while the blue dotted line corresponds to a Flat Spectrum Radio Quasar (FSRQ). Each SED is plotted in relative units.

BLR is characterized by short flux variability and is located close to the black hole, within $10^{-2} - 1\,\mathrm{pc}$. The NLR has a more extended shape and is located above a few hundred parsecs.

1.2.5 Dusty Torus

From X-ray and optical observations, it results that some AGN are less bright in X-rays, have a fainter, redder continuum, and lack broad emission lines. This implies that a dense structure along our line of sight is absorbing radiation from both the central engine and the BLR. According to its location, this absorber must be between the narrow-line region (NLR) and the supermassive black hole (SMBH) [31], typically at a distance of $1 - 10\,\mathrm{pc}$ from the SMBH. This structure, made of dust grains, re-emits the radiation it absorbs in an energy range that ranges from the millimeter to the far-infrared [41]. This kind of emission is shown in the SED in Figure 1.6 by the red dashed line.

In order to explain why not all AGN show signs of this structure, [31] hypothesizes that the geometry is a torus. The toroidal shape generates an anisotropic absorption of photons, and depending on the viewing angle, the observed spectrum can be different. The distribution of dust within may either follow a homogeneous distribution [264] or have a clumpy shape due to the existence of clouds of dust [207].

1.2.6 Relativistic jets

AGN can form jets that are observed on scales from astronomical units to megaparsecs and from radio frequencies to TeV energies. High-resolution radio imaging and multi-wavelength and multi-messenger campaigns are elucidating the conditions under which

this happens [49]. Jets were more common when the Universe was a few billion years old and black holes and massive galaxies were growing. Furthermore, jets have a huge influence on the life of their host galaxy: they stimulate and limit its growth. This phenomenon is called *AGN feedback* [114].

Radio observations were the fundamental step that showed that jets are relativistic. A characteristic signature is the presence of superluminal knots. They are areas of enhanced flux intensities within the jet, mostly ascribed to the presence of shocks in the plasma outflow. Two main relativistic effects characterize AGN's jet:

- The superluminal motion is a projection effect due to relativistic motion at small angles to the line of sight. Suppose a blob in a radio jet emits radiation at a time t_1 in the core at the position A in Figure 1.7. In the comoving frame, the blob moves with velocity v to B in a time interval $\delta t = t_2 - t_1$, where t_2 is the instant at which a second photon is emitted. For an observer in O at a distance D_L, the two photons arrive at t'_1 and t'_2. The apparent angular separation between the core and the blob is given by:

$$\delta\phi' = \frac{v\delta t \sin\theta}{D_L} \tag{1.7}$$

  where θ is the angle between the jet direction and the line of sight. Due to the finite speed of light, the time interval between the arrival of the two photons in O is shorter than δt. The second photon has to travel a shorter distance along the line of sight by an amount $v\delta t \cos\theta$, leading to

$$\delta t' = \delta t - \frac{v\delta t \cos\theta}{c} = \delta t(1 - \beta\cos\theta) \tag{1.8}$$

  where $\beta = v/c$. The apparent transverse velocity inferred by the observer O is:

$$\beta_{\rm app} = \frac{v_{\rm app}}{c} = \frac{D_L\,\delta\phi'}{c\,\delta t'} = \frac{\beta\sin\theta}{(1-\beta\cos\theta)}. \tag{1.9}$$

  For relativistic velocities ($\beta \simeq 1$) and small viewing angles, $\beta_{\rm app}$ can exceed unity, giving rise to the phenomenon of apparent superluminal motion.

- The Doppler boosting. Suppose a blob is moving at relativistic speed in the jet. The radiation it emits is beamed at an angle $\theta \sim 1/\Gamma$, where $\Gamma = (1-\beta^2)^{-1/2}$ is the bulk Lorentz factor of the jet. If I is the intensity of the radiation emitted at a frequency ν_0, considering the relativistic transformation of frequencies, time, and solid angle, between the observer's frame and the jet rest frame (for more details refer to [153]), the intensity is:

$$I(\nu_0) = D^3 I'(\nu'_s) \tag{1.10}$$

  where $D = \{\Gamma[1 - \beta cos(\theta)]\}^{-1}$ is the Doppler factor, θ is the viewing angle, I' and ν_s are the intensity and the frequency seen by the observer. Integrating over frequencies, we obtain the flux transformation:

$$F = D^4 F' \tag{1.11}$$

  The Doppler factor is larger with a smaller viewing angle and can be very large when the velocity of the blob is close to c.

Thanks to the observations of AGN at different frequencies, it is possible to define three scales of AGN jets:

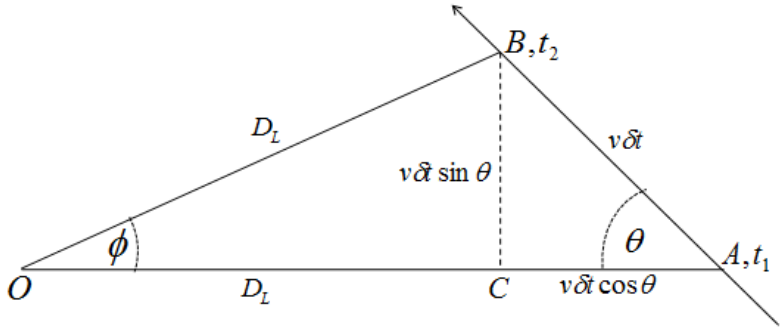

Figure 1.7: schematic view to explain how superluminal motion works inside a radio AGN jet. This relativistic phenomenon happens when an observer in A sees a radio source moving from B to B' at a velocity larger than the velocity of light in the void.

- Black hole jets, which are the most inward part of the AGN jet. Here, the environment is dominated by the black hole potential and the inflow onto an accretion disk and the outflow from it [49]. This scale extends from the gravitational radius of the black hole $R_g = GM_{BH}/c^2 = 1.5(M_{BH}/10^6 M_\odot)$ to the radius in which the influence of the SMBH ends: $R_{inf} = GM/\sigma^2$, where σ is the 1D central stellar velocity dispersion. Most Very Long Baseline Interferometry (VLBI) images are on scales larger than R_{inf}, so there are a few studies that show this region. One of these is shown in Figure 1.8. These kinds of studies are opening a new understanding of how collimation of the jets is working.

- Galaxy jets ($R_{inf} \lesssim R \lesssim 0.1R_{lobe}$), where R_{lobe} is the maximal extent of the jet. These are the canals along which energy, momentum, mass, and magnetic flux flow from the black hole and its accretion disk to the giant radio lobes [49]. What we see is strictly linked to the interaction the jets have with their environment, their radiative losses, and their shape when they were originated. The structure and the kinematics in radio of these jets have three main characteristics. The first is that they are one-sided [325], which means that only one jet is visible in radio observations, typically extending from the core to the lobe, while the opposite jet is not detected or is much fainter. This effect is due to the orientation of the jet in comparison to the line of sight and to the Doppler boosting. The second one is that their structure is characterized by a compact flat-spectrum core at one end of a steep-spectrum jet [269]. The last one is components, called knots, often seen to expand or to move along the jet away from the core at superluminal speeds [334]. Their apparent velocity ranges from $0.03c$ to $40c$. Almost all the AGN with the fastest moving components have been detected by the *Fermi Gamma-ray Space Telescope*, indicating a strong correlation between bulk Lorentz factor and γ-ray emission. The majority of the features observed within the first parsec are superluminal and are accelerating.

- Lobe jets ($0.1R_{lobe} \lesssim R \lesssim R_{lobe}$). Here, the jet is controlled by its backflow and by the circumgalactic medium. They have compact regions, called hot spots, as well as compact cores in their nuclei. This supported a continuous energy supply from the nucleus to the lobes by jets.

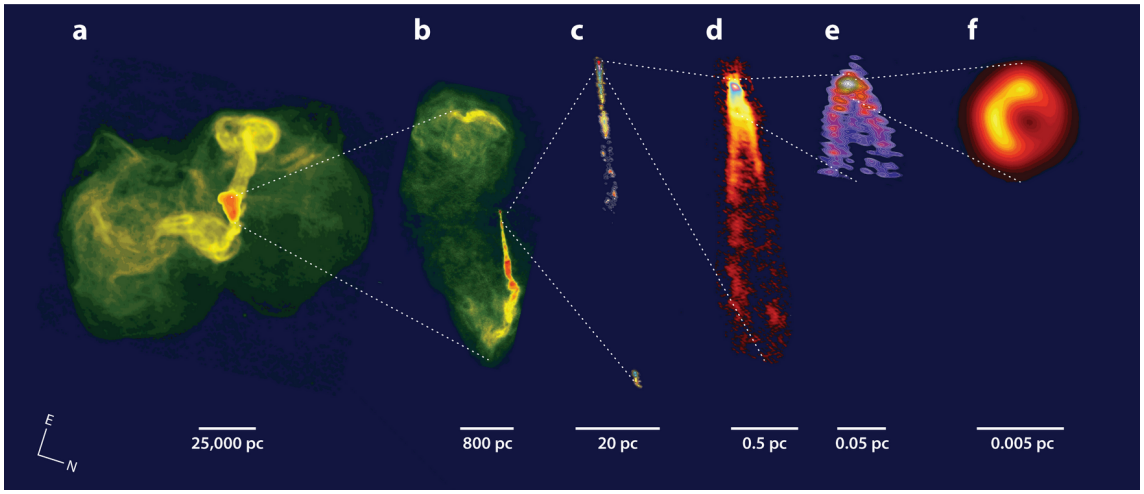

Figure 1.8: Montage of the FR-I radio galaxy M87 on scales from the outer lobes to near the black hole. (a) Lobe jet and outer lobes, showing the present outburst and a more ancient one almost perpendicular to the former; (b) galaxy jet and inner lobes; (c) full view of the black hole jet; (d) innermost jet; (e) jet launching region near supermassive black hole; and (f) inner accretion disk and black hole. The images are from the following projects (a) NRAO, 90-cm VLA; (b) NRAO, 20-cm VLA; (c) NRAO, 20-cm VLBA [76]; (d) NRAO, 7-mm VLBA [317]; (e) 3-mm global VLBI network [197]; (f) 1.3-mm Event Horizon Telescope [82] image of an accretion disk and a supermassive black hole. Abbreviations: FR-I, Fanaroff–Riley type 1; VLA, Very Large Array; VLBA, Very Long Baseline Array; VLBI, very long baseline interferometry [49].

1.2.7 AGN Unification

Historically, AGN were classified depending on the energy band in which they were observed, without thinking about a correlation between different bands [257]. Hence, the classification of AGN is still under debate. The unification of AGN is a theory that proposes that different observed types of AGN are actually the same basic object viewed from different angles. This means that the apparent differences in their observed properties, like luminosity and spectral features, are due to the orientation of the AGN relative to the observer [308]. A simplified classification will be given in order to provide an overview of the actual state of the AGN unification, but to have a broader and deeper explanation of it, refer to [257]. A simplified model of AGN unification is shown in Figure 1.5.

Radio-quiet galaxies

From Figure 1.5, it is possible to identify the class of radio-quiet galaxy, whose spectral energy distribution is shown by the continuous black line in Figure 1.6. Radio-quiet galaxies do not exhibit a large-scale relativistic jet; therefore, they are also called “non jetted” AGN. The lack of prominent radio emission of these sources is not due to orientation effects, but reflects intrinsic properties of the source. Indeed, radio-quiet AGN are characterized by a radio-to-optical flux ratio smaller than 10 and by an emission that is largely dominated by thermal components arising from the accretion disk and the dusty torus [259]. While weak outflows or compact radio structures may be present in some radio-quiet AGN, they are typically confined to sub-kiloparsec scales and do not develop into the powerful, collimated relativistic jets observed in radio-loud sources (see Section 1.2.7).

There are 2 types of radio-quiet galaxies, based on the orientation of the line of sight:

- Type 1: the central system, the accretion disk, and the BLR are not obscured by the torus. As a result, the observer observes bright X-ray emission and a blue optical continuum, with both narrow and broad spectral lines coming from these regions.
- Type 2: the line of sight intercepts the dusty torus, so the observer does not see the broad lines coming from the BLR and the emission coming from the central engine caused by the high absorption of the torus. Hence, this type of AGN have much weaker X-ray emission, and a redder optical spectrum with only narrow lines coming from the NLR.

Radio-quiet galaxies are Seyfert galaxies, which have very low luminosity, and it is still possible to observe the host galaxy, which is typically of spiral morphology, and radio-quiet Quasi-Stellar Object (QSO), which are more luminous. Radio-quiet galaxies are $\sim 90\%$ of the AGN [258].

Radio-loud galaxies

Radio-loud galaxies or jetted galaxies are $\sim 10\%$ of all AGN. The non-thermal radiation coming from the jet dominates the SED from radio to TeV energies. In this case, too, the difference between types depends on the angle between the line of sight and the relativistic jet:

- Fanaroff-Riley (FR) galaxies: these galaxies are viewed at large angles relative to the jet's axis ($> 10\,\text{deg}$ [48]). This means that the relativistic effects are affecting less the radiation we see. Hence, we can see the host galaxy in the optical and large-scale radio structures formed when the jets interact with the interstellar medium (ISM). There are two types of FR galaxies:
  - FR-I galaxies are brighter toward their center and display a decrease of the radio emission along the jet as the distance from the core increases, for this reason they are referred as "edge-darkened". FR-I are usually double-sided. On kiloparsec scales, FR-I jets appear more symmetric.
  - FR-II galaxies are bright in the central region and at the hotspots, located at the ends of the radio lobes. They are referred as "edge-brightened". FR-II are usually generally more powerful and remain relativistic over larger distances. In both FR-I and FR-II galaxies, relativistic beaming affects the observed jet emission in the same way. Depending on the viewing angle and jet speed, the approaching jet can appear Doppler boosted, leading to an apparent one-sided morphology that is not intrinsically related to the FR classification.
  - Blazars are radio-loud galaxies whose jet is aligned with the line of sight (see Figure 1.5). The small viewing angle relative to the jet ($\leq 10\,\text{deg}$) results in a strong Doppler beaming of the observed emission and shorter its variability time scales due to the relativistic effects [19, 23]. As a result, the SED of blazars is completely dominated by the non-thermal jet emission. Furthermore, the variability of these sources can be as short as a few hours or as long as months. These sources can be further divided into two subclasses, which will be discussed in the following section.

It is believed that the FR-I and FR-II galaxies are the misaligned parent population of blazars [309]. In Figure 1.5, Broad Line Radio Galaxy (BLRG) and Narrow Line

Radio Galaxy (NLRG) are indicated. BLRG are radio galaxies where the torus does not obscure the central engine, while NLRG have it obscured.

1.2.8 Blazar

Blazars are detected across the whole electromagnetic spectrum, spanning about 15 decades in energy from radio frequencies to the most energetic gamma rays at energies above 1 TeV. Their SED is shown in Figure 1.6 in brown and by the grey dashed lines. They are characterized by a first hump, which spans from radio to X-rays and is due to synchrotron radiation from relativistic electrons accelerated in the jet, while the second hump has more than one explanation. The first explanation is that the particle population of the jet is dominated by electrons and positrons that are being accelerated. This is the leptonic scenario. In this case, the second hump can be explained as Inverse Compton scattering (IC) of high-energy electrons with the low-energy photon fields coming from within the jet itself. The photon fields are produced by synchrotron emission from the same electron-positron population, so this phenomenon is called Self-Synchrotron Compton [SSC, e.g. 184]. The photon fields can come from regions outside the jet, like the BLR, the accretion disk, or the dusty torus; this is called External Compton [EC, e.g. 99, 100]. In both cases, the photons can reach the typical energies of the γ-ray emission. The second explanation is that protons and ions are accelerated in the jets. Here, the second peak can be explained as a contribution of hadronic and leptonic models (lepto-hadronic scenario).

Blazars are divided into two categories:

- Flat Spectrum Radio Quasars (FSRQs) are characterized by strong emission lines with width > 5 Å. They have an accretion disc that emits in the UV and optical energy bands, which is sometimes directly visible in the SED. Those features indicate the presence of a dense photon field that is emitted isotropically close to the black hole. The energy output is dominated by the high-energy emission component. They are typically high-redshift sources.
- BL Lacertae (BL Lac) show a very weak presence or none of emission lines [281]. The width of the lines is < 5 Å. The SED of BL Lac type objects have both hump at higher energies than the FSRQ ones: the first hump can be in the hard X-ray band (~ 10 keV), while the second can be above ~ 50 GeV. BL Lacs are typically fainter than FSRQs.

Another classification for blazars is based on the spectral localization of the peak of their synchrotron emission. There are three classes based on the position in frequency ν_{peak}^{syn} of the first peak of the SED [7]:

- Low sychrotron peaked (LSP), $\nu_{peak}^{syn} < 10^{14}$ Hz.
- Intermediate synchrotron peaked (ISM), $10^{14} < \nu_{peak}^{syn} < 10^{15}$ Hz.
- High synchrotron peaked (HSP), $\nu_{peak}^{syn} > 10^{15}$ Hz.

Almost all FSRQs are LSP, with few ISP and HSP objects, while BL Lacs are evenly distributed in all three classes. [120] proposed a relationship between the ν_{peak}^{syn} and the luminosity of blazars: sources with the highest luminosities have the smallest ν_{peak}^{syn} and the IC peak is in the MeV energy range. This relationship was

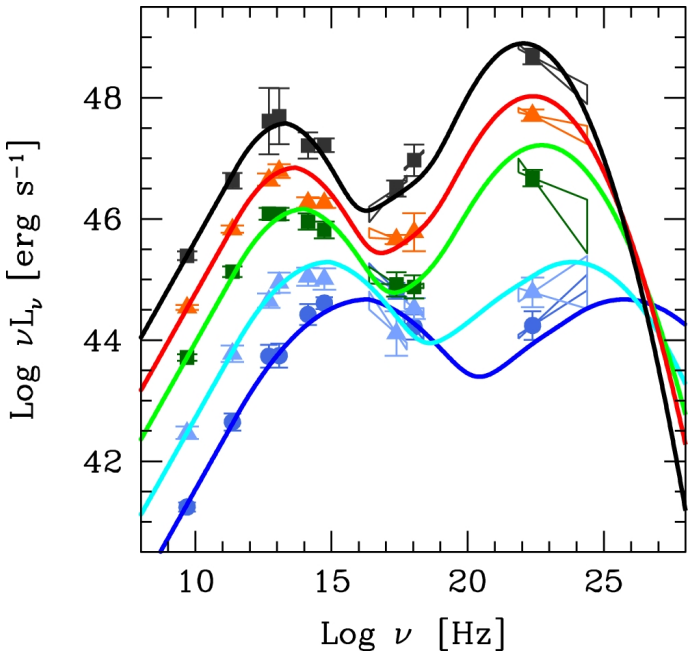

Figure 1.9: The blazar sequence from [120],[104] and [149].

built considering a sample of 126 blazars into 5 GHz radio luminosity bins, and their luminosities at selected frequencies were averaged in order to build the average SED of blazars in each bin of radio luminosity [149]. This is called "blazar sequence", it is shown in Figure 1.9 and it was confirmed by [149] using 4-year of *Fermi*-LAT data.

Despite its success in describing the average properties of blazars, the existence of a universal blazar sequence is still debated. Several studies have argued that the observed anti-correlation between bolometric luminosity and synchrotron peak frequency may be strongly influenced by selection effects related to flux-limited samples and band-dependent source selection [150, 156]. In particular, samples selected at radio frequencies tend to be dominated by luminous LSP sources, while X-ray–selected samples preferentially include HSP blazars, potentially biasing the inferred population trends.

Moreover, the discovery of high-luminosity blazars with high synchrotron peak frequencies challenges the idea of a strict luminosity ν_{peak}^{syn} relation and suggests that blazars may populate a broader region of parameter space than predicted by the original sequence [253]. These results indicate that the blazar sequence may represent a trend emerging from observational biases rather than a universal physical law.

Particle acceleration in blazar jets

There are a few questions to answer, which are fundamental in the understanding of how particles can reach energies above 100 TeV: where and how are the emitting relativistic particles accelerated? How are they transported before they cool down?

To explain how particles are accelerated, a basic mechanism involves charged particles gaining energy when exposed to an electric field. In this case, the acceleration is called electrostatic. This kind of acceleration likely occurs in the magnetospheres

of SMBH; however, it cannot explain most of the observed jet emission [49].

The main invoked mechanism to explain particle acceleration is the *diffusive shock acceleration* (see Section A.1.3 for more details). Shocks at high Mach number can accelerate particles efficiently, as observed in SNRs. [107] shows that a simple strong planar shock with a compression ratio $r \sim 4$ can explain most of the synchrotron and Compton spectral shapes often observed. Weaker shocks can account for steeper-spectrum sources. The shock can accelerate particles to high energy because a magnetic field is also created at the shock front by the accelerating particles. The maximum energy that the particles can reach is determined by the shock width or radius of curvature. The complication of this model is that the very highest-energy particles can escape upstream from the curved shock front, although most accelerated particles will be transmitted downstream and can lose energy during the expansion of the shock front and through cooling. Despite this limitation, shocks remain a good candidate for particle acceleration in galaxy jets, the hot spots, and the radio lobes [49].

However, shock acceleration may not be efficient in the magnetically dominated relativistic plasma [45, 288, 290]. Hence, another proposed mechanism is *magnetic reconnection*, which can explain the SED broadband emission. *Magnetic reconnection* occurs when two magnetized plasma regions of opposite polarity come in proximity. The magnetic field lines that originally belonged to one or the other polarity domains come together and reconnect with one or more X-points where the current-perpendicular magnetic field goes to zero [233]. *Magnetic reconnection* offers a natural way of producing compact magnetized structures, called plasmoids, moving at relativistic speeds with respect to the co-moving frame of the jet [236]. Plasmoids can accelerate particles, can grow in size through mergers with other neighboring plasmoid, and are the main candidate sites for the production of short-duration, as short as minutes, γ-ray flares from blazars [154, 263]. A schematic view that represents this mechanism inside the jet of a blazar is shown in Figure 1.10.

Another mechanism that is used to explain particle acceleration in scenarios where turbulent magnetic fields dominate the energy gain process is *stochastic acceleration* or *second-order Fermi acceleration* (see Section A.1.3 for more details). In this case, charged particles undergo random scatterings moving in magnetic inhomogeneities or plasma waves. This process naturally leads to particle energy distributions that deviate from simple power laws, often producing curved or log-parabolic spectra [229, 305]. The curvature arises from the balance between stochastic acceleration and radiative cooling, with the former being particularly efficient in regions of strong turbulence, such as those expected downstream of shocks or in magnetic reconnection sites [312]. Stochastic acceleration models have been successfully applied to explain both the steady-state emission and short-timescale variability in blazars.

Leptonic processes

In a purely leptonic approach, the mechanism responsible for the first hump of the low-energy component in the SED of blazars is the synchrotron radiation emitted by non-thermal electrons. Synchrotron radiation is emitted when a charged relativistic particle is accelerated in a magnetic field. When a particle with charge e and Lorentz factor γ moves through a uniform and static magnetic field B', it experiences a Lorentz force perpendicular to its direction and follows a helical trajectory around

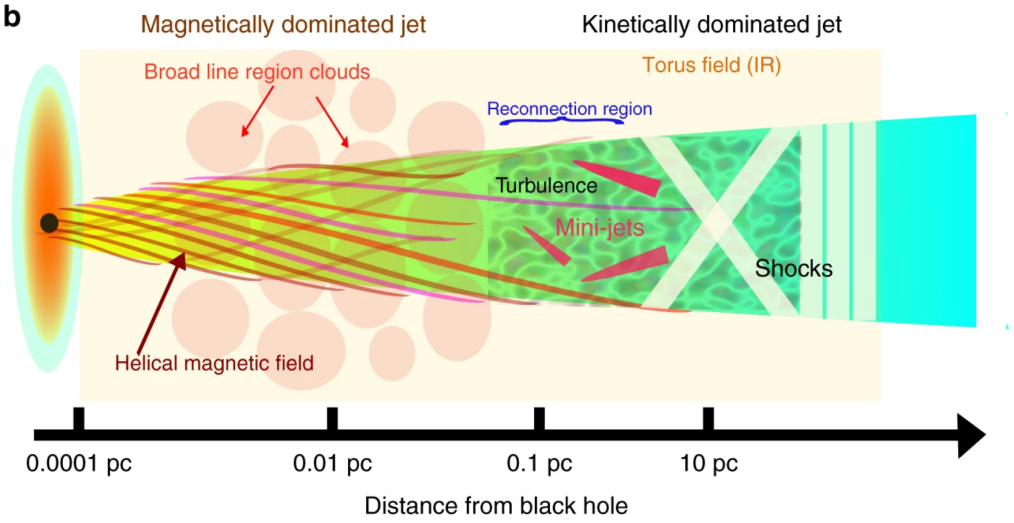

Figure 1.10: Schematic view of the inner regions of a blazar's jet. In this scenario, the magnetic field fragments into small plasmoids that interact and grow within the reconnection region. Subsequently, these massive plasmoids lead to the formation of mini-jets, which produce optically thin minute-scale γ-ray flares. This picture is courtesy of [288].

the magnetic field lines. The characteristic gyration frequency is given by:

$$\nu = \frac{eB'}{2\pi\gamma mc} \tag{1.12}$$

where m is the mass of the charged particle and γ is the Lorentz factor in the comoving frame [153]. A scheme of this motion is shown in Figure 1.11. The bolometric synchrotron luminosity radiated by a population of electrons with number density N' is given by [299]:

$$L_{syn} = \frac{4}{3}\sigma_T c U'_B \langle\gamma^2\rangle N' V' \delta^4 \tag{1.13}$$

where σ_T is the Thompson cross section, $U'_B = B'^2/8\pi$ is the magnetic energy density, $\langle\gamma^2\rangle$ is the mean squared Lorentz factor of the electrons in the comoving frame, V' is the comoving emitting volume, and δ is the Doppler factor accounting for relativistic boosting [300].

To successfully interpret the synchrotron spectrum of most blazars, it is necessary to assume that the number density of the electrons follows a simple power-law in the form:

$$N(E) = N_0 E^{-\delta} \tag{1.14}$$

The resulting emission spectrum is a power-law with a flux density:

$$S_{syn}(\nu) \propto \nu^{\alpha} \tag{1.15}$$

where α is the spectral index defined as: $\alpha = (\delta - 1)/2$ with typical values $0.5 < \alpha < 1$. In the real-case scenario, the spectrum is not a simple power law but shows a break at a certain frequency ν_{max}, due to the transition from a range of frequencies where the source is optically thick to a range where it is optically thin. In this case, we talk about optically thick material, and this effect is called *synchrotron self-absorption* [42]. Below ν_{max}, the spectrum follows a power law shape with $\alpha^{5/2}$;

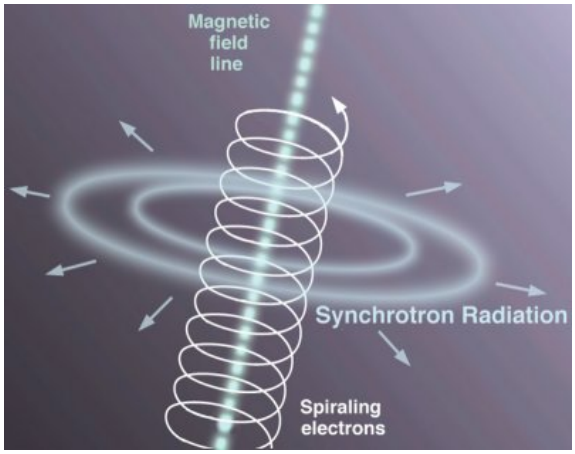

Figure 1.11: Schematic representation of the synchrotron emission process. Image: Jon Lomberg/Gemini Observatory.

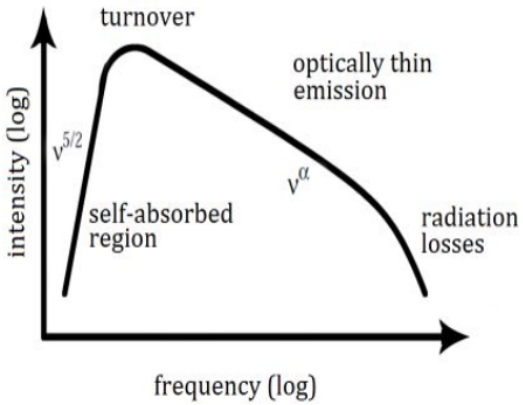

Figure 1.12: Schematic representation of a typical synchrotron spectrum. The spectral index α is negative. Courtesy of Special Astrophysical Observatory of the Russian Academy of Sciences: `http://www.sao.ru/hq/giag/gpsen`.

above ν_{max}, the spectrum follows the power law in Equation 1.15. Figure 1.12 shows a typical synchrotron spectrum.

The second hump of the SED can be explained by the up-scattering of low-energy photons by the relativistic electrons. This process is the IC and is responsible for giving energy to the photons from radio to γ-ray energies. The frequency of up-scattered photon scales as $\nu_{IC} \sim \gamma^2 \nu$. The luminosity produced at high energy via the IC process depends on the electron Lorentz factor, on the density of seed photons, and on the photon-electron cross section:

$$L_{IC} = \frac{4}{3} \frac{v_e}{c} \sigma_T \gamma^2 U_{ph} \tag{1.16}$$

where U_{ph} is the energy density of the seed photon and σ_T is the Thomson cross section. This expression is valid in the so-called Thompson scattering regime in which photons have energies $h\nu \ll m_e c^2$. For higher seed photon energies, the process occurs in the so-called Klein-Nishina regime, where the Compton cross section reduces as the photon energy increases [53]. The IC spectrum then cuts off sharply at high energies.

A useful quantity used to estimate the ratio between the energy densities of electrons and magnetic field in SSC models is the *Compton dominance*, given by the ratio of the IC luminosity to the synchrotron luminosity:

$$\frac{U_{ph}}{U_B} = \frac{L_{IC}}{L_{syn}} \tag{1.17}$$

The peak frequencies of the two components of the SED (synchrotron and SSC), are related to this relation: $\nu_{IC} \sim \gamma_{max}^2 \nu_{syn}$ where γ_{max} is the maximum Lorentz factor in the electron distribution.

Hadronic processes

The second hump of the SED of blazars may also be produced by hadronic particles. Hadronic models are taken into account since blazars are considered to be candidate sources of UHCRs, as mentioned in 1.1.1.

In astrophysical environments, a direct signature of the presence of accelerated protons is provided by the presence of neutrinos and γ-rays [291]. Both of them are mainly generated in the decay of charged and neutral pions, respectively. These particles are produced in proton-proton collisions:

$$p + p \rightarrow \pi^{\pm}, \pi^0, K^{\pm}, K^0, p, n, ... \tag{1.18}$$

This process is called *astrophysical beam dump*. A second process that produces charged and neutral pions is the leptohadronic interactions. In leptohadronic interactions, the SSC component from the primary electrons can also contribute to the high-energy SED component. These interactions are due to high-energy protons interacting with low-energy photons and producing the Δ^+ resonance:

$$p + \gamma_\epsilon \rightarrow \Delta^+ \rightarrow \pi^0 + p, \tag{1.19}$$

$$\rightarrow \pi^+ + n, \tag{1.20}$$

Neutral pions decay into γ-rays:

$$\pi^0 \rightarrow \gamma\gamma \tag{1.21}$$

This decay is important for the contribution to the γ-ray emission observed in the SED. Charged pions (π^+) decay into neutrinos:

$$\pi^+ \rightarrow \mu^+\nu_\mu \rightarrow e^+\nu_e\overline{\nu_\mu}\nu_\mu \tag{1.22}$$

Another process is the Bethe–Heitler pair production:

$$p + \gamma \rightarrow p' + e^+ + e^- \tag{1.23}$$

The photons from the neutral pion decay and the synchrotron radiation of the pairs, produced by the decay of π^+ and the Bethe-Heitler process, are sufficiently energetic such that they can interact with the ambient low-energy photon and develop electromagnetic cascades. The high-energy hump in the SED is produced by the photons emitted in these cascades. Also, the synchrotron emission from protons and muons can contribute. As [72] shows, hadronic and leptohadronic models have a huge disadvantage: they require a very high luminosity of the proton population to describe the SED. The luminosity can be several orders of magnitude higher than the Eddington luminosity, implying super-Eddington accretion rate by the black hole. This is valid only in the case of FSRQ and LSP, which are the brightest blazars and are the main focus of this work.

The connection between γ-ray emission and VLBI kinematics

Several studies linked the γ-ray variability from AGN jets, in particular radio galaxies, to their inner pc-scale jet changes, thanks to VLBI observations.

The earliest VLBI images showed that the emission from high VLBI frequencies occurs closer to the central engine [269]. These observations show the optically thick, flat-spectrum core at the end of the jet close to the SMBH. In general, the higher the radio frequency emission is, the closer to the SMBH the photon is produced than the lower frequency emission.

The interesting question here is whether the same is true when going to even higher energy bands, including γ-rays [49]. Since only VLBI offers milli-arcsecond resolution, most of the studies of the relative locations of the emission regions in different observing bands regard variability and SED studies. The Max Planck Institute for Radio Astronomy (MPIfR) multi-frequency "FGAMMA" monitoring survey showed significant correlations between the radio and γ-ray flux density variations in some AGN [123]. In all such cases, the radio variations lagged behind the γ-ray variations by about a hundred days. Hence, it is clear that in some AGN the γ-ray emission regions are closer to the SMBH than the radio emission regions. However, there are also observations that show that in some AGN the γ-ray and radio emission regions are the same [188, 189, 226]. It appears that γ-ray emission from AGN occurs at a variety of sites, some close to the SMBH and some close to the radio-emitting regions.

To deepen the knowledge about the radio and γ-ray correlation, [68], [188], and citation therein, studied the evolution of the pc-scale radio jet of some AGN during a period of γ-ray activity. They found that every period coincident with a γ-ray

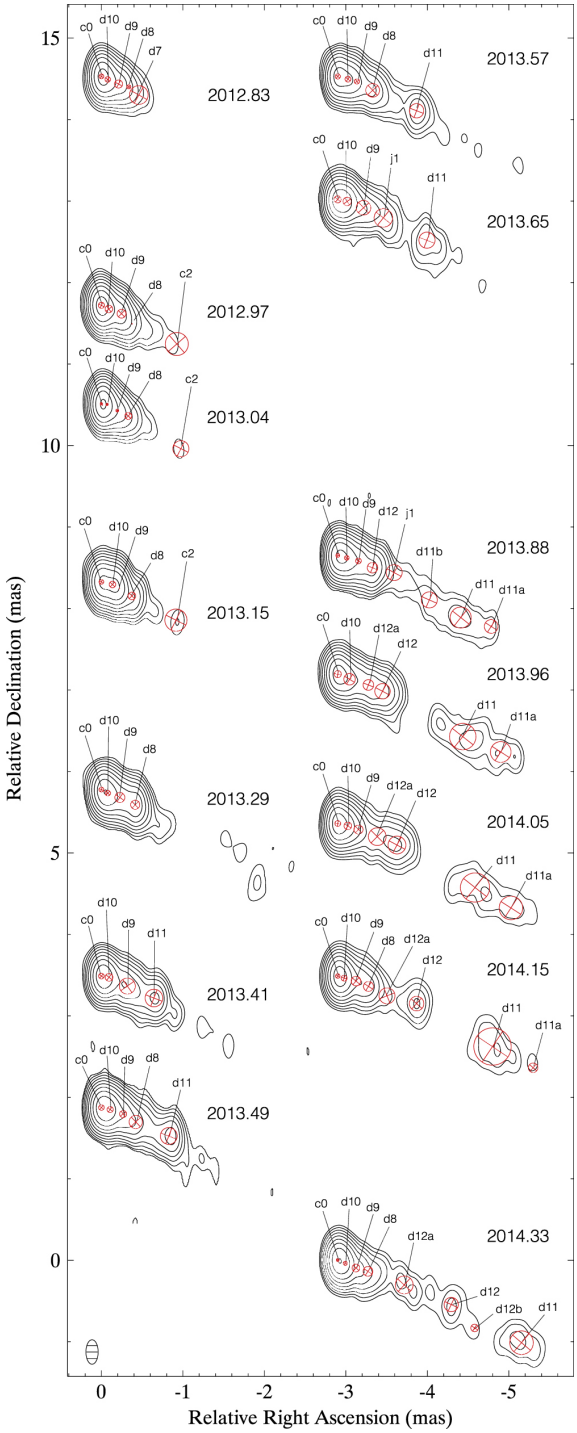

Figure 1.13: Sequence of total intensity 43 GHz Very Large Baseline Array (VLBA) images from the VLBA-BU-BLAZAR monitoring program of 3C 120. Red circles represent the components. Courtesy of [68].

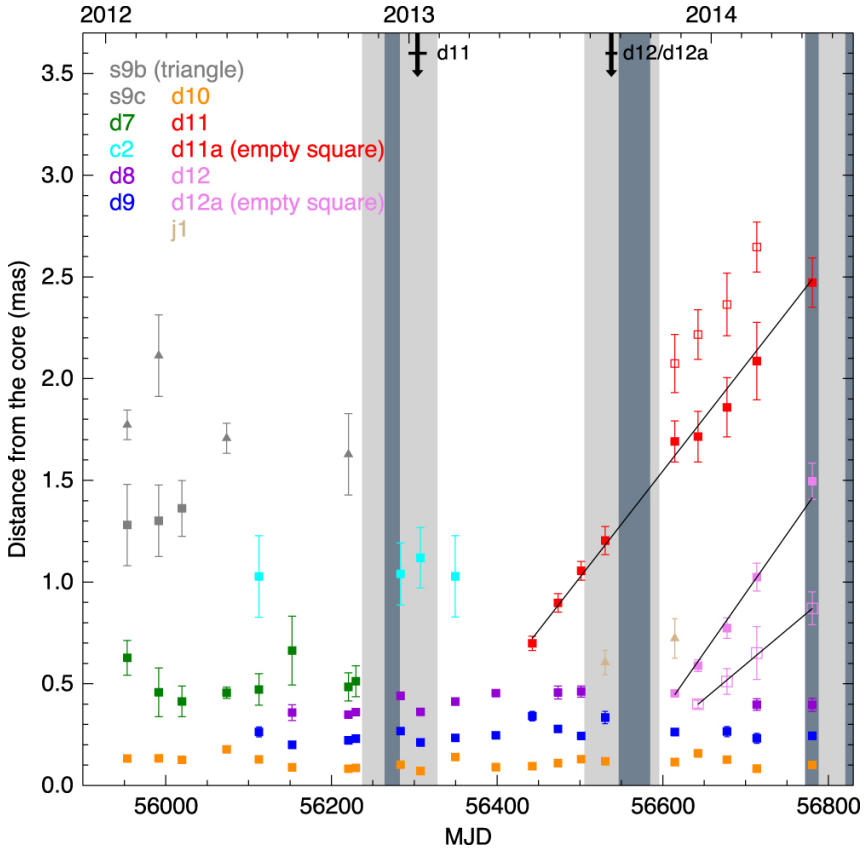

Figure 1.14: Distance from the core versus time in MJD for the 43 GHz components with linear fits overlaid. Downward black arrows mark the time of ejection of each component. Gray vertical lines indicate *Fermi*-LAT γ-ray detections in the 15-day bin (dark gray) and 3 month bin (light gray) light curves in the energy band 500 MeV–100 GeV. Courtesy of [68].

detection corresponds to the ejection of a new superluminal component, called knot, from the radio core, but the opposite is not true. The ejection and the time of the flaring γ-ray activity could be lagged depending on the position of the γ-ray emitting region, as explained above. An example of this kind of long-term study, which shows the ejection of new knots from the core and the kinematic study that derives from it, is shown in Figure 1.13 and Figure 1.14.

Chapter 2

Space and Earth-based Telescopes

In this Chapter, different space and Ground-based telescopes and techniques will be shown. The techniques shown here are used in the next parts of the thesis for the analysis and simulations of the data.

2.1 Gamma-ray space telescopes

As Figure 1.2 shows, γ-rays are completely absorbed by the Earth's atmosphere, so to directly detect them, it is necessary to use experiments on balloons or space telescopes. γ-rays pass through most materials, so they cannot be reflected by a mirror. Hence, space-based γ-ray detectors generally use scintillators or solid-state detectors to transform the γ-ray into optical or electronic signals. Scintillators are materials, either crystals, liquids, or plastics, that emit light when a high-energy particle or photon deposits energy in them. Solid-state detectors detect radiation by converting ionizing energy into electron–hole pairs inside a semiconductor. Detectors of these types rely on the nature of the γ-ray interaction process to calculate the arrival direction of the incoming photon, such as pair production or Compton scattering. Compton scattering occurs when a photon hits an electron and some of the photon energy is transferred to the charged particle. The Compton scatter telescopes are typically two-level instruments and work at energies between 100 keV and 30 MeV. In the top level, the cosmic γ-ray Compton scatters off an electron in a scintillator. The scattered photon then travels down into a second level of scintillator material that completely absorbs the scattered photon. Phototubes determine the interaction points at the two layers and the amount of energy deposited in each layer. Instead, the pair telescope works at energies above 30 MeV. The instrument design is a layered telescope, with layers that convert γ-rays into electron-positron pairs ($e^- - e^+$ pairs) interspersed with silicon strip layers that track those pairs, which travel with a kinetic energy given by $E_{pair} = E_\gamma - 2m_e c^2$. The converter is typically a heavy metal, like tungsten. By reconstructing the tracks of the charged pair, the γ-ray direction, and therefore its origin on the sky, is calculated. In addition, through the absorption of the pair by a scintillator detector or a calorimeter after they exit the tracker, the total energy of the initial gamma-ray is determined.

The first γ-ray detector in orbit was carried on board the Explorer 11 satellite in

1961, which picked up fewer than 100 photons. These photons were coming from all directions in the sky, so they were attributed to a uniform γ-ray background. This background was expected to be produced by the interaction of cosmic rays with the interstellar medium (ISM) [206]. Significant γ-ray emission was detected by the space telescope COS-B [47], which confirmed the earlier detection of a γ-ray background and produced the first map of the γ-ray sky, and detected several point sources. However, the resolution of the instrument was insufficient to identify most of these point sources with specific known objects. To have better sensitivity and a first catalog of the γ-ray sky at energies above 100 MeV, the scientific community had to wait until the 90s, when the Compton Gamma-ray Observatory (CGRO) was launched. The Energetic Gamma-Ray Experiment Telescope (EGRET) was the high-energy instrument on CGRO, covering the energy range from 20 MeV to 30 GeV [291]. It contributed to breakthrough observations of AGN, pulsars, Gamma-ray Bursts (GRBs), solar flares, and diffuse γ-ray emission, with a total of 271 objects in the last EGRET's catalog [168]. The INTEGRAL satellite (INTErnational Gamma-Ray Astrophysics Laboratory), developed by the European Space Agency (ESA) in partnership with the United States and Russia, was launched in 2002 on a mission to observe γ-rays in the energy range $3\,\text{keV} - 10\,\text{MeV}$, X-rays between $3 - 35\,\text{keV}$, and optical wavelength between $500 - 580\,\text{nm}$. Its principal targets were GRBs, SNRs, and regions that may contain black holes. In April 2007, the Astro-rivelatore Gamma a Immagini Leggero (AGILE) of the Italian Space Agency was launched. AGILE was devoted to γ-ray observations within the $30\,\text{MeV} - 50\,\text{GeV}$ energy range, with simultaneous hard X-ray imaging in the $18 - 60\,\text{keV}$ band, and optimal timing capabilities for the study of transient galactic and extragalactic phenomena. DAMPE (DArk Matter Particle Explorer) is a satellite mission of the Science of the Chinese Academy of Sciences (CAS). It was launched in December 2015, and its main goal is to detect electrons and photons in the range $5\,\text{GeV} - 10\,\text{TeV}$ in order to identify possible Dark Matter signatures.

2.1.1 Fermi Gamma-ray space telescope

The *Fermi* γ-ray Space Telescope (*Fermi*) is an international mission funded by the space agencies of the USA (NASA), France, Germany, Italy, Japan, and Sweden. It was launched on June 11, 2008, and carries two instruments: the Large Area Telescope (LAT) and the Gamma-ray Burst Monitor (GBM). The telescope is located at the 565 km altitude orbit. The latest *Fermi*-LAT source catalog, 4FGL-DR4, contains more than 7194 sources [37].

The Large Area Telescope

After *Fermi* launch, an overwhelming amount of data has significantly improved the knowledge of high-energy astrophysics. The LAT is a γ-ray telescope which detects photons with energies within the energy range 20 MeV - 300 GeV.

The LAT is a pair conversion detector made of a 4×4 array of converter-tracker modules, each including 16 converter planes of tungsten, interleaved by two orthogonal layers of silicon strip detectors used to reconstruct the position of the pair. Two additional tracker layers are present at the bottom of each module. The detector has a calorimeter to measure the pair's energy at the bottom and reconstruct the original energy of the γ-ray photon. The calorimeter is made of 96 CsI(Tl) crystals,

arranged in 8 layers of 12 crystals each, with each layer orthogonal to the previous one to provide a 2-D position. The calorimeter and the converter-tracker are fitted into an Anti-Coincidence Detector (ACD). The ACD is necessary for background rejection, since the spacecraft is subject to a high flux of cosmic rays that can interact with the detector. Hence, the detector is protected by a layer of plastic scintillator, which has a high efficiency to interact with charged particles. If an event is detected by both the ACD and the tracker, the event is rejected since it is a cosmic ray. Figure 2.1(a) shows a schematic view of how a γ-ray photon propagates in the LAT tracker and calorimeter, and Figure 2.1(b) shows the LAT tracker and calorimeter themselves. Table 2.1 provides a summary of the LAT instrument parameter and performances from [36], while Figure from 2.2(a) to 2.2(d) show the LAT performances as a function of the energy.

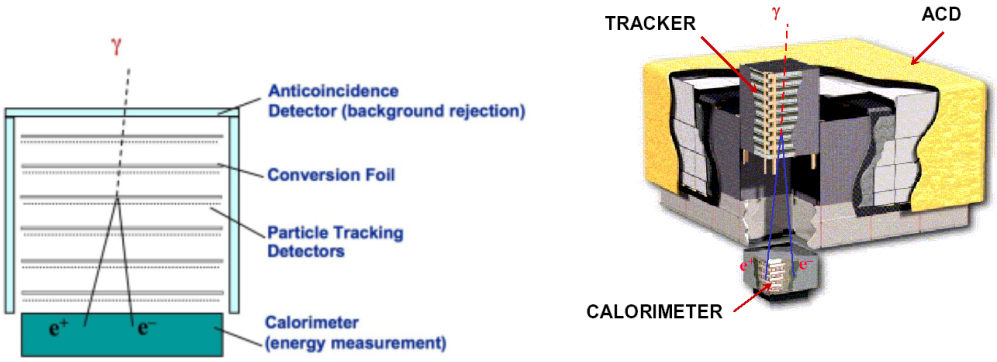

(a) (b)

Figure 2.1: a) Pair production inside the LAT and its energy measurement in the calorimeter. b) Schematic view of the LAT. These Figures are available at `https://www-glast.stanford.edu/instrument.html`.

All these plots were made after the Pass 8 event selection was published [35]. Event selections of LAT data are important to select events based on the instrument performances and background properties. There are four event selections, called passes, which have been released since 2008. The last one is the Pass 8 selection [35], which is the one used in all the analyses presented in this thesis. The Pass 8 event selection divides events into classes, and for each class, a set of Instrument Response Function (IRFs) is calculated. Moreover, there is an additional classification that depends on the event characteristics. The event hierarchies are three:

- Standard, which included all the classes recommended for LAT analysis, like the SOURCE class used for point source analysis, and lower contamination classes like ULTRACLEAN, ULTRACLEANVETO, SOURCEVETO. Standard also contains two TRANSIENT classes with higher background rate, for the short GRBs.
- Extended.
- no-ACD.

Extended and no-ACD hierarchies include classes that are defined with a less restrictive fiducial selection, such as events with projected trajectories that do not cross

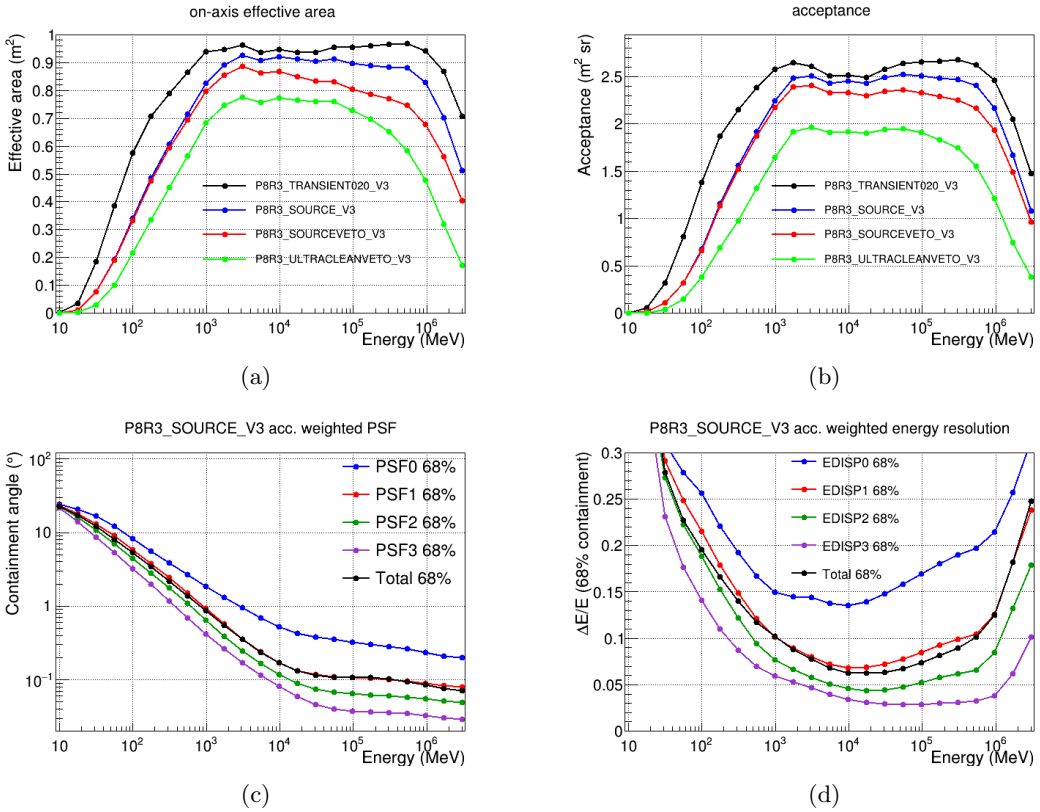

Figure 2.2: a) Effective area as a function of energy for a normal incident photon, for different event types and total. b) Acceptance (the effective area integrated over the solid angle, as a function of energy for different event types and total) versus energy. c) Acceptance Point Spread Function (PSF) as a function of energy for different PSF types and the total case. d) Point source differential sensitivity for 10 years of integration on a steady source with a uniform background, for four different sky positions (in Galactic coordinates). These Figures are available at `https://www.slac.stanford.edu/exp/glast/groups/canda/lat_Performance.htm`.

Table 2.1: LAT on board performances. This table is adapted from Table 1 in [36].

Parameters	Range
Energy range	$20\,\text{MeV} - 300\,\text{GeV}$
Effective area[a]	$9500\,\text{cm}^2$
Energy resolution (equivalent Gaussian 1σ):	
$100\,\text{MeV} - 1\,\text{GeV}$	$9\% - 15\%$
$1\,\text{GeV} - 10\,\text{GeV}$	$8\% - 9\%$
$10\,\text{GeV} - 300\,\text{GeV}$	$8.5\% - 18\%$
Angular resolution (on-axis, 68% containment radius):	
$> 10\,\text{GeV}$	$\leq 0.15^\circ$
$1\,\text{GeV}$	0.6°
$100\,\text{MeV}$	3.5°
Field of View (FoV)	$2.4\,\text{sr}$
Timing accuracy	$< 10\,\mu\text{s}$
Point source location determination[b]	$< 0.5'$
Point source sensitivity[c]	$3 \times 10^9\,\text{photons}\text{cm}^{-2}\text{s}^{-1}$

[a] Maximum (as a function of energy) effective area at normal incidence.
[b] High latitude source of $10^{-7}\,\text{cm}^{-2}\text{s}^{-1}$ flux at $> 100\,\text{MeV}$ with a photon spectral index of -2.0 above a flat background and assuming no spectral cutoff at high energy; 1σ radius; one-year survey.
[c] For a steady source at high galactic latitude, with one year of integration.

the Calorimeter section. These classes are called TRANSIENT classes.

Furthermore, Pass 8 divides events into types:

- Front for events that undergo conversion in the front of the silicon tracker;
- Back for events that undergo conversion in the back of the silicon tracker;
- PSF, which indicates the quality of the reconstructed direction with data divided into quartiles, from the lowest quality quartile (PSF0) to the best quality quartile (PSF3);
- EDISP, which indicates the quality of the energy reconstruction. The lowest quality quartile is EDISP0, and the best quality quartile is EDISP3.

In Figure 2.2(a), the LAT has performances in the energy range 1 GeV and 300 GeV, and its top performance energy range is between 1 GeV and 10 GeV. Below 1 GeV, it is difficult to reconstruct the direction of the photons, since the separation between the electron-positron is small, and the energy dispersion, which is the difference between the reconstructed and true energy of the photon, increases. Above 300 GeV, the number of events decreases, and the area of the calorimeter is not enough to contain the energy of the photons. In Figure 2.2(c), it is illustrated how the angular resolution depends on the energy: the 68% containment radius is large at 100 MeV, but it drops quickly.

Another aspect to consider when evaluating the LAT performance is the location of the target source. In Figure 2.3 it is shown that, in Galactic coordinates, the point source sensitivity can change by almost an order of magnitude depending on the target's location to the galactic plane due to the presence of diffuse emission from the galaxy.

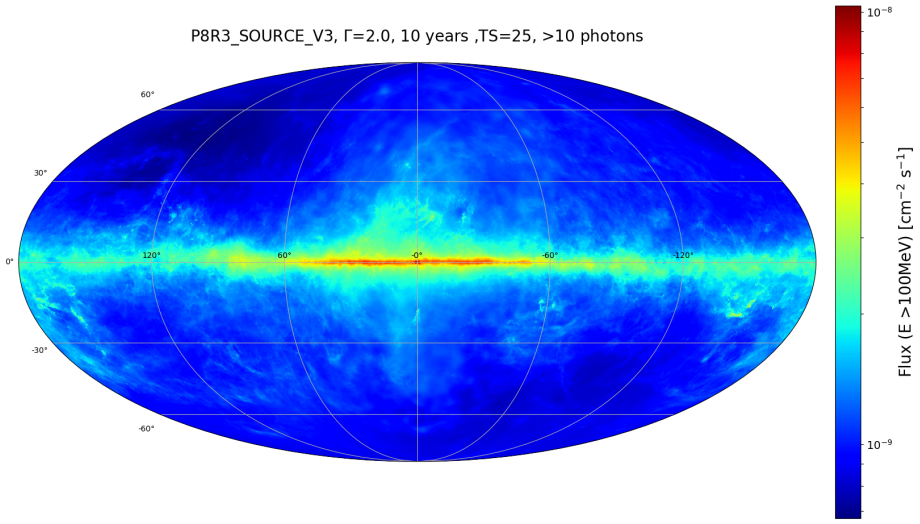

Figure 2.3: Map of the LAT 10-year integrated point-source sensitivity in Galactic coordinates, for an isolated source with a power-law spectrum with spectral index equal to 2. This is defined as the lowest flux a point source can have to reach a 5σ significance (with at least 10 detected photons) under the given conditions. This picture is taken from: `https://www.slac.stanford.edu/exp/glast/groups/canda/lat_Performance.htm`.

The Gamma-ray Burst Monitor

The Gamma-ray burst monitor (GBM) is made of twelve sodium iodide (NaI) scintillators and two cylindrical bismuth germanate (BGO) scintillation detectors, which together cover an energy range from 8 keV − 40 MeV. The GBM's field of view is larger than the LAT's and is larger than 8 sr.

The main goal of the GBM is to detect GRBs, and in addition, solar flares, terrestrial gamma-ray flashes (TGFs), and magnetars. However, GBM is also important since it is fundamental in the discovery of gravitational wave events with an electromagnetic counterpart, as a neutron star merger. This case happened in 2017 when a neutron star merger triggered a short GRB [5, 6].

Fermi-LAT data reduction

The LAT Pass 8 raw data are publicly available in the website of the *Fermi* Science Support Center (FSSC)[1]. The data are provided in the form of an event file, FT1, which contains the raw photon data, and a spacecraft file, FT2, which contains the spacecraft position and orientation in the sky in the selected time range.

The official analysis tools developed to analyze LAT data are the *Fermi Science Tools*[2] available in the Python package *fermitools*. The actual official Python wrapper is called *fermipy*[328].

[1] `https://fermi.gsfc.nasa.gov/cgi-bin/ssc/LAT/LATDataQuery.cgi`
[2] `https://fermi.gsfc.nasa.gov/ssc/data/analysis/software/`

LAT data analyzed with *fermipy* requires a `config` file which defines the data selection and analysis parameters. The most important required parameters in the `config` file are: the FT1 and FT2 files, the region of interest (ROI) usually of 15° centered at the coordinates of the target source, the spatial and energy bin size, the galactic and isotropic diffuse templates, the IRF, the LAT catalog (in this thesis both 4FGL-DR3 [10] and 4FGL-DR4 [37] catalogs were used), the energy bin, the time range of the analysis, the event class, the quality cut and the maximum zenith angle to avoid contamination from the emission due to the Earth's limb. A ROI of 15° is usually adopted in LAT analyses to properly account for the broad point-spread function below a few hundred MeV, which extends over several degree, and to accurately model the contribution of nearby sources and diffuse backgrounds [e.g. 36, 328]. Hence, a 15° ROI ensures a robust modeling of these effects while maintaining a reasonable computational cost.

Then, after importing *fermipy*'s `GTAnalys` module, it is possible to run the analysis loading the configuration file and running the `setup()` tool, which implements the *fermitools*'s `gtselect`, `gtmktime`, `gtbin`, `gtexpcube`, `gtsrcmap` routines. `gtselect` performs the selection cuts on event data files, `gtmktime` creates Good Time Intervals (GTIs) based on selections made using the spacecraft data file, `gtbin` bins the event lists in time, energy, and/or space, `gtexpcube` generates a binned exposure map, which takes into account the exposure at each position in the sky, and `gtsrcmap` creates model counts maps for use with the binned likelihood analysis.

When the `setup()` routine has finished, it is possible to start the likelihood analysis where the data are fitted.

The likelihood $\mathcal{L}$ is defined as the probability of obtaining the observed data, given an input model. The data can be binned or unbinned. Binned data counts mean that they are binned along different parameter space quantities like energy, space, and time. In this case, the likelihood is defined as the product of the probabilities of observing the detected counts in each bin. Since the number of counts per bin is small in *Fermi*-LAT, these probabilities are given by the Poisson distribution:

$$p_i = e^{-m_i} \frac{m_i^{n_i}}{n_i!} \tag{2.1}$$

where n_i are the detected counts in the i-th bin, m_i is the predicted number of counts given the model, and therefore p_i is the probability of detecting these counts given the model. The likelihood is then defined by the product of these probabilities:

$$\mathcal{L} = e^{-N_{exp}} \prod_i \frac{m_i^{n_i}}{n_i!} \tag{2.2}$$

where $N_{exp} = \sum_i m_i$ is the total expected number of counts predicted given the model, and $e^{-N_{exp}}$ is the product of all the e^{-m_i}, for all bins. This likelihood definition is the basis of the binned likelihood analysis. It implies a good adjustment between a small bin size and an acceptable number of counts per bin to obtain a statistically reliable fit.

In the unbinned case the likelihood is defined as:

$$\mathcal{L} = e^{-N_{exp}} \prod_i m_i \tag{2.3}$$

where i is the index over the counts. The unbinned approach is usually more accurate than the binned one since the counts are taken into account individually and are not averaged inside a bin. However, the unbinned approach is more computationally expensive when the number of counts is large.

The Test Statistic gives the detection significance of a source:

$$TS = 2 \ln \frac{\mathcal{L}_{max,1}}{\mathcal{L}_{max,0}} \tag{2.4}$$

where $\mathcal{L}_{max,1}$ and $\mathcal{L}_{max,0}$ are the maximum likelihood of the model to test and of the *null-hypothesis*, respectively. If the source is detected, the *null-hypothesis* model differs from the alternative model only for the exclusion of the source of interest.

For a large number of counts, the TS behaves asymptotically as a χ^2 distribution, and therefore, if the two models differ by only 1 degree of freedom (dof), the significance can be calculated as the $\sqrt{TS}$. For a larger number of dof the significance can be calculated by converting the p-value into the number of σ relative to a normal distribution.

The tool that executes the likelihood fitting in *fermipy* is the `fit()` routine.

To compute the spectral energy distribution (SED), *femipy*'s `sed()` routine can be employed. The `sed()` method fits the flux normalization in each energy bin using a power-law spectrum with a fixed index $\alpha = 2$ in the default case.

To compute the light curve, *femipy*'s `ligtcurve()` routine can be employed. `ligtcurve()` fits multiple times the spectral parameters of the target source in a sequence of time bins, in order to study the evolution of these parameters with time. A method that is used in this thesis to obtain the light curves is the *adaptive binning* algorithm [221]. This algorithm produces bins with a variable size that depends on the intensity of the source and the precision of the flux measurement. The condition that is satisfied for each bin is:

$$\frac{\sigma_{F_i}}{F_i} = const \tag{2.5}$$

where F_i is the flux in the i-th bin and σ_{F_i} is its uncertainty. The width of each bin is smaller during periods of enhanced activity of the source and longer during quiescent periods. This algorithm is used to resolve the smallest variability timescales and to have a detailed picture of the flaring activity of a source.

The Flare Advocate pipeline

The Flare Advocate (FA) shift is one of the available duties in the LAT collaboration. The all-sky monitoring of LAT is complemented by the figure of the Flare Advocate (a.k.a. Gamma-ray Sky Watcher, FA-GSW). The FA-GSW shifter inspects and daily reviews the γ-ray sky observed by LAT. In the daily review, the shifter points out the transients, the flaring, and new sources detected by LAT in the six-hour and 1-day time interval runs. For every interesting event, Astronomer's Telegrams (ATels)[3] and General Coordinates Networks (GCNs) [4] are published by the shifter on behalf of the whole LAT collaboration.

[3] `https://astronomerstelegram.org/`
[4] `https://gcn.nasa.gov/`

The data collected by LAT are organized as data runs. Before the collected data can be made available for scientific projects, they need to be processed for storage and archiving purposes. The data processing pipeline consists of three levels: telemetry and database ingestion (level 0), data quality and `FITS` / `ROOT` file creation (level 1), and ASP pipeline processing [level 2, 16]. Before being processed by the ASP, the data are organized in 6 hr data runs. Every time one of these data runs is ready, the ASP pipeline is triggered. Hence, the data are processed to perform the classification of the trigger events, to apply quality cuts, and to obtain the reconstruction of the event energy, timing, and direction information.

The results of the ASP stage represent the input of the FA analysis pipeline. The FA analysis scripts perform a likelihood analysis on all the sources characterized by a $TS > 25$. In addition to the likelihood analysis of all the most significant detection candidates, the pipeline computes the all-sky exposure maps of each run and uses the derived information to estimate the flux of the confirmed sources.

The output of the FA analysis pipeline is a report containing the results of the likelihood analysis, a list of the possible associations, and a comparison with the average status of previously known sources. The FA-GSW has to inspect this report to identify the potentially interesting events, such as strong flares, substantial high-energy emission, or new transient phenomena. Then, an FA follow-up analysis is performed on the interesting events.

The FAfup script is a Python script used by the shifter to perform a follow-up Fermi-LAT analysis on specific γ-ray transients seen in the Flare Advocate daily monitoring. The script uses the 4FGL-DR4 catalog as an input.

The analysis begins with event selection, exposure mapping, and XML model creation, followed by an initial fit of the region. Since catalog sources may not represent the current sky state, the script identifies new significant excesses in the TS map and iteratively fits them. If a transient source is identified with $TS > 10$, its position is localized and its SED is computed. Otherwise, the script derives upper limits. Other steps include catalog comparison to determine whether it matches a known source or represents a new detection. Photons above 10 GeV are also analyzed, and those likely associated with the source are recorded. The outputs include a summary of the detection, the coordinates, flux, index, localization error information, TS maps, and SED maps.

As an FA coordinator, my duty is to check the correct use of the pipeline, ensure its compatibility with the latest version of `fermipy`, and approve interesting events for the publication of ATels.

2.2 Gamma-ray ground-based telescopes

Above a few hundred GeV, the γ-ray space telescopes cannot provide enough statistics for a spectral and temporal study at these energies. This limitation on the photon statistics is due to the constraints on the maximum size and weight of an instrument that can be delivered into space and on the decreasing photon flux with increasing energy.

However, from a few hundred GeV to a few hundred TeV, two different kinds of facilities can be used to detect these photons and reconstruct their energy and arrival direction. The first facility is the *air shower array*, which records the particles coming

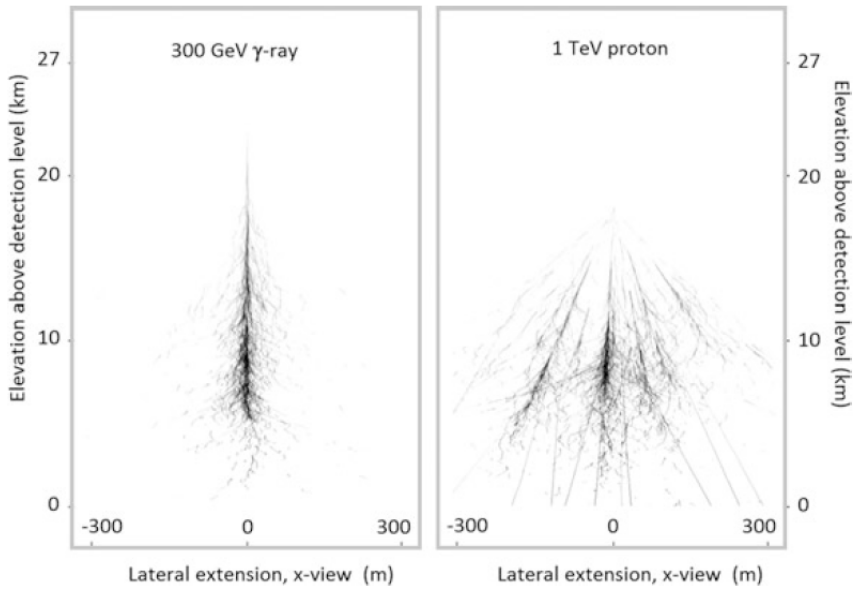

Figure 2.4: Comparison of a pure electromagnetic shower produced by a 300 GeV γ-ray and a shower initiated by a 1 TeV proton. The plot shows the projection of secondary particle trajectories onto a plane in which the ordinate corresponds to the elevation [291].

from atmospheric showers. The second one is the *Imaging Atmospheric Cherenkov Telescope* (IACT), which detects the Cherenkov light produced by particles that propagate in the atmosphere. This thesis will focus on this last kind of facility.

2.2.1 Extensive air showers and Cherenkov radiation

Extensive air showers are produced by the interaction of CRs, called primary CRs, with a nucleon of a nucleus in the Earth's atmosphere. The decay of short-lived hadrons leads to a cascade of high-energy photons, electrons, and positrons (the electromagnetic component) and a penetrating component of muons and neutrinos [291]. These secondary particles propagate through the atmosphere at relativistic speeds, approximately along the direction of the primary CR. The measurement of the secondary particles with ground-based detectors, called indirect measurements, allows for reconstructing the CR flux up to the highest energies.

To discriminate between a shower produced by a CR from one produced by a γ-ray, we have to take into account that γ-rays produce a pure electromagnetic shower and the shower has a compact elliptical shape as shown in Figure 2.4. Indeed, when a γ-ray photon reaches the atmosphere, it scatters with an atmospheric nucleus and produces an electron-positron pair. This pair emits photons through bremsstrahlung, which then scatter with other nuclei and produce 2 other pairs. This process continues until a critical energy E_C is reached. E_C is reached when the ionization energy loss of charged particles starts dominating over bremsstrahlung. In the atmosphere $E_C \sim 80$ MeV [95]. Hence, an *air shower array* needs to have a good angular resolution to separate the signal produced by a γ-ray and a CR. Otherwise, the experiment should be able to detect muons in hadronic showers to reject them from γ-ray induced showers.

Another technique to detect γ-ray and hadronic showers is to detect the *Cherenkov*

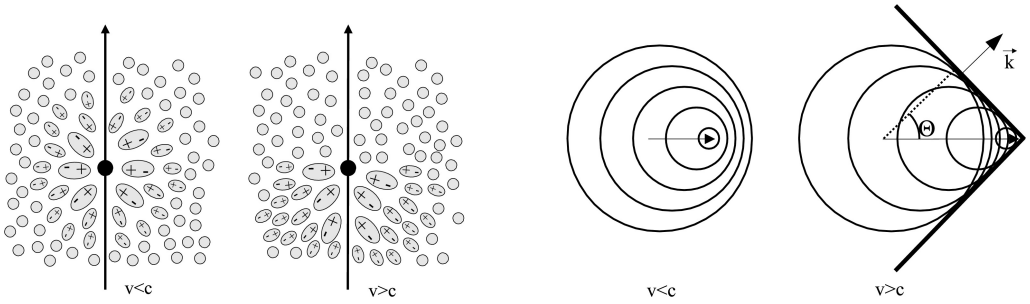

Figure 2.5: The first two plots on the left show how the polarization of the medium works due to the movement of a charged particle, with non-relativistic and ultra-relativistic velocity, respectively. The two plots on the right show the wave fronts of the radiation emitted by the dipoles when they return to their initial state. The right-most plot shows the formation of the shock waves of *Cherenkov radiation*. Courtesy of [251].

radiation. *Cherenkov radiation* is produced when ultra-relativistic charged particles travel with a velocity higher than the speed of light in the atmospheric medium. If the velocity of a charged particle is v, the medium has a refractive index n, c is the speed of light, and $v > c/n$, the charged particle polarizes the medium. When the dipoles in the medium return to their original state of random orientation, they emit radiation and generate an electromagnetic shock wave, which is the *Cherenkov radiation* (see Figure 2.5). The radiation is emitted at frequencies that fall in the near ultraviolet range: $300 - 350\,\text{nm}$. This radiation propagates with a characteristic angle with respect to the particle track θ_C:

$$\cos\theta_C = \frac{1}{\beta c} \tag{2.6}$$

where $\beta = \text{v/c}$ and v is the particle velocity.

The detectors that can detect *Cherenkov radiation* are of two kinds: the Water Cherenkov Detector (WCD) and the Imaging Atmospheric Cherenkov Telescopes (IACTs).

A WCD uses water tanks to detect secondary particles produced in the extensive air shower. The secondary charged particles, which travel at a velocity higher than $0.77c$ in the water, produce *Cherenkov radiation*. This radiation can be detected by Photo-Multiplier Tubes (PMTs). This category of detectors is placed at high altitudes to collect the secondary particles at the ground, and they are spread across a large area, to enable a good reconstruction of the morphology of the extensive air shower and a large field of view. However, they have bad angular and energy resolution, and the classification of the nature of the primary particle is difficult. Current examples of such detectors include The High-Altitude Water Cherenkov Gamma-Ray Observatory (HAWC)[5] and LHAASO[6]. The latter consists of three detectors located in China: the Water Cherenkov Detector Array (WCDA), the Kilometer Square Array (KM2A) and the Wide Field-of-view Cherenkov Telescope Array (WFCTA). A simple comparison of the typical performance parameters of these WCDs detectors is in Table 2.2. Since no data from these detectors has been used in this thesis, the reader is referred to look at the literature.

[5] `https://www.hawc-observatory.org/`
[6] `https://english.ihep.cas.cn/nw/han/y21/202101/t20210107_298072.html`

Table 2.2: Performances of the HAWC and LHAASO observatories. HAWC performances are taken from [12], while LHAASO's are taken from [65].

Parameter	HAWC	LHAASO
Location	Mexico	Sichuan, China
Detector Type	Water Cherenkov array	Hybrid: WCDA, KM2A, WFCTA
Field of View (FoV)	$> 1.5\,\mathrm{sr}$	$\sim 2.24\,\mathrm{sr}$
Energy Range	$\sim 300\,\mathrm{GeV}$ - $\sim 100\,\mathrm{TeV}$	$\sim 300\,\mathrm{GeV}$ - $> 1\,\mathrm{PeV}$
Effective Area	$\sim 2 \times 10^4\,\mathrm{m2}$	$> 10^5\,\mathrm{m}^2$ (WCDA); $\sim 1\,\mathrm{km}^2$ (KM2A)
Duty Cycle	$> 90\%$	$> 95\%$

The imaging Cherenkov technique is another possible method to study the showers that γ-rays and CRs produce when interacting with the Earth's atmosphere. IACTs use a single reflector to focus the Cherenkov light onto a camera to reconstruct an image of the shower. The reflectors are made of specific mirrors with spherical surfaces. Another interesting design of reflectors is the Schwarzschild-Couder, which is a dual-mirror design that allows for a large field of view, enhances the optical quality of the focused light, and allows to install highly-efficient photo-sensors in the telescope camera. The light collected by the telescope, both single-mirror and double-mirror, is focused on an optical plane composed of thousands of photo-sensors like PMTs or Silicon Photo-Multipliers (SiPMd). The camera allows the construction of a two-dimensional angular distribution of the observed light. From the angular distribution is possible to reconstruct the energy and direction of the primary particle and to determine its type. A schematic view of the technique used by the IACTs is shown in Figure 2.6. Unfortunately, IACTs can operate on a limited duty cycle since they require almost total darkness; instead, the WCDs are always operative.

Current examples of IACTs are Major Atmospheric Gamma Imaging Cherenkov (MAGIC)[7], High Energy Stereoscopic System (H.E.S.S.)[8] and Very Energetic Radiation Imaging Telescope Array System (VERITAS)[9]. A simple comparison of the typical performance parameters of these IACTs detectors is in Table 2.3. Since no data from these detectors has been used in this thesis, the reader is referred to look at the literature.

Table 2.3: Performances of the MAGIC, H.E.S.S., and VERITAS telescopes. MAGIC performances are taken from [28], H.E.S.S. performances are taken from [170], and VERITAS performances are taken from [174].

Parameter	MAGIC	H.E.S.S.	VERITAS
Location	La Palma	Namibia	Arizona
Telescope's diameter	$2 \times 17\,\mathrm{m}$	$4 \times 12\,\mathrm{m} + 1 \times 28\,\mathrm{m}$	$4 \times 12\,\mathrm{m}$
Field of View (FoV)	3.5°	5° (CT1–4), 3.2° (CT5)	3.5°
Energy Range	$\sim 50\,\mathrm{GeV}$ - $\sim 50\,\mathrm{TeV}$	$\sim 30\,\mathrm{GeV}$ - $\sim 100\,\mathrm{TeV}$	$\sim 85\,\mathrm{GeV}$ - $\sim 30\,\mathrm{TeV}$
Effective Area	$\sim 10^5\,\mathrm{m}^2$	$\sim 10^5\,\mathrm{m}^2$	$\sim 10^5\,\mathrm{m}^2$
Angular Resolution	$\sim 0.07^\circ$	$\sim 0.05^\circ$	$\sim 0.1^\circ$
Duty Cycle	$\sim 15\%$	$\sim 15\%$	$\sim 15\%$

[7] https://magic.mppmu.mpg.de/
[8] https://www.mpi-hd.mpg.de/HESS/pages/about/telescopes/
[9] https://veritas.sao.arizona.edu/

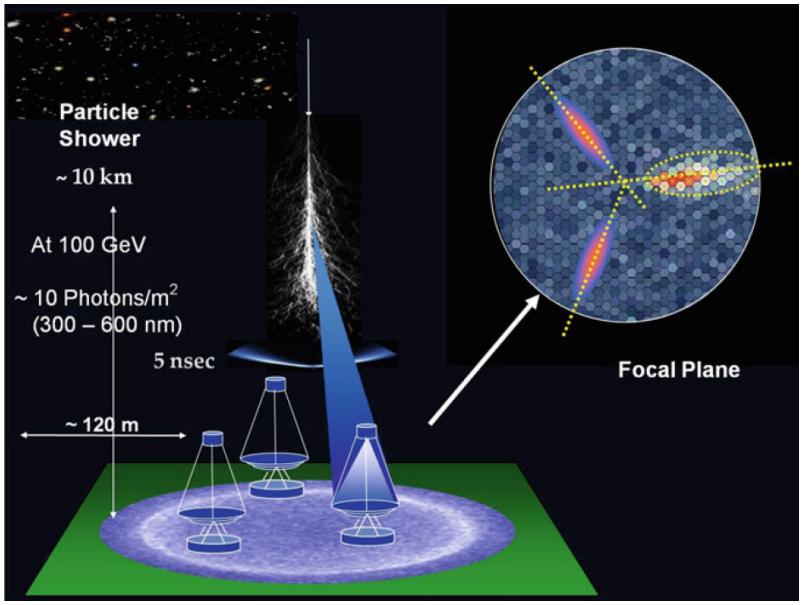

Figure 2.6: Schematic view of the imaging atmospheric Cherenkov telescopes single-dish technique. Modified from an original drawing by Prof. W. Hofmann.

2.2.2 CTAO

The Cherenkov Telescope Array Observatory (CTAO)[10] will be the next generation of IACTs. It will detect photons from 20 GeV up to 300 TeV, it will have an almost full-sky coverage and a larger field of view compared to the other IACTs. CTAO will host several different telescopes in order to be the largest ground-based γ-ray detection observatory. The telescopes will be located in both Hemispheres, in the so-called "Alpha Configuration". The "Alpha Configuration" will use three different types of telescopes:

- Large-Sized Telescopes[11] (LSTs) that are characterized by a reflector of 23 m of diameter and a reflective surface of 370 m^2. The camera has a total field of view of about 4.3°. The sensitivity of the LSTs is between 20 and 150 GeV.
- Medium-Sized Telescopes[12] (MSTs) that are characterized by a reflector of 12 m of diameter and a reflective surface of 88 m^2. The camera has a total field of view of about 8°. The sensitivity of the MSTs is between 150 GeV and 5 TeV.
- Small-Sized Telescopes[13] (SSTs) that are characterized by a primary reflector of 4.3 m of diameter, a secondary reflector of 1.8 m of diameter, and a reflective surface $> 5\,m^2$. The camera has a total field of view of about 8.8°. The sensitivity of the SSTs is between 5 and 300 TeV.

Another Medium-Sized Telescope, for a scenario beyond the "Alpha Configuration", is the Schwarzschild-Couder Telescopes (SCTs)[14]. SCTs are characterized by a primary reflector of 9.7 m of diameter, a secondary reflector of 5.4 m of diameter. The

[10] https://www.ctao.org/
[11] https://www.ctao.org/it/emission-to-discovery/telescopes/lst/
[12] https://www.ctao.org/it/emission-to-discovery/telescopes/mst/
[13] https://www.ctao.org/it/emission-to-discovery/telescopes/sst/
[14] https://www.ctao.org/news/sct-first-light

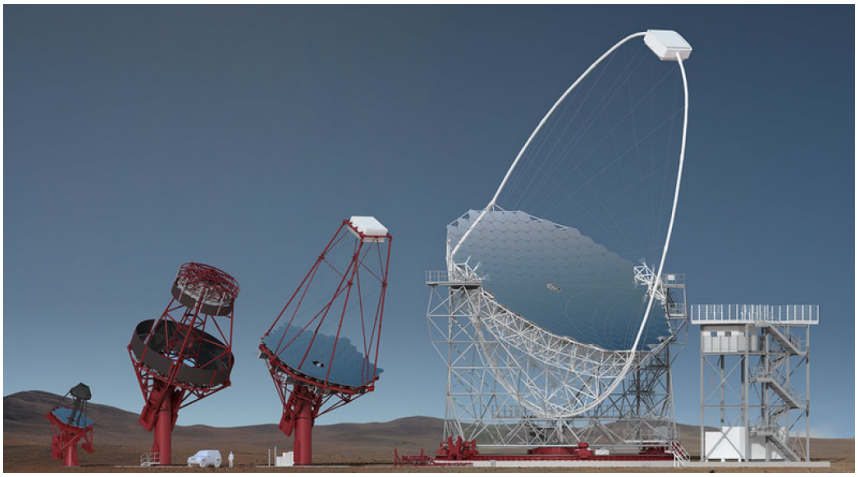

Figure 2.7: Models of the different telescopes, from left to right - SST, SCT, MST, and LST. All except for SCTs are part of the Alpha Configuration, while the SCTs could be part of CTAO-South later. Courtesy of CTAO.

camera has a total field of view of about 8°. The sensitivity of the SCTs is between 80 GeV and 50 TeV. The technical aspects of these telescopes are reported in Table 2.4. The models of the different telescopes are shown in Figure 2.7.

The current differential sensitivity of CTAO performance can be seen in Figure 2.8, compared with the performance of various current IACTs experiments. CTAO will have more than an order of magnitude better sensitivity as compared to the earlier generation telescopes, like LAT and the other very-high-energy instruments. Coupled with the sensitivity, CTAO's will have a better angular resolution ($\leq 0.05°$ at $E \geq 1$ TeV) with respect to currently operating IACTs, as shown in Figure 2.9.

CTAO North

In the Northern hemisphere, CTAO's array is located on the island of La Palma in the Canary Islands, Spain, at the Instituto de Astrofísica de Canarias' (IAC's) Observatorio del Roque de los Muchachos in Villa de Garafía [89]. The Northern hemisphere array will focus on the low and mid-energy ranges from 20 GeV to 5 TeV, which implies the northern array will focus on the observations of extragalactic sources. For this reason, the Northern hemisphere site will not host any Small-Sized Telescopes, which are tuned to capture the highest-energy gamma rays.

The layout of the CTAO Northern array includes the geographical location of 13 telescopes distributed over an area of about 0.5 km^2: four Large-Sized Telescopes and nine Medium-Sized Telescopes. The prototype of an LST, the LST-1, was completed on site in October 2018. The layouts of the telescopes in CTAO-North can be seen in Figures 2.10.

CTAO South

CTAO-South is located less than 10 km southeast of the European Southern Observatory's (ESO) existing Paranal Observatory in the Atacama Desert in Chile.

Table 2.4: Telescope specifications of CTAO. For MSTs, the two values correspond to those to be placed in CTAO-North with FlashCam Camera and in CTAO-South with NectarCam Camera, respectively.

Characteristic	LST	MST	SCT	SST
Energy range	20 - 150 GeV	150 GeV - 5 TeV	80 GeV - 50 TeV	5–300 TeV
Number	4 (North) 4 (South)	9 (North)	11 (South)	37 (South)
Optical design	Parabolic	Parabolic	Schwarzschild Couder	Schwarzschild Couder
Reflector diameter	23 m	12 m	9.7 m(Primary) 5.4 m	4.3 m(Primary) 1.8 m
Effective mirror area	370 m^2	88 m^2	$> 40\ m^2$	$> 5\ m^2$
Field of view	4.3°	7.5°, 7.7°	8°	8.8°
Number of pixels	1855	1764 / 1855	11328	2048
Pixel size (imaging)	0.1°	0.17°	0.07°	0.16°
Photodetector type	PMT	PMT	SiPM	SiPM
Telescope readout event rate (before array trigger)	> 7.0 kHz	> 6.0 kHz/ > 7.0 kHz	10.0 kHz	600 Hz
Telescope data rates	24 Gb/s	12 Gb/s	30 Gb/day	2.55 Gb/s

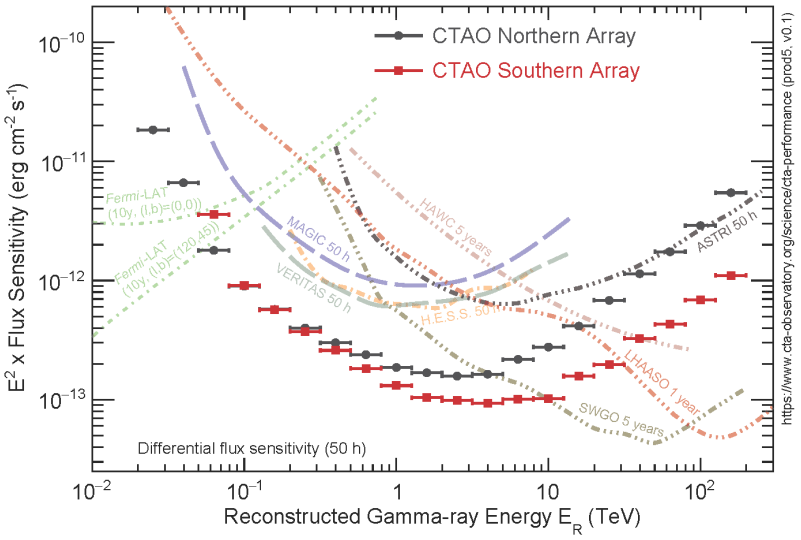

Figure 2.8: Comparison of the CTAO performance with existing γ-ray instruments. The differential sensitivity (on axis and with 50 hr of observations) is defined as the minimum flux needed by CTAO to obtain a 5σ detection of a point-like source, calculated in non-overlapping logarithmic energy bins (five per decade). Besides the significant detection, it was required at least ten detected γ-rays per energy bin, and a signal/background ratio of at least 1/20. The analysis cuts in each bin have been optimized to achieve the best flux sensitivity to point-like sources. Courtesy of CTAO.

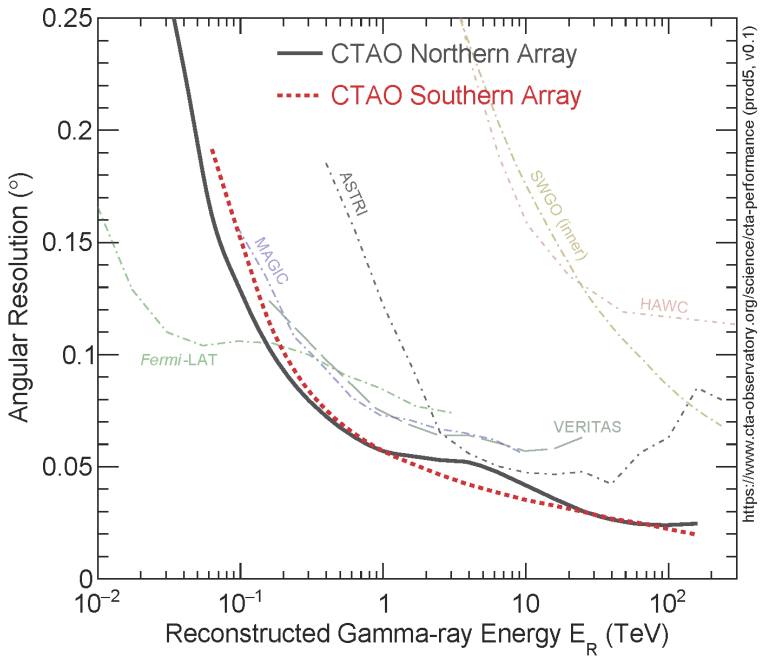

Figure 2.9: The angular resolution versus reconstructed energy curve (E_R) shows the angle within which 68% of reconstructed γ-rays fall, relative to their true direction. γ-ray photon/hadron separation cuts are applied for the Monte-Carlo events used to determine the angular resolution. Credit: CTAO webpage.

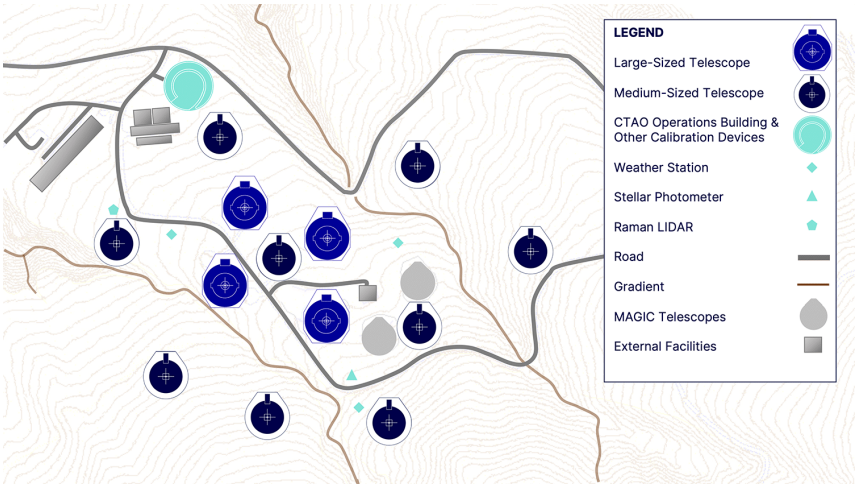

Figure 2.10: CTAO's North layout of the telescopes. This diagram also includes the existing MAGIC telescopes. Courtesy of CTAO.

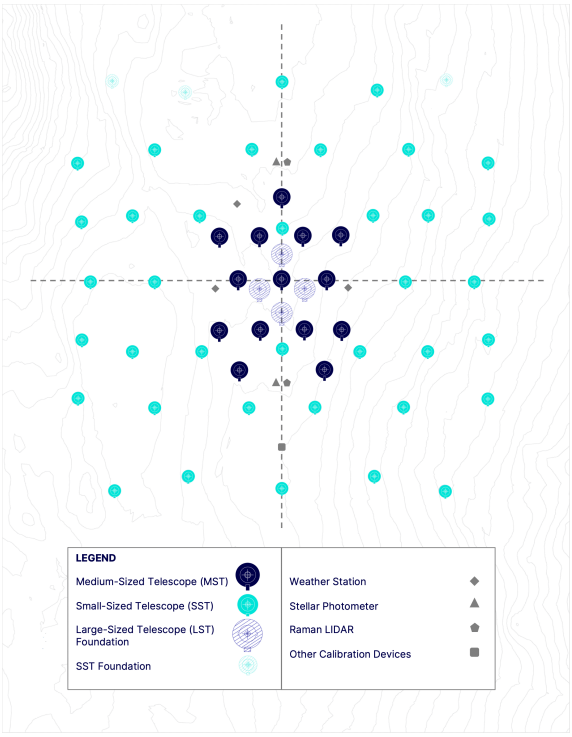

Figure 2.11: CTAO's South layout of the telescopes. Courtesy of CTAO.

The southern hemisphere array will be optimized for the medium and high-energy ranges of the CTAO, from 150 GeV to 300 TeV, which implies the southern array will focus on the observations of galactic sources. The approved Alpha Configuration will include an array spread over three square kilometers with 14 Medium-Sized Telescopes to cover CTAO's core energy range and 37 Small-Sized Telescopes to cover CTAO's highest energy γ-rays[90].

The Alpha Configuration does not consider LSTs and SCTs in the CTAO southern array, but it includes the preparation of the foundation for four LSTs, as well as the foundation for three more SSTs, to allow for the construction of these telescopes in the future. The layouts of the telescopes in CTAO-South can be seen in Figures 2.11.

Regarding a scenario beyond the Alpha configuration, SCTs are proposed as the best candidate thanks to their exceptional performance in terms of angular resolution and background rejection. The dual optics ensures the correction of chromatic aberrations and a high de-magnification of the shower images, which can be detected by a high-resolution camera consisting of SiPMs in place of the traditional PMTs [101]. These characteristics allow for a better resolution on the reconstruction of the emission from extended γ-ray sources on the Galactic Plane, as Supernova Remnants, and better off-axis performances.

In Figure 2.12, some of the proposed configurations of MSTs and SCTs in CTAO-South are shown.

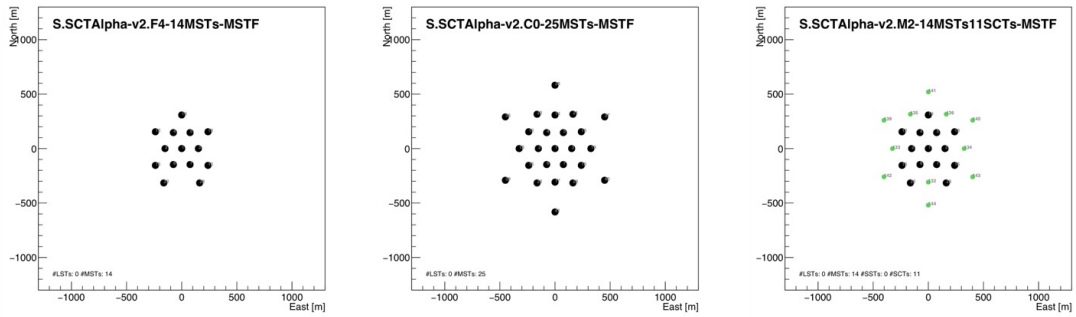

Figure 2.12: Different configuration of Medium-Sized Telescopes in CTAO-South. On the left is shown the configuration with 14 MSTs, called F4, which is part of the Alpha configuration. In the middle is shown the proposed configuration with 25 MSTs, called C0, and on the right is shown the proposed configuration with 14 MSTs, in black, and 11 SCTs, in green, called M2. Courtesy of CTAO - SCT collaboration.

2.2.3 GammaPy software for CTAO simulations

`Gammapy`[15] [102] is an open-source Python package for γ-ray astronomy built on `numpy`[16], `scipy`[17] and `astropy`[18]. The CTAO collaboration has chosen `gammapy` as the Python library for its Science Analysis tools, but it is also already widely used in the analysis of other existing γ-ray instruments, such as MAGIC, VERITAS, and H.E.S.S. Figure 2.13 illustrates the standard analysis flow and the corresponding sub-package structure of `gammapy`.

`Gammapy`'s sub-packages allow for performing binned simulations, as Poisson fluctuation of predicted counts maps or spectra, as well as event sampling to simulate DL3 (data level 3 FITS files) events data. DL3 data consists of event lists, using the corresponding CTAO's IRFs, which are publicly available on their latest version prod5 version v0.1 [19]. In this thesis, I will largely use `gammapy` v 1.3 to create DL3 observations and simulate binned datasets, called DL4 in Figure 2.13, using prod 3 and prod 5 IRFs.

To simulate Cherenkov Telescope Array Observatory (CTAO) datasets, the necessary observational parameters must be defined: the duration of the observation, or livetime, the integration radius of the source, the offset, the reconstructed energy range, the true energy range, and the spectral, which can include different shapes and the EBL, and spatial models, which can include different shapes. Another required parameter is the CTAO's IRF. After all the required parameters are listed, it is possible to simulate the observation and the spectrum using the `SpectrumDatasetMaker` routine. Then, to do an on-off spectral analysis, which is the usual science case, since γ-ray observations contain both signal and background events, `gammapy` uses the `SpectrumDatasetOnOff` routine, which takes the spectrum dataset for 1D on-off likelihood fitting. `SpectrumDatasetOnOff` bundles together the binned on and off counts, the binned IRFs, as well as the on and off acceptances.

[15] `https://docs.gammapy.org/dev/index.html`
[16] `https://numpy.org/`
[17] `https://scipy.org/`
[18] `https://www.astropy.org/`
[19] `https://zenodo.org/records/5499840`

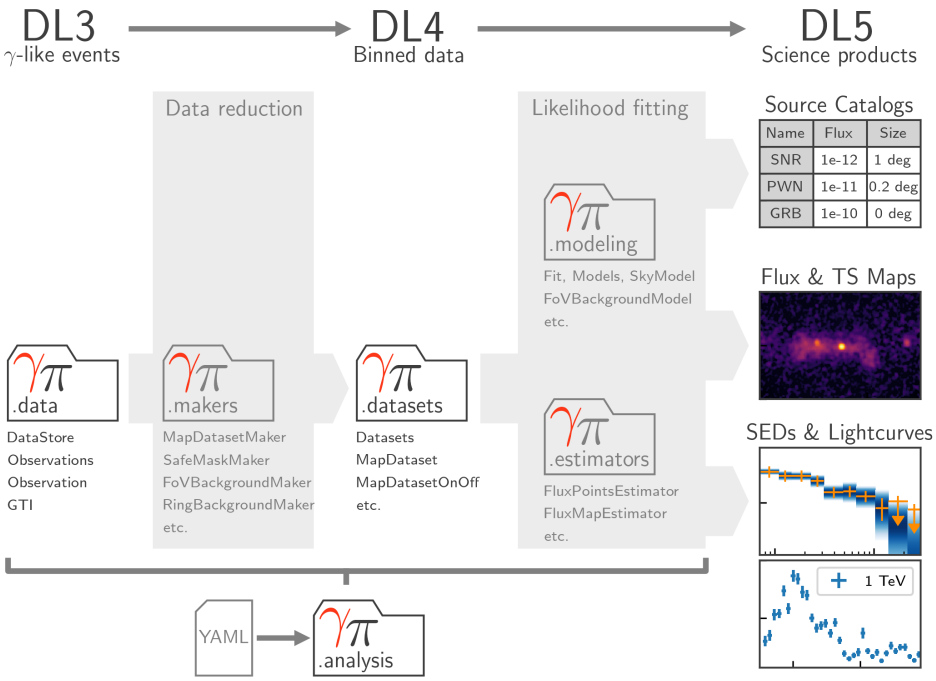

Figure 2.13: Data flow and sub-package structure of `gammapy`. The folder icons represent the corresponding sub-packages. The direction of the data flow is illustrated with shaded arrows. The top section shows the data levels as defined by CTAO. Courtesy of `gammapy`.

After the datasets and the spectra are simulated, `gammapy` has a routine, called `Fit()`, that performs the statistical algorithms used for fitting datasets and to estimate parameter values. The two statistical approaches used by `gammapy` to fit the data are the *Cash* statistic [70] and the *Wstat* one [313]. Both of them will be used in this thesis.

`Gammapy` uses *Cash* statistics as the default. *Cash* statistics is equivalent to Chi-Square statistics for counts or bins larger than 10. The number of counts, n, is a Poisson random variable of mean value $\mu_{sig}+\mu_{bkg}$, where μ_{sig} is the expected number of counts from the source and μ_{bkg} is the number of expected background counts. Considering this expression, the likelihood C is:

$$C = 2 \times (\mu_{sig} + \mu_{bkg} - n \times \log(\mu_{sig} + \mu_{bkg})) \tag{2.7}$$

The *Cash* statistic is implemented in `cash` and is used as a `stat` function by the `MapDataset` and the `SpectrumDataset`.

The *Wstat* statistic is used when a reliable background model is missing. In the OFF region, which contains background only, the number of counts n_{OFF} is a Poisson random variable of mean value $\alpha\mu_{bkg}$, and μ_{bkg} is the number of expected background counts in the ON region. In the ON region, which contains signal and background contributions, the number of counts n_{sig} is a Poisson random variable of mean value $\mu_{sig}+\mu_{bkg}$, where α is the ratio of the ON and OFF region acceptances and μ_{sig} is the number of expected signal counts in the ON region [20]. This yields the so-called *Wstat* or ON-OFF statistics, which are traditionally used for ON-OFF measurements in

[20] `https://docs.gammapy.org/dev/user-guide/stats/fit_statistics.html`

ground-based γ-ray astronomy:

$$W = 2(\mu_{sig} + (1 + 1/\alpha)\mu_{bkg} - n_{ON}\log(\mu_{sig} + \mu_{bkg}) - n_{OFF}\log(\mu_{bkg}/\alpha)) \quad (2.8)$$

In this case, the likelihood ratio, which gives the goodness of the fit, is given by:

$$TS = -2\log\frac{\mathcal{L}(n_{ON}, n_{OFF}, \alpha; \mu_{sig}, \mu_{bkg})}{n_{ON}, n_{OFF}, \alpha; n_{ON} - \alpha n_{OFF}, \alpha n_{OFF}} \quad (2.9)$$

After the fitting, it is possible to compute the SED flux points and the light curves using the `FluxPointsEstimator` and the `LightCurveEstimator`, respectively, to realize the science products listed in the DL5 column in Figure 2.13.

2.3 X-ray telescopes

X-ray telescopes can operate only in space to observe the Universe because Earth's atmosphere blocks high-energy X-rays. The typical X-ray energy range is between 0.1 keV to 100 keV. To focus X-rays on the camera, telescopes use grazing-incidence optics, relying on the fact that photons can undergo total reflection when the angle of incidence is small with respect to the plane of the surface ($\lesssim 1°$). The critical angle for reflection, θ_{crit}, depends on the photon energy E and the mirror material density, approximately scaling as $\theta_{crit} \propto \sqrt{\rho}/E$ [33]. The most widely adopted optical designs are the Wolter Type-I configurations, which combine a paraboloid and a hyperboloid surface to eliminate spherical and coma aberrations and bring the X-rays to a true focus. In addition, the Type-I design offers the possibility of nesting several telescopes inside one another, thereby increasing the useful reflecting area.

A fundamental element that describes the sensitivity of X-ray telescopes is the effective area A_{eff}:

$$A_{eff}(E, \theta, x, y) = A_{geom}R(E)V(E, x, y)QE(E, x, y) \quad (2.10)$$

where A_{geom} is the geometric collecting area of the mirrors, $R(E)$ is the reflectivity of the mirror's coating, which usually is iridium or gold, $V(E, x, y)$ is the vignetting function accounting for off-axis response, Q(E) is the detector quantum efficiency and θ is the grazing angle. To maximize the effective area, multiple concentric mirror shells ("nesting") are employed to increase the reflecting area.

When X-ray photons enter the telescopes, they are reflected by the mirrors in the focal plane where charge-coupled device (CCD) arrays are placed.

Grazing-incidence optics, nested mirror designs, and advanced photon-counting detectors allow X-ray telescopes to achieve arcsecond-scale imaging [322], broad energy coverage, and high sensitivity. These capabilities make it possible to study high-energy astrophysical environments such as accretion disks around black holes, relativistic jets, intracluster gas, and supernova remnants.

The statistical methods used to analyze X-ray data are the χ^2 [261] and the *Cash* statistic (see Section 2.2.3). The standard chi-square approach is only valid in the high-count regime, while for low-count data, the Cash statistic or its background-inclusive modification, the W-statistic (see Section 2.2.3) is used. These methods allow maximum-likelihood fitting of spectral and imaging data without bias from binning or Gaussian approximations.

Nowadays, some of the X-ray telescopes that are still taking data are: the *Chandra* X-ray Observatory [21], the X-ray Multi-Mirror Mission (XMM) Newton [22], NuSTAR [23], and the *Neil Gehrels Swift Observatory* X-ray Telescope (*Swift*-XRT)[24]. This last one telescope's data are part of the analysis presented in this thesis.

2.3.1 *Swift*-XRT

The XRT, onboard the Neil Gehrels *Swift* Observatory, is designed to measure the fluxes, spectra, and light curves of GRBs and afterglows over a wide range of energy ($0.2 - 10\,\mathrm{keV}$). The XRT can point to a GRB position with a 5 arcsec accuracy in 10 seconds after the target acquisition for a typical GRB. Furthermore, it can observe the X-ray counterparts of GRBs from the burst discovery to the following days and weeks.

XRT uses a Wolter-I grazing incidence mirror assembly inherited from JET-X, built for the Spectrum-X mission, focusing X-rays onto a CCD-22 detector at the focal plane. XRT offers multiple readout modes that balance spectral and timing resolutions and pile-up mitigation. These modes allow observations from bright GRB afterglows to faint active galactic nuclei (AGN). Table 2.5 summarizes the instrument's parameters.

Table 2.5: Performances of *Swift*-XRT taken from [148].

Property	Description
Energy range	0.2–10 keV
Telescope	JET-X Wolter I
Detector	E2V CCD-22
Focal Length	3.5 m
Field of View	23.6 arcsec × 23.6 arcsec
Effective Area	$110\,\mathrm{cm}^2$ at 1.5 keV
Telescope PSF	18 arcsec HPD at 1.5 keV
Detection elements	600 × 602 pixels
Detector Operation	Imaging, Timing, and Photon-counting
Pixel Scale	2.36 arcsec/pixel
Energy Range	$0.2 - 10\,\mathrm{keV}$
Sensitivity	$8 \times 10^{-14}\,\mathrm{ergcm^{-2}s^{-1}}$ (1 mcrab) in 10^4 seconds

Swift-XRT data reduction

Swift-XRT data are publicly available at the UK *Swift* Science Data Centre website[25][113]. From the webpage, it is possible to download the data depending on the science goal: spectra, images, light curves, or to find the position of a new source. This means that the downloaded data are already cleaned (Level 2 data). Otherwise, it is possible to download Level 1 data and clean the data using the `xrtpipeline`,

[21] `https://www.nasa.gov/mission/chandra-x-ray-observatory/`
[22] `https://www.cosmos.esa.int/web/xmm-newton`
[23] `https://nustar.caltech.edu/`
[24] `https://science.nasa.gov/mission/swift/`
[25] `https://www.swift.ac.uk/user_objects/`

which is part of the HEASOFT software package[26]. In this thesis, the HEASOFT software version used is v.6.33.1, together with the calibrated source background (CALDB, v20220331), and response file. The `xrtpipeline` applies calibration, generates cleaned event files, and applies good-time intervals (GTIs) using the latest available CALDB. In this thesis, the data used are directly Level 2 data obtained from the UK *Swift* Science Data Centre. These data include pre-extracted source and background spectra, as well as the corresponding response files, generated through the standard automated processing pipeline described in [113]. This approach allows for an efficient analysis of a large number of observations and is commonly adopted for quick-look and multi-wavelength studies. However, it should be noted that this procedure does not involve a manual extraction of the source and background regions using the `XSELECT` HEASOFT tool, nor a dedicated generation of the Auxiliary Response File (ARF) for each spectrum, using `xrtmkar`. Since the ARF depends on the extraction region and source position, a fully customized X-ray spectral analysis would require a case-by-case definition of the source and background regions, verification and correction for pile-up effects, and the regeneration of the response files. For this reason, the X-ray spectra used in this thesis should be considered suitable for broad-band spectral modeling and variability studies, but not intended to replace a dedicated and fully optimized XRT spectral analysis.

Hence, it was possible to directly fit the data to produce the fitted spectra and obtain the spectrum parameters. The spectral fitting package XSPEC v12.13.1 [32] and the Python package PyXspec v2.1.4, available in HEASOFT software, are employed. XSPEC requires four different files to perform the fit:

- the source spectrum (.pi file);
- the background spectrum (bkg.pi file);
- the Auxiliary Response File matrix, which takes into account the instrument-specific effects like effective area, vignetting, and detector efficiency (.arf file);
- the Redistribution response matrix, which contains information about energy redistribution (.rmf file).

All of them are included in the Level 2 data folder.

After loading the source spectrum in XSPEC, it is possible to ignore spectral bins flagged as bad, which usually are at low and high energies, ignore spectral bins below 0.3 keV and above 7 keV, select the statistic (*Cash* or χ^2) and select the desired binning, if necessary. Then, XSPEC requires to define a model that describe the spectrum. The model can be made of different components that are linked to the X-ray emission of the source. One parameter that is fundamental during the fitting procedure is the Galactic absorption, which can be obtained using the command `nH` in XSPEC and must be included and frozen in the spectrum model using the `phabs` component. After the spectral model is defined, it is possible to fit the data until a good fit is obtained and modify the spectral model if required.

2.4 Optical and UV telescopes

Optical and ultraviolet (UV) telescopes are designed to collect and analyze electromagnetic radiation in the wavelength range spanning from the visible, 400–700 nm,

[26] `https://heasarc.gsfc.nasa.gov/docs/software/heasoft/`

to the ultraviolet, 10–400 nm. The location and the structures of both telescopes depend strongly on the properties of Earth's atmosphere, which transmits visible light but absorbs most of the ultraviolet light. For this reason, there are two categories of optical and ultraviolet telescopes: the ground-based telescopes and the space-based telescopes.

The ground-based optical telescopes have been the most important detectors in human history for centuries, allowing us to explore Earth's transparent window in the visible band. The atmosphere strongly absorbs most ultraviolet radiation below ~ 300 nm, but modern optical telescopes can detected radiation above 300nm into the near-UV, with limited but valuable observations. Ground-based facilities provide both deep imaging and continuous monitoring of the sky with the development of large reflecting mirrors, adaptive optics to correct atmospheric distortions, wide-field cameras, which are designed to capture a large portion of the sky in a single exposure, and narrow-field cameras, which can observe in detail several arcminutes portion of the sky to provide high angular resolution imaging and spectroscopy. One of the major problems of ground-based telescopes is the atmospheric "seeing". Seeing is the degradation of the image of an astronomical object due to turbulence in the atmosphere of Earth. Another major effect happens when light passes through a telescope's aperture, like a mirror or a lens; it doesn't form a perfectly sharp point. Instead, because of the wave nature of light, it spreads out into a pattern called an Airy disk [26]. Hence, the sharpness of an image is limited not only by the telescope's optics quality, by the seeing but also fundamentally by diffraction. When a telescope achieves diffraction-limited imaging means that its resolution is limited only by this physical effect, not by distortions such as atmospheric turbulence or imperfections in the optics.

Some of the major facilities that currently are on:

- The Very Large Telescope (VLT) at Paranal in Chile[27]. It is characterized by four 8.2 m telescopes offering diffraction-limited imaging with adaptive optics, used for detailed studies of stars, galaxies, and exoplanets. The telescopes can work together to form an interferometer (see Section 2.5.1). VLT is characterized by one of the best narrow-field cameras, called MUSE. MUSE is an Integral Field Spectrograph. It splits the field of view into 24 image segments or channels which are further sliced into 48 slices or mini slits, giving a total of 1152 mini slits. Each set of 48 mini slits is injected into one of the segments to produce a set of medium resolution spectra.
- The Zwicky Transient Facility (ZTF)[28] uses two telescopes both part of the Palomar Observatory in the USA. The wide-field camera is mounted on the 48-inch Samuel Oschin Schmidt telescope [167]. ZTF is a wide-field survey instrument capable of imaging 47 square degrees at once, optimized for transient detection [46].
- The Pan-STARRS in Hawaii[29] is made by a pair of 1.8 m telescopes with wide-field cameras, producing deep all-sky surveys useful for asteroid detection, galaxy evolution studies, and transient discovery [74].
- The Catalina Sky Survey (CSS) in the USA and Australia[30] is designed for

[27] https://www.eso.org/public/teles-instr/paranal-observatory/vlt/
[28] https://www.ztf.caltech.edu/
[29] https://www2.ifa.hawaii.edu/research/Pan-STARRS.shtml
[30] http://nesssi.cacr.caltech.edu/DataRelease/

near-Earth object detection and contributes to valuable long-term photometric monitoring of variable stars and transients located all over the sky [105]. The last data release includes the photometry for 500 million objects from an area of 33,000 square degrees.

Ultraviolet astronomy can only be performed from space. Space telescopes avoid atmospheric turbulence, providing diffraction-limited imaging in both the optical and UV. They are made by compact mirrors, with an aperture smaller than 3 m, and filter systems for imaging and spectroscopy in the UV band.

Some of the current facilities are:

- The Hubble Space Telescope (HST)[31]. It was launched in 1990 and is still operating. It covers near-infrared to UV wavelengths (115–2500 nm), with high-resolution imaging and spectroscopy. It revolutionized astrophysics by enabling precise measurements of distant galaxies, exoplanets, and star-forming regions.
- The *Swift* Ultraviolet Optical Telescope (UVOT) is a 30 cm telescope aboard the *Swift* Observatory, covering 170–600 nm, optimized for rapid transient follow-up such as gamma-ray burst afterglows and supernovae. More details on this telescope are in Section 2.4.1

My colleagues performed the analysis of optical data, while the data reduction of ultraviolet data is shown in Section 2.4.1 and was done by me.

2.4.1 *Swift*-UVOT

Observations of GRBs have shown that optical afterglows typically decline in brightness rapidly from $t^{-1.1}$ to $t^{-2.1}$. Therefore, rapid response is required to observe these counterparts and determine their redshift while they are still bright. The *Swift*-UVOT is uniquely suited for afterglow studies. Its observations provide rapid optical images of the GRB field so that any optical or infrared counterpart can be quickly identified and studied. Stars in the FoV of the UVOT provide an astrometric grid for the GRB field [295].

The UVOT is a Ritchey-Chrétien diffraction-limited reflector of 30 cm. It is sensitive to magnitude 22.3 in a 17 minute exposure. The filters available on UVOT are: v (with effective wavelength $\lambda_{eff} = 544$ nm), b (with effective wavelength $\lambda_{eff} = 439$ nm), u (with effective wavelength $\lambda_{eff} = 345$ nm), white (with effective wavelength $\lambda_{eff} = 385$ nm), uvw1 (with effective wavelength $\lambda_{eff} = 251$ nm), uvw2 (with effective wavelength $\lambda_{eff} = 217$ nm), and uvw3 (with effective wavelength $\lambda_{eff} = 188$ nm) [273]. In Table 2.6 are shown the characteristics of UVOT taken from [273].

Swift-UVOT data reduction

Swift-UVOT are publicly available at the UK *Swift* Science Data Centre website[32][113]. UVOT data are usually analyzed by a pipeline which is part of the HEASOFT software package, and as is the case with XRT data, the downloaded data are Level 2 products, so they are already cleaned and calibrated. The standard

[31] `https://science.nasa.gov/mission/hubble/`
[32] `https://www.swift.ac.uk/user_objects/`

Table 2.6: *Swift*-UVOT specifications [273].

Property	Modified Description
Aperture	30 cm
Focal ratio	12.7
Filters	7
Wavelength range	170–650 nm
Detector	CCD
Detector operation	Photon Counting
Sensitivity	$m_B = 22.3$ in white light in 1000 s
Field of view	$17 \times 17\,\mathrm{arcmin}^2$
Detection element	256× 256 pixels
Sampling element	2048×2048 after centroiding
Point Spread Function	0.9 arcsec FWHM at 350 nm
Pixel scale	0.502 arcsec

analysis of UVOT data begins with the `uvotimsum` task, which co-adds exposures in the same filter to improve the signal-to-noise ratio. Source counts are then extracted with `uvotsource`, which performs aperture photometry using predefined calibration apertures, applies corrections for coincidence loss (important for bright sources), background subtraction, and converts count rates into flux densities or magnitudes, based on the most recent calibration files. The resulting photometry is typically stored in FITS or ASCII files and can be used to build light curves or to provide photometric points for an SED. Since UVOT magnitudes are affected by Galactic extinction, they must be corrected using extinction maps[33] before further analysis. To carry out the spectral energy distribution or the light curve, it is necessary to convert the magnitudes into counts per second and then into energy flux units. Usually, the conversion from count rate (C), in counts s^{-1}, to magnitude in the Vega system is given by

$$m = -2.5 \log_{10}(C) + ZP, \tag{2.11}$$

where ZP is the filter-dependent photometric zero point provided in the UVOT CALDB [57]. The corresponding flux density can then be obtained from the Pogson relation [187]:

$$F_\nu = F_{\nu,0} \times 10^{-0.4\,m}, \tag{2.12}$$

where $F_{\nu,0}$ is the zero-point flux for the filter, expressed in $\mathrm{ergs}^{-1}\mathrm{cm}^{-2}\mathrm{Hz}^{-1}$.

2.5 Radio telescopes

The radio band is the widest energy band that is observable from the ground, with almost no absorption from the Earth's atmosphere. The only limitations to the observations of the radio frequencies are the absorption of the radiation by the water molecules in the atmosphere at frequencies $\gtrsim 300$ GHz and the reflection of the radiation by the ionosphere at frequencies $\lesssim 30$ MHz.

Radio emission is detected by focusing incoming waves on a dipole and measuring its electric field, which is then converted into an electric signal. This is done through

[33] `https://irsa.ipac.caltech.edu/applications/DUST/`

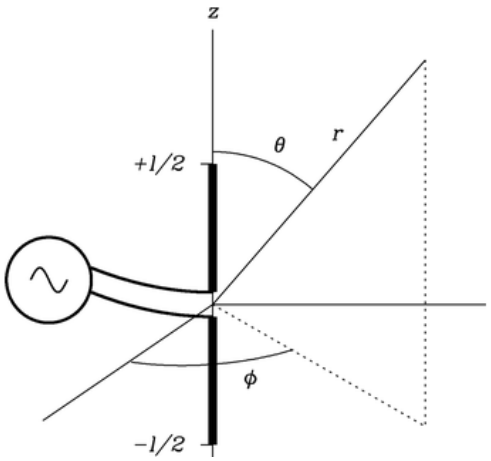

Figure 2.14: Schematic view of a short dipole antenna. Courtesy of National Radio Astronomy Observatory, Charlottesville.

an antenna. An antenna, usually parabolic, is a passive device that converts electromagnetic radiation in space into electrical currents when used for receiving, or vice versa, when used for transmitting, due to the reciprocity theorem. The simplest antenna is a short dipole antenna, with length $l \ll \lambda$, where λ is the wavelength of the oscillating current source that drives the dipole. Hence, the radiation from a dipole depends on the transmitter frequency. A schematic view of a short dipole antenna is shown in Figure 2.14.

Most radio telescopes use large parabolic reflectors to collect and focus power onto their small feed antennas connected to receivers, which are in the focal point, or focus, of the optical system. This means that the larger is the dish, the finer is the angular resolution, and the fainter the sources that can be detected.

The power gain measured from a point source as a function of off-axis angle is called *beam pattern*, and it has a characteristic shape given by the diffraction pattern associated with the antenna aperture. This shape can be described with a `sinc` function $sinc(l) \equiv \sin(\pi l)/(\pi l)$, where the absolute maximum is called *beam* or *main lobe* and the secondary maxima are called *side-lobes*. A schematic view of the diffraction pattern and of the `sinc` function is shown in Figure 2.15. The Full-Width Half-Maximum (FWHM) of the *main lobe* indicates the angular resolution of the antenna, and is given by $\theta = 1.22\lambda/D$, where λ is the wavelength of the observed radiation, and D is the antenna diameter. Unfortunately, the power gain is extremely weak and dominated by noise, so the system temperature T_{sys}, which includes the receiver noise, the sky background, and the atmospheric contributions, sets an important sensitivity limit. Hence, the radiometer equation gives the minimum detectable flux density σ_S:

$$\sigma_S = \frac{2k_B T_{sys}}{A_{eff}\sqrt{\Delta\nu} t_{int}} \tag{2.13}$$

where k_B is the Boltzmann constant, A_{eff} is the effective area of the antenna, $\Delta\nu$ is the bandwidth and t_{int} is the integration time. Increasing dish size, receiver bandwidth, or integration time improves sensitivity.

It is possible to observe radio sources in space using just one antenna. Single telescopes that are observing sources in the sky are called *single-dish*. Single-dishes

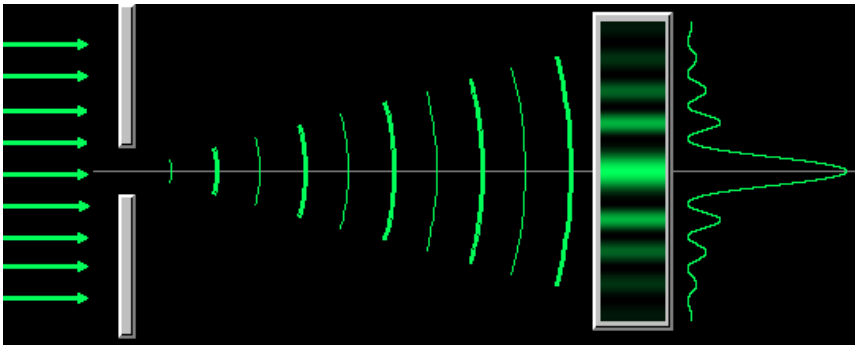

Figure 2.15: Schematic view of the diffraction pattern and the *beam pattern* described as a `sinc` function. Courtesy of `https://fiatlux.altervista.org/il-modec-e-l-esperimento-di-young.html`.

are unmatched for their broadband and long-term observations and monitoring, but they have a fundamental limitation: their resolution is of the order of arcminutes. This means that the physical scale they can observe is of the order of the kpc. The physical processes associated with jet formation, acceleration, and collimation of AGNs take place on the sub-parsec scale. To probe the physical processes happening inside the jets of AGN, it is necessary to combine the observations of the radio antennas located in the same place or around the globe. These techniques are called Very Large Baseline Array (VLBA) and Very Large Baseline Interferometry (VLBI), which will be treated in the Section 2.5.1.

Some examples of single-dish facilities and projects that use single-dish to perform interferometric observations are:

- The Metsähovi Radio Observatory[34], located in Finland, operates primarily at 22 and 37 GHz. The observations are radio continuum observations, and the goal is to obtain the total flux density of the source. At 22 and 37 GHz it is used a dual-horn dual beam-switching method which eliminates the effects of the background very efficiently. One integration typically takes ~ 30 minutes, and the detection limit under normal conditions (signal-to-noise ratio > 4) is of the order of 0.2 Jy. The main research topics of Metshäovi's AGN research teams are: the radio variability and the multifrequency studies (radio to γ-ray connection in blazars).
- The Quasar Intraday Variability at Effelsberg [35], in Germany, and Radio Telescopes (QUIVER) project [205] is a 100-meter antenna that works on frequencies between 2.6–43 GHz, to perform high-cadence observations (hourly sampling) to measure flux density variations on timescales shorter than 24 hours. Such rapid variability can arise from extremely compact emission regions in relativistic jets.
- The F-GAMMA project [124] which performed monthly monitoring of a sample of about 60 sources at up to twelve radio frequencies between 2.64 and 228.39 GHz using different single-dish facilities:
  - the Metsähovi Radio Observatory;
  - Effelsberg;

[34] `https://www.aalto.fi/en/metsahovi-radio-observatory`
[35] `https://www.mpifr-bonn.mpg.de/en/effelsberg`

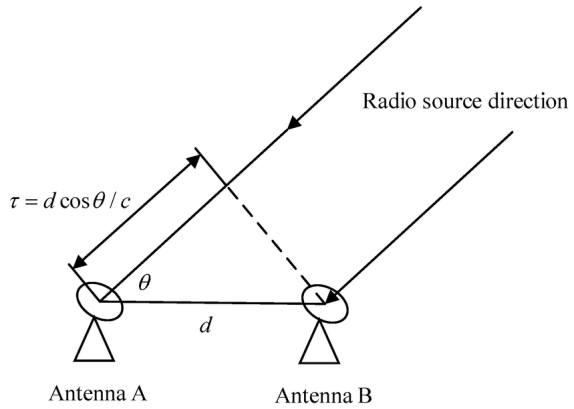

Figure 2.16: Schematic representation of an interferometer made by two elements. The two antennas are separated by a distance d and are looking at the target at an angle θ. τ is the geometrical delay between the two antennas. Courtesy of [335].

* IRAM[36], which is a 30-meter antenna that works on frequencies between 86–270 GHz.

Its main scientific goal was to provide quasi-simultaneous multi-frequency spectra and long-term light curves of γ-ray bright AGN detected by Fermi-LAT. The dense spectral sampling allowed the study of spectral evolution during radio flares, shock-in-jet scenarios, and time lags between radio and γ-ray activity.

2.5.1 Interferometry

In Figure 2.16, a simple schematic view of an interferometer composed by two antennas is presented. When the antennas point at the same radio source, located at an angle θ that is the angle between the baseline d and the direction of the source, the second antenna will receive the signal with a geometrical delay given by:

$$\tau = d\cos\theta/c \tag{2.14}$$

The output voltages of antenna 1 and antenna 2 at the time t are:

$$V_1 = V\cos[\omega(t-\tau)] \tag{2.15}$$

$$V_2 = V\cos(\omega t) \tag{2.16}$$

where V is the voltage and ω is the angular frequency.

The two signals are then correlated through the *correlator*, which requires a good estimation of τ and multiplies the signal:

$$V_1V_2 = \left(\frac{V^2}{2}\right)[\cos(2\omega t - \omega\tau) + \cos(\omega\tau)] \tag{2.17}$$

The term $2\omega t - \omega\tau$ varies rapidly. Therefore, with a time average long enough ($\Delta t \gg (2\omega)^{-1}$), it is possible to cut off this term. In this way, it is possible to obtain the *correlator response* R, which corresponds to the output voltage:

$$R =< V_1V_2 >= \left(\frac{V^2}{2}\right)[\cos(\omega\tau)] \tag{2.18}$$

[36] https://iram-institute.org/observatories/30-meter-telescope/

The *correlator response* R varies sinusoidally with time since the antennas track the source on the sky. These sinusoids are called *fringes*. The fringe phase is given by: $\phi = 2\pi(d/\lambda)\cos\theta$ where λ is the detected wavelength. Hence, the *correlator* multiplies the source brightness by the fringes pattern and integrates the results over the sky. If the source is a point source, the response of the interferometer is the sinusoid $\cos(\phi)$ spanning the sky. On the other hand, if the source is slightly extended, R is obtained by treating the extended source as the sum of independent point sources:

$$R_c = \int I(\hat{s})\cos(2\pi\vec{d}\times\hat{s}/\lambda)d\Omega \tag{2.19}$$

Where $I(\hat{s})$ is the brightness distribution of the source located in the direction defined by $\hat{s}$. This *even cosine component* of the signal is sensitive only to the even part (I_E) of the source brightness distribution I:

$$I = I_E + I_O \tag{2.20}$$

This means that to obtain the source brightness distribution, it is necessary to detect the odd part of the brightness distribution, which is given by the *odd sine component* of the signal:

$$R_s = \left(\frac{V^2}{2}\right)[\sin(\omega\tau)] \tag{2.21}$$

The combination of the cosine and sine correlators is called *complex correlator* or *complex visibility*:

$$\mathcal{V} = R_c - iR_s = \int I(\hat{s})\exp(-i2\pi\vec{d}\times\hat{s}/\lambda)d\Omega \tag{2.22}$$

To express the distribution of the *complex visibility* of an interferometer, a Cartesian coordinate system called *u-v plane* is used, where u represents the E-W direction and v the N-S direction, in units of the observed wavelength. During an observation with an interferometer composed of two or more antennas, each baseline d provides a visibility point in the *u-v plane*. Hence, radio interferometry takes advantage of the Earth's rotation to maximize the sampling of the *u-v plane*, also called *uv-coverage*. For each scan, the Earth's rotation will imply that the vector distance between antennas as seen by the source will be different, providing a new point in the *u-v plane*. This effect creates circular tracks in the *u-v plane* as the integration time of the observation increases. Ideally, to recover the true brightness distribution of the source, the *u-v plane* should have perfect sampling, which is not feasible given the limited number of antennas an interferometer can have. This means that the imaging and data reduction of the data is quite challenging. An example of the *u-v coverage* that a configuration of the Very Large Array (VLA)[37] interferometer can achieve is shown in Figure 2.17.

Some examples of interferometric facilities that use the interferometric principles are:

- The Very Large Array (VLA), characterized by 28 movable antennas in a Y shape, is located in the Plains of San Agustin in New Mexico and can observe frequencies from 1.0 GHz to 50 GHz. Every antenna has a 25 m of diameter and the baseline between the antennas can change:

[37] `https://public.nrao.edu/telescopes/vla/`

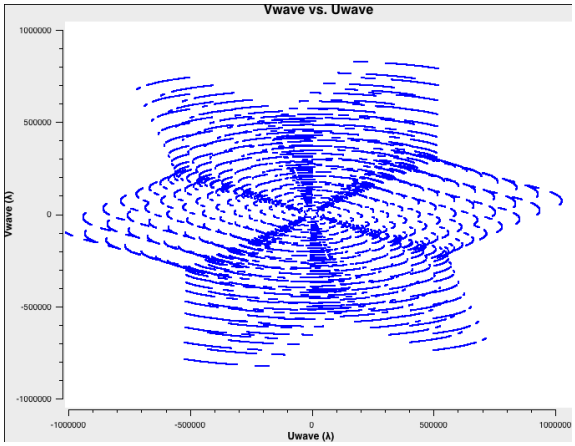

Figure 2.17: *UV-coverage* of the A-configuration of the VLA.Courtesy of `https://public.nrao.edu/telescopes/vla/`.

  - In the A configuration, the distance between the antennas is 36 km;
  - In the B configuration, the distance between the antennas is 11 km;
  - In the C configuration, the distance between the antennas is 3 km;
  - In the D configuration, the distance between the antennas is 1 km.

  Thanks to these configurations, the angular resolution can vary in the range $0.2 - 0.04$ arcseconds.

- The Submillimiter Array (SMA) [38] is an 8-element radio interferometer located near the summit of Maunakea in Hawaii. Operating at frequencies from 180 GHz to 420 GHz, the 6 m diameter dishes may be arranged into configurations with baselines as long as 509 m, producing a beam of sub-arcsecond width. Each antenna can observe with two receivers simultaneously, with up to 48 GHz total bandwidth. SMA is also a polarimetric facility, through the so-called **S**MA **M**onitoring of **A**GNs with **POL**arization program (SMAPOL). Polarimetric observations are a key diagnostic in radio and submillimeter monitoring because synchrotron emission — the dominant process in AGN jets — is intrinsically polarized. Measuring the degree and angle of polarization provides direct information on the magnetic field structure and its evolution during flares.

Then, some VLBI observational programs with VLBA instruments are:

- The Monitoring Of Jets in AGN with VLBA Experiments (MOJAVE) program[39] monitors radio brightness and polarization variations in jets associated with active galaxies visible in the northern sky. The observations are made with the Very Long Baseline Array (VLBA) at 15 GHz, which enables polarization images with an angular resolution better than 1 milliarcsecond.
- the VLBA-BU-BLAZAR program [40] at 43 GHz is a VLBA program. The higher frequency yields finer resolution, probing closer to the central engine. Polarimetric imaging reveals magnetic field structures and has shown strong temporal

[38] `https://lweb.cfa.harvard.edu/sma/`
[39] `https://www.cv.nrao.edu/MOJAVE/`
[40] `https://www.bu.edu/blazars/`

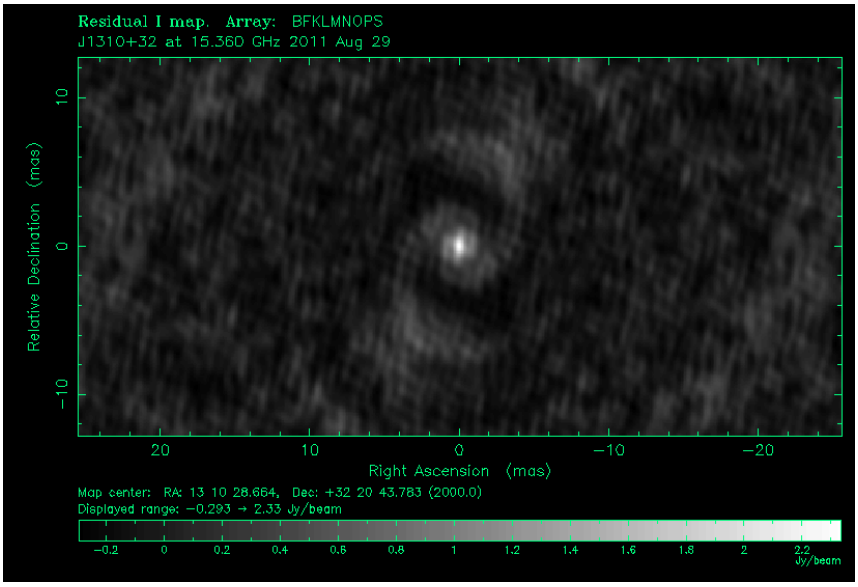

Figure 2.18: The uncleaned map of OP 313, with a map size of $10^{24} \times 10^{24}$, and cell size 0.1 mas/pixel. The bright region at the center is OP 313, and the spiral shape is an indication of the *uv-coverage*, or side-lobes, of the antennas.

correlations between γ-ray flares and the ejection of new jet components with an angular resolution of 0.2 milliarcseconds.

Interferometry data reduction

The interferometric visibilities (see Equation 2.22) are a complex quantity, described by an amplitude $A = (R_c^2 + R_s^2)^{1/2}$ and a phase $\phi = \tan^{-1}(R_s/R_c)$. The output of the antenna's receivers is in arbitrary units and has to be converted into a physical flux through a correction factor. This process is called amplitude calibration. Additional corrections also need to be applied to the phases, due to imperfect knowledge of the antennas' positions and due to variable atmospheric effects. These effects are corrected through phase calibration.

To realize the VLBI/VLBA images, it is necessary to perform a hybrid mapping technique, implemented in the software Difmap [287].

To understand what Difmap does, we have to know that the visibilities can be defined as the Fourier transform of the true source brightness on the sky, convolved with the instrumental response, which is called *dirty map*. In order to recover the true brightness distribution of the source, removing the contamination provided by the instrumental response, the data must be deconvolved: the footprint of the *dirty beam* has to be removed.

This corresponds to the Fourier transform of the *uv-coverage*, and therefore carries all the effects given by its incompleteness, inhomogeneity, and asymmetry. These effects manifest themselves in the form of the so-called side-lobes, which are spurious bright structures in the dirty map following the pattern given by the *uv-coverage*. In Figure 2.18, a picture of the blazar OP 313 with side-lobes is shown before the subtraction of the dirty beam. It can be challenging to disentangle such structures from the real source brightness distribution.

In Difmap, to find the true brightness of the source and the jet components the `CLEAN` algorithm [173] is used. This procedure consists in finding the map peak, subtracting a given fraction of it from the map convolved with the dirty beam, and storing it in a model in the form of several point-like components, called clean components. This procedure is iterated, as fainter structures of the source emerge and are cleaned out, until only noise is left in the dirty map. To improve the convergence of the process, each clean iteration is followed by a phase self-calibration step, where the visibility phases are calibrated against the model itself. After obtaining a reasonable starting model, the visibilities can also be self-calibrated in amplitude. The model resulting from this iterative process is convolved with a clean beam, a Gaussian fit of the main lobe of the dirty beam, to produce the clean map.

In this thesis, another method was used. Using the `modelfit` of Difmap, the data were directly modeled with a series of circular Gaussian components that best fit the data, instead of using point-like components. Model fitting is useful when it is difficult or inappropriate to make an image from the visibility data, or as a way of characterizing an image with a fairly small number of free parameters. After a semi-decent model for the source is produced using the Gaussian components, it is possible to iterate their fitting on the map until a good χ^2 is reached. Then, it is possible to repeat the procedure until only noise is left in the dirty map.

2.6 Neutrino telescopes

The basic structure of a detector for cosmic neutrinos is a matrix of light detectors inside a transparent medium. This medium, such as ice or water at great depths [291]:

- Offers a large volume of free target nucleons for neutrino interactions;
- Provides shielding against secondary particles produced by CRs;
- Allows the propagation of Cherenkov photons emitted by relativistic particles produced by the neutrino interaction.

Neutrinos interact with matter via weak interactions. In particular, a high-energy neutrino interacts with a nucleon N of a nucleus, via charge current (CC):

$$\nu_l + N \rightarrow l + X \tag{2.23}$$

where $l = e, \mu, \tau$, or via neutral current (NC):

$$\nu_l + N \rightarrow \nu_l + X \tag{2.24}$$

where X is a hadronic system which carries part of the incoming neutrino energy. The charged secondary particles, produced by the neutrino interaction, travel through the medium until they decay or interact. The mean distance traveled by them is called the *path length* and it depends on their energy and energy loss in the medium. The detection principle of the detectors for neutrinos with energies above the TeV range is based on the detection of the photons produced by the Cherenkov effect (see Section 2.2.1) [78]. The Cherenkov radiation is measured through the use of a three-dimensional array of PMTs. From the number of detected photons and their arrival times, it is possible to infer the neutrino flavor, direction, and energy.

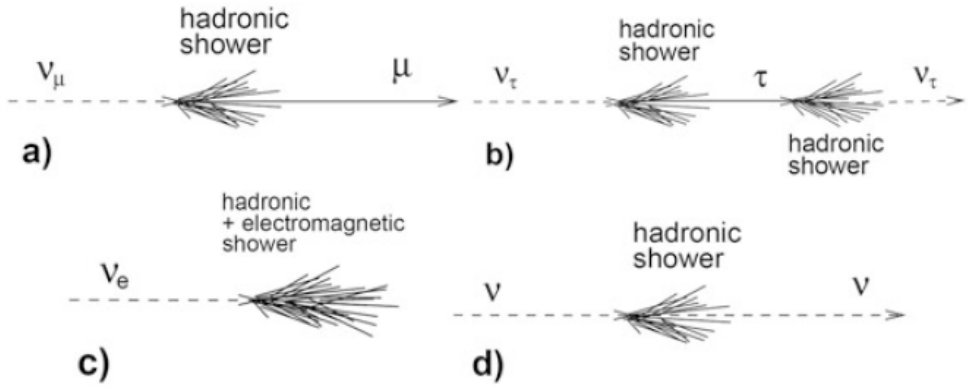

Figure 2.19: Event topologies for different neutrino flavors and interactions: (a) CC interaction of a ν_μ produces a muon and a hadronic shower; (b) CC interaction of a ν_τ produces a τ that decays into another ν_τ, tracing a signature called double bang. (c) CC interaction of ν_e produces both an electromagnetic and a hadronic shower; (d) a NC interaction produces a hadronic shower. Courtesy of [291].

The equation that defines the number of Cherenkov photons, N_C, emitted per unit wavelength interval, $d\lambda$, and unit distance travelled, dx, by a charged particle of charge e is given by the *Frank-Tamm* formula:

$$\frac{d^2N_C}{dxd\lambda} = \frac{2\pi}{137\lambda^2}\left(1 - \frac{1}{n^2\beta^2}\right) \tag{2.25}$$

where λ is the wavelength of the radiation, n is the refracting index and $\beta \sim 1$ for relativistic particles. From this equation, it is clear that the lower the wavelength, the more Cherenkov photons are emitted.

To detect a neutrino coming from an astrophysical source, a huge detector is necessary. Detectors with large volumes are able to distinguish between events with a *long track* due to the presence of muons, and events with a *shower*, without muons. In Figure 2.19 are shown a schematic view of ν_e, ν_μ and ν_τ charged current (CC) events and of a neutral current (NC) event.

Neutrino and anti-neutrino reactions are not distinguishable. Hence, no separation between particles and anti-particles can be made. One element to take into account is that in CC ν_μ, often only the muon track is detected, as the *path length* of a muon in water exceeds that of a shower by more than three orders of magnitude for energies above 2 TeV. Therefore, such an event might very well be detected even if the interaction has taken place outside the instrumented volume and the muon pass through the detector.

The techniques that a large volume detector uses to identify a cosmic neutrino signal are:

- If the track can be accurately reconstructed, the neutrino is identified through the observation of an excess of events in a small solid angle region $\Delta\Omega$ over the expected background. In this case, only ν_μ CC interactions can be reconstructed with a precision better than 1°.
- For all neutrino interaction candidates, a cosmic neutrino signal is detected by the observation of an excess of events above a given observed energy. The

spectrum of the cosmic signal is expected to be $\frac{d\phi_\nu}{dE} \propto E^{-\alpha_\nu}$, with $\alpha\nu \sim 2$ while $\alpha_\nu \sim 3.7$ for the background.

– The detection of a neutrino candidate in temporal/spatial coincidence with an external trigger, such as that resulting from a GRB, a GW event, or from an AGN.

This last point is the focus of this thesis.

Furthermore, neutrino telescopes, in contrast with every other instrument devoted to astronomy, are " downward looking". The reason why it is necessary to look for ν_μ's coming from "underneath", so the ones that crossed the Earth, is related to the need to avoid being swamped by the enormous background of atmospheric muons. Hence, large-volume neutrino detectors can identify neutrino candidates from all directions, using a part of the detector as a veto, and one of the veto duties is to detect the atmospheric muons signals to allow us to reject them.

The current neutrino telescopes that are still working, or will work soon, in the ice or in the water are:

– Baikal Gigaton Volume Detector (Baikal-GVD) at Lake Baikal in Russia;

– IceCube in Antarctica, which will be described in detail in Section 2.6.1;

– KM3NeT is a research infrastructure that will house the next-generation neutrino telescope in the Mediterranean Sea. It will host two different structures, one called Astroparticle Research with Cosmics in the Abyss (ARCA) in Sicily, which is dedicated to the search for very high-energy cosmic neutrinos, and one called Oscillation Research with Cosmics in the Abyss (ORCA) in France, which is optimised for the study of neutrinos created by cosmic rays in the Earth's atmosphere. On the 13th of February 2023, an extremely high-energy muon traversed the ARCA detector. This event is referred to as KM3-230213A. The reconstructed neutrino energy is $\sim 220\,\text{PeV}$ [25].

2.6.1 IceCube

At the South Pole, where the ice is about 2800 m deep, the first neutrino experiment that was built is the Antarctic Muon And Neutrino Detector Array (AMANDA). The researchers drilled holes in the ice using a hot water drill and lowered strings of optical sensors before the water in the holes could freeze again. This detector worked as expected, and AMANDA detected its first atmospheric neutrinos. This success led to AMANDA-II, which consisted of 19 strings holding 677 optical sensors [291]. In 2005, after 9 years of operation, AMANDA officially became part of her successor project, the IceCube Neutrino Observatory[41].

IceCube is the only running km^3-scale neutrino observatory. A schematic view of IceCube is shown in Figure 2.20.

IceCube uses an array of 5160 Digital Optical Modules (DOMs) deployed on 86 strings at a depth of 1.5–2.5 km deep in the ice. Strings are arranged at the vertices of equilateral triangles that have sides of 125 m. The DOMs are spherical, pressure-resistant glass housing a 25 cm diameter photomultiplier tube (PMT) plus electronics for waveform digitization, and vertically spaced 17 m from each other along each

[41] `https://icecube.wisc.edu/`

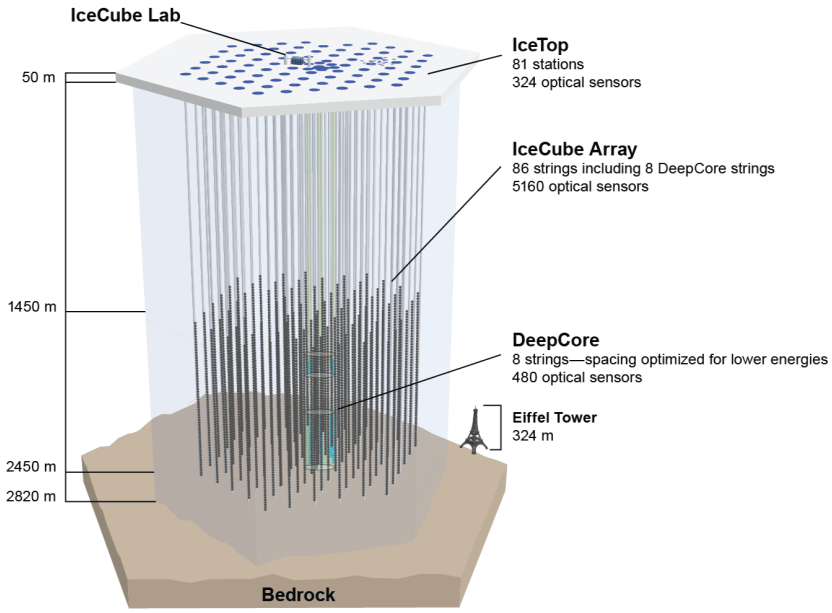

Figure 2.20: Schematic view of the structure of IceCube detector, which is characterized by 86 strings buried in the ice. Courtesy of the IceCube collaboration.

string. High quantum efficiency PMTs are used in a denser sub-array located in the center of the detector. This sub-array, called DeepCore, enhances the sensitivity to low-energy neutrinos. A surface CR detector, called IceTop, completes the IceCube Observatory.

Three different topologies are expected in IceCube after the interaction of astrophysical neutrinos:

- Tracks-like events trace the CC interactions of ν_μ, where the muon produced during the interaction passes through the detector, losing energy mostly by ionization in the ice. Just 1% of its total energy is lost by Cherenkov radiation. Therefore, the energy resolution of such events is quite poor. On the other hand, their direction can be very well reconstructed, with a resolution of the order of $\sim 1°$. This resolution allows the search for the sources of cosmic neutrinos. The muons that create the track-like pattern inside IceCube can be the result of neutrino interactions that happen outside the instrument volume (through-going tracks), or interactions that happen inside it (starting tracks). This last kind of track has a lower angular resolution due to the shorter muon path inside the detector. An example of a track event measured by the DOMs is shown in Figure 2.21(b).
- Cascade-like events can be either traces of CC or NC interactions. Regarding CC interactions, ν_e produces a secondary electron that interacts, producing an electromagnetic shower initiated by its bremsstrahlung photons. The radiation pattern in the detector is approximated as a spherical shape, as shown in

Figure 2.21(a). In the majority of cases, the cascade is well contained inside the detector volume, and since the majority of energy losses are through the electromagnetic and hadronic showers, it is possible to have a good calorimetric measurement and a good energy resolution. However, the resulting angular resolution is $\sim 10^{\circ}$ for energies above 60 TeV [1]. Hence, it is not suitable to locate the astrophysical source that generates the neutrino. Cascade-like radiation patterns are also tracers of NC interactions and are initiated by the charged particles produced in the hadronic showers. The pattern of the hadronic showers cannot be distinguished from that one produced by electromagnetic showers. As a consequence, the reconstruction of the neutrino's energy is worse.

– Double Bangs is produced during a ν_τ CC interaction. The shape of the light pattern has features from track-like and cascade-like events since it is composed by two cascades connected by a track-like pattern, as shown in Figure 2.22. The first cascade is created by the hadronic shower from the ν_τ CC interaction and the produced τ travels in the ice, creating a track-like pattern similar to the one of a muon. However, the τ has a decay length of about 50 m at PeV energy, so it will decay in an electron inside the detector. In this case, a second cascade is observed due to the electromagnetic shower initiated by the electron. Another possible interaction is the scattering of a neutrino with an electron instead of a nucleus of ice. This process is rare because of the small mass of the electron. This event is called *Glashow resonance*, due to the center of mass energy equals the mass of the W boson at the Glashow resonance energy, which is $E^{res}_{\bar{\nu}_e} \sim 6.3\,\text{PeV}$ [157] when an $\bar{\nu}_e$ interacts with an electron.

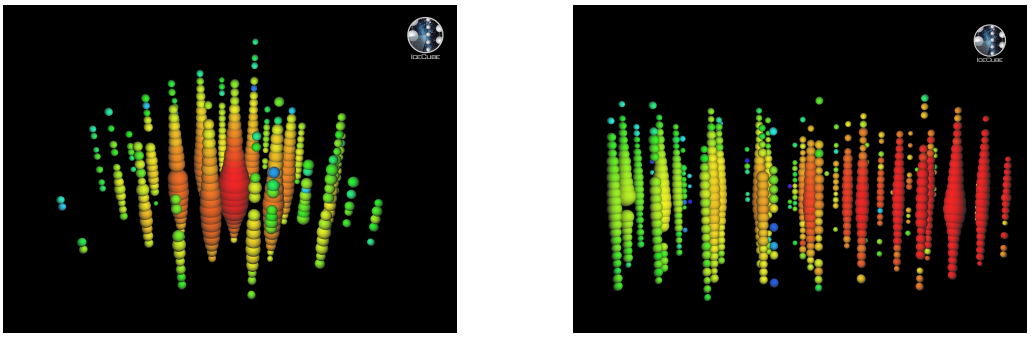

(a) (b)

Figure 2.21: a) Event displays of the Cherenkov light pattern measured in the IceCube DOMs for a cascade-like event. b) Event displays of the Cherenkov light pattern measured in the IceCube DOMs for a track-like event. Each sphere represents a DOM, with its size proportional to the number of detected photons and the colormap describing the arrival time from the earliest hits in red to the latest in green. Courtesy of the IceCube collaboration.

Three main methods are used in IceCube to discriminate the astrophysical neutrino component from the atmospheric one:

– The selection of through-going, track-like events from the Northern hemisphere, considering that the Earth is shielding the telescopes from the atmospheric muons, and the discrimination between the signal and the background is based on the spectral shapes (see Section 1.1.3). This method can be applied to events

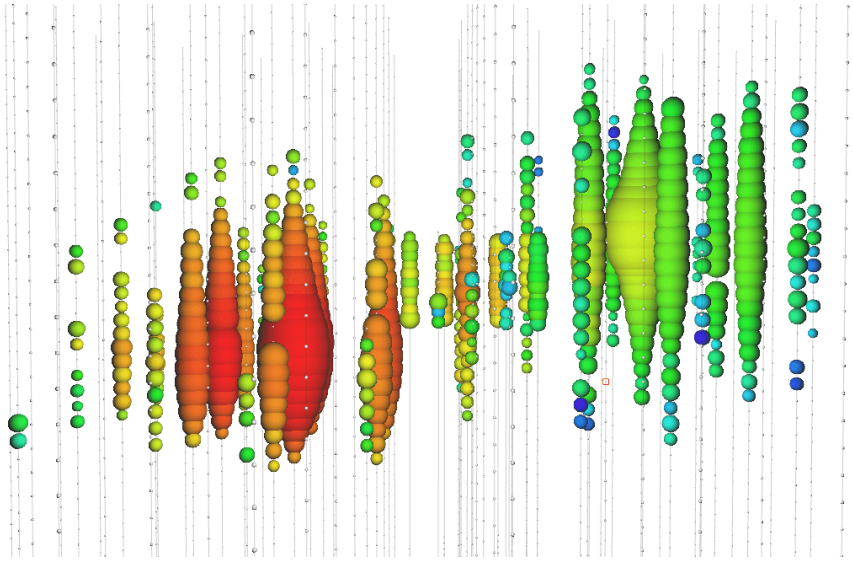

Figure 2.22: vent displays of the Cherenkov light pattern measured in the IceCube DOMs for a double bang event. Courtesy of the IceCube collaboration.

arriving from the Northern hemisphere and is only sensitive to track-like events.

- A selection of both track-like and cascade-like events, requiring that the interaction happens within the detector volume. These events are called High Energy Starting Events (HESE) and for this selection, the peripheral strings of IceCube are used as a veto to exclude the atmospheric muons. This method is sensitive to arrival directions from both hemispheres, but has a lower effective area for ν_μ.
- Selection of only cascade-like events, from ν_e and ν_τ events. The problem of this method is the liability in pinpointing astrophysical sources due to worse worse angular resolution of cascade-like events.

Chapter 3

Long-term multi-wavelength analysis of the Flat Spectrum Radio Quasar OP 313

This Chapter presents a long-term multi-wavelength study performed on the FSRQ OP 313. OP 313 was observed during a strong flaring state between November 2023 and March 2024. The behavior of this source from γ-ray to radio frequencies is deeply studied and presented in detail in the following sections. The results of this analysis are summarized in a publication submitted to the *Astronomy & Astrophysics* journal in August 2025, on behalf of the *Fermi*-LAT Collaborations. The content reported in this Chapter could be different from the one in the published paper. I am the corresponding author, together with Elina Lindfors (Professor at the University of Turku, Finland), who contributed to the interpretation of the behaviour of the source.

3.1 OP 313

The project on OP 313 started following one of the FA shifts (see Section 2.1.1), due to the unprecedented γ-ray emission of this source seen by Large Area Telescope (LAT) and by CTAO's Large-Sized Telescope (LST)-1 located at La Palma [1].

OP 313, also known as B2 1308+326, is an FSRQ at a redshift of $z = 0.997$ [282] and coordinates $R.A. = 197.619433$ and $Dec. = 32.345495$ [331]. Due to its variable emissions and uncertain classification [e.g. 58, 125, 319], this blazar has been observed several times at different wavelengths. Starting with [293], OP 313 was classified as a BL Lac due to its nearly featureless optical spectra [326], which indicates synchrotron emission from a relativistic jet viewed close to the line of sight and no thermal emission from the accretion disk and host galaxy. Nevertheless, [125], using VLBI polarization images, observed the polarized flux from the inner part of its jet with a position angle perpendicular to the jet, and they detected superluminal motion in its jet [260]. Polarization measurements trace the magnetic field structure of the emitting region, providing insight into jet dynamics and geometry. Since all of these are characteristics of a quasar, [125] classified OP 313 as an FSRQ with weak

[1] `https://www.ctao.org/`

emission lines. Furthermore, OP 313 is detected by the LAT [36], and it is identified as a Flat Spectrum Radio Quasar FSRQ in the *Fermi*-LAT Catalog 4FGL [11].

The LAT detected an increase in flaring activity from OP 313, for the first time in April 2014. An Astronomer's Telegram (ATel) was published [60] showing that the peak of activity was reached on the 14th of April with an average γ-ray flux above 100 MeV of $(1.1 \pm 0.2) \times 10^{-6}$ photons/cm^{2}s^1, about 13 times its average daily flux from the 2FGL catalog [8]. The other two ATels were published in 2021 and 2022 [145, 222], showing increasing activity from this source. In 2022, OP 313 showed the same flux as in 2014 but it was compared with the 4FGL catalog and it resulted increased by 20 times the value reported in the catalog [2.4×10^{-9} photons/cm^{2}s from 0.1-100 GeV 9, 10]. Again, the LAT detected an increase in flaring activity from OP 313 on the 22nd of November, 2023. The first peak of activity was reached on the 24th of November 2023 with an averaged γ-ray flux at energies larger than 100 MeV of $(1.8 \pm -0.2) \times 10^{-6}$ photons/cm^{2}s, approximately 40 times larger than the value reported in the fourth *Fermi* Large Area Telescope (4FGL) catalog. Additionally, the spectrum photon index was significantly harder (1.80 ± 0.06) than the value reported in the 4FGL (2.34 ± 0.02). This flare led the *Fermi* collaboration to publish an ATel on the renewed activity of this source [40]. The high state of OP 313 was remarkably seen by the Large-Sized Telescope-1 (LST-1) of the CTAO located at La Palma in December 2023 [87]. This quasar is the most distant quasar observed at VHE so far. Another major flare from this source was seen on the 27th of February, 2024. The detected flux was the highest ever observed by the LAT for OP 313: $(3.1 \pm 0.4) \times 10^{-6}$ photons/cm^{2}s, 60 times larger than the value reported in the 4FGL catalog, with photon index 1.81 ± 0.09. Another ATel was published by the LAT collaboration [39].

Given that this source has exhibited prolonged activity since 2022, as shown in the LAT lightcurve repository[2][11] following more than a decade of quiescence, and is the farthest blazar ever observed at VHE, I and my collaborators decided to analyze 15 years of data, from the beginning of the *Fermi* mission on the 4th of August 2008, from radio to γ-rays to unveil the mechanisms responsible for the observed flares. In order to uncover the correlation between γ-ray emission and other energy bands emissions and to perform a multi-wavelength SED modeling during the flaring periods of OP 313, the energy bands analyzed are: the radio energy band from 2.64 to 353 GHz, used also to perform a study of the jet kinematic, the optic one from 464 to 690 nm, the UV one form 170 to 650 nm, the X-ray one from 0.3 to 10 keV and the γ-ray one form 20 to 300 GeV.

3.2 Multi-wavelength Datasets

In Table 3.1, the instruments whose data were included in our analysis starting from the 4th of August 2008 are listed.

[2] `https://fermi.gsfc.nasa.gov/ssc/data/access/lat/LightCurveRepository/`

Table 3.1: Instruments whose datasets were used for the long-term multi-wavelength (MWL) analysis of OP 313. The sensitivity range and the range of time are listed. The final MWL light curves with all these data are reported in Figure 3.2. The optical wavelength refers to the standard effective wavelength midpoint of the filter.

Instrument	Sensitivity range	MJD start	MJD stop
Fermi-LAT	$20\,\mathrm{MeV} - 300\,\mathrm{GeV}$	54682	60378
Swift-XRT	$0.2 - 10\,\mathrm{keV}$	54698	60378
Swift-UVOT	*v, b, u, w1, m2, w2* $170 - 650\,\mathrm{nm}$	54698	60378
ZTF	g, r, i $464, 658, 806\,\mathrm{nm}$	58202	60162
CRTS	V $551\,\mathrm{nm}$	54807	57505
ATLAS	o, c $534, 690\,\mathrm{nm}$	57362	60375
KAIT	R $658\,\mathrm{nm}$	55938	58966
Tuorla	R	55733	60425
SMA	$0.99\,\mathrm{mm}$	54722	60112
VLBA-BU-BLAZAR	$7\,\mathrm{mm}$	54922	60391
Metsähovi	$8\,\mathrm{mm}$	54704	60132
MOJAVE	$2\,\mathrm{cm}$	54838	60407
SMA and SMAPOL	$0.9,\ 1.1,\ 1.3\,\mathrm{mm}$	54722	60379.5
QUIVER	$0.7,\ 0.8,\ 1.4,\ 2.1\,\mathrm{cm}$ $2.9,\ 6.2,\ 11.6\,\mathrm{cm}$	60261	60399
F-GAMMA	$2.9, 3.6, 6.2, 11.4\,\mathrm{cm}$ $0.7, 0.9, 1.3, 2.1,\ \mathrm{cm}$	54700	56809

3.2.1 Fermi-LAT data reduction

To analyze 15 years of Pass 8 data collected by the LAT, the version of the LAT *ScienceTools* [3] [4] that was used is the v2.2 and the `fermipy` [328] v1.1 Python package. The $P8R3\_SOURCE\_V3$ instrument response functions, the Third Data Release 4FGL-DR3 [10], and the Galactic and the isotropic diffuse gamma-ray emission models provided by the standard templates $gll\_iem\_v07.fits$ and $iso\_P8R3\_SOURCE\_V3\_v1.txt$ [5] were used. The photon events with reconstructed energy between 100 MeV and 300 GeV were analyzed, selecting a region of interest (ROI) of 15×15 deg centered on the γ-ray source position and applying a standard quality cut (`'DATA_QUAL>0 && LAT_CONFIG==1'`) to select only good quality events. Furthermore, a zenith angle cut of 90 deg was used to reduce the contamination from the Earth limb. In a configuration file, all these requests were included, and the `GTAnalys setup` tool was run (see Section 2.1.1).

To perform a maximum-likelihood test statistic (TS) analysis (see Section 2.1.1), the normalization of all sources at 5 deg from OP 313 with a $TS \geq 25$ were left free to vary, same for all the parameters of the Galactic, of the isotropic diffuse and of OP 313. The TS was defined as $TS = 2(logL_1 - logL_0)$ with L_1 and L_0 being the likelihood of the data given a model with and without a point source in the position of OP 313, respectively. Then, the light curve was computed using the algorithm developed by [221] to perform the adaptive binning and identify statistically significant variations with the Bayesian Blocks algorithm [279] as implemented in `astropy`[6]. In [221], the algorithm evaluates the bin width by requiring a constant relative flux uncertainty: $\sigma_{\ln F} = \Delta_0$ in each bin, where the constant flux uncertainty Δ_0 is fixed at the beginning of the procedure. The algorithm is structured in the following points:

- The Equation that the algorithm solves is:

$$\sigma_{\ln F}(T_0, T_1, \bar{F}, \bar{\Gamma}) = \Delta_0 \tag{3.1}$$

  where $\bar{F}$ and $\bar{\Gamma}$ are the average flux and photon spectral index over the interval $[T_0, T_1]$. The detection time of the earliest photon leading to the fulfillment of the condition $\sigma_{\ln_F} < \Delta_0$ is taken as T_1.
- Then, $\bar{F}$ is estimated over $[T_0, T_1]$. If $\sigma_{\ln F}$ is equal to Δ_0 within a predefined tolerance, convergence is achieved T_1 becomes the new T_0 for evaluate the next bin width. Otherwise, T_1 is reevaluated with the updated value of $\bar{F}$.
- The whole procedure is repeated until convergence is achieved.

This method allows for more information to be encapsulated within the light curve and avoids upper limits. The adaptive binning method is designed specifically for constructing flux light curves. Instead, the Bayesian Blocks algorithm [279] identifies the most probable segmentation of the unbinned data by maximizing a fitness function based on the Poisson likelihood under a Bayesian framework. The light curve is represented as a series of contiguous "blocks" within which the event rate is modeled as a constant. The determination of the location of the *change points*, or boundaries between the blocks, and the rates within the blocks is made via a Bayesian analysis

[3] `https://fermi.gsfc.nasa.gov/ssc/data/analysis/documentation/`
[4] `https://fermi.gsfc.nasa.gov/ssc/data/analysis/software/`
[5] `https://fermi.gsfc.nasa.gov/ssc/data/access/lat/BackgroundModels.html`
[6] `https://docs.astropy.org/en/stable/api/astropy.stats.bayesian_blocks.html`

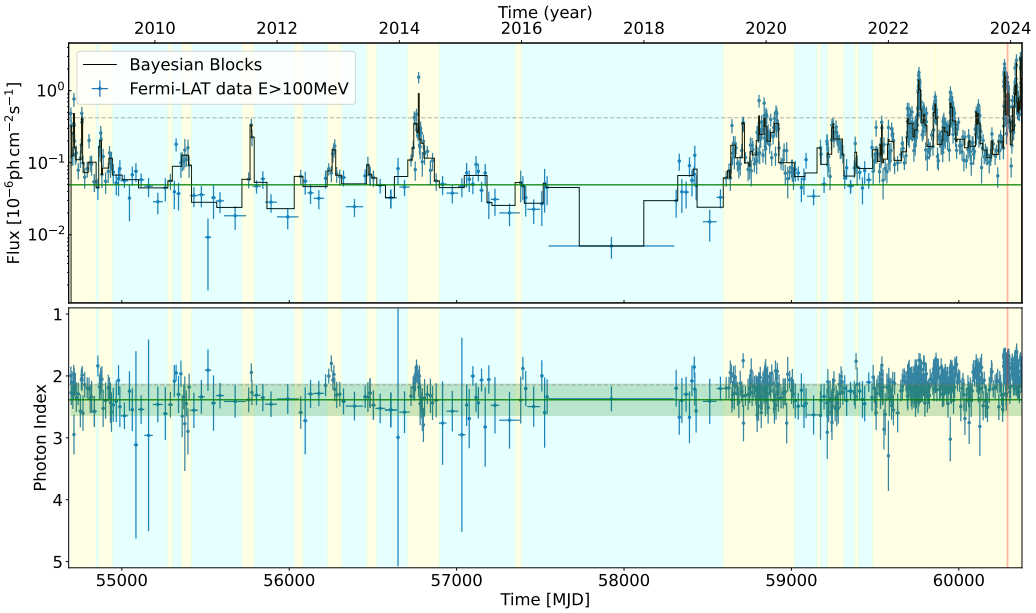

Figure 3.1: Top: 15-year Fermi-LAT light curve of OP 313, divided into two states: quiescent (blue) and flaring (yellow). The green line shows the average flux of 4.93×10^{-8} photons/cm^{2}s weighted by the time in each bin between the 9th of December 2014 and 9th of August 2018. The grey line is the average weighted flux in the total considered time window of 4.21×10^{-7} photons/cm^{2}s. Bottom: the Fermi-LAT spectral index across the same 15-year period. The green line shows the average photon index between the 9th of December 2014 and 9th of August 2018 ($\Gamma = 2.39$) and the green band is its respective 1σ uncertainty. The grey line shows the average photon index in the 15-year time window ($\Gamma = 2.14$). The red vertical bands represent the period in which OP 313 was detected by LST-1 at La Palma.

assuming Poisson statistics. The user can assign the prior probability for the number of blocks, which is similar to assigning a significance level threshold for each detected block.

The approach to distinguish flaring states from quiescent states of the source is the following [272]: it was considered the average flux, weighted by the time duration of each bin, in the low-activity period from the 9th of December 2014 to the 9th of August 2018 as a proxy of the quiescent state. All Bayesian blocks with a flux level higher than this value (4.93×10^{-8} photons/cm^{2}s) represent the flaring states of the source, and all the blocks with a flux level lower than this represent the quiescent states, in yellow and blue in Figure 3.1, respectively. The red band in Figure 3.1 represents the period in which LST-1[7] detected OP 313. Since late 2021, the source has consistently remained in a flaring state. The photon index from the beginning of 2022, shown in Figure 3.1, is generally harder than the 15-year average ($\Gamma = 2.14 \pm 0.09$, in grey) and the average from the 9th of December, 2014 to the 9th of August, 2018 ($\Gamma = 2.39 \pm 0.25$, in green).

[7] `https://www.ctao.org/emission-to-discovery/telescopes/lst/`

3.2.2 Neil Gehrels Swift Observatory Data

For this study, the *Neil Gehrels Swift Observatory* (*Swift*)-X-Ray Telescope (XRT) observations of OP 313 from the 20th of August 2008 to the 9th of March 2024 were analyzed. During the analysis, it was used the spectral fitting package XSPEC v12.13.1 [32] and the Python package PyXspec v2.1.4 available in the HEASOFT[8] software v.6.33.1, together with the calibrated source background (CALDB, v20220331), and response files. The analysis that was performed is described in 2.3.1.

The spectrum was fitted with XSPEC using a `phabs*powerlaw` and `phabs*zpowerlw` models. The `phabs` component is the photoelectric absorption given by $M(E) = \exp[-\eta_H \sigma(E)]$, where $\sigma(E)$ is the photoelectric cross-section, and η_H is the equivalent hydrogen column, in units of 10^{22} atoms cm^{-2}. The hydrogen column density was fixed at $N_H = 1.23 \times 10^{20}\,\mathrm{cm}^{-2}$ [9]. In these models, `phabs` includes the Galactic line-of-sight absorption, while `powerlaw` and `zpowerlw` are defined as:

$$\frac{dN}{dE} = N_0(E)^{-\alpha} \tag{3.2}$$

$$\frac{dN}{dE} = N_0[E(1+z)]^{-\alpha} \tag{3.3}$$

where N_0 is the normalization in units of photons/keV/cm^2/s at 1 keV, E is the energy, z is the redshift and α is the photon index of the power law. The two models returned comparable results. From now on, the `phabs*powerlaw` spectral results will be used.

Ultraviolet/Optical Telescope (UVOT) data from the same period were processed and analyzed using the `uvotimsum` and `uvotsource` tasks in HEASOFT (see Section 2.4.1). The available UVOT observations were performed using the photometric broad-band filters in optical *v, b, u* and UV *w1, m2, w2*. To derive the source instrumental magnitude using `uvotsource`, it was adopted a circular source region of 5″ radius centered at the object position and a circular nearby region of 20″ radius were adopted to derive the background contamination. Then, the data were corrected for Galactic extinction using $E(B-V) = 0.0115 \pm 0.0005$ [10][280], and the computed magnitudes were converted to energy flux units.

3.2.3 Optical

The optical dataset analysis was performed by collaborators of this project. More details on this analysis are in [202] and [203].

The long-term optical light curve is constructed by combining data from all-sky surveys and from dedicated blazar monitoring programs (see Section 2.4). The following surveys and programs are included: Zwicky Transient Facility [ZTF, 46], Catalina Real-Time Transient Survey [CRTS, 105], Irsa's Image and Spectrum Server

[8] `https://heasarc.gsfc.nasa.gov/docs/software/heasoft/`

[9] This value was obtained for OP 313 using NASA's HEASARCH tool available at: `https://heasarc.gsfc.nasa.gov/cgi-bin/Tools/w3nh/w3nh.pl`

[10] Mean value of E(B-V) for OP 313 available at NASA/IPAC Infrared Science Archive at: `https://irsa.ipac.caltech.edu/applications/DUST/`

(ATLAS) [11], Katzman Automatic Imaging Telescope [12][KAIT, 116] at the Lick Observatory and the Tuorla Observatory (Tuorla) blazar monitoring program[13] [254]. Data from all optical filters were included (see Table 3.1).

The survey data have been extracted from the databases, while the dedicated observations of this source from Tuorla blazar monitoring were analyzed using standard procedures of differential photometry using a semi-automatic pipeline [e.g. 254]. An aperture of 5 arcseconds was used for the photometry.

The survey data and dedicated observations were combined following the prescriptions of [202] and [203]. In short, data from simultaneous and quasi-simultaneous nights were used to estimate the shifts between different observatories. Data from other observatories were shifted using Tuorla blazar monitoring data as a reference point.

3.2.4 Metsähovi

The 37 GHz observations were made with the 13.7 m diameter Metsähovi radio telescope (see Table 3.1). The detection limit of the telescope at 37 GHz is on the order of 0.2 Jy under optimal conditions. Data points with a signal-to-noise ratio < 4 are handled as non-detections. The flux density scale is set by observations of DR 21. Sources NGC 7027, 3C 274, and 3C 84 are used as secondary calibrators. A detailed description of the data reduction and analysis is given in [301]. The error estimate in the flux density includes the contribution from the measurement root mean square (rms) and the uncertainty of the absolute calibration. More details on Metsähovi radio telescopes are in Section 2.5.

3.2.5 F-GAMMA, QUIVER and SMAPOL

The F-GAMMA and QUIVER observations are performed at several radio bands (depending on receiver availability and weather conditions) from 2.6 GHz to 44 GHz (11 cm to 7 mm wavelength) using nine receivers located at the secondary focus of the 100-m Radio Telescope. The polarized intensity, position angle, and polarization percentage were derived from the Stokes I, Q, and U cross-scans. Mainly the calibrators 3C 286, 3C 48 and NGC 7027 were used for the total flux and polarization calibration (e.g. [205, 246]). In this thesis, the F-GAMMA data from the 22nd of August 2008 to the 1st of June 2014 were used, while the QUIVER data from the 13th of November 2023 to the 30th of March 2024 were used.

The SMA [171] was used to obtain total flux and polarimetric millimeter radio measurements at 1.3 mm (225 GHz) within the framework of two complementary programs: the standard SMA flux monitoring campaign [161] and the more recent SMAPOL program. SMAPOL follows the evolution of forty gamma-ray loud blazars, including OP 313, since June 2022 on a fortnightly cadence. The polarized intensity, position angle, and polarization percentage were derived from the Stokes I, Q, and U visibilities. Mainly MWC 349 A, Callisto, Uranus, Neptune, and Ceres were used for the total flux calibration according to their visibility, and the calibrator 3C 286, which has a high linear polarization degree and a stable polarization angle, was

[11] https://irsa.ipac.caltech.edu/applications/Atlas/

[12] https://www.lickobservatory.org/explore/research-telescopes/katzman-automatic-imaging-telescope/

[13] https://users.utu.fi/kani/1m/

observed regularly as a cross-check of the polarization calibration. The SMA data used in this work span from 13 September 2008 to 10 March 2024, and include observations from both the flux monitoring and SMAPOL programs at 225, 273, and 350 GHz.

3.2.6 VLBA data

The publicly available sky brightness distributions in the (u, v) visibility plane were modeled starting from the 1st of April 2009 to the 22nd of March 2024 for the VLBA-BU-BLAZAR and from the 7th of January 2009 to the 7th of April 2024 for the Monitoring Of Jets in Active galactic nuclei with VLBA Experiments (MOJAVE) project. To represent the total intensity structure of each source at each epoch, the data were modeled with a series of circular Gaussian components that best fit the data using the `modelfit` task in the Difmap v2.5o software package [286] (see Section 2.5.1). From now on, these Gaussian components will be referred to using the term "knots", which are usually compact features of enhanced brightness in the jet. The first single circular Gaussian component is the one that approximates the brightness distribution of the core, which is typically the brightest feature on the map, located close to the base of the jet, and then knots were added at the other approximate locations of bright features. Every time a knot is added, the `modelfit` task is used to determine the parameters of the knot that yield the best agreement between the model and (u, v) data, according to a χ^2 test. This process ended when the addition of a new knot did not significantly improve the χ^2 value. Often, the model of a previous epoch is used as the starting model for the next epoch for a given source, under the assumption that the jet does not drastically change structure between roughly monthly observations [320].

3.3 Results

In this Section, the main results of the analyses are described for the multi-wavelength datasets.

3.3.1 Multi-wavelength light curves of OP 313

The light curves from γ-ray to radio frequencies are shown in Figure 3.2. All of them show the emission of OP 313 from the beginning of the *Fermi* mission, on 4th of August 2008, to the 9th of March 2024 (MJD 54682.7 - 60378.0).

The trend of the light curves in γ-rays, X-rays, UV, and optical shows an increasing flux starting from 2022. Before then, the source is characterized by small flares marginally visible in the γ-ray light curve. Instead, in the radio light curves, the source exhibits significant variability over 15 years. The common trend between all the different radio frequencies is that the source was characterized by high fluxes from the beginning of the analysis in 2008. Then, it shows a decreasing trend until 2019, when it started to increase again (see more details in Section 3.3.4).

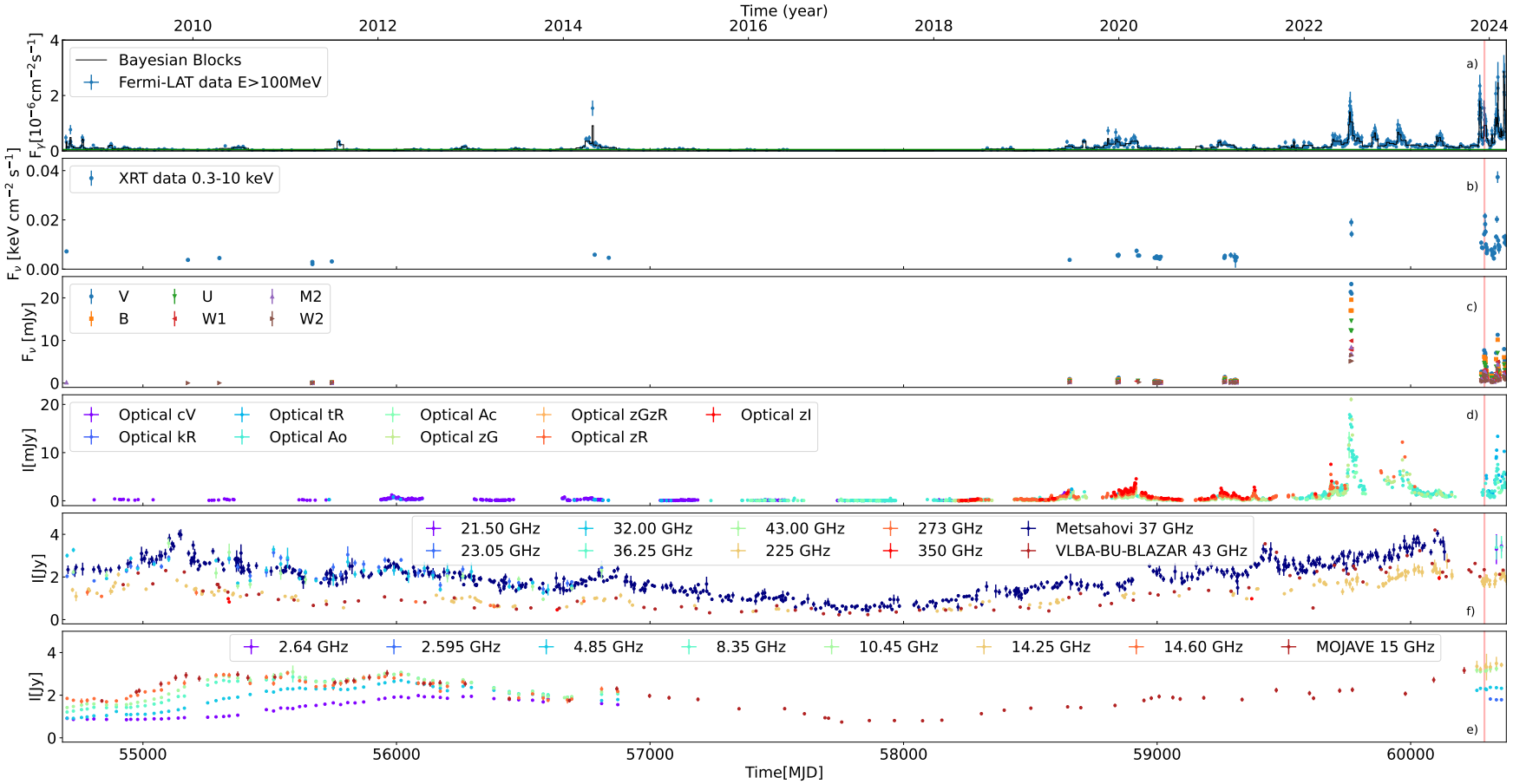

Figure 3.2: Multi-wavelength light curves of OP 313. The red vertical bands represent the period in which OP 313 was detected by LST-1 at La Palma. a: OP 313's LAT light curve from August 4th, 2008, to March 9, 2024. b: *Swift*-XRT X-ray light curve from 0.3 to 10 keV. c: *Swift*-UVOT light curve. u, v and b optical *Swift*-UVOT filters are included. d: Optical light curve from different datasets and filters. CRTS V-filter data are shown with the cV label, KAIT R-filter data are shown with the label kR, Tuorla R-filter data are shown with the label tR, ATLAS o and c-filters data are shown with the label Ao and Ac, and Palomar ZTF g, r, and i-filters data are shown with the label zG, zR, and zI. The label zGzR refers to observations in which both filters were used. e: Radio Single Dish F-GAMMA light curves above 15 GHz, SMA data at 225, 273 and 350 GHz, including SMAPOL data at 225 GHz light curves, Metsähovi at 37 GHz and VLBA-BU-BLAZAR at 43 GHz light curves. f: Radio Single Dish F-GAMMA light curves below 15 GHz and MOJAVE VLBA light curve.

3.3.2 Selection of the flaring periods of interest

From Figure 3.1, the source started to show consistently flaring activity at the end of 2021. In this period, the photon index of OP 313 is mostly harder than the average photon index value (2.14 ± 0.09) weighted in every bin from the 4th of August 2008 to the 9th of March 2024. Of particular interest is the flaring activity, from γ-ray to optical frequencies, which started in 2022 and continued until the last day of this study. Figure 3.3 shows the γ-ray and optical light curves from the 1st of January 2022 to the 9th of March 2024. There is a visible good correlation between the two datasets, even if there is a lack of optical data in the flaring period reported in [40].

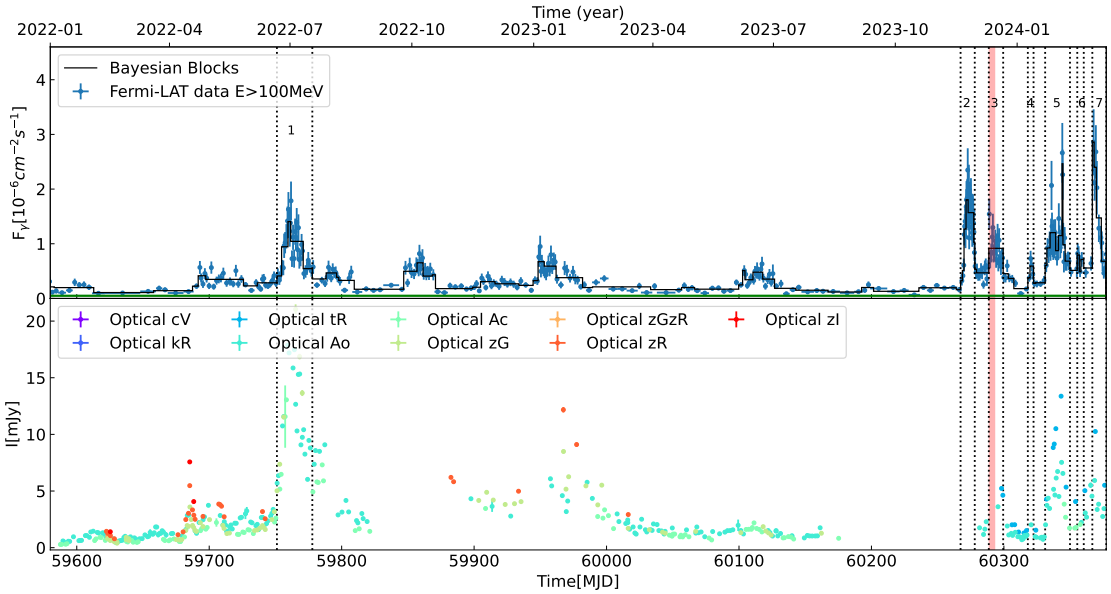

Figure 3.3: *Fermi*-LAT (top) and Optical (bottom) light curves from the 1st of January 2022 to 9th of March 2024. The dashed black lines indicate the brightest γ-ray flaring periods. The fourth and sixth flaring periods are not among the brightest but are located in time between the ATels [40] and [39] published by the LAT collaboration. For each γ-ray flare, there seems to be a corresponding optical flare. The red vertical bands represent the period in which OP 313 was detected by LST-1 at La Palma.

The highest γ-ray flaring periods in this time window were identified by looking at the Bayesian blocks that contained the highest average flux. Seven different flaring periods were identified, indicated with black dashed lines in Figure 3.3. The fourth and sixth flaring periods are not between the brightest but are located in time between the ATels [40] and [39] published by the LAT collaboration. Since the goal of this project is to study the mechanisms responsible for this intense flaring activity, my collaborators and I decided to include them. Table 3.2 shows: (1) ID of the flaring period, (2) flaring period in MJD, (3) flux peak and its error, (4) photon index corresponding to the flux peak, (5) fluence, defined as the time-integrated flux, in the flaring period. In Figure 3.3, the first flaring period is more intense in the optical wavelengths than in the γ-rays, while the others are more intense in the γ-ray energies.

Table 3.2: Flaring periods of OP 313 starting from January 2022. The photon index α_{peak} corresponds to the maximum flux F_{peak} in the flaring period in column 2.

ID	Period (MJD)	F_{peak} (ph/cm^2/s)	α_{peak}	Fluence (ph/cm^2)
1	59751 - 59778	$(1.79 \pm 0.35) \times 10^{-6}$	2.31 ± 0.19	1.87 ± 0.07
2	60267 - 60278	$(2.35 \pm 0.4) \times 10^{-6}$	1.68 ± 0.1	1.08 ± 0.03
3	60289 - 60299	$(1.54 \pm 0.28) \times 10^{-6}$	1.78 ± 0.11	0.79 ± 0.04
4	60318 - 60322	$(7.3 \pm 1.41) \times 10^{-7}$	1.95 ± 0.14	0.12 ± 0.01
5	60331 - 60350	$(2.65 \pm 0.55) \times 10^{-6}$	2.15 ± 0.17	1.52 ± 0.06
6	60355 - 60360	$(8.23 \pm 1.83) \times 10^{-7}$	2.1 ± 0.18	0.18 ± 0.02
7	60367 - 60377	$(2.86 \pm 0.6) \times 10^{-6}$	1.75 ± 0.12	1.22 ± 0.1

Search for hysteresis patterns

Looking at Figure 3.1, it is clear that the number of γ-ray photons seen by the LAT is large, which is not always the case in LAT data. Given this outstanding number of γ-ray photons, it was possible to look for hints of hysteresis patterns starting from the 2022 flaring activity. The hysteresis plots show how the spectral index of a source, on the y-axis, changes with the flux, on the x-axis. The hysteresis pattern [198] is a loop-like pattern that gives information about the acceleration and cooling processes of the particles in the blazar's jet. There are two different kinds of hysteresis patterns:

- the most common clockwise pattern, which arises from the interplay between the characteristic timescales of particle injection, acceleration, and radiative cooling. This pattern is expected when synchrotron cooling dominates the evolution of the electron population. Since the synchrotron cooling timescale decreases with increasing electron energy, high-energy electrons cool more rapidly than low-energy ones. During a flare, the flux initially increases together with a hardening of the spectrum due to the injection of energetic particles. After the flux peak, the rapid cooling of the highest-energy electrons leads to a progressive softening of the spectrum while the flux is still high, producing a clockwise loop in the flux–index plane [198, 298];
- the rare anti-clockwise pattern, which indicates a different physical regime. In this case, the particle acceleration timescale is comparable to or longer than the cooling timescale, and the flare development proceeds from lower to higher energies. As a result, the flux increases while the spectrum remains relatively soft, and spectral hardening occurs with a delay, leading to an anti-clockwise loop in the hysteresis plot. This behavior suggests a gradual energization of the particle population rather than an instantaneous injection of high-energy electrons.

Visual inspection of Figure 3.4(a) suggests for the 1st flare an anti-clockwise pattern arising on the 4th of July 2022. Instead, hints of clockwise hysteresis patterns were found for the second, as shown in Figure 3.4(c), and fifth flaring periods, as shown in Figure 3.4(b), in which it is possible to see two hints of hysteresis patterns in one plot. This means that these flaring periods are dominated by the cooling. There are no hints of hysteresis patterns for the rest of the flaring periods.

Evaluating the statistical significance of hysteresis patterns is non-trivial, but one

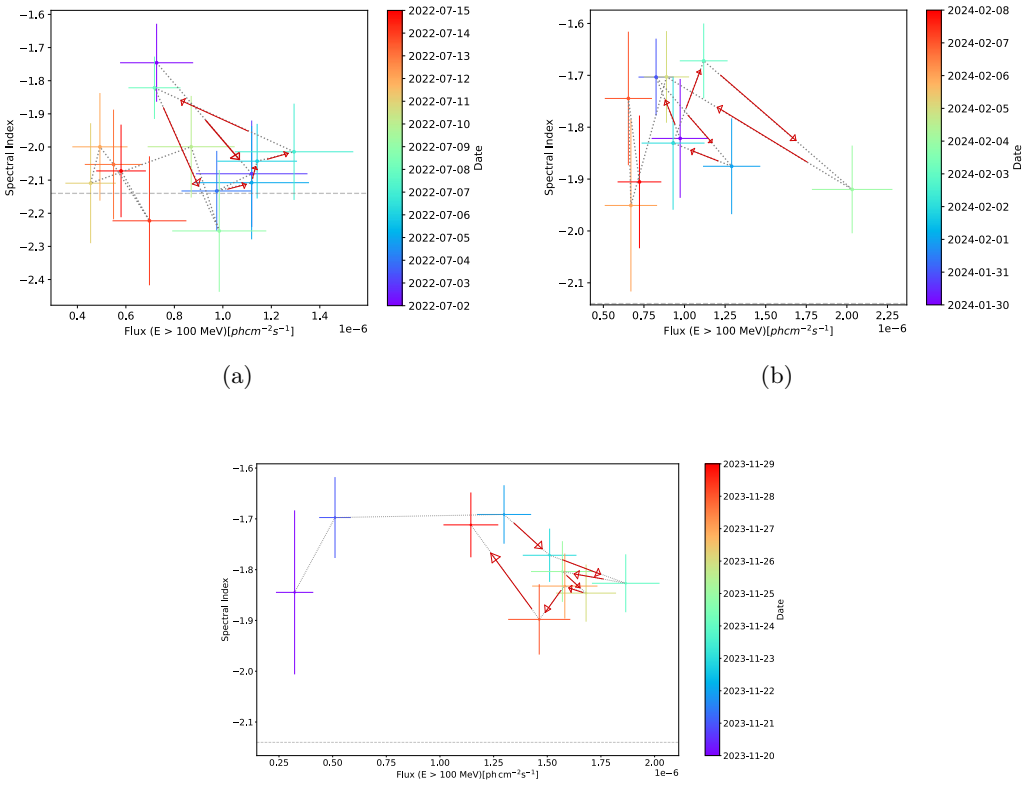

(a) (b)

(c)

Figure 3.4: a) First flaring period hysteresis pattern from the 2nd of July 2022 to the 15th of July 2022. The hint of the hysteresis pattern is anti-clockwise. The grey dashed line is drawn to help seek the correct order of the points. b) Fifth flaring period hysteresis pattern from the 30th of January 2024 to the 8th of February 2024. The hint of hysteresis pattern is clockwise. c) Second flare from the 20th of November 2023 to the 29th of November 2023. The hint of the hysteresis pattern is clockwise.

possible test is to bin the data differently. In Figure 3.5(a), 3.5(b) and 3.5(c), it is shown how the hysteresis patterns of the first, the second, and the fifth flaring periods are if it is considered the average photon index in 2-day-long time bins. In this case, there are fewer points with smaller error bars, and the hints of a hysteresis pattern are anti-clockwise for the first and fifth flaring periods and clockwise for the second flaring period. Therefore, we conclude that our search for hysteresis patterns was inconclusive even for these extremely bright flares.

X-ray telescopes, like *XMM*-Newton and *Chandra*, provide adequately constrained sub-hour flux and photon index values, which make them the best instruments to reconstruct the hysteresis pattern. Nevertheless, it is still outstanding the number of γ-ray photons detected by the LAT, which gave the possibility to try to perform a hysteresis study.

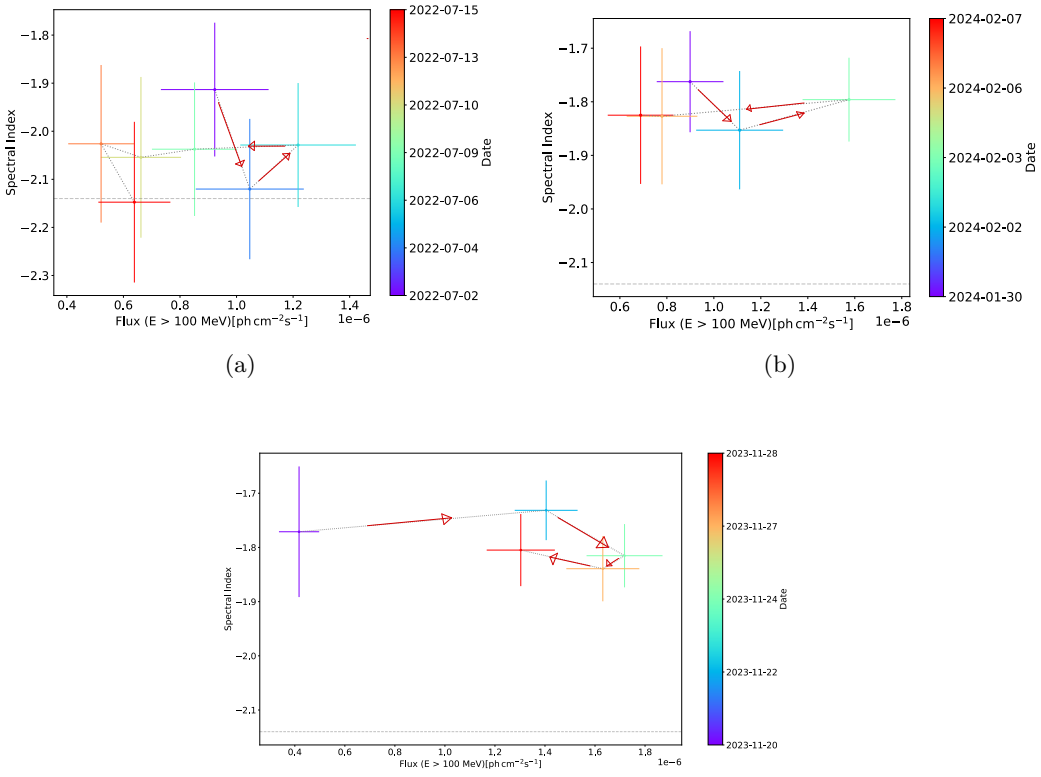

(a) (b)

(c)

Figure 3.5: a) First flaring period hysteresis pattern from the 2nd of July 2022 to the 15th of July 2022, considering 2-day-long time bins. The grey dashed line is drawn to help seek the correct order of the points. b) Fifth flaring period hysteresis pattern from the 30th of January 2024 to the 8th of February 2024, considering 2-day-long time bins. c) Second flaring period hysteresis pattern from the 20th of November 2023 to the 29th of November 2023, considering 2-day-long time bins.

Compton dominance

In Figure 3.3 the first optical flaring period is stronger than the γ-ray one, whereas the opposite trend is observed for the subsequent ones. This difference between flaring periods at different wavelengths suggests a change in the origin of the seed photons for Comptonization. In the case of FSRQs such as OP 313, the soft seed photons are expected to come from outside the jet (the so-called External Compton (EC)) [248], like from BLR [97], the accretion disks [289] or the hot dusty torus (DT) [52]. Hence, studying the relative difference between the two SEDs peaks of blazars can be used to constrain the source of this photon field. When the two peaks in the SED of a blazar have similar heights, a moderate level of jet magnetization is present, and Synchrotron Self-Compton (SSC) is the dominant radiative process responsible for the high-energy emission [117, 266]. In the SSC scenario, the same population of relativistic electrons that produces the synchrotron radiation also scatters these photons via inverse Compton (IC) scattering within the jet. If the high-energy peak is significantly higher than the synchrotron peak, the Compton dominance is high, and EC scattering becomes the dominant mechanism. A high synchrotron

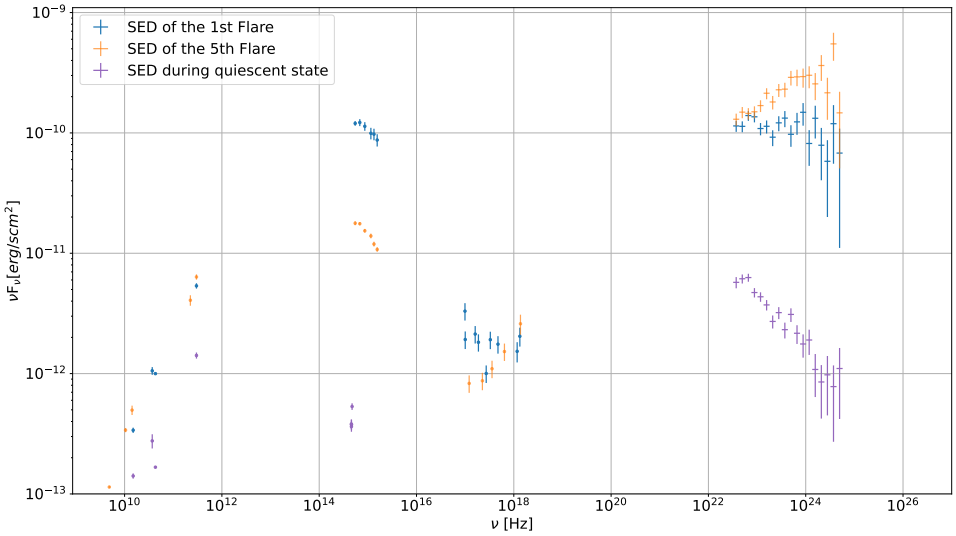

Figure 3.6: SED comparison between the 1st (2022), in orange, the 5th flaring periods (January 2024), in blue, and a quiescent period that goes from the 1st of March 2016 to the 1st of January 2018, in purple. The X-ray, UV, optical, and radio SED points are the mean of all points in the period at the respective frequency. No *Swift*-XRT and UVOT data were available during the quiescent period. The 1st one is less Compton-dominated than the 5th one. More details about their modeling are in Section 3.3.5.

luminosity ($L_{syn} > 10^{47}$erg/s, [185]) implies the emitting region in blazar jets is highly magnetized and the synchrotron cooling is efficient [185]. Figure 3.6 shows the SEDs of the first, fifth flaring periods, and a quiescent period that goes from the 1st of March 2016 to the 1st of January 2018. It is possible to notice that the first flaring period SED has the peaks located at the same height, while the fifth one has peaks at different heights. This means that the Compton dominance is low for the first flaring period, while the fifth flaring period is more Compton-dominated. All the flaring periods from November 2023 to February 2024 are more Compton-dominated. A lower Compton dominance suggests that the scattering may be dominated by SSC with a relatively weak external photon field, while a stronger dominance may be interpreted as a signature of dominating EC scattering, where seed photons come from outside the jet [289]. In Section 3.3.5, for coherence, it is discussed in detail the SED modeling study of these 2 flaring periods done to find where these different photon fields come from.

Multi-band correlation

To understand jet emission and its dynamics in blazars, researchers examine the changes in blazar physical properties that cause multifrequency light curve variations [240]. A cross-correlation approach effectively identifies plausible links across different blazar emission bands, distinguishes emission components in the jet, constrains the emission zone's location, and differentiates between SSC and EC models [215].

The z-transformed Discrete Correlation Function (zDCF, [29], [30]) was used to obtain the cross-correlation between γ-ray and optical data. The zDCF is used to evaluate the delay-dependent multi-band cross-correlations. This method is more sophisticated than the Discrete Correlation Function [DCF; 110] because it uses equal-population binning and Fisher's z-transform, and it is developed for sparse and unevenly sampled astronomical time series. To evaluate the zDCF, a Python implementation of the original Fortran zDCF algorithm called the pyZDCF package [186] was used. The significance of the zDCF of the observed light curves is obtained by simulating a light curves population with the same power spectral density (PSD) as the true ones. The DELCgen Python package [86] was used to generate the fake light curves population using [112] (EM). The EM method was used because it also takes into account the distribution of the observed light curves' fluxes, whereas the [303] (T&K) method simulates light curves assuming the observed fluxes follow a Gaussian distribution.

The cross-correlation between the optical and γ-ray datasets was investigated both in the long-term period (see Figure 3.2) and in the short-term period from 2022-2024 (see Figure 3.3). The zDCF evaluation was performed using bins of delay of 2, 3, and 4 days. For all the delay bin sizes, the zDCF showed a peak at a delay compatible with 0 days. For the long-term (short-term) period, the zDCF at zero delay was found to be equal to 0.8 (0.6, see Figure 3.7(a)). The PSDs of the observed light curves were fitted using a power-law function $PSD(\omega) = A\omega^{-\beta}$. The PSD slope was estimated through a maximum-likelihood fit. Its uncertainty was evaluated via bootstrap resampling of the periodogram, yielding for the γ-ray lightcurve $\beta_\gamma = 1.2\pm$ 0.4, in agreement with [297], whereas for the optical R-band light curve was found $\beta_{OPT} = 1.2 \pm 0.4$, which is comparable with the typical ranges reported in [254] for blazars. To assess the impact of the uncertainty on the PSD slope, additional Monte Carlo simulations were performed by varying the PSD index within its 1σ confidence interval. The resulting zDCF confidence bands were consistent with those obtained using the best-fit value, and no significant variation in the correlation significance at zero lag was observed. This demonstrates that the result is robust against reasonable variations of the PSD slope.

The estimation of the significance of the correlation was performed by simulating 10^4 pairs of uncorrelated optical and γ-ray light curves. These light curves were generated using the corresponding best-fit PSD models and flux distributions of the observed light curves. These pairs of simulated light curves were employed to build the confidence bands of the zDCF under the hypothesis of non-correlation. The 1σ and 3σ bands for the 2022-2024 period are shown in Figure 3.7(a). In the bin of zero delay, the positive correlation with zero delay between the optical and γ-ray light curves was found to be significant above the 95% confidence level, corresponding to a confidence level of roughly 2σ (see Figure 3.7(b)).

This correlation suggests a common origin for the flaring emission in the two bands, indicating that leptonic processes primarily dominate the γ-ray emission, though a subdominant hadronic contribution cannot be ruled out [14].

3.3.3 VLBA jet kinematics results

The VLBA analysis consisted of the analysis of the publicly available visibilities from the MOJAVE and VLBA-BU-BLAZAR programs. New components, called knots,

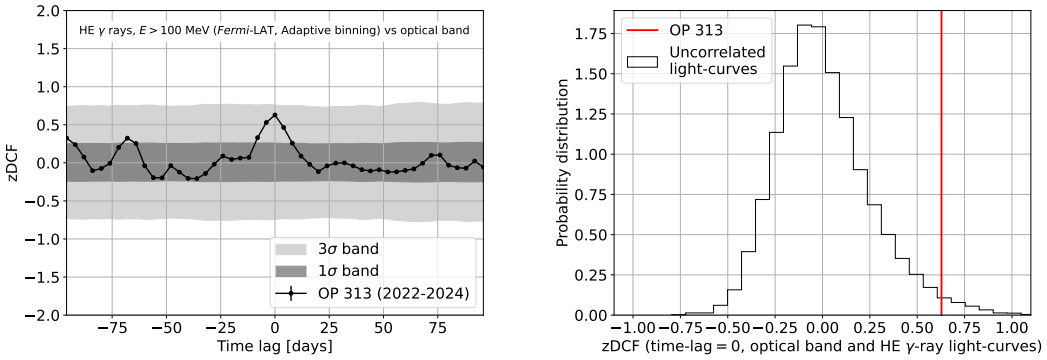

(a) (b)

Figure 3.7: (a) zDCF analysis on the short-term period of OP 313 optical and γ-rays light curves; (b) distribution of the reconstructed zDCF at zero time-lag for 10^4 simulated uncorrelated γ-ray and optical light curves. The red line marks the reconstructed zDCF value with the observed OP 313 light curves in Figure 3.3.

in the parsec-scale jet were found that can be responsible for the flaring activity of OP 313. To explain these multi-wavelength flaring events in the jet of this source, a kinematic study of the new components was performed.

MOJAVE VLBA analysis results

The OP 313 jet components and kinematic results from 1995 to August 2019 are published in [219] and [217]. Since this long-term multi-wavelength study extends to March 2024, the public visibilities were analyzed until the 4th of April 2024, which is the closest observation to the 9th of March, using the method reported in Section 3.2.6. The main results of the analysis are:

- The results of the fitting process of the visibilities from 2008 to August 2019 are mainly in agreement with those of [219] and [217]. For this reason, in Figure 3.8 the components and their distance from the core in this period are the same as reported in the literature;
- Starting from the 13th of April 2021, a new robust component appeared.

The same approach as [217] was used to determine if this new component is a robust cross-identification. Hence, it was checked that the feature was present across at least 5 epochs and considered the consistency of the sky position and flux density of the features over time. The new component was named "Component 24" and is colored in red in Figure 3.8.

The kinematics of all individual robust jet features, from August 2008 to April 2024, were analyzed using the method reported in [217]. The sky positions of these features were fitted at a reference middle epoch t_{mid}, as follows:

$$x(t) = x_{mid} + \mu_x(t - t_{mid}) + \frac{\dot{\mu}_x}{2}(t - t_{mid})^2 \tag{3.4}$$

$$y(t) = y_{mid} + \mu_y(t - t_{mid}) + \frac{\dot{\mu}_y}{2}(t - t_{mid})^2 \tag{3.5}$$

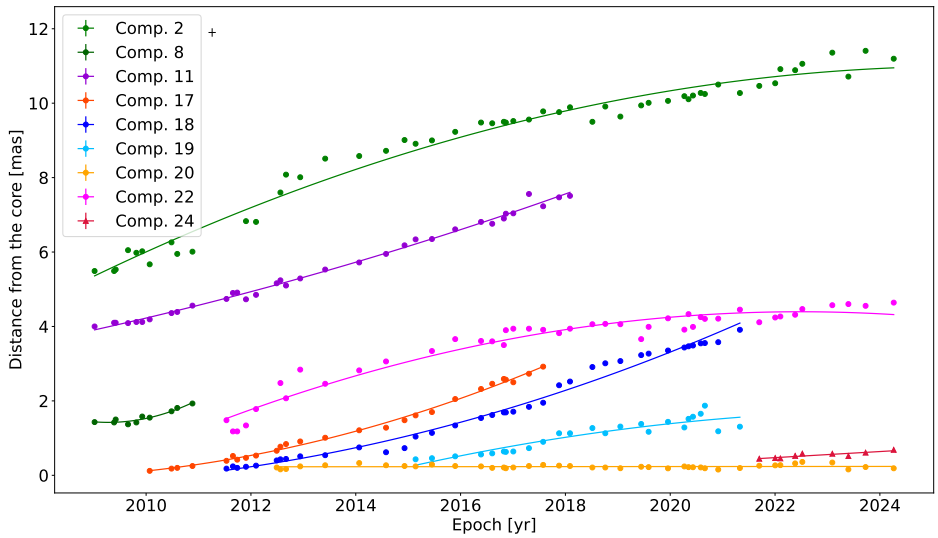

Figure 3.8: Plot of angular separation from the core versus time for Gaussian jet features of the MOJAVE data. Colored symbols indicate robust features for which kinematic fits were obtained. The 1σ positional errors on the individual points typically range from 10% of the FWHM restoring beam dimension for isolated compact features to 20%, represented as a black cross in the plot, of the FWHM for weak features [see e.g. 217–219].

where t_{mid} is the mean of the first and last observation epoch dates of the feature, μ_x and μ_y are the fitted angular speeds in each sky direction, and and $\dot{\mu_x}$ and $\dot{\mu_y}$ are the fitted accelerations. The 1σ uncertainty on the position of the knots ranges from 10% of the full-width half maximum (FWHM) restoring beam dimension (a median reference value is 0.096 along the major axis of the restoring beam and 0.056 along its minor axis) for isolated compact features to 20% of the FWHM for weak features (around 0.19 along the major axis and 0.11 along the minor axis) [see e.g. 217–219]. For the new "Component 24", it was not possible to calculate the acceleration, since the condition of several epochs in which the component is present ≥ 10 is not satisfied. Instead, "Component 20" is a static shock. To calculate the proper motion vector modulus and apparent velocity in units of speed of light, it was used the following equations:

$$\mu = \sqrt{\mu_x^2 + \mu_y^2} \tag{3.6}$$

$$\beta_{app} = \mu D_A (1 + z) \tag{3.7}$$

where D_A is the angular distance and z is the redshift of the source.

Table 3.3 describes the fits' results as follows: 1- ID of the component; 2— mean flux density and error in mJy; 3- mean projected distance from the core feature in mas; 4- mean position angle of feature with respect to the core component; 5- angular proper motion in milliarcseconds per year; 6- proper motion in units of the speed of light; 7- acceleration in milliarcsecond per square year; 8- date of reference (middle) epoch used for fit.

Table 3.3: Jet structure and kinematic parameters of the MOJAVE dataset.

ID	$< S >$ (mJy)	$< R >$ (mas)	P.A. (deg)	MOJAVE μ (mas/yr)	β_{app}	$\dot{\mu}$ (mas/yr^2)	Middle epoch
2	0.020 ± 0.007	8.94 ± 0.19	284.6 ± 15	0.345 ± 0.039	18.06 ± 2.06	0.018 ± 0.008	2016.69
8	0.028 ± 0.001	1.57 ± 0.19	300.3 ± 21.4	0.272 ± 0.048	14.24 ± 2.52	0.210 ± 0.09	2009.93
11	0.026 ± 0.01	5.54 ± 0.18	302.1 ± 5.5	0.436 ± 0.007	22.84 ± 0.36	0.01 ± 0.003	2013.34
17	0.261 ± 0.013	1.28 ± 0.16	309.1 ± 39	0.375 ± 0.005	19.64 ± 0.27	0.029 ± 0.003	2013.84
18	0.214 ± 0.011	1.84 ± 0.17	303.8 ± 47.6	0.382 ± 0.019	20.01 ± 1.46	0.018 ± 0.007	2016.51
19	0.057 ± 0.003	1.06 ± 0.19	284.6 ± 16.2	0.193 ± 0.028	10.11 ± 1.46	0.015 ± 0.014	2018.44
20	0.516 ± 0.026	0.24 ± 0.18	295.2 ± 6.7	0.007 ± 0.002	0.16 ± 0.03	0.002 ± 0.001	2018.42
22	0.013 ± 0.001	3.57 ± 0.17	294.2 ± 37	0.157 ± 0.032	8.23 ± 1.71	0.026 ± 0.01	2017.96
24	0.223 ± 0.011	0.54 ± 0.16	316.1 ± 33.7	0.085 ± 0.011	4.42 ± 0.59		2022.80

VLBA-BU-BLAZAR analysis results

The VLBA-BU-BLAZAR OP 313 jet components and kinematic results from 2009 to 2018 are published in [192] and [320]. The public visibilities were analyzed until the 7th of April 2024, using the method reported in Section 3.2.6. The main results of the analysis are:

- The results of the fitting process of the visibilities from 2008 to 2018 are mainly in agreement with those of [192] and [320]. For this reason, in Figure 3.9, the components from "B1" to "B8", "A1" and "A2" as well, and their distances from the core are the same as reported in the literature;
- As shown in Figure 3.9, starting from 2019, a new set of components appeared.

Regarding the model parameters, the uncertainties of the flux and of the coordinates of the different components, presented in Table 3.4, were calculated using the formalism described in [192]. This formalism is based on an empirical relation between the uncertainties and the brightness temperatures of knots: $T_{b,obs} = 7.5 \times 10^8 S/a^2$ K, where $T_{b,obs}$ is the brightness temperature of the knot in Kelvin, S is the flux density in Jy and a is the angular size in mas of the knot [e.g. 69, 190, 320]. The errors are calculated as follows: the 1σ uncertainty on the x-axis is $\sigma_x \approx 1.3 \times 10^4 T_{b,obs}^{-0.6}$, the uncertainty on the y-axis is $\sigma_y \approx 2\sigma_x$, the flux uncertainty is $\sigma_S \approx 0.09 T_{b,obs}^{-0.1}$ and the angular size uncertainty is $\sigma_a = 6.5 \times T_{b,obs}^{-0.25}$. To σ_x and σ_y, a minimum positional error of 0.005 mas (related to the resolution of the observations) was added and a typical amplitude calibration error of 5% [192, 320].

Then, the kinematic properties of the jet components were calculated following the same approach shown in [320]. It was assumed that knots detected more than 4 epochs, and with consistent sky position and flux density of the features over time, as in Section 3.3.3, have their positions in the sky fitted by a trend given by Equation 3.4 and Equation 3.5. The `statsmodels` package [14] [284] weighted least-squares program was used to calculate the best-fit parameters. From the comparison between the χ^2 obtained in the fitting process and χ^2_{crit} at a significance level of $\zeta = 0.05$ values, it was found which knots are accelerating ($\chi^2 > \chi^2_{crit}$) and needed to be fitted by different segments that represent the different speeds characterizing their motion. For this reason, in Table 3.4 some components have two angular proper motion and apparent speed entries, calculated using the equations 3.6 and 3.7. In Figure 3.9, the same ones have two segments fitting them. Using this method, the jet structure and kinematics parameters are comparable with those reported in [192] and [320]. The parallel and perpendicular accelerations are given by: $\dot{\mu}_{\parallel} = \dot{\mu}_x \sin\langle\Theta_{jet}\rangle + \dot{\mu}_y \cos\langle\Theta_{jet}\rangle$ and $\dot{\mu}_{\perp} = \dot{\mu}_x \cos\langle\Theta_{jet}\rangle - \dot{\mu}_y \sin\langle\Theta_{jet}\rangle$, where $\langle\Theta_{jet}\rangle = -64.9 \pm 4.7$ is the average jet position angle for OP 313 [320]. The average jet position angle describes the orientation of the jet on the sky plane, measured from north to east [218]. In Table 3.4 are reported the kinematic properties of the new components rising after 2018. Table 3.3 describes the fits as follows: 1- ID of the component; 2— mean flux density and error in mJy; 3- mean projected distance from the core feature in mas; 4- mean position angle of feature with respect to the core component; 5- angular proper motion in milliarcseconds per year; 6- proper motion in units of the speed of light; 7- acceleration in milliarcsecond per square year; 8- date of reference (middle) epoch used for fit. From the results, there may be an agreement between "Component

[14] `https://www.statsmodels.org/stable/index.html`

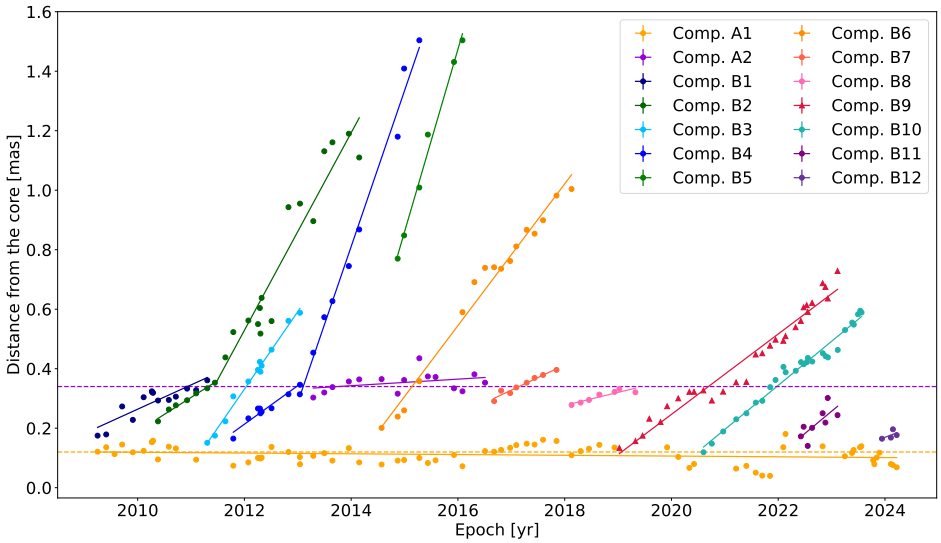

Figure 3.9: Plot of angular separation from the core versus time for Gaussian jet features of the VLBA-BU-BLAZAR (VLBA-BU-BLAZAR) data. Colored symbols indicate robust features for which kinematic fits were obtained. The 2 dashed lines in yellow and purple represent the static shocks' mean distance from the core.

24" and the component "B9", both in red in Figures 3.8 and 3.9. Both components are at equal distances from the core and have a comparable proper motion vector modulus and apparent speed, as shown in Table 3.3. Hence, "Component 24" and "B9" could be the same component. Similarly, further observational data would be required to robustly confirm the identification of some of the later components, such as "B12", which is present for just 4 epochs in our analysis, and some others which started to appear when the analysis was stopped. For more comprehensive details and information about later components, we suggest the reader look at Jorstad et al.'s forthcoming publication.

Lorentz Factor and Viewing Angle of Jet Components

Blazar jets are known for their extraordinarily fast variability, boosted emission, and apparent superluminal motion of jet components. These are due to relativistic processes that dominate the jet's emission. The relativistic effects result from the favored direction of the jet near $< 20^{\circ}$ to our line of sight [48, 268, 269]. Far away from the supermassive black hole, the jets remain highly relativistic. Quantifying the jets' beaming properties is required to understand their energetics on large scales [214]. These relativistic effects are quantified by Lorentz factor (Γ), the Doppler factor (δ), and viewing angle (Θ_0), which is the angle between the jet axis and the line of sight to the observer [176]. Using the obtained apparent velocities, we calculated them for the new components using the formalism presented in [192] and [320]. Using this approach the Lorentz factor (Γ) and viewing angle (Θ_0) are given by:

$$\Gamma = \frac{\beta_{app}^2 + \delta_{var}^2 + 1}{2\delta_{var}} \tag{3.8}$$

Table 3.4: Jet structure and kinematic parameters of the VLBA-BU-BLAZAR dataset.

VLBA-BU-BLAZAR Boston							
ID	¡S¿ (Jy)	¡R¿ (mas)	P.A. (deg)	μ (mas/yr)	β_{app}	$\dot{\mu}_{\parallel}$ (mas/yr^2)	$\dot{\mu}_{\perp}$ (mas/yr^2)
B1	0.09 ± 0.01	0.29 ± 0.01	-0.1 ± 3.1	0.100 ± 0.007	5.25 ± 0.35		
B2(1^{st})	0.24 ± 0.02	0.63 ± 0.1	-50.1 ± 2	0.118 ± 0.003	6.16 ± 0.16	0.086 ± 0.015	-0.018 ± 0.018
B2(2^{nd})				0.294 ± 0.029	15.39 ± 1.53		
B3	0.4 ± 0.02	0.37 ± 0.02	-67.4 ± 1.5	0.275 ± 0.007	14.38 ± 0.36		
B4(1^{st})	0.27 ± 0.02	0.57 ± 0.08	-64.5 ± 3.3	0.128 ± 0.004	6.73 ± 0.21	0.220 ± 0.006	-0.021 ± 0.007
B4(2^{nd})				0.502 ± 0.008	26.29 ± 0.40		
B5	0.03 ± 0.01	1.12 ± 0.22	-56.1 ± 6.7	0.611 ± 0.014	32.00 ± 0.74		
B6	0.07 ± 0.01	0.67 ± 0.11	-83.9 ± 7.4	0.271 ± 0.017	14.16 ± 0.87		
B7	0.05 ± 0.01	0.35 ± 0.03	-77.6 ± 3.9	0.085 ± 0.002	4.46 ± 0.11		
B8	0.05 ± 0.01	0.31 ± 0.05	-72.4 ± 8.2	0.013 ± 0.003	0.68 ± 0.17		
B9	0.26 ± 0.01	0.43 ± 0.02	-45.1 ± 9	0.085 ± 0.009	4.46 ± 0.46		
B10	0.24 ± 0.01	0.51 ± 0.03	-53.8 ± 12.7	0.123 ± 0.007	6.44 ± 0.34		
B11	0.21 ± 0.01	0.4 ± 0.03	-49.7 ± 18	0.175 ± 0.007	9.18 ± 0.35		
B12	0.58 ± 0.01	0.18 ± 0.01	-66.8 ± 11.4	0.033 ± 0.003	1.73 ± 0.16		

Table 3.5: Doppler factor (δ_{var}), Lorentz factor (Γ), and viewing angle (Θ_0) of the new components arisen from 2019 in the visibilities of the VLBA-BU-BLAZAR project. The values reported here are obtained using the technique reported in [320].

ID	B9	B10	B11	B12
δ_{var}	12.94 ± 2.77	14.95 ± 0.68	7.8 ± 0.99	24.86 ± 1.55
Γ	8.12 ± 0.37	8.05 ± 0.54	6.83 ± 0.36	12.51 ± 0.50
Θ_0 (deg)	3.55 ± 1.22	1.93 ± 0.39	7.29 ± 1.07	0.32 ± 0.05

Table 3.6: Lorentz factor (Γ_{var}) and viewing angle (Θ_0) of the new components arisen from 2019 in the visibilities of the VLBA-BU-BLAZAR project. The values reported here are obtained using the Doppler factor reported in [212] $\delta_{var} = 13.87^{+7.87}_{-3.72}$.

ID	B9	B10	B11	B12
Γ_{var}	$8.47^{+0.17}_{-0.72}$	$7.55^{+0.41}_{-0.63}$	$8.58^{+0.1}_{-0.73}$	$7.08^{+0.46}_{-0.52}$
Θ_0 (deg)	$3.17^{+2.96}_{-1.4}$	$2.22^{+2.37}_{-1.17}$	$3.24^{+2.85}_{-1.35}$	$1.02^{+1.15}_{-0.55}$

$$\tan \Theta_0 = \frac{2\beta_{app}}{\beta_{app}^2 + \delta_{var}^2 - 1} \tag{3.9}$$

where δ_{var} is the variability Doppler factor and is given by:

$$\delta_{var} \approx \frac{16 s D_{\rm Gpc}}{\tau_{var}(1+z)} \tag{3.10}$$

where $D_{\rm Gpc}$ is the luminosity distance of OP 313 in Gpc, s is the diameter of a face-on disk given by $s = 1.6a$ where a is the angular size of the knot in mas obtained in the model fits, which is the FWHM of a presumed Gaussian brightness distribution, and τ_{var} is the timescale of variability given by $\tau_{var} = |1/k|$. The parameter k is obtained by approximating the flux density decay of the knots in the exponential form: $\ln(S(t)/S_0) = k(t - t_{max})$, where S is the flux density, S_0 is the flux density of a least-squares fit to the light curve decay at time t_{max}, and k is the slope of the fit [320]. The results of the calculation of the Doppler, Lorentz factors, and viewing angle for the components from "B9" to "B12" are listed in Table 3.5. For the other components, these parameters are available in [320]. The Doppler factor values for the knots from "B9" to "B12" are between 8 and 15, while the Lorentz factor values for these components are between 7 and 13. These values are in agreement with the general trend for FSRQs reported in [177] and [214]. The viewing angles were obtained using the equation 3.9 and their values are between 2 and 7 deg. Since the component "B12" was detected for a few epochs, the accuracy of its results in Table 3.5 could be low. Future analysis of other VLBA-BU-BLAZAR visibilities and the upcoming paper from Jorstad et al. could lead to better results.

Moreover, using equations 3.8 and 3.9, and the Doppler factor at 37 GHz $\delta_{var} = 13.9^{+7.9}_{-3.7}$, reported in [212], the viewing angle and Lorentz factor were calculated again to be compared with the values obtained in the Table 3.5. The results are reported in Table 3.6 and are mainly in agreement with those of Table 3.5, except for B12, which has few available data.

The values reported in Table 3.5 and in Table3.6 are in agreement with the general trend in which $\delta_{var} < 40$ and $\Gamma_{var} \sim 10$ for FSRQ [177, 214].

Table 3.7: Epoch of ejection T_0 and epoch in which the knot encounters the static shock T_1 for the new knots found in the VLBA-BU-BLAZAR data.

	B9	B10	B11
T_0 (MJD)	58378 ± 51	58813 ± 26	59535 ± 115
T_1 (MJD)	58540 ± 10	59043 ± 82	59817 ± 153

3.3.4 Search for the origin of the γ-ray flaring periods

The radio behavior, shown in Figure 3.2, shows that the radio flux was increasing until 2010 and then started to increase again around 2019. Visually, there appears to be a long-term pattern in the light curve. However, the studies of the radio behavior of OP 313, using Metsähovi data from 1985 to 2023, find that for this object, there is not a constrained timescale [194]. This is an indication that it is not possible to attribute the flaring activity beginning in 2022 to a defined periodicity.

Other interesting results are presented in Figure 3.10. In this figure, a comparison between the LAT and MOJAVE total flux density light curves from 2018 to March 2024 is presented. Looking at them, it seems that there is a time delay between the two emissions. In [204], this time lag between γ-ray and radio emission was investigated for OP 313, and it is equal to 96^{+16}_{-11} days. A positive time lag means that the γ-ray emission is leading the radio one, and the region in which the γ-ray flaring periods are produced is closer to the central engine than the radio emission region. This value is smaller than the value obtained by analyzing the delay between γ-ray and radio emissions between 2020 and 2021, shown in Figure 3.10: 201 ± 16 days. This value was obtained by calculating the difference between the dates on which the radio emission and γ-ray emission had a peak. From the time delay [204] found, they obtained the distance between the region of the γ-ray emission production and the central engine, taking the radio core opacity as the main source of the time lag. For OP 313, they found that the γ-ray emission region is $4.96^{+12.53}_{-12.96}$pc [204] from the central engine, so beyond the BLR of external radius $\simeq 0.1\,$pc (see Section 3.3.5 to see how the BLR radius was calculated). This led us to look for a photon field responsible for the EC in the dusty torus, outside the BLR.

Furthermore, Figure 3.10 shows with dashed colored lines the period in which the new knots from "B9 to "B11" passed the core, in blue, and passed the static shock "A1", in yellow. The green dashed line shows the period in which the component "B12" began to be visible in the jet. To calculate the epoch of ejection, T_0, and the date at which the knots encounter the static shock, T_1, the same approach reported in [320] was used. Hence, for T_0 and T_1, the first ten observations of a knot were considered or the points in the first segment in case of acceleration, and the linear fits to X and Y back to (0, 0) and to "A1" were extrapolated. This extrapolation provides the time of ejection along each coordinate, T_{x_0} and T_{y_0}, and T_{x_1} and T_{y_1}, and then the true time of ejection and its 1σ uncertainty are given by:

$$T_0 = \frac{T_{x_0}/\sigma^2_{T_{x_0}} + T_{y_0}/\sigma^2_{T_{y_0}}}{1/\sigma^2_{T_{x_0}} + 1/\sigma^2_{T_{y_0}}} \tag{3.11}$$

$$\sigma_{T_0} = \sqrt{\frac{(T_0 - T_{x_0})^2/\sigma^2_{T_{x_0}} + (T_0 - T_{y_0})^2/\sigma^2_{T_{y_0}}}{1/\sigma^2_{T_{x_0}} + 1/\sigma^2_{T_{y_0}}}} \tag{3.12}$$

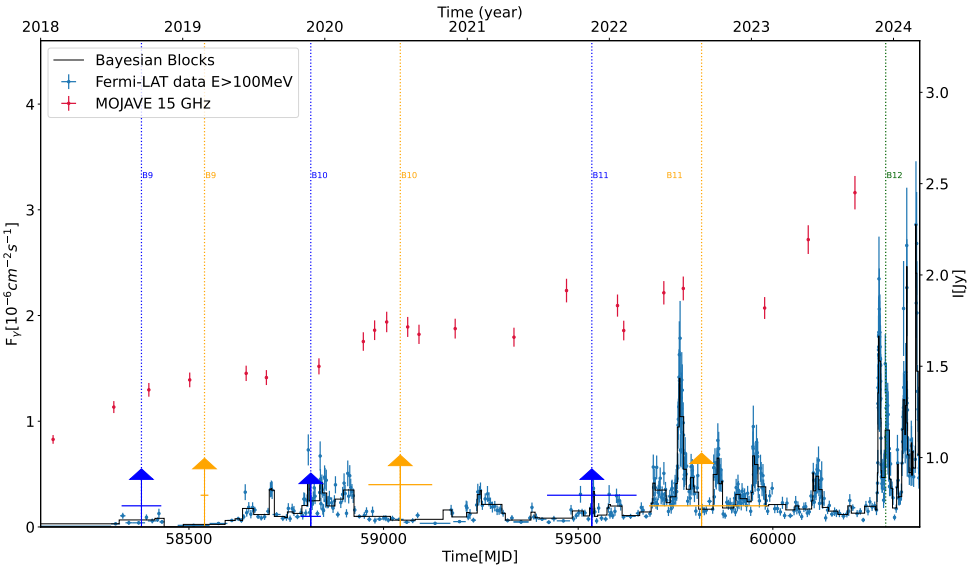

Figure 3.10: Comparison between the *Fermi*-LAT data (in blue) with their Bayesian blocks (in black) and the total flux density of MOJAVE at 15 GHz data (in red). The dashed blue lines represent the time of ejections for different knots, found in the VLBA-BU-BLAZAR visibilities, and the blue horizontal lines are the corresponding errors, while the orange dashed lines represent the epochs when the knots encounter the standing shock "A1" with the corresponding errors. In green, the epoch in which "B12" was found.

where $\sigma^2_{T_{x_0}}$ and $\sigma^2_{T_{y0}}$ are the 1σ propagated uncertainties on T_{x_0} and T_{y_0}. The same equations were used to calculate T_1 and σ_{T_1} substituting T_{x_0}, $\sigma_{T_{x_0}}$, T_{y_0} and $\sigma_{T_{y_0}}$ with T_{x_1}, $\sigma_{T_{x_1}}$, T_{y_1} and $\sigma_{T_{y_1}}$.

Component "B12" is present for too few epochs to allow us to calculate the epoch of ejection and the time at which this component met the static shock. Looking at Figure 3.10, we argue that the ejection and the encounter of "B9" and "B10" with the static shock could be responsible for the flaring activity that occurred from 2019 to the beginning of 2020. Since the knot "B9" could be consistent with Component 24 of the MOJAVE data, it was calculated T_0 and T_1 using equations 3.11 and 3.12 also for Component 24. In this case, component 20 was considered as the first static shock encountered by the knot since its distance from the core and its trend are consistent with "A1". Table 3.8 shows the result of this calculation. Instead, the ejection and the encounter of "B11" with the static shock could be responsible for the flaring activity that is seen from the end of 2021 to the end of 2022. Hence, component "B12" and other possible components could be responsible for all the flaring emissions seen from the end of 2023 and the beginning of 2024. In summary, the results suggest that Flare 1 could result from the interaction of "B11" with the standing shock, while Flare 2 to 7 could be linked to "B12", for which more VLBA observations are needed in order to confidently derive its parameters or zero separation epoch accurately. However, the timing hints that the flaring started when the knot was still within the core or even before it reached the core. This and the appearance of further new VLBA components will be analyzed in Jorstad et al. *in prep.*

Table 3.8: Epoch of ejection T_0 and epoch in which the knot encounters the static shock T_1 for the new component 24 found in the MOJAVE data.

ID	T_0 (MJD)	T_1 (MJD)
24	57586 ± 233	58673 ± 450

3.3.5 SED modeling

The analysis in 3.3.4 suggests a slightly different site for the flaring region within the jet for Flare 1 with respect to flares from 2 to 7. Of the flares 2 to 7, the best sampled SED is Flare 5's one, which is why it was selected for our Compton Dominance analysis 3.3.2 that showed Flare 1 and Flare 5 to be clearly different. In this section, the focus is on investigating whether it is possible to model the spectral energy distributions of these two states self-consistently.

For the modeling and fitting of the two radiative states of OP 313, the JetSeT framework [304, 305, 307] was used. This is an open-source framework written in C/Python designed to simulate the radiative, accelerative processes, and adiabatic expansion occurring in relativistic jets and galactic objects, both beamed and unbeamed. This enables the fitting of numerical models to observational data, supporting the definition of complex numerical radiative scenarios, including synchrotron, SSC, and EC processes. The broadband emission has been interpreted in the context of a one-zone (blob) leptonic scenario, where the low-energy emission arises from synchrotron radiation, and the high-energy emission is interpreted as SSC/EC emission. The jet has conical geometry, with a semi-opening angle, $\theta_{\rm open}$. The emitting region has a spherical geometry with a radius R, a tangled magnetic field B, and it is moving with a bulk Lorentz factor Γ along the jet axis, with a viewing angle θ. The radius of the blob is implemented as a functionally dependent parameter in JetSeT, depending on its distance from the black hole (BH), R_H, and the jet opening angle according to: $R = R_H \tan\ \theta_{\rm open}$.

The electron population is characterized by a broken power-law distribution depending on the Lorentz factor, according to:

$$n(\gamma) = \begin{cases} NK\gamma^{-p_1}, & \gamma_{\rm min} \leq \gamma < \gamma_{\rm break}, \\ NK\gamma_{\rm break}^{p_1-p_2}\gamma^{-p_2}, & \gamma_{\rm break} \leq \gamma \leq \gamma_{\rm max}. \end{cases} \tag{3.13}$$

where $\gamma_{\rm min}$, $\gamma_{\rm break}$, and $\gamma_{\rm max}$ are, respectively, the minimum, break, and maximum Lorentz factors, p_1 and p_2 are the spectral indices below and above the break, respectively, and N is the number density of the emitters. The normalization factor K is such that:

$$N = \int_{\gamma_{\rm min}}^{\gamma_{\rm max}} n(\gamma)\, d\gamma \tag{3.14}$$

In addition to the SSC emission, it was also taken into account the presence of external radiative fields emitted by the DT, and the BLR, the accretion disk, contributing to the EC emission. Furthermore, the EBL model from [121] was taken into account due to the high redshift of the source.

The disk is modeled as a single-temperature blackbody, with the disk luminosity $L_{\rm Disk}$ and temperature $T_{\rm Disk}$. The value of temperature is set to $T_{disk} = 5 \times 10^4$ K.

The luminosity is set at $L_{\rm Disk} = 5 \times 10^{45}\,{\rm erg/s}$ and frozen during the fit. This value has been chosen based on [151].

The radii of the BLR and DT are determined based on the disk luminosity according to [81, 195], and are implemented as functionally-dependent parameters in JetSeT:

$$R_{BLR,in} = 10^{17} \left(\frac{L_{\rm disc}}{10^{45}} \right)^{0.5} {\rm cm} \tag{3.15}$$

$$R_{\rm BLR,out} = 1.1 \times R_{\rm BLR,in} \tag{3.16}$$

$$R_{\rm DT} = 2.5 \times 10^{18} \left(\frac{L_{\rm disc}}{10^{45}} \right)^{0.5} {\rm cm} \tag{3.17}$$

The SSC model depends only on the Doppler factor δ defined as:

$$\delta = \frac{1}{\Gamma(1 - \beta \cos\theta)} \tag{3.18}$$

which combines the effects of the bulk Lorentz factor Γ and the viewing angle θ. However, in the current implementation of JetSeT, the fitting and MCMC procedures are defined in terms of the bulk Lorentz factor Γ, while a direct sampling of the Doppler factor δ is not straightforward to implement. For this reason, Γ was used as a free parameter in the fitting procedure, while the viewing angle θ was fixed. This choice does not affect the physical interpretation of the results.

A model fitting using the `JeTSet ModelMinimizer` module with an `iminuit minimisation` [96] was performed. The fit is performed considering the data in Figure 3.6 for both flaring periods, adding a systematic error of 10% to all frequency ranges. The two resulting models are shown in Fig. 3.11(a) and Fig.3.11(b). Furthermore, starting from the best-fit models found applying the `ModelMinimizer` module, the `JetSet McmcSampler` interface was used with the `emcee`[119] Python library to perform a Monte-Carlo-Markov chain (MCMC). Our goal was to obtain the posteriors of Flare 1 and Flare 5. The two resulting models with their confidence levels are shown in Figure 3.12(a) and 3.12(b), while the contour plots are in Figure 3.13 and 3.14. The parameters describing each model are reported in Table 3.9.

The magnetic energy density over the electron energy density (u_B/u_e) ratio was computed for the two flaring periods to assess the magnetization of the emitting region. Using the values reported in Table 3.9, u_B/u_e values equal to 0.031 and 0.013 for Flare 1 and Flare 5, respectively, with

$$u_B = B^2/8\pi \tag{3.19}$$

$$u_e = m_e c^2 \int_{\gamma_{\rm min}}^{\gamma_{\rm max}} \gamma\, n(\gamma)\, d\gamma \tag{3.20}$$

where $m_e c^2$ is the rest energy of the electron and $n(\gamma)$ is the electron population described in Equation 3.13. These values indicate that the emission region is particle-dominated, with a relatively low magnetic energy density compared to the energy carried by relativistic electrons. Similar values have been reported in [71] and [299].

The SEDs observed during the two flaring periods exhibits the typical two-bump structure commonly associated with blazar sources, where the low-energy peak is attributed to synchrotron radiation and the high-energy peak arises from inverse Compton scattering. However, the relative contributions of different components vary between the two flaring periods, reflecting distinct physical conditions in the jet and its surroundings. The observed fluxes for both flaring periods at high energy are well explained by the model with SSC and EC emission mechanisms, as seen in Figure 3.11(a) and 3.11(b). In both cases, the EC dominates over the SSC emission, with a lower Compton Dominance (CD) in the first one (CD ≈ 1).

As discussed in 3.3.4, the γ-ray flares are likely associated with new components merging from the VLBA core, which places the emission regions rather far from central engine. This is also in agreement with the studies of [204] and [88] that the γ-ray emission is produced is outside the BLR. Hence, for both flaring periods, R_H was set in order to have our emission region outside the BLR and show the DT as the main source of seed photons. The change in the parameters between Flare 1 and 5, i.e. an increase of R_H, and a consequent increase of R (due to the jet geometry), with a decrease of the magnetic field, are qualitatively consistent with an adiabatically expanding blob moving along the axis of a conical jet. This could be in agreement with the results presented in Section 3.3.4. This scenario, investigated in [306], would also imply a very mild decrease in the total number of particles (if particle escape is very inefficient), and a magnetic field value dictated by flux-freezing theorem $B(R(t)) = B_0(R_0/R(t))^{m_B}$ [44]. However, this interpretation is not unique. The inferred distance traveled over the time interval between flares suggests only mildly relativistic motion, which is inconsistent with the assumed bulk Lorentz factor. A purely adiabatic expansion would likely produce a more continuous high-flux state rather than temporally distinct flares, as Figure 3.3 shows. In Section 3.3.4, it was found that before the flaring activity, new components arise from the jet in 2024 and could collide with the first static shock present in the jet and be responsible for the flaring activity detected in γ-rays. Hence, it is likely that, on top of the expansion, during Flare 5, an additional shock acceleration occurred. So, while our modeling suggests the adiabatic expansion as a plausible scenario, alternative combinations of parameters (e.g., lower B, higher Γ) and physical mechanisms, like turbulence and kink instabilities, may yield comparable fits, and further multi-wavelength constraints would be required to break this degeneracy.

Another possibility, presented in [93], is that a hadronic component contributed to the flaring emission. [93] suggests that, in the period in which the Flare 2 and 3 were identified, the inclusion of the photo-meson process along with the leptonic emission component can successfully reproduce the SED, while the leptonic one cannot. It is fundamental to notice that this is the period in which the very high energy (VHE) gamma-ray emission from OP 313 was detected, and the goodness of the leptonic fit will be further investigated in the upcoming paper by the MAGIC and LST Collaborations. The VHE emission is not part of this project.

3.4 Summary

This chapter presents several multi-wavelength observations of the high redshift FSRQ OP 313 from 2008 to 2024. The datasets include radio-to-γ-ray data collected by LAT, *Swift*, ATLAS, CRTS, KAIT, Tuorla, ZTF, Metshäovi, VLBA, QUIVER,

Table 3.9: Posterior parameters for the broadband SEDs of OP 313 in the Flare 1 and Flare 5. $\gamma_{\rm min}$, $\gamma_{\rm break}$, and $\gamma_{\rm max}$ are, respectively, the minimum, break, and maximum Lorentz factors, p_1 and p_2 are the spectral indices below and above the break, respectively, N is the emitter density, $R_{\rm DT}$ is the dusty torus radius, $\tau_{\rm DT}$ and $\tau_{\rm BLR}$ are, respectively, the BLR and DT optical depth, $R_{\rm BLR,in}$ and $R_{\rm BLR,out}$ are the inner and outer BLR radius, L_{disk} is the disk luminosity, T_{disk} is the temperature of the disk, R is the emitting region radius with a spherical geometry, R_H is the emitting region position in the jet, B is the tangled magnetic field, θ is the viewing angle, $\theta_{\rm open}$ is the semi-opening angle of the conical jet, Γ is the bulk Lorentz factor along the jet axis.

Parameter	Flare 1	Flare 5	Frozen
γ_{min}	$2.3^{+0.1}_{-0.1}$	$2.1^{+0.1}_{-0.1}$	False
γ_{max}	$(6.8^{+0.7}_{-0.8}) \times 10^4$	$(9.4^{+0.4}_{-0.6}) \times 10^4$	False
N [cm^{-3}]	$(1.5^{+0.3}_{-0.3}) \times 10^1$	$(2.0^{+0.5}_{-0.5}) \times 10^1$	False
γ_{break}	$(6.9^{+1.3}_{-1.2}) \times 10^3$	$(5.8^{+1.0}_{-1.0}) \times 10^3$	False
p_1	$2.0^{+0.1}_{-0.1}$	$2.1^{+0.1}_{-0.1}$	False
p_2	$3.4^{+0.3}_{-0.3}$	$3.6^{+0.2}_{-0.2}$	False
$*R_{\rm DT}(L_{\rm Disk})$ [cm]	1.4×10^{19}	1.4×10^{19}	True
$\tau_{\rm DT}$	0.1	0.1	True
$\tau_{\rm BLR}$	0.1	0.1	True
L_{Disk} [erg s^{-1}]	5.0×10^{45}	5.0×10^{45}	True
T_{Disk} [K]	5×10^4	5×10^4	True
$*R(R_H, \theta_{\rm open})$ [cm]	8.2×10^{17}	8.78×10^{17}	True
R_H [cm]	$(8.1^{+1.4}_{-1.2}) \times 10^{18}$	$(9.1^{+1.9}_{-1.5}) \times 10^{18}$	False
B [G]	$(1.7^{+0.2}_{-0.1}) \times 10^{-1}$	$(8.5^{+0.8}_{-0.9}) \times 10^{-2}$	False
θ [°]	3.5	3.5	True
$\theta_{\rm open}$ [°]	5.00	5.00	True
Γ	$13.1^{+0.2}_{-0.2}$	$14.6^{+0.2}_{-0.2}$	False

SMAPOL, and the F-GAMMA project. OP 313 exhibited strong variability in the optical - γ-ray wavelength range, increasing its flux starting from 2022. The optical, UV, X-ray, and γ-ray light curves are well correlated. A different behavior has been observed in radio, with the flux being high in 2008 and a new increasing trend in 2019, without a clear correlation with the other bands.

Focusing on the γ-ray observations, especially those after 2021, eight flaring periods were identified to investigate the interplay between particle acceleration and radiative cooling in the source's jet by means of hysteresis plots. No clear hysteresis pattern for the first, second, and fifth flaring periods was found. The SED of the fifth γ-ray flaring period shows a significant Compton dominance, suggesting that photon fields outside the jet are responsible for the IC scattering. This is in agreement with the results shown in [204] that identify the γ-ray emission region to be outside the BLR. Moreover, an overall correlation has been observed between optical and γ-ray bands without significant time lag, suggesting that the emission in these two bands has a common origin and is produced by leptonic processes.

The kinematics of the jet were studied by analyzing high-resolution radio images collected from the VLBA-BU-BLAZAR and MOJAVE projects. New components arose in the jet starting from 2021, and some of these new components could be responsible for the flaring activity observed since 2022. To investigate this possibility, the epoch of ejection and the epoch at which the knots encountered a standing shock in the jet were calculated. As a result, the knots named "B11" could be responsible for the flaring activity observed in 2022-2023.

The possible association between γ-ray flaring activity and the ejection of new radio components observed in OP 313 was already reported for several blazars. Temporal connections between high-energy flares and the arising of superluminal knots have been observed in both FSRQs and BL Lac objects [e.g. 21, 59, 191, 227], supporting a scenario in which part of the γ-ray emission originates at distances comparable to the radio core or standing shocks in the jet.

At the same time, it is well known that this behavior is not unique among blazars. In several sources, no clear temporal association between γ-ray activity and radio knot ejections has been found. This reflects differences in jet geometry, viewing angle, or location of the emission region. OP 313 appears to belong to the class of FSRQs where high-energy activity is possibly connected to knots propagating along the jet, interacting with stationary features such as standing shocks.

Moreover, the results presented here strengthen the picture where several emission sites may coexist in blazar jets, and where the location of the γ-ray emitting region can vary both among sources and between different flaring episodes of the same object. To support that the γ-ray emitting region is far from the central engine, and thus the dusty torus is the possible source of seed photons, the SEDs of the first and fifth flaring periods using a SSC and EC single-zone model were modeled. This analysis shows that the DT component is more prominent in the fifth flaring period SED, as expected. This highlights how much the DT's photon fields are important to describe the γ-ray emission of OP 313.

The SED modeling of OP 313 is also consistent with results obtained for other FSRQs, which often exhibit strong Compton dominance and require external photon fields to reproduce the observed γ-ray emission. Previous studies have shown that, especially during high-activity states, inverse Compton scattering of infrared photons from the dusty torus can dominate over synchrotron self-Compton processes

[e.g. 152, 204]. OP 313 confirms that external Compton scenarios are a feasible ingredient to explain the high-energy emission of powerful, high-redshift FSRQs. The variability observed between different flaring periods further supports the relative importance of external photon fields that can evolve with time, possibly reflecting changes in the location of the emission region along the jet.

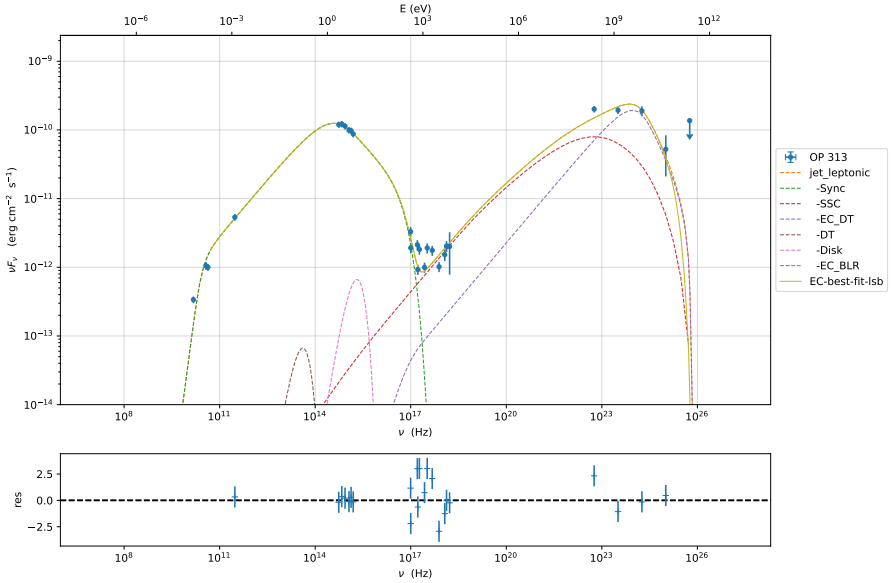

(a)

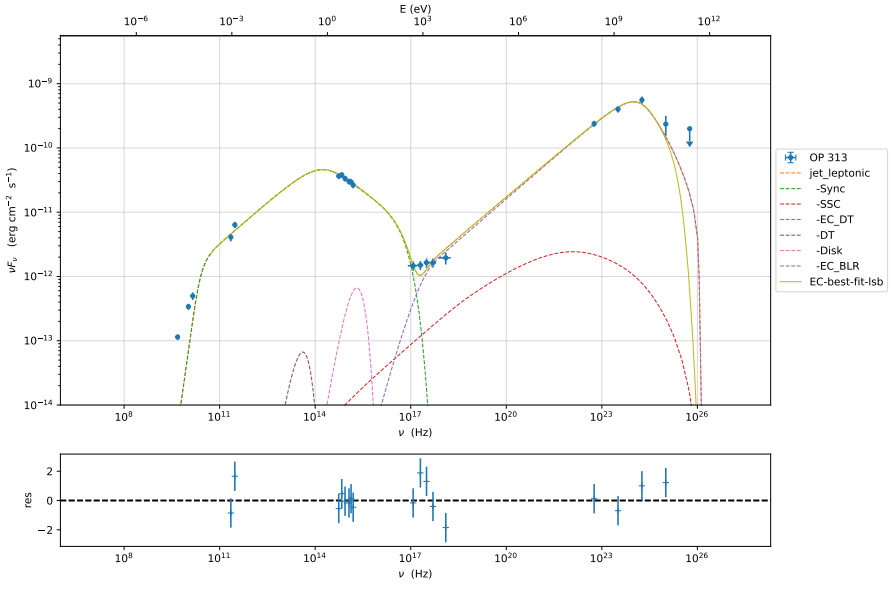

(b)

Figure 3.11: (a) Model-fit broadband SED of OP 313's Flare 1 and (b) model-fit broadband SED of OP 313's Flare 5 using `JeTSet ModelMinimizer` module with an `iminuit minimization`. The legends provide the color coding for the different components.

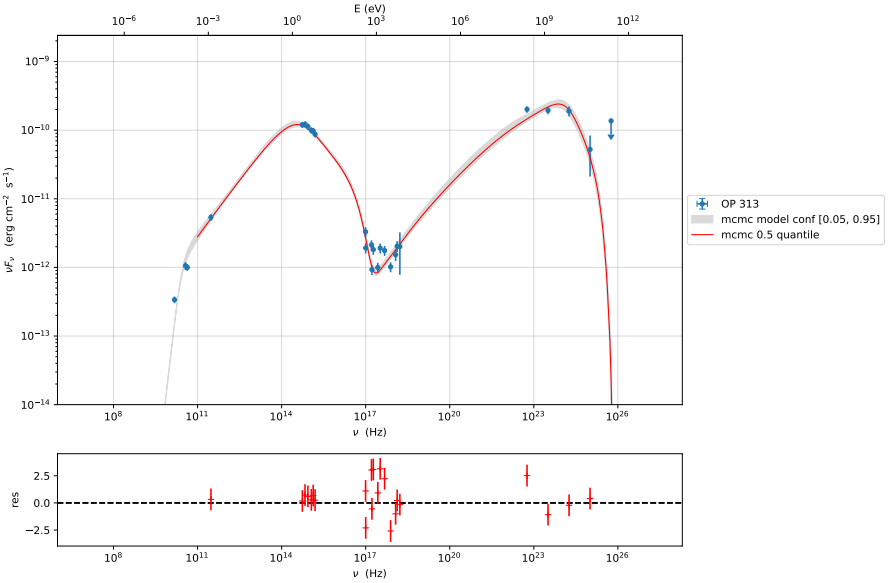

(a)

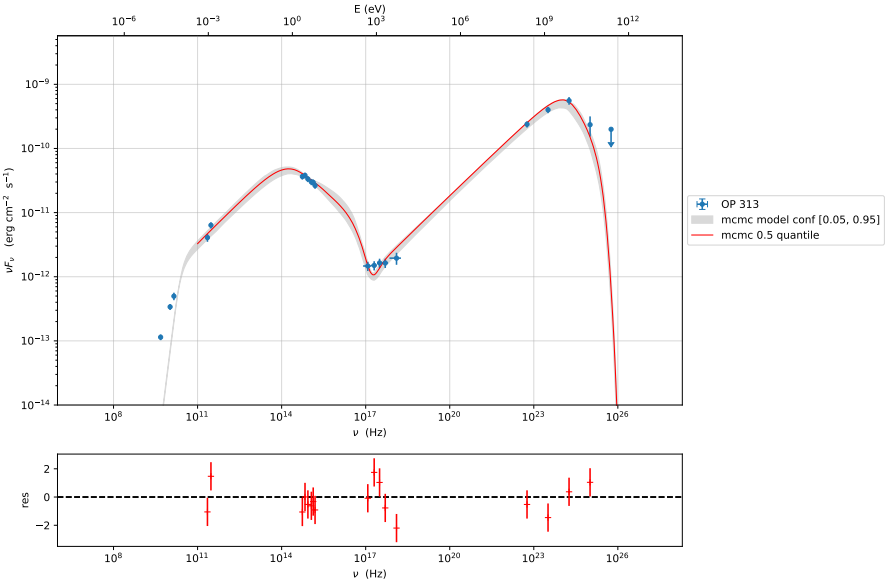

(b)

Figure 3.12: (a) Model-fit broadband SED of OP 313's Flare 1 and (b) model-fit broadband SED of OP 313's Flare 5 using `JeTSet McmcSampler`. The legends provide the colour coding for the MCMC information.

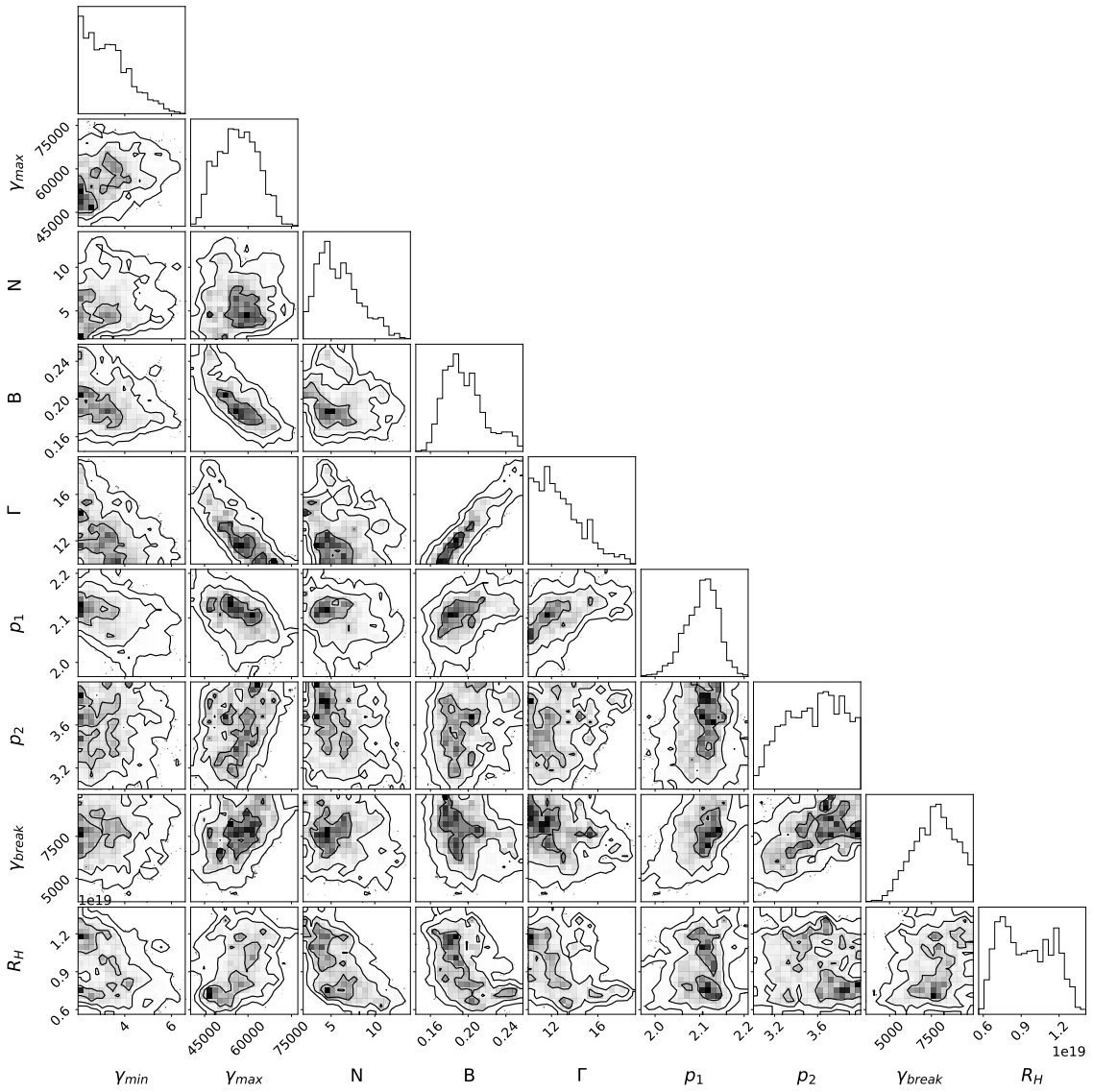

Figure 3.13: Corner plot showing the posterior probability distributions of the model parameters obtained from the MCMC fit for Flare 1. The diagonal panels display the one–dimensional marginalized posterior distributions for each parameter, while the off–diagonal panels show the two–dimensional joint posterior distributions, highlighting parameter correlations. Contours correspond to the 1σ, 2σ, and 3σ confidence levels.

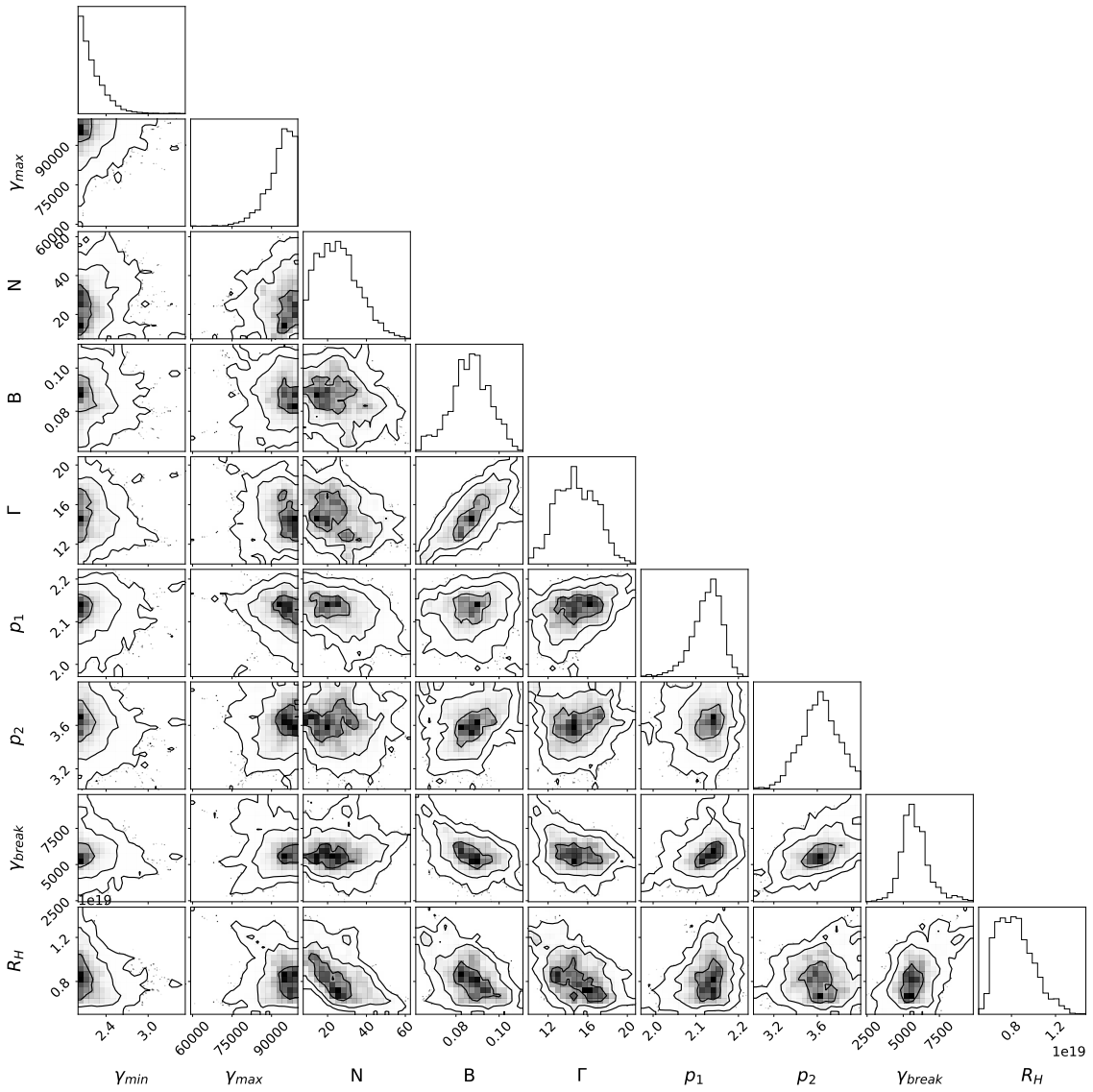

Figure 3.14: Corner plot showing the posterior probability distributions of the model parameters obtained from the MCMC fit for Flare 5. The diagonal panels display the one–dimensional marginalized posterior distributions for each parameter, while the off–diagonal panels show the two–dimensional joint posterior distributions, highlighting parameter correlations. Contours correspond to the 1σ, 2σ, and 3σ confidence levels.

Chapter 4

Exploring the high-energy spectral cut-off of FSRQs using CTAO

This chapter presents the simulations and the analysis of a sample of FSRQs using different configurations of CTAO. Models like a power-law distribution with a high energy cut-off, a log-parabola, or a broken power law can typically describe the γ-ray energy spectrum for AGN. The LAT can probe many AGN for which the curvature of the energy spectrum sits in the GeV domain. However, measurement of the curvature requires large photon statistics, which are not always available because of *Fermi*-LAT's limited sensitivity above 100 GeV. CTAO will provide a wider energy range, larger effective area, better angular resolution, and flux sensitivity in comparison to any existing γ-ray detector. In this chapter, LAT real data and CTAO simulated observations for different CTAO's configurations between 0.1 GeV and 10 TeV are combined to obtain constraints on the cutoff energy parameter under the assumption that a power law with an exponential cutoff describes the spectral energy distribution of the sources in this energy range. Furthermore, each dataset was fitted with different physically motivated models to assess the effectiveness of the various CTAO configurations for spectral studies.

A sensitivity study like this one is fundamental to assess the capability of the instrument to detect the flaring activity of FSRQs, which have a sharp decline of their γ-ray spectrum above a few tens of GeV, with only a small number of photons detected at the energy range where Middle-Sized Telescopes (MSTs) are sensitive. Furthermore, since the reconstruction of the SEDs of blazars at VHE is not always possible, it is fundamental to assess if CTAO will be able to do it and give clearer hints on the spectral model that describes them.

The content of this publication is under review by the CTAO consortium, so the content reported in this Chapter could be different from the one in the published paper. I am the corresponding author, together with Francesco Schiavone (Ph.D. student at Dipartimento di Fisica "M. Merlin" dell'Università e del Politecnico di Bari and Istituto Nazionale di Fisica Nucleare, Sezione di Bari), who contributed to the statistical approach of this analysis, Reshmi Mukherjee (Professor at Barnard College, Columbia University, USA), who contributed to the selection of the physically motivated spectral models, and Elina Lindfors (Professor at University of

Turku, Finland), who contributed to the spectral cut-off energy interpretation.

4.1 Starting points of the project

The origin of the second peak of the SED of blazars is still debated. In the leptonic scenarios, γ-rays originate from inverse Compton scattering of synchrotron photons (SSC; [184]) or external photons (EC; [99, 100]) interaction with the relativistic electrons in the jet. In the Thomson regime, the γ-ray spectrum reflects the energy distribution of the accelerated electrons [310]. Hence, the γ-ray spectrum deviation from a power law may arise from a non-power-law electron population or from the transition from the Thomson regime to the Klein–Nishina one [53, 99]. In hadronic models, proton–photon interactions produce pions that decay into γ-rays, neutrinos, and pairs, making blazars key targets for multimessenger astrophysics [144, 181, 231]. This project is restricted to leptonic models in the Thomson regime, as including hadronic models and the Klein–Nishina regime introduce additional complexity beyond the actual goal, which is to perform a sensitivity study.

Different physically motivated models were compared within the γ-ray spectrum of eight FSRQs selected from both the 4FGL-DR4 [9, 10] and the TeVCat [316], except for one that was taken from the list of galaxies available in the CTAO Internal Science Data Challenge. The LAT instrument detected multiple times increasing flaring activity from the FSRQs sample, and different fast publications on the Astronomer's Telegram were published. Furthermore, the selected sample of FSRQs includes different redshifts, ranging from low-redshift to high-redshift. This is important to assess if the redshift affects CTAO during the observations of flaring activity. The sample is characterized by: PKS 0736+01, PKS 1222+216. Ton 599, OP 313, and PKS 1502+106, located in the Northern Hemisphere, and PKS 1520-089, 3C 279, and PKS 0346-27, located in the Southern Hemisphere.

4.2 Sample of Flat Spectrum Radio Quasars

The FSRQs considered in this work were chosen according to the following criteria:

- The FSRQ needs to have had a flaring activity seen by LAT which was reported in an Astronomer's Telegram;
- The same FSRQ flaring activity needs to be seen by one ground-based γ-ray telescope at least once. FSRQs usually show a sharp decline in their γ-ray spectra above a few tens of GeV, with only a small number of photons detected at very high energies [e.g. 18]. This criterion ensures that the flare could be seen by CTAO.

Only one FSRQ in our sample does not satisfy both criteria, but it is reported among the possible flaring sources that could be seen by CTAO in the CTAO Internal Science Data Challenge. Our sample is composed of eight candidates located in the Northern and Southern Hemispheres, whose coordinates and redshifts are reported in Table 4.1:

– PKS 0736+01 showed flaring activity in November 2014, seen by LAT [92] and in February 2016. The High Energy Stereoscopic System (H.E.S.S.)[1] detected VHE emission in February 2015 [73], during a γ-ray flaring episode that had been previously identified by *Fermi*-LAT and triggered the VHE observations.

– PKS 1222+216, also known as 4C +21.35, showed enhanced flaring activity from April 2009 to February 2011 seen by LAT [79, 103, 180, 220]. The Major Atmospheric Gamma-ray Imaging Cherenkov Telescopes (MAGIC) collaboration[2] detected VHE emission from this source in June 2010 [225].

– Ton 599 was characterized by flaring activity in September 2017, in December 2020, and in January 2023 seen by LAT [75, 146, 147, 267]. The Very Energetic Radiation Imaging Telescope Array System (VERITAS) [3] observed VHE emission from Ton 599 in December 2017 [243].

– OP 313 was characterized by intense flaring activity in November 2023 and February 2024 seen by LAT [39, 40]. CTAO's LST-1 detected VHE emission from this FSRQ in December 2023 [87].

– PKS 1502+106 showed intense flaring activity in January 2009 and in July 2015 seen by LAT [80, 175]. No ground-based γ-ray detectors detected VHE emission from this source, but it was considered in the CTAO Internal Data Challenge as one of the possibly detectable flaring sources by CTAO. Moreover, we decided to include it as an example of a source with a very high redshift compared to the others.

– PKS 1510-089 was characterized by intense flaring activity in July and October 2011 seen by LAT[91, 179]. This source was detected at VHE by both H.E.S.S and MAGIC in May 2016 [238, 249].

– 3C 279 was characterized by intense flaring activity in January and April 2018, seen by LAT [256, 336]. This source was detected at VHE by H.E.S.S. in January 2018 [250] and by MAGIC in April 2018 [239].

– PKS 0346-27 was characterized by intense flaring activity in November 2021, seen by both LAT and H.E.S.S. [314].

4.3 Theoretical models

The considered physically motivated models are the leptonic emission processes presented in [310], in which γ-rays are produced by Compton scattering in the Thomson regime of relativistic electrons. The Thomson regime is valid as long as the photon energy is much smaller than the mass energy of the electron: $h\nu \ll mc^2$. The models presented here will be used to fit the LAT and CTAO datasets. Also, hadronic models are capable of reproducing the observed emission from blazars [e.g. 24, 55, 224, 241, 242], but as explained above, they are not part of this project.

It is fundamental to stress that the spectral models adopted are phenomenological representations of the observed γ-ray spectra and should not be interpreted as exact analytical solutions of inverse Compton emission in the Thomson regime. Even in the simplest case of inverse Compton scattering by relativistic electrons in the

[1] `https://www.mpi-hd.mpg.de/HESS/`
[2] `http://www.magic.iac.es/`
[3] `https://veritas.sao.arizona.edu/`

Table 4.1: Sources of interest in our study, their redshifts and location on the sky, the time windows in which we focus our LAT analysis on, and lightcurves binning.

Source	R.A.	Dec.	z	Hemisphere
PKS 0736+01	$07^h39^m18^s.0339$ [208]	$+01°37'04''.617$	0.19 [159]	North
PKS 1222+216	$12^h24^m54^s.4584$ [331]	$+21°22'46''.388$	0.43 [27]	North
Ton 599	$11^h59^m31^s.8339$ [208]	$+29°14'43.826'$	0.72 [159]	North
OP 313	$13^h10^m28^s.6638$ [331]	$+32°20'43''.782$	0.99 [282]	North
PKS 1502+106	$15^h04^m24^s.9797$ [329]	$+10°29'39''.198$	1.84 [27]	North
PKS 1510-089	$15^h12^m50^s.5329$ [208]	$-09°05'59''.829$	0.36 [302]	South
3C 279	$12^h56^m11^s.1665$ [331]	$-05°47'21''.525$	0.54 [228]	South
PKS 0346-27	$03^h48^m38^s.1445$ [208]	$-27°49'13''.565$	0.99 [323]	South

Thomson regime, the resulting photon spectrum generally depends on several factors and does not necessarily possess the same functional form as the underlying electron distribution [98].

Therefore, spectral shapes such as exponential cut-off power laws, log-parabolic laws, or broken power laws should be regarded as descriptions of the emerging γ-ray emission over the limited energy range probed by LAT and CTAO, rather than as direct physical templates of the inverse Compton process.

Furthermore, FSRQs internal absorption due to $\gamma - \gamma$ pair production on broad-line region or dusty torus photon fields may further modify the intrinsic high-energy spectrum [e.g. 56, 118]. These effects can introduce spectral curvature or cut-offs that are not directly related to the underlying electron distribution. These absorption processes are not modeled explicitly in the phenomenological fits performed here and may partly contribute to the observed spectral curvature at high energies.

The spectral models used to fit the spectra are introduced starting from the underlying electron energy distributions. These distributions do not translate in a one-to-one way into the observed photon spectra, even in the simplest case of inverse Compton scattering in the Thomson regime [e.g. 98, 118]. The resulting photon spectrum depends on several factors, including the seed photon field, the geometry of the emitting region, and possible radiative or absorption effects.

Nevertheless, for broad-band spectral fitting in the GeV–TeV energy range, simple phenomenological photon models are commonly adopted as effective descriptions of the emerging γ-ray spectra. These models capture the main spectral features expected from leptonic emission in the Thomson regime and provide a practical framework for model comparison, without implying a unique or exact correspondence with the underlying particle distributions. Hence, the spectral models are applied directly to the photon spectra measured by LAT and CTAO, and should be

interpreted as phenomenological representations, rather than as direct inversions of the electron energy distributions.

The first model is a Exponential Cutoff Power-Law (ECPL). This model provides an effective description of spectra expected from scattered electrons in a first-order Fermi shock acceleration scenario [more details in Section A.1.3 and 199, 294]. In this scenario, the electron distribution, n_e, is described by a power law with an exponential cut-off due to a limiting process as a decreasing chance for them to cross the shock front a large number of times or radiative cooling:

$$n_e(\gamma_e) = n_{e,0}\gamma_e^{-\Gamma}\exp(-\gamma_e/\gamma_c) \tag{4.1}$$

where γ_e is the electron Lorentz factor, γ_c is the cut-off Lorentz factor, and Γ is the spectral index. In this project, the spectral models that were used are the one from the open-source Python package for γ-ray astronomy `gammapy` v.1.3[4]. The ones corresponding to this theoretical case are the `ExpCutoffPowerLaw3FGLSpectralModel`[5] or the `ExpCutoffPowerLawSpectralModel`[6].

The second model is a Log Parabola (LP). This model arises in the framework of stochastic acceleration processes, where the probability for particles to gain energy depends on their initial energy [229, 305] but does not represent a unique prediction of IC emission. In this case, the electron distribution can be described by a log-parabolic law:

$$n_e(\gamma_e) = n_{e,0}, \gamma_e^{-(\alpha+\beta,\log(\gamma_e/\gamma_0))} \tag{4.2}$$

where α is the spectral index at the reference Lorentz factor γ_0 and β describes the curvature of the spectrum. In the context of γ-ray astronomy, this distribution translates into a curved photon spectrum that can account for gradual steepening at high energies. The corresponding spectral model implemented in `gammapy` is the `LogParabolaSpectralModel`[7]

The third model is a Broken Power-Law (BPL). This model describes a scenario where two different physical processes dominate in different energy ranges. An example is radiative cooling and adiabatic cooling. Then, the electron distribution is given by:

$$n_e(\gamma_e) = n_{e,0}\begin{cases}(\gamma_e/\gamma_b)^{-a} & \text{if}\,\gamma_e \leq \gamma_b \\ (\gamma_e/\gamma_b)^{-b} & \text{if}\,\gamma_e > \gamma_b\end{cases} \tag{4.3}$$

where a and b are the spectral indices of the low and high-energy power laws, respectively [310]. The spectral model that was used in this theoretical case to describe radiation is `gammapy`'s `BrokenPowerLawSpectralModel`[8].

The fourth model is a Power-Law Log-Parabola (PL-LP). This model is analogous to the LP one, but it combines a power-law behavior at low energies with a log-parabolic curvature at higher energies [230, 305]. This model still considers stochastic accelerations. In [305], it is shown that an electron distribution with a low-energy power

[4] `https://gammapy.org/`

[5] `https://docs.gammapy.org/dev/api/gammapy.modeling.models.ExpCutoffPowerLaw3FGLSpectralModel.html`

[6] `https://docs.gammapy.org/dev/api/gammapy.modeling.models.ExpCutoffPowerLawSpectralModel.html`

[7] `https://docs.gammapy.org/dev/api/gammapy.modeling.models.LogParabolaSpectralModel.html`

[8] `https://docs.gammapy.org/dev/api/gammapy.modeling.models.BrokenPowerLawSpectralModel.html`

law tail and a high-energy log-parabolic peak is obtained by solving a diffusion equation with radiative losses and with continuous injection. The electron distribution is given by:

$$n_e(\gamma_e) = n_{e,0} \begin{cases} (\gamma_e/\gamma_b)^{-\Gamma} & \text{if}, \gamma_e \leq \gamma_b \\ (\gamma_e/\gamma_b)^{-(\alpha+\beta,\log(\gamma_e/\gamma_b))} & \text{if}, \gamma_e > \gamma_b \end{cases} \tag{4.4}$$

where Γ is the spectral index of the low-energy power law, while α and β characterize the log-parabolic curvature above the break Lorentz factor γ_b. This hybrid model provides additional flexibility to reproduce spectra that show both a power-law regime and a gradual curvature. Since it is not directly implemented in `gammapy`, I implemented a new spectral class in `gammapy`'s source code.

4.4 Data analysis

4.4.1 Fermi-LAT

For every FSRQ included in this study, a specific time window was selected where the sources were having flaring activity. The available *Fermi*-LAT Light Curve Repository (LCR) [9] was used to identify the highest flaring periods seen by LAT and the rapid publications on the Astronomer's Telegram website. The time windows identified for every FSRQ are reported in Table 4.2 with the applied light curve binning.

To analyze the different datasets of Pass 8 data collected by LAT, the version of LAT *ScienceTools*[10] v2.2 and the `fermipy` v1.1 Python package were used. The files that were used to start the analysis are the $P8R3\_SOURCE\_V3$ instrument response functions, the Fourth Data Release 4FGL-DR4 [10, 37] catalog, and the Galactic and the isotropic diffuse γ-ray emission models provided by the standard templates $gll\_iem\_v07.fits$ and $iso\_P8R3\_SOURCE\_V3\_v1.txt$ [11]. The photon events with reconstructed energy between 100 MeV and 500 GeV were analyzed, selecting a region of interest (ROI) of 15×15 deg centered on the γ-ray source position and applying a standard quality cut ('`DATA_QUAL>0 && LAT_CONFIG==1`'). Furthermore, a zenith angle cut of 90 deg was used to reduce the contamination from the Earth limb.

4.4.2 Fermi-LAT Light curves

In order to realize the LAT light curves, a maximum-likelihood test statistic (TS) analysis was computed on each dataset. The TS was defined as Equation 2.4 and all the sources at 5 deg from our sample of FSRQs with a $TS \geq 25$ were considered, letting free to vary their normalization parameter. All the parameters of the sources with a $TS \leq 25$ were frozen. The model took into account the Galactic and the isotropic diffuse, and the source of our interest, with all parameters set free to vary during the fitting process. Then, it was computed the 3-day binned light curve for PKS 1222+216, OP 313, PKS 1510-089, and PKS 0346-27 and the weekly-binned light curve for PKS 0736+01, Ton 599, and 3C 279, as reported in Table 4.2. As in [20], the light curve time binnings, reported in Table 4.2, were chosen for each

[9] `https://fermi.gsfc.nasa.gov/ssc/data/access/lat/LightCurveRepository/`
[10] `https://fermi.gsfc.nasa.gov/ssc/data/analysis/software/`
[11] `https://fermi.gsfc.nasa.gov/ssc/data/access/lat/BackgroundModels.html`

Table 4.2: Sources of interest in our study, their redshifts and location on the sky, the time windows in which the LAT analysis was done, and light curves binning.

Source	z	Hemisphere	Period	LC Binning (days)
PKS 0736+01	0.19	North	2014/01/01 - 2021/01/01	7
PKS 1222+216	0.43	North	2008/08/04 - 2015/03/01	3
Ton 599	0.72	North	2020/10/15 - 2025/01/01	7
OP 313	0.99	North	2022/01/01 - 2025/03/31	3
PKS 1502+106	1.84	North	2014/01/01 - 2018/06/01	3
PKS 1510-089	0.36	South	2008/08/04 - 2017/01/01	3
3C 279	0.54	South	2013/01/01 - 2020/01/01	7
PKS 0346-27	0.99	South	2017/01/01 - 2023/01/01	3

source depending on its typical strength to avoid having an excessive number of bins with no detection. The time bins with a TS less than 9 were removed from the light curves.

To take into account the statistically significant variations in the light curves, Bayesian blocks [279] implemented inside `astropy`[12] and the Eisenstein-Hut HOP algorithm [111] used by [315] available on GitHub [13] were used. The flares were identified as groups of blocks, following [237] using the method called "baseline" in [315]. The starting time and end time of the so-called HOP groups are determined by the flux exceeding or dropping below a predefined flux level. In our case, to define the flux level, the equation reported in [332] was used:

$$F_{\gamma}^{th} = F_{\gamma}^{q} + s\langle F_{\gamma}^{err} \rangle \tag{4.5}$$

where F_{γ}^{q} is the γ-ray quiescent flux level, s corresponds to the significance above the quiescent flux level in units of the standard deviation σ ($\sigma = 5$ was used), $\langle F_{\gamma}^{err} \rangle$ is the the average uncertainty of the γ-ray fluxes. The quiescent flux was defined as the Bayesian block with the lowest flux that contained more data points than the mean number of data points per block [106]. For each source of our sample, the start, end time, and peak time of each flare were obtained. The peak time is defined as the center of local maxima in the block representation, and every block that is subsequently lower to the left and right belongs to that peak. Since the goal of this project is not studying every flaring period of each source, only the one flare with the highest flux peak without considering the presence of short-term flares inside the highest flaring period was selected. A list of the selected flaring periods is reported in Table 4.3, while the light curves of each source in the sample are presented in Figure from 4.1 to 4.8. The light red areas indicate the flare that was considered in the analysis, which has the highest flux peak in the time window. In pink and light pink are shown the other flaring periods found using the HOP algorithm and the Equation 4.5 to define the flux's threshold. The two tonalities of pink were used to help the reader distinguish those flaring periods that are close. From now on, the time range that goes from "start time" to "peak time" will be called "rising time", while every time range that goes from "peak time" to "end time" will be called "decaying time".

[12] `https://docs.astropy.org/en/stable/api/astropy.stats.bayesian_blocks.html`
[13] `https://github.com/swagner-astro/lightcurves`

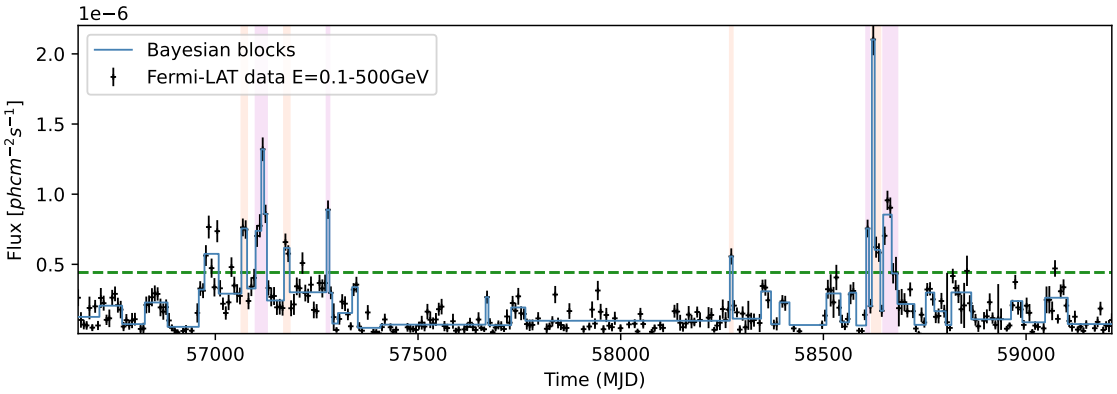

Figure 4.1: Light curve of PKS 0736+01. The red area indicates the flare that was analyzed in our analysis, while the pink areas are the ones found by the HOP algorithm. The green dashed line is the flux threshold above which the HOP algorithm found the flaring periods.

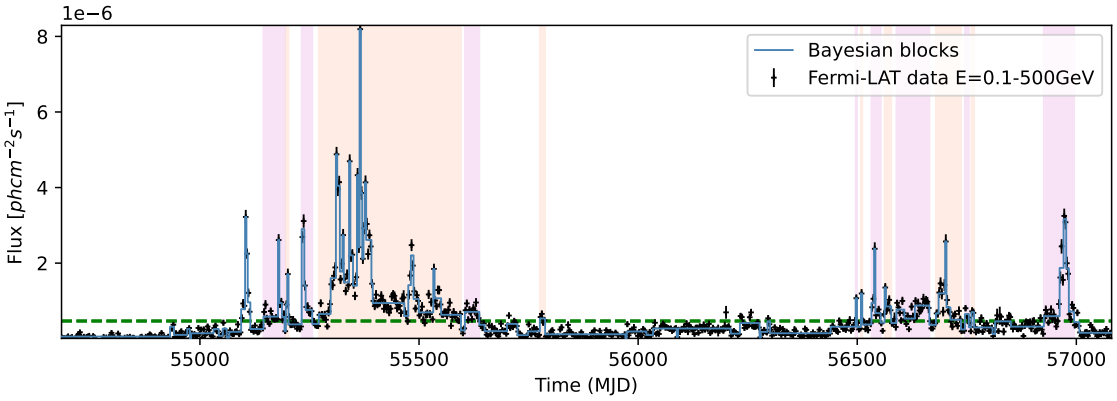

Figure 4.2: Light curve of PKS 1222+216. The red area indicates the flare that was analyzed in our analysis, while the pink areas are the ones found by the HOP algorithm. The green dashed line is the flux threshold above which the HOP algorithm found the flaring periods.

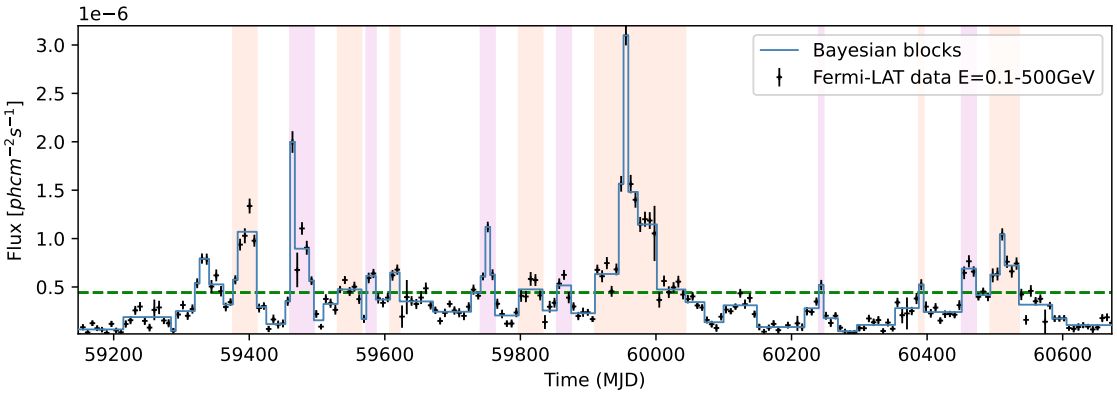

Figure 4.3: Light curve of Ton 599. The red area indicates the flare that was analyzed in our analysis, while the pink areas are the ones found by the HOP algorithm. The green dashed line is the flux threshold above which the HOP algorithm found the flaring periods.

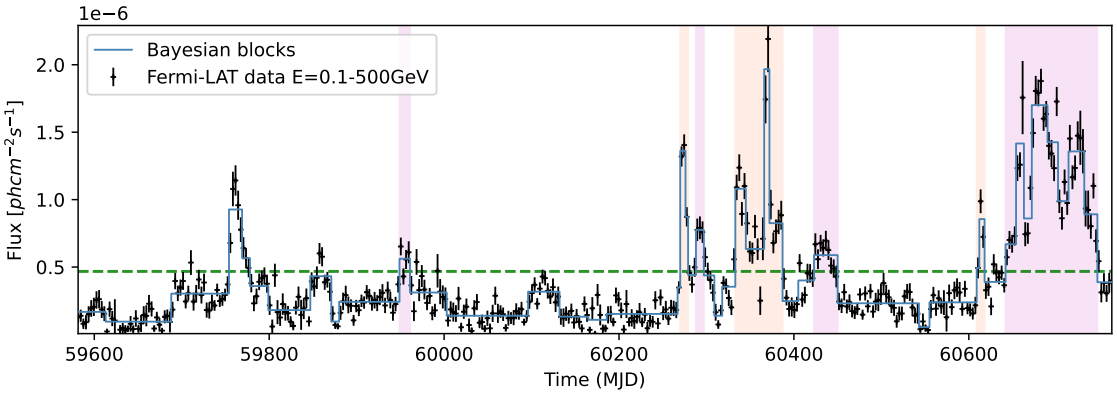

Figure 4.4: Light curve of OP 313. The red area indicates the flare that was analyzed in our analysis, while the pink areas are the ones found by the HOP algorithm. The green dashed line is the flux threshold above which the HOP algorithm found the flaring periods.

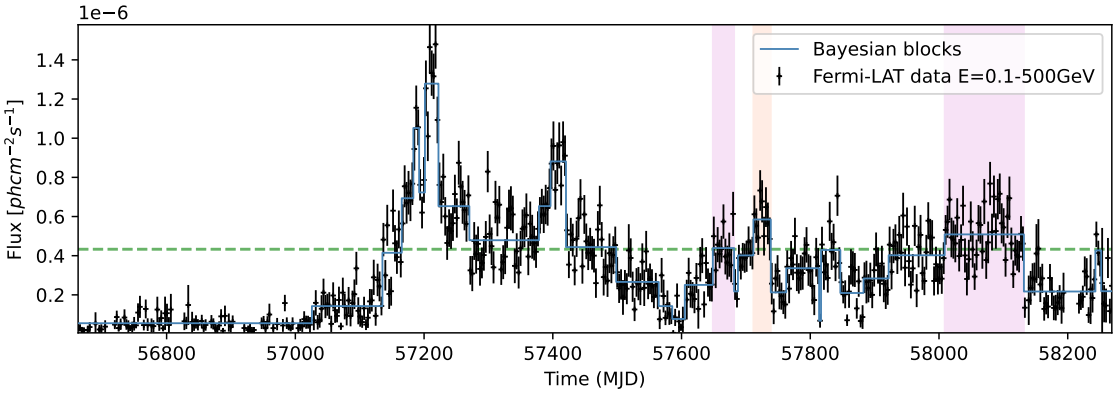

Figure 4.5: Light curve of PKS 1502+106. The red area indicates the flare that was analyzed in our analysis, while the pink areas are the ones found by the HOP algorithm. The green dashed line is the flux threshold above which the HOP algorithm found the flaring periods.

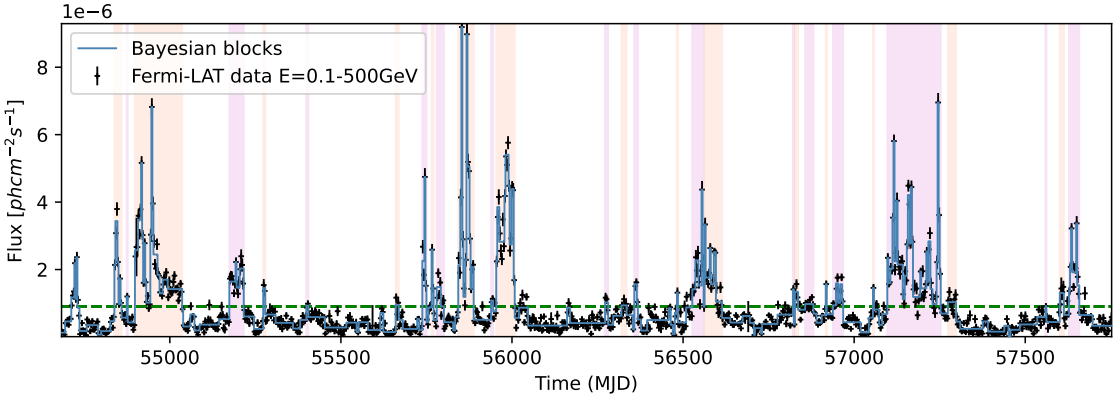

Figure 4.6: Light curve of PKS 1510-089. The red area indicates the flare that was analyzed in our analysis, while the pink areas are the ones found by the HOP algorithm. The green dashed line is the flux threshold above which the HOP algorithm found the flaring periods.

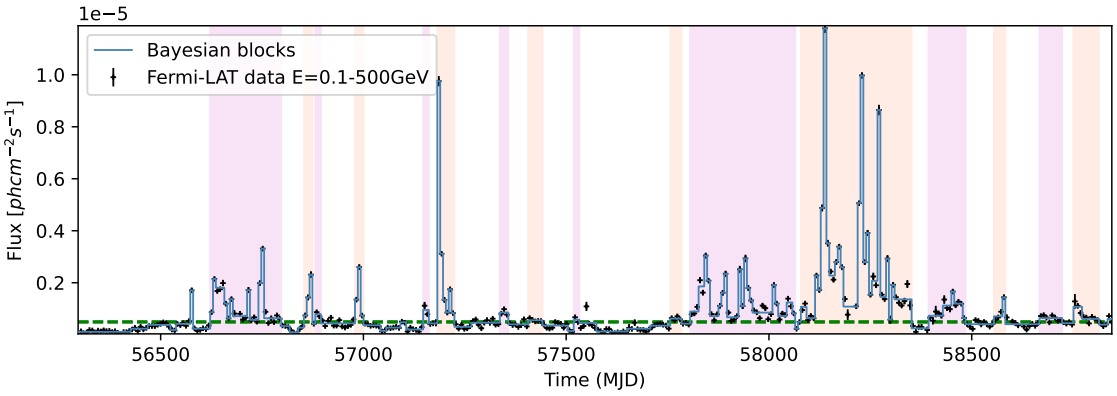

Figure 4.7: Light curve of 3C 279. The red area indicates the flare that was analyzed in our analysis, while the pink areas are the ones found by the HOP algorithm. The green dashed line is the flux threshold above which the HOP algorithm found the flaring periods.

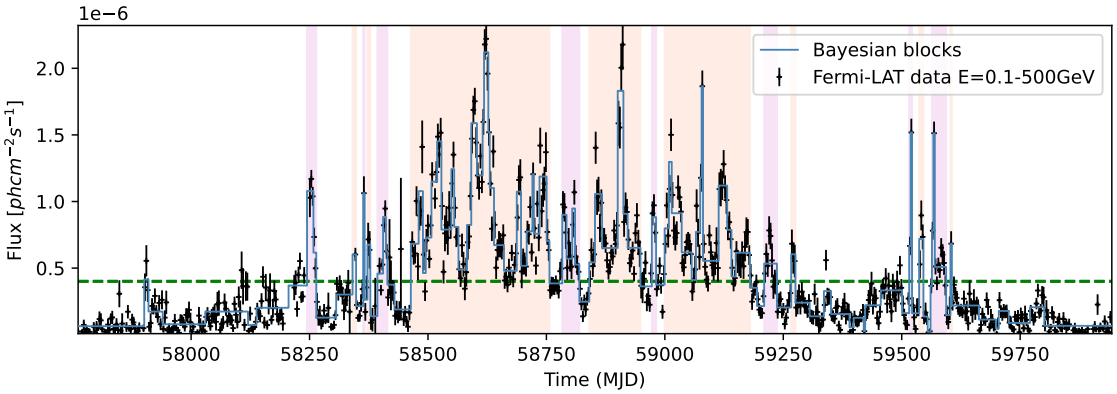

Figure 4.8: Light curve of PKS 0346-27. The red area indicates the flare that was analyzed in our analysis, while the pink areas are the ones found by the HOP algorithm. The green dashed line is the flux threshold above which the HOP algorithm found the flaring periods.

Table 4.3: Peak flux, start time, peak time, and end time of the most intense flare of each source. An SED for each timing period, starting from the start time to the peak time and from the peak time to the end time, was realized.

Source	Peak flux ($\mathrm{phcm^{-2}s^{-1}}$)	Start time	Peak time	End time
PKS 0736+01	2.10×10^{-6}	58619.5	58623	58640.6
PKS 1222+216	8.19×10^{-6}	55271.2	55365.8	55595.5
Ton 599	3.1×10^{-6}	59910	59955.7	60043.5
OP 313	1.97×10^{-6}	60333	60369	60387
PKS 1502+106	1.28×10^{-6}	57165.3	57211.8	57498.5
PKS 1510-089	9.19×10^{-6}	55843	55853.5	55888
3C 279	1.18×10^{-5}	58078.7	58138.2	58295.8
PKS 0346-27	2.12×10^{-6}	58463.8	58622.9	58756.5

4.4.3 Fermi-LAT analysis with `gammapy`

For each interval in Table 4.3 an SED was realized using `gammapy`.

The used strategy is the same as presented in [275]. The LAT dataset is managed as a `3D MapDataset` which has 1 coordinate for the energy, from 100 MeV to 500 GeV, and 2 coordinates for the position. To use LAT data with `gammapy`, the input files are the event list, the exposure cube, the effective point spread function (psf), and the detector response matrix (DRM), which maps the true counts spectrum from the measured counts spectrum. These files were obtained using `fermipy GTAnalysis` class. Using these files, there were created the 3D counts map, the energy dispersion matrix, the energy dispersion map with diagonal response, and the 3D exposure map. The same models used in Section 4.4.2 for the galactic and isotropic background were used. There were taken into account all the sources at 5 deg from the FSRQ of interest with a $TS \geq 25$, and the normalization and amplitude parameters were left free to vary. Regarding the source of interest, the spectral model chosen to fit the data is the `ExpCutoffPowerLaw3FGLSpectralModel`, which is a cutoff power law spectrum used for the LAT third *Fermi* Large Area Telescope (3FGL) sources [13]. All its parameters were left free to vary, except for the reference energy, which was taken from the 4FGL-DR4. The coordinates of the source and the EBL parameters were fixed, where the used EBL absorption model is the Saldana-Lopez [277]. After the fit process ended, the 3D dataset and the models of the FSRQ of interest and the nearby sources were saved. Using `gammapy`'s `FluxPointsEstimator` function, the SED points of the source of interest were extracted from the dataset and fit them using the model obtained in the previous step. An example of two SEDs obtained using this process are shown in Figure 4.9(a) and Figure 4.9(b). In Figure 4.9(b), the SED points of PKS 1510-089, which is a Southern source, don't reach 150 GeV, where the sensitivity of MSTs is optimized. Hence, it is not expected to have good Test Statistic (TS) when you simulate and fit CTAO data in this case.

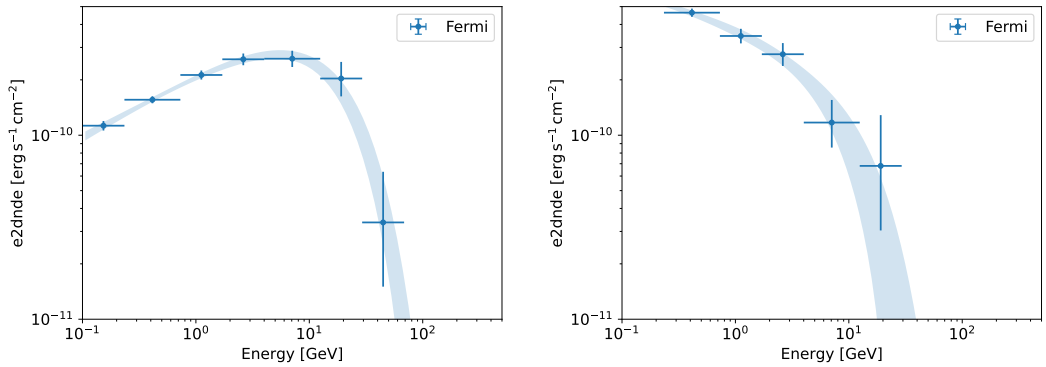

(a) (b)

Figure 4.9: a) OP 313's "rising flare" SED obtained using `gammapy` instead of `fermipy`. The model used to fit the LAT is `gammapy`'s `ExpCutoffPowerLaw3FGLSpectralModel`. b) PKS 1510-089's "rising flare" SED obtained using `gammapy` instead of `fermipy`. The model used to fit the LAT is `gammapy`'s `ExpCutoffPowerLaw3FGLSpectralModel`. The *Fermi*-LAT data don't reach 150 GeV, which is the minimum threshold where MSTs have an optimized sensitivity.

4.5 Generate and simulate data

4.5.1 Simulation of CTAO datasets and joint fit with Fermi-LAT data

To simulate CTAO datasets, the necessary observational parameters were defined: the duration of the observation, the integration radius of the source, fixed at 0.11 deg, the offset, fixed at 0.5 deg, the reconstructed energy range, from 30 GeV to 10 TeV, the true energy range, from 10 GeV to 15 TeV, and the spectral model. The integration radius defines the angular region around the source position used to extract signal events and is chosen to optimize the signal-to-background ratio. The offset is the angular distance between the source position and the telescope pointing direction. During Cherenkov observations, sources are typically observed at a non-zero offset to allow a simultaneous and unbiased estimation of the background from the same field of view.

The spectral model used to simulate the CTAO datasets was the best-fit model obtained from the LAT analysis, including absorption by the extragalactic background light (EBL). This choice ensures spectral continuity between the LAT and CTAO energy ranges and allows the simulated CTAO data to extend the observed γ-ray spectrum toward higher energies. Regarding the observation duration, different livetimes were considered depending on the scientific goal of the simulation. The livetime was progressively increased to determine the minimum exposure required for a significant detection ($\sqrt{TS} \geq 5$) and for discriminating among different spectral models, except for a few cases reported in Tables 4.4 and 4.9. Another required parameter is the Instrument Response Function (IRF). Concerning the IRFs, the following were used:

– prod5 version v0.1[14] IRFs for the sources located in the Nothern Hemisphere.

[14] `https://zenodo.org/records/5499840`

In particular, the CTAO configurations composed by 4LSTs and by 4LSTs and 9MSTs, 20 deg zenith angle, azimuth-averaged pointing, optimized for 30 minutes and 5 hours of observation time were used;

– IRFs based on the prod3 version v3.0.0 [15]IRFs for the sources located in the Southern Hemisphere. In particular, the CTAO configurations composed by 14MSTs and by 14MSTs and 11Schwarzschild-Couder Telescopes (SCTs) in a scenario beyond the Alpha Configuration, 20 deg zenith angle, azimuth-averaged pointing, optimized for 50 hours of observation time were used.

After the CTAO dataset was correctly simulated, in order to fit both LAT and CTAO datasets, both of them were put in a single dataset and fitted using `gammapy`'s `Fit` function. After the fit, the new model parameters and the SED points were saved. Figure 4.10, Figure 4.11, and Figure 4.12 show the SEDs of the FSRQs of the sample with *Fermi*-LAT and simulated CTAO data fitted with the best fit `ExpCutoffPowerLaw3FGLSpectralModel`.

4.5.2 CTAO datasets fitting statistical approach for spectral models discrimination

To assess the capability of the different CTAO configurations to distinguish between different spectral models, this definition of test statistic (TS) was used:

$$TS = -2 \ln \lambda \tag{4.6}$$

where λ is:

$$\lambda = \frac{\mathcal{L}(\tilde{\mu}, \hat{\hat{b}}(\tilde{\mu}); \alpha | N_{ON}, N_{OFF})}{\mathcal{L}(\hat{\mu}, \hat{b}; \alpha | N_{ON}, N_{OFF})} \tag{4.7}$$

where $\tilde{\mu}$ is the expected number of counts in the null-hypothesis, $\hat{\hat{b}}$ is the maximization of the likelihood for fixed $\tilde{\mu}$, α is the ratio between the exposures of background and signal regions, N_{ON} are the counts from the source region, N_{OFF} are the counts from the background region in n energy bins, $\hat{\mu}$ and $\hat{b}$ are the maximum-likelihood estimators. In the numerator, the likelihood is maximized by $\hat{\hat{b}}$ for fixed $\tilde{\mu}$, while in the denominator it is maximized for μ, the expected number of counts in the alternative hypothesis, and b, the expected background counts. To calculate the maximum-likelihood in the denominator, a one-dimensional single on-off dataset is needed (see [234] and [235]), which is given by `SpectrumDatasetOnOff` of `gammapy` that is required to simulate CTAO data. Hence, this statistical approach was applied to the CTAO datasets only. A similar method was employed in [234] in the case of axion-like particle searches. In our study, the hypotheses are:

– The "null-hypothesis" is our FSRQs flaring periods have an SED with a spectral shape of an `ExpCutoffPowerLaw3FGLSpectralModel`;

– The "alternative hypothesis" is our FSRQs flaring periods have an SED with a spectral shape of one of the other models explained in 4.3.

Hence, in order to consider the "alternative hypotheses", all the LAT datasets were fitted with the LP model, the BPL model, and the PL-LP model, and the best-fit

[15] `https://zenodo.org/records/5163273`

parameters for each of them were saved. Then, the best-fit parameters were used to simulate the CTAO datasets with a spectral shape different from a power law with exponential cut-off.

Next, all the datasets were fitted using an`ExpCutoffPowerLaw3FGLSpectralModel` with the reference energy fixed at 0.5 GeV, 1 GeV or 1.5 GeV depending on the reference energy of the FSRQ in the 4FGL-DR4 catalog. After the fit, $-2\ln\mathcal{L}$ was retrieved, where $\mathcal{L}$ is the likelihood obtained during the fitting procedure. This likelihood represents the likelihood in the numerator of the Equation 4.7.

The `wstat` formula[16] implemented in `gammapy` through the function `wstat` was used to obtain the likelihood in the denominator. The `wstat` formula defines the likelihood using the number of counts in the ON region n_{ON}, which contains signal and background contributions, and in the OFF region n_{OFF}, which contains background only, the parameter α, that is the ratio of the ON and OFF region acceptances, and the number of expected signal and background counts in the ON region $\mu_{sig} = n_{ON} - \alpha n_{OFF}$ and $\mu_{bkg} = \alpha n_{OFF}$.

Given the two likelihoods, the test TS was calculated as presented in Equation 4.6. This fitting procedure was repeated to retrieve the TS 200 times for each livetime, each IRF, each spectral model, and each source. Given the 200 TS, the cumulative distribution of the TS in the "null-hypothesis" case was plotted, and compared with the average value of the TS in the "alternative hypothesis" for each spectral model, each livetime, and each CTAO configuration. From the comparison, to have a significance level that defines the capability of CTAO to distinguish between 2 spectral models, the p-value was extracted as:

$$p - value = \sum_{i=0}^{n} (TS_{ECPL,n} > TS_{average})/n \tag{4.8}$$

where $TS_{ECPL,n}$ is the n-th TS value in our "null-hypothesis" case, $TS_{average}$ is the average TS in one of the "alternative hypothesis" and n is the number of simulations equal to 200.

I want to highlight that this statistical approach is not part of the paper, but was part of the process that led to the following statistical approach, which is included in the publication.

4.5.3 Statistical approach for spectral models discrimination with *Fermi*-LAT and CTAO datasets

We employed another statistical approach based on the likelihood-ratio test (LRT).

The definition of the likelihood function depends on the type of dataset. For the *Fermi*-LAT datasets, a Poissonian likelihood is used:

$$\mathcal{L}_{Fermi}(m|n) = \prod_{i,k} e^{-m_{i,k}} \frac{m_{i,k}}{n_{i,k}!} \tag{4.9}$$

where the indices run over both spectral and spatial bins, $m_{i,k}$ are the expected counts in bin (i, k) under the assumed model (including both signal and background),

[16] `https://docs.gammapy.org/dev/user-guide/stats/wstat_derivation.html`

and $n_{i,k}$ are the observed counts. On the other hand, for ON-OFF spectral datasets such as those simulated for CTAO, the likelihood function is given by:

$$\mathcal{L}_{\rm CTAO}(\mu, b|n_{\rm ON}, n_{\rm OFF}) = \prod_i \frac{(\mu_i + \alpha\, b_i)^{n_{{\rm ON},i}}}{n_{{\rm ON},i}!} \\ e^{-(\mu_i+\alpha\, b_i)} \frac{b_i^{n_{{\rm OFF},i}}}{n_{{\rm OFF},i}!} e^{-b_i} \tag{4.10}$$

where the index runs over energy bins only, μ_i is the number of expected signal counts in the ON region in bin i, b_i is the number of expected counts in all OFF regions, while $n_{{\rm ON},i}$ and $n_{{\rm OFF},i}$ are the corresponding observed counts.

The joint likelihood is then given by:

$$\mathcal{L} = \mathcal{L}_{Fermi} \times \mathcal{L}_{\rm CTAO}\,. \tag{4.11}$$

When fitting a spectral model to the observed data, its free parameters are varied so that the expected counts $\hat{\mu}$ and $\hat{b}$ maximize the likelihood function. In practice, it is often preferable to minimize the quantity $-2\ln\mathcal{L}$, which for Equation (4.9) corresponds to the Cash statistics [70]:

$$C = 2\sum_{i,k}(m_{i,k} - n_{i,k}\ln m_{i,k})\,, \tag{4.12}$$

while for eq. (4.10) gives the WSTAT function:

$$\mathrm{WSTAT} = 2\sum_i [\mu_i + (\alpha+1)b_i \\ -n_{{\rm ON},i}\ln(\mu_i + \alpha b_i) - n_{{\rm OFF},i}\ln b_i]\,. \tag{4.13}$$

In both above expressions, terms that do not depend on μ and b have been neglected.

For a joint dataset D with counts $(n, n_{\rm ON}, n_{\rm OFF})$, the test statistic is defined as:

$$\mathrm{TS} = -2\ln\frac{\mathcal{L}_{\rm LP}(D)}{\hat{\mathcal{L}}(D)}\,, \tag{4.14}$$

where $\mathcal{L}_{\rm LP}$ is the maximum likelihood obtained for an LP spectral shape, which corresponds to our null hypothesis and to the spectral shape our FSRQs have in the 4FGL-DR4 catalog, while $\hat{\mathcal{L}}$ is the analytical maximum of the likelihood function. The latter is obtained by maximizing the product of Equations (4.9) and (4.10), or equivalently, minimizing the sum of Equations (4.12) and (4.13), with respect to (m, μ, b), which is done by setting:

$$m_i = n_i \tag{4.15}$$

and

$$\mu_i = n_{{\rm ON},i} - \alpha n_{{\rm OFF},i}\,, \quad b_i = n_{{\rm OFF},i}\,. \tag{4.16}$$

A similar method was applied in [235] to the case of axion-like particle searches.

In order to test the hypotheses of alternative models, all the LAT datasets were fitted with an ECPL model, a LP model, a BPL model, and a PL-LP model, and the best-fit parameters for each of them were saved. Then, they were used to simulate

CTAO observations, and for each joint dataset, the TS defined in Equation (4.14) was computed. For the likelihood in the numerator, all the datasets were fitted using as a spectral model an `LogParabolaSpectralModel` with general parameters free to vary, unless the reference energy, which was fixed depending on the reference energy of the FSRQ in the 4FGL-DR4 catalog. After the fit, the $-2\ln\mathcal{L}$ value was retrieved.

This fitting procedure was repeated to compute the TS 200 times for each livetime, each IRF, each spectral model, and each source. Then, the $\Delta TS_i = TS_{alt,i} - TS_{LP,i}$ was computed, where i goes from 1 to 200. A negative ΔTS_i indicates that the alternative model provides a better fit than the LAT catalog model for that specific simulation. To have a confidence level at which CTAO would be able to distinguish between the null-hypothesis and an alternative spectral model, p-value as [158]:

$$p = \frac{\sum_{i=0}^{N}(\Delta TS \leq 0)}{N} \tag{4.17}$$

where $N = 200$. Using $\Delta TS \leq 0$ means that the alternative model is systematically fitting better than the LP model, so the $TS_{alt,i}$ are smaller than the $TS_{LP,i}$. In this case, to interpret the p-values, there are 3 possibilities:

- if all or mostly the ΔTS are smaller than 0, the p-value would be equal or close to 1. This means that the alternative model outperforms the catalog model, LP, and systematically gives a better fit. So the 2 models are perfectly distinguished by CTAO;
- if all or mostly the ΔTS are larger than 0, the p-value would be equal or close to 0 means that the catalog model, LP, model always wins. So the 2 models are perfectly distinguished by CTAO;
- in the intermediate case, p-values are around 0.5 and correspond to a situation where ΔTS is equally likely to be positive or negative, indicating that the two models cannot be statistically distinguished given the available simulations.

4.6 Results

In this Section, the important results obtained from the fitting procedure and statistical approach for model comparison are summarized, with a deeper focus on the Northern sources.

4.6.1 Detection of the flaring states

From the fitting of the LAT and CTAO joint datasets, the TS for the detection of each "rising flare" and "decaying flare" was retrieved for each source. Since the goal is to know when CTAO's different configurations can detect these flaring episodes, the simulations started to simulate CTAO data with a livetime of 30 minutes, and increased it by 30 minutes in each simulation until 2 hours of observation were reached. If in 2 hours of observation, after the joint fit, the source has not been detected with a $\sqrt{TS} \geq 5$, the livetime was increased by 1 hour until 5 hours of observation were reached, which is less than 1 night. This procedure was done 100 times for each "rising flare" and "decaying flare" of each source, for each livetime,

Table 4.4: TS of the "rising flare" and "decaying flare" periods of each source for 2 configurations of CTAO and 2 livetimes.

Source	Flaring period	4LSTs $\sqrt{TS}$ 30 min	4LSTs + 9MSTs $\sqrt{TS}$ 30 min	4LSTs $\sqrt{TS}$ 2 h	4LSTs + 9MSTs $\sqrt{TS}$ 2 h
PKS 0736+01	rising	17.86 ± 1.09	17.82 ± 1.13	35.71 ± 1.11	35.63 ± 1.14
	decaying	3.63 ± 1.11	3.92 ± 0.97	7.62 ± 1.12	7.56 ± 1.11
PKS 1222+216	rising	48.4 ± 1.03	50.26 ± 1.11	97.06 ± 1.16	100.59 ± 1.18
	decaying	10.41 ± 1.13	10.88 ± 1.17	21.07 ± 1.05	21.73 ± 1.06
Ton 599	rising	9.62 ± 1.19	9.69 ± 1.15	19.53 ± 1.12	19.51 ± 1.03
	decaying	67.57 ± 1.14	70.13 ± 1.13	135.26 ± 1.1	140.5 ± 1.06
OP 313	rising	58.49 ± 1.17	59.55 ± 1.22	117.11 ± 1.13	119.11 ± 1.11
	decaying	59.74 ± 1.2	61.46 ± 1.22	119.79 ± 1.09	122.97 ± 1.03
PKS 1502+106	rising	13.74 ± 1.13	13.79 ± 1.14	27.51 ± 1.04	27.54 ± 1.08
	decaying	5.05 ± 1.08	5 ± 1.06	10.19 ± 1.08	10.09 ± 1.11

for each one of the 4 CTAO configurations reported in Section 4.5.1. The resulting TSs reported here are the mean of the 100 values obtained from 100 simulated and jointly fitted datasets. Table 4.4 reports the results for the Northern sources, while Figure 4.13 and 4.14 shows a plot that reports the mean TS of flaring episode as a function of different livetimes for the 2 configurations of CTAO North: 4LSTs and 4LSTs and 9MSTs.

Looking at Table 4.4, it is clear that the flaring activity, both in the rising and decaying period, of the FSRQs in the Northern Hemisphere is detected after 30 minutes. To explain these high TS values, also in high-redshift blazars like PKS 1502+106, it is fundamental to consider that the LAT data are integrated over the total duration of the "rising flare" or "decaying flare", which can last several days. Hence, the LAT model parameters that are used to simulate the CTAO datasets consider the integrated spectra in these periods of time, which could lead to higher fluxes than a future real-case scenario where researchers consider day-by-day or night-by-night LAT and CTAO observations. This could not happen to a less intense flare or quiescent FSRQs, which could possibly not be detected by CTAO due to the low flux or low energy or both of them in a high-redshift source where the EBL plays a huge role in the absorption of γ-ray photons [155]. However, these kinds of results could be helpful for studies that consider data taken over the whole flaring period for SED modeling or long-term studies.

The main result that is shown in Table 4.4 is that the $\sqrt{TS}$ values of the 4LSTs configuration are comparable, within the error, with the $\sqrt{TS}$ in the 4LSTs+9MSTs case. This means that the sensitivity of the 4LSTs is enough to detect the flaring activity of FSRQs at different redshifts, and adding the MSTs is not contributing to their detection. In future observation plans, it would be possible to use the 4LSTs to observe the flaring activity of FSRQs and point the 9MSTs to other targets of interest.

4.6.2 Spectral parameters estimation

From the fitting of the LAT data, the error on the cut-off energy ($\Delta E_{cutoffFermi}$) was retrieved. The error on the cut-off energy was also retrieved from the joint fit of the LAT and CTAO data ($\Delta E_{cutoffFermi+CTAO}$). From these two errors, the error

Table 4.5: Error ratio of the "rising flare" and "decaying flare" periods of each source for 2 configurations of CTAO and 2 livetimes.

Source	Flaring period	4LSTs ΔE 30 min	4LSTs + 9MSTs ΔE 30 min	4LSTs ΔE 2 h	4LSTs + 9MSTs ΔE 2 h
PKS 0736+01	rising	0.21 ± 0.03	0.20 ± 0.02	0.16 ± 0.02	0.15 ± 0.01
	decaying	0.25 ± 0.03	0.26 ± 0.03	0.2 ± 0.02	0.2 ± 0.02
PKS 1222+216	rising	0.23 ± 0.01	0.21 ± 0.01	0.16 ± 0.01	0.14 ± 0.01
	decaying	0.43 ± 0.06	0.41 ± 0.05	0.29 ± 0.02	0.27 ± 0.02
Ton 599	rising	0.28 ± 0.02	0.28 ± 0.02	0.23 ± 0.01	0.23 ± 0.01
	decaying	0.12 ± 0.01	0.1 ± 0.01	0.06 ± 0.01	0.05 ± 0.01
OP 313	rising	0.26 ± 0.02	0.23 ± 0.01	0.16 ± 0.01	0.14 ± 0.01
	decaying	0.17 ± 0.01	0.15 ± 0.01	0.09 ± 0.01	0.08 ± 0.01
PKS 1502+106	rising	0.33 ± 0.03	0.33 ± 0.03	0.27 ± 0.02	0.27 ± 0.02
	decaying	0.65 ± 0.06	0.64 ± 0.05	0.43 ± 0.02	0.43 ± 0.02

ratio was calculated as:

$$\Delta E = \frac{\Delta E_{cutoffFermi+CTAO}}{\Delta E_{cutoffFermi}} \tag{4.18}$$

This quantity was calculated for each flaring period, each source, each configuration, and each livetime, and it is useful to quantify the improvement on the spectral energy parameters estimation using CTAO data instead of LAT data only. The resulting error ratios reported here are the mean of the 100 values obtained from 100 simulated and jointly fitted datasets. Table 4.5 reports the results for the Northern sources, while Figure 4.15 and 4.16 show plots that report the mean error ratios of a flaring episode as a function of different livetimes for the 2 configurations of CTAO North: 4LSTs and 4LSTs and 9MSTs.

Table 4.5 shows that the use of CTAO's both configurations improves the estimation of the error on the spectral energy cut-off than using LAT only. The $\Delta E_{cutoffFermi+CTAO}$ are $30\%-70\%$ smaller than the $\Delta E_{cutoffFermi}$ after 30 minutes of observation and $60\%-90\%$ smaller after 2 hours of observation. This is an indication of how much CTAO can improve the determination of the spectral parameters of flaring FSRQs. This also means that the use of CTAO can improve of $30\%-70\%$ the reconstruction of the high-energy shape of FSRQ's SEDs after 30 minutes of observation for Northern sources. As in Section 4.6.1, the error ratios obtained for 4LSTs are comparable within the errors with the one obtained using 4LSTs+9MSTs. This means that LSTs are powerful telescopes to detect these sources, and adding MSTs does not give a large contribution to the spectral parameters estimations and cut-off shape reconstruction since FSRQs do not reach energies at which the MSTs have good sensitivity.

4.6.3 Spectral models comparison fitting CTAO datasets only

The results reported in this section are not part of the paper, but are important to understand the process that led to the following section's results.

Using the statistical approach shown in 4.5.2, different physically justified spectral models were compared to obtain an estimation of when the different configurations of CTAO can distinguish between 2 of them for each flaring period. In particular, the null-hypothesis that was used is the `ExpCutoffPowerLaw3FGLSpectralModel`, and as an alternative hypothesis, one of the other. Since the goal is to obtain

the number of hours required by CTAO's configuration to distinguish between the models, different livetimes were used starting from 1 hour and adding 1 hour until reaching 14 hours, which is close to 2 nights of observation. The simulations stopped when the calculated p-value was $\lesssim 0.05$. This means there's a low probability (less than 5%) that the observed results occurred by random chance. In Table 4.6 and Table 4.7, the results for the Northern sources are reported. In Figure 4.17, the cumulative distribution of the TS in the null-hypothesis case, in blue, is shown versus the TS values obtained in the fitting process for the "decaying flare" of Ton 599. The red dashed line shows the average TS value obtained by fitting the "decaying flare" of Ton 599 with an LP model. This plot was obtained using 1 hour livetime and the 4LSTs+9MSTs configuration.

From Table 4.6 and Table 4.7, it is clear that both configurations of CTAO can distinguish between different spectral models in the "rising flare" for low and intermediate-redshift of our FSRQs after a few hours of observation. On the other hand, this is not true for the "decaying flare" of these sources, where, after 14 hours of observation, it is not always possible to separate the null-hypothesis from the alternative one, as the large p-values indicate, except for Ton 599. For the high-redshift FSRQs, it is not possible to discriminate between the different models, except for the ECPL and BPL in OP 313. Another interesting result is the ability of 4LSTs to distinguish between the spectral models after the same time of observation or just after one or two hours more than the 4LSTs+9MSTs configuration. This suggests the possibility of pointing MSTs to another target during the observation of a FSRQ in a flaring state.

This inability to discriminate between different spectral models after 14 hours of observation is attributed to the presence of upper limits in the CTAO flux points. As shown in Figure 4.11(a), another explanation is that the shape of the CTAO SED itself can be well fitted by the different spectral models.

A solution to this issue for a future project could be fitting both datasets, LAT and CTAO (see section 4.6.4), and retrieving the p-values or using a Bayesian approach.

4.6.4 Spectral models comparison fitting the joint datasets

Using the statistical approach shown in 4.5.3, different physically justified spectral models were compared to obtain an estimation of when the different configurations of CTAO can distinguish between two of them for each flaring period. In particular, as the null-hypothesis was used the `LogParabolaSpectralModel`, which is the model our sources have in the 4FGL catalog, and as the alternative hypothesis, one of the other models. Since the goal is to obtain the number of hours required by CTAO's configuration to distinguish between the models, different livetimes were used, starting from 1 hour and adding 1 hour until reaching 14 hours, which is close to 2 nights of observation. The simulations were stopped when the calculated p-value was $\lesssim 0.05$ or $\gtrsim 0.95$. In both cases, this means there's a low probability that the observed results occurred by random chance. In Table 4.8, the results for the Northern sources 4LSTs are reported. The results of the 4LSTs+9MSTs are in line with those of 4LSTs, so they are not reported. This suggests the possibility of pointing MSTs to another target during the observation of a FSRQ in a flaring state. In Figure 4.18, the distribution of the test statistic difference $\Delta TS_i = TS_{alt,i} - TS_{LP,i}$ is shown for $N = 200$ simulations. The shaded red area marks the fraction of

Table 4.6: CTAO's configurations required hours to distinguish between an ECPL model and the models reported in the fourth column for different flaring periods of different sources located in the Northern Hemisphere.

Source	Flaring period	Configuration	Spectral model	Livetime(h)	p-value
PKS 0736+01	rising	4LSTs	LP	1	0.025
			BPL	1	0.05
			PL+LP	2	0.01
		4LSTs+9MSTs	LP	2	0.055
			BPL	1	0.005
			PL+LP	1	0.005
	decaying	4LSTs	LP	14	0.365
			BPL	14	0.42
			PL+LP	14	0.38
		4LSTs+9MSTs	LP	14	0.375
			BPL	14	0.41
			PL+LP	14	0.36
PKS 1222+216	rising	4LSTs	LP	3	0.01
			BPL	4	0.005
			PL+LP	2	0.025
		4LSTs+9MSTs	LP	2	0.035
			BPL	3	0.01
			PL+LP	1	0.04
	decaying	4LSTs	LP	14	0.225
			BPL	14	0.2
			PL+LP	14	0.2
		4LSTs+9MSTs	LP	14	0.29
			BPL	14	0.175
			PL+LP	14	0.165
Ton 599	rising	4LSTs	LP	2	0.035
			BPL	3	0.02
			PL+LP	8	0.03
		4LSTs+9MSTs	LP	1	0.055
			BPL	2	0.065
			PL+LP	6	0.015
	decaying	4LSTs	LP	3	0.05
			BPL	2	0.04
			PL+LP	1	0.035
		4LSTs+9MSTs	LP	1	0.01
			BPL	2	0.015
			PL+LP	1	0.03

Table 4.7: CTAO's configurations required hours to distinguish between an ECPL model and the models reported in the fourth column for different flaring periods of the high-redshift sources located in the Northern Hemisphere.

Source	Flaring period	Configuration	Spectral model	Livetime	p-value
OP 313	rising	4LSTs	LP	14	0.28
			BPL	14	0.445
			PL+LP	14	0.2
		4LSTs+9MSTs	LP	14	0.32
			BPL	6	0.02
			PL+LP	14	0.255
	decaying	4LSTs	LP	14	0.355
			BPL	1	0.005
			PL+LP	14	0.16
		4LSTs+9MSTs	LP	14	0.385
			BPL	1	0.001
			PL+LP	14	0.11
PKS 1502+106	rising	4LSTs	LP	14	0.42
			BPL	14	0.445
			PL+LP	14	0.42
		4LSTs+9MSTs	LP	14	0.37
			BPL	14	0.44
			PL+LP	14	0.385
	decaying	4LSTs	LP	14	0.485
			BPL	14	0.475
			PL+LP	14	0.455
		4LSTs+9MSTs	LP	14	0.515
			BPL	14	0.515
			PL+LP	14	0.5

simulations with $\Delta TS \leq 0$, which corresponds to the empirical p-value. Small p-values, $p \leq 0.05$, indicate that the catalog (null-hypothesis) model provides a significantly better fit, while values close to unity imply that the alternative model systematically yields a better fit. Intermediate values around 0.5 reflect the case where the two models cannot be statistically distinguished. This histogram shows the result obtained in the fitting process for the "decaying flare" of Ton 599 using 1 hour livetime and the 4LSTs configuration.

From Table 4.8, it is clear that CTAO can not distinguish between spectral models in all our sample. In particular, CTAO can not distinguish between different spectral models for the low-redshift FSRQ PKS 0736+01 and the high-redshift Ton 599, except for the ECPL versus LP case in the 'decaying flare" part. On the other hand, regarding PKS 1222+216, in both 'rising flare" and 'decaying flare" the LP model is disfavored in favor of the BPL and PL-LP models, while, compared with the ECPL, the LP is still favored. For OP 313, in the 'rising flare" part, the LP is disfavored, same in the 'decaying flare" part of PKS 1502+106. Even if the CTAO data were simulated using the preferred 4FGL catalog model, it is not always preferred the LP model when jointly fitting the datasets. This is due to the bad sensitivity of Fermi-LAT data, which does not allow a good statistical model discrimination at high energies. Nevertheless, adding CTAO data led to better parameter estimations and better spectral shape reconstruction. These results indicate that adding CTAO data to the SED could improve model selection. With a better reconstruction of the SED shape, researchers could obtain information about the distribution of the primary particles.

A possible future approach is to compare the new favored models to find the best one or use a Bayesian approach.

Furthermore, the joint *Fermi*-LAT and CTAO spectral analyses presented in this section are based on *Fermi*-LAT datasets integrated over time intervals longer than the simulated CTAO exposures. This approach is justified in the context of this chapter, as the main goal is to assess the capability of CTAO to reconstruct and discriminate different spectral shapes when combined with *Fermi*-LAT data.

However, in real case scenarios, the strong flux and spectral variability of blazars make simultaneity between space-based and ground-based observations fundamental. Joint *Fermi*-LAT and CTAO analyses will rely on quasi-simultaneous datasets with comparable exposure times. In such cases, the reduced photon statistics of the *Fermi*-LAT data may limit the achievable spectral reconstruction and the power of model discrimination, especially at the highest energies. Therefore, the results presented here should be interpreted as an optimistic upper limit on the spectral discrimination capabilities achievable by CTAO when combined with long-term *Fermi*-LAT observations, rather than as a direct representation of standard future observing strategies.

4.6.5 SCT results for Southern sources

Regarding Southern Hemisphere sources, the same approaches presented in Section 4.6.1, 4.6.2, and 4.6.4 were applied.

In Table 4.9, the $\sqrt{TS}$ values are reported for the three flaring periods. Figure 4.19 shows the $\sqrt{TS}$ versus livetime plots for the three Southern sources. Since the $\sqrt{TS}$

Table 4.8: CTAO's 4LSTs configuration required hours to distinguish between an LP model and the models reported in the fourth column for different flaring periods of different sources located in the Northern Hemisphere.

Source	Flaring period	Spectral model	Livetime(h)	p-value
PKS 0736+01	rising	ECPL	14	0.4
		BPL	14	0.535
		PL+LP	14	0.52
	decaying	ECPL	14	0.585
		BPL	14	0.695
		PL+LP	14	0.705
PKS 1222+216	rising	ECPL	1	0.001
		BPL	1	1
		PL+LP	1	0.995
	decaying	ECPL	14	0.215
		BPL	1	0.98
		PL+LP	1	0.965
Ton 599	rising	ECPL	14	0.3
		BPL	14	0.16
		PL+LP	14	0.37
	decaying	ECPL	1	0.03
		BPL	14	0.475
		PL+LP	14	0.7
OP 313	rising	ECPL	1	0.99
		BPL	14	0.86
		PL+LP	1	0.975
	decaying	ECPL	14	0.14
		BPL	14	0.195
		PL+LP	14	0.085
PKS 1502+106	rising	ECPL	14	0.06
		BPL	14	0.65
		PL+LP	14	0.71
	decaying	ECPL	14	0.875
		BPL	1	1.0
		PL+LP	1	1.0

of PKS 1510-089 and 3C 279 after 2 hours was lower than 5, the simulations were executed until a lifetime of 5 hours was reached. For Southern sources, adding 11SCTs to the configuration leads to higher $\sqrt{TS}$ values after a few hours of observation. In particular, the improvement of using 14MSTs + 11SCTs is $30-35\%$ after 2 hours of observations and $32-35\%$ after 5 hours of observations, compared to using just 14MSTs. Similar results are reported in Table 4.10 and Figure 4.20. The error ratio shows that using CTAO South for flaring FSRQs helps to have smaller errors on the spectral cut-off parameters, so this means a better reconstruction of the shape of the SED cut-off area. In particular, the $\Delta E_{cutoffFermi+CTAO}$ are $39\%-63\%$ smaller for 14MSTs + 11SCTs, and $22\%-78\%$ fo 14MSTs compared to the $\Delta E_{cutoffFermi}$ after 2 hours of observation, and $22\%-78\%$ smaller for 14MSTs + 11SCTs and $39\%-82\%$ smaller for 14MSTs after 5 hours of observation. Furthermore, the configuration with 14MSTs + 11SCTs, shows smaller error ratios than the 14MSTs configuration: the error ratios of 14MSTs + 11SCTs are $19\%-33\%$ smaller than 14MSTs.

Regarding the model comparison, unfortunately, when CTAO data only are fitted, it is not possible to distinguish between different models in PKS 1510-089 (see Table 4.11). This was expected since there is no sign of emission above 100 GeV, so MSTs and SCTs do not have enough sensitivity to detect the source. So, for this source, the simulations were stopped after 5 hours of livetime. For the other sources, 3C 279 and PKS 0346-27, CTAO's 14MSTs + 11SCTs can distinguish between different spectral models in mainly all cases.

Regarding the model comparison using the joint datasets, unfortunately, it is not possible to distinguish between different models in the PKS 1510-089 case (see Table 4.12), except in the "decaying flare" part when the ECPL and LP models were compared. This was expected for the same reasons explained above. So, for this source, the simulations were stopped after 5 hours of livetime. For the other sources, 3C 279 and PKS 0346-27, CTAO's 14MSTs + 11SCTs can distinguish between different spectral models, except for the PL+LP model "decaying flare" of 3C 279, the BPL in the "rising flare" of 3C 279, and the ECPL in both flaring periods of PKS 0346-27. Nevertheless, using CTAO can still improve model selection over the use of LAT only.

As Figures 4.21(a) and 4.21(b) show, the $\sqrt{TS}$ and error ratios obtained by adding 11SCTs are similar to the value obtained by adding 11MSTs. The $\sqrt{TS}$ values of 14MSTs + 11SCTs configuration are $4\%-7\%$ larger than 25MSTs values, while the error ratios values of 14MSTs + 11SCTs are similar to the 25MSTs ones. These results were expected since SCTs are optimized for the observation of extended sources. Hence, the improvement in the detection of FSRQs and the better reconstruction of the spectral parameters is due to the addition of telescopes and not to the better performances of SCTs.

4.7 Summary

The highest LAT γ-ray flare of a sample of eight FSRQs using `gammapy` was analyzed. The sources are located in the Northern and Southern Hemispheres, allowing us to simulate CTAO data to compare different CTAO configurations: 4LSTs and by 4LSTs and 9MSTs for the Northern sources and 14MSTs and by 14MSTs and 11SCTs in a scenario beyond the CTAO Alpha Configuration for the Southern ones.

Table 4.9: TS of the "rising flare" and "decaying flare" periods of each Southern source for 2 configurations of CTAO and 2 livetimes.

Source	Flaring period	14MSTs $\sqrt{TS}$ 2 h	14MSTs + 11SCTs $\sqrt{TS}$ 2 h	14MSTs $\sqrt{TS}$ 5 h	14SCTs + 11MSTs $\sqrt{TS}$ 5 h
PKS 1510-089	rising	0.85 ± 1.16	1.09 ± 1.02	1.16 ± 1.11	1.85 ± 0.99
	decaying	3.03 ± 1.15	4.59 ± 1.06	4.94 ± 1.07	7.54 ± 1.09
3C 279	rising	4.49 ± 1.23	6.67 ± 1.06	7.13 ± 0.99	10.5 ± 1.01
	decaying	4.17 ± 1.13	6.4 ± 1.09	6.65 ± 1.03	10.26 ± 1.12
PKS 0346-27	rising	10.28 ± 1.16	14.49 ± 1.1	–	–
	decaying	7.14 ± 1.13	10.18 ± 1.06	–	–

Table 4.10: Error ratio of the "rising flare" and "decaying flare" periods of each Southern source for 2 configurations of CTAO and 2 livetimes. Since PKS 0346-27 shows a $\sqrt{TS} > 5$ after 2 hours of livetime, the simulations were not performed and the fitting until 5 hours of livetime.

Source	Flaring period	14MSTs ΔE 2 h	14MSTs + 11SCTs ΔE 2 h	14MSTs ΔE 5 h	14MSTs + 11SCTs ΔE 5 h
PKS 1510-089	rising	0.41 ± 0.06	0.32 ± 0.04	0.31 ± 0.04	0.23 ± 0.03
	decaying	0.32 ± 0.02	0.25 ± 0.01	0.22 ± 0.01	0.18 ± 0.01
3C 279	rising	0.36 ± 0.02	0.28 ± 0.01	0.25 ± 0.01	0.2 ± 0.01
	decaying	1.08 ± 0.02	0.88 ± 0.02	0.78 ± 0.02	0.61 ± 0.01
PKS 0346-27	rising	0.27 ± 0.01	0.22 ± 0.01	–	–
	decaying	0.32 ± 0.01	0.26 ± 0.01	–	–

From each simulation, the TS for the detection of the source was retrieved, the error ratio ΔE, and the p-value when different spectral models were compared.

For the Northern sources, it was shown that the addition of 9MSTs to the 4LSTs will not improve either the detection of the FSRQs nor the spectral parameter estimation nor the model discrimination. The performances of the LSTs are enough to perform spectral studies of the FSRQs. MSTs can be used to observe other scientific targets, while LSTs can be used to detect flaring activity by FSRQs seen by LAT.

For the Southern sources, it was shown that adding 11SCTs contributes to larger TS and better spectral parameter estimations. However, these results are comparable with those obtained by adding 11MSTs. These results were expected since SCTs are optimized for the observation of extended sources. A future possibility is to include 4LSTs in the Southern array. An analogous study of these sources with the addition of LSTs could be performed when the prod6 IRFs would be available. The same for an extended sources study with SCTs.

Regarding the model comparison, it is not always possible to distinguish between different spectral models. However, it was found that the null-hypothesis (LP model) is not always the favorite one, even if it is the favorite by the LAT 4FGL catalog. The better sensitivity of CTAO will determine the spectral shape of FSRQs and will find the spectral model that fits the SED.

The limitations of this study are:

- LAT and CTAO simultaneous datasets were not considered. The LAT datasets are integrated over the whole "rising flare" and "decaying flare" periods.
- We did not consider the Klein-Nishina regime or other physically motivated models ($\gamma\gamma$ absorption), which require adding spectral models to the `gammapy` source code.

Table 4.11: CTAO's configurations required hours to distinguish between an ECPL model and the models reported in the fourth column for different flaring periods of different sources located in the Southern Hemisphere.

Source	Flaring period	Configuration	Spectral model	Livetime(h)	p-value
PKS 1510-089	rising	14MSTs	LP	5	0.105
			BPL	5	0.37
			PL+LP	5	0.365
		14MSTs+11SCTs	LP	5	0.075
			BPL	5	0.36
			PL+LP	5	0.115
	decaying	14MSTs	LP	5	0.16
			BPL	5	0.235
			PL+LP	5	0.165
		14MSTs+11SCTs	LP	5	0.18
			BPL	5	0.175
			PL+LP	5	0.32
3C 279	rising	14MSTs	LP	3	0.03
			BPL	3	0.02
			PL+LP	5	0.08
		14MSTs+11SCTs	LP	2	0.005
			BPL	2	0.002
			PL+LP	2	0.005
	decaying	14MSTs	LP	14	0.370
			BPL	2	0.02
			PL+LP	14	0.385
		14MSTs+11SCTs	LP	14	0.14
			BPL	5	0.045
			PL+LP	14	0.315
PKS 0346-27	rising	14MSTs	LP	3	0.055
			BPL	1	0.05
			PL+LP	14	0.235
		14MSTs+11SCTs	LP	2	0.02
			BPL	3	0.045
			PL+LP	14	0.165
	decaying	14MSTs	LP	4	0.04
			BPL	5	0.01
			PL+LP	14	0.095
		14MSTs+11SCTs	LP	5	0.035
			BPL	4	0.03
			PL+LP	14	0.105

Table 4.12: CTAO's 14MSTs+11SCTs configuration required hours to distinguish between an ECPL model and the models reported in the fourth column for different flaring periods of different sources located in the Southern Hemisphere.

Source	Flaring period	Spectral model	Livetime(h)	p-value
PKS 1510-089	rising	ECPL	5	0.225
		BPL	5	0.725
		PL+LP	5	0.675
	decaying	ECPL	1	0.01
		BPL	5	0.86
		PL+LP	5	0.21
3C 279	rising	ECPL	1	0.001
		BPL	14	0.81
		PL+LP	1	0.975
	decaying	ECPL	1	0.985
		BPL	1	1.0
		PL+LP	14	0.245
PKS 0346-27	rising	ECPL	14	0.87
		BPL	1	0.995
		PL+LP	1	0.97
	decaying	ECPL	14	0.82
		BPL	1	0.995
		PL+LP	1	0.001

– It was not considered the 4LSTs in the Southern array and extended sources for the SCTs performances.

All these limitations could be addressed in a future study when prod6 IRFs would be available.

It is fundamental to notice that this study represents one of the first attempts to quantify the capability of different CTAO configurations to constrain the spectral shape and high-energy cut-off of flaring FSRQs through joint LAT and simulated CTAO observations. While several works have explored CTAO performances for steady sources or generic spectral shapes, a dedicated investigation focused on flaring states of FSRQs and on model discrimination has not been addressed in the literature so far.

The measurement of the spectral cut-off in the γ-ray band has important physical implications for blazar studies. The position and shape of the cut-off offer information on the maximum energy reached by the emitting particles, on the dominant cooling mechanisms, and on the scattering regime of inverse Compton emission.

In the case of FSRQs, improving constraints on the cut-off energy unravels the intrinsic curvature from absorption effects due to photon fields in the broad-line region or dusty torus, as well as from attenuation by the extragalactic background light or internal $\gamma - \gamma$ absorption within the source. Therefore, the enhanced sensitivity of CTAO above tens of GeV offers the possibility to probe the physical conditions in the emitting region and its location along the jet more effectively than currently possible with LAT alone.

In summary, the results presented in this chapter should be interpreted as an exploration of CTAO's potential for spectral-curvature and cut-off studies in flaring FSRQs. While they highlight the efficiency of LSTs for this particular goal in the Northern Hemisphere, they do not imply a reduced scientific relevance of MSTs within the broader CTAO science program, nor do they exclude their importance for alternative studies of blazars and other classes of γ-ray sources.

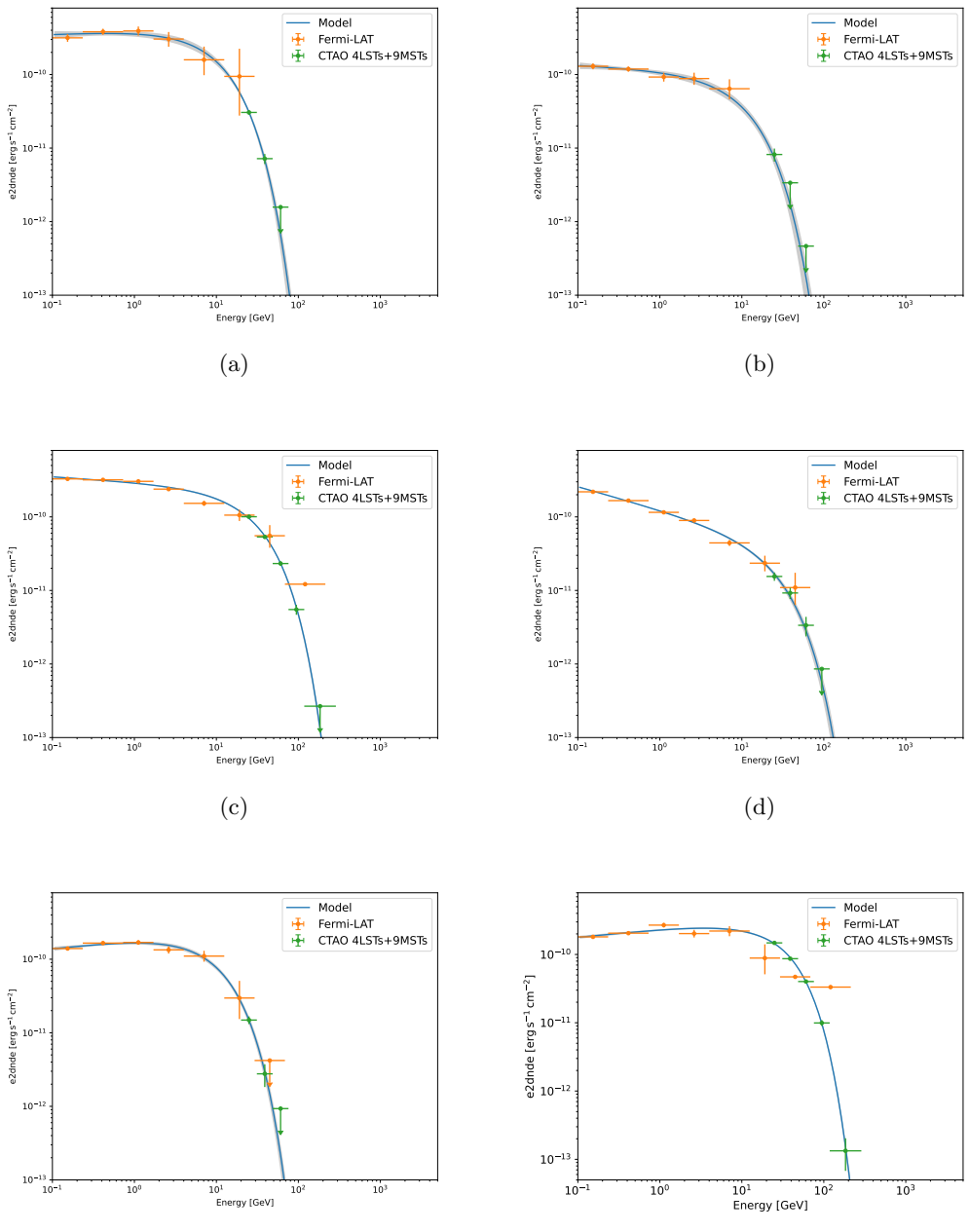

Figure 4.10: a) PKS 0736+01's "rising flare" SED with LAT and CTAO flux points. b) PKS 0736+01's "decaying flare" SED with LAT and CTAO flux points. c) PKS 1222+216's "rising flare" SED with LAT and CTAO flux points. d) PKS 1222+216's "decaying flare" SED with LAT and CTAO flux points. e) Ton 599's "rising flare" SED with LAT and CTAO flux points. f) Ton 599's "decaying flare" SED with LAT and CTAO flux points. The model used to fit the LAT is `gammapy`'s `ExpCutoffPowerLaw3FGLSpectralModel`. The IRF used to simulate the CTAO data is the prod5 with 4LSTs and 9MSTs. The solid blue line represents the fit, while the grey area is the butterfly area.

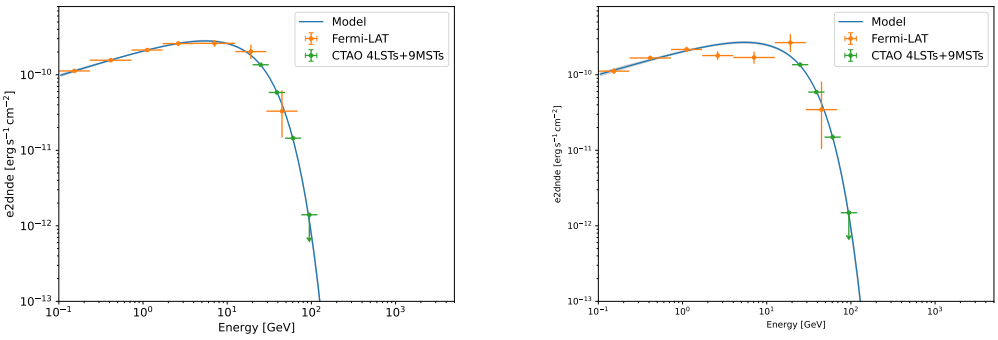

(a)

(b)

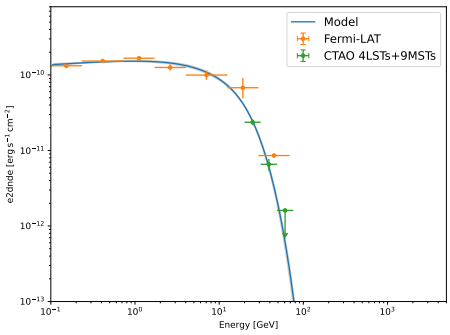

(c)

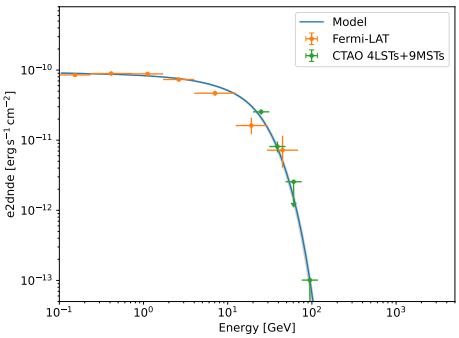

(d)

Figure 4.11: a) OP 313's "rising flare" SED with LAT and CTAO flux points. b) OP 313's "decaying flare" SED with LAT and CTAO flux points. c) PKS 1502+106's "rising flare" SED with LAT and CTAO flux points. d) PKS 1502+106's "decaying flare" SED with LAT and CTAO flux points. The model used to fit the LAT is `gammapy`'s `ExpCutoffPowerLaw3FGLSpectralModel`. The IRF used to simulate the CTAO data is the prod5 with 4LSTs and 9MSTs. The solid blue line represents the fit, while the grey area is the butterfly area.

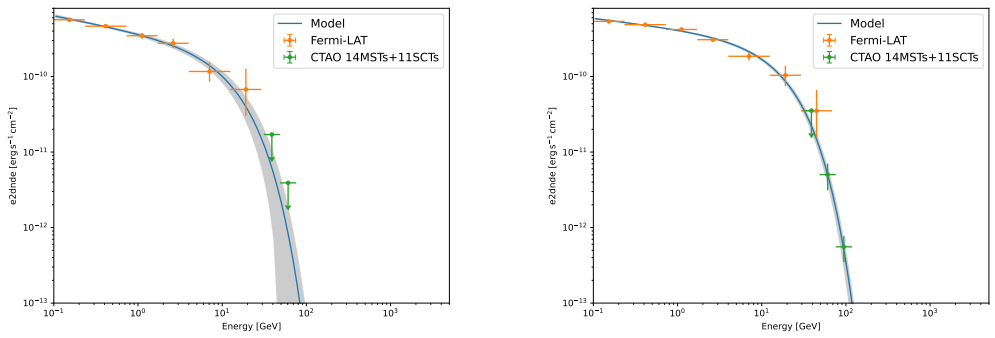

(a)

(b)

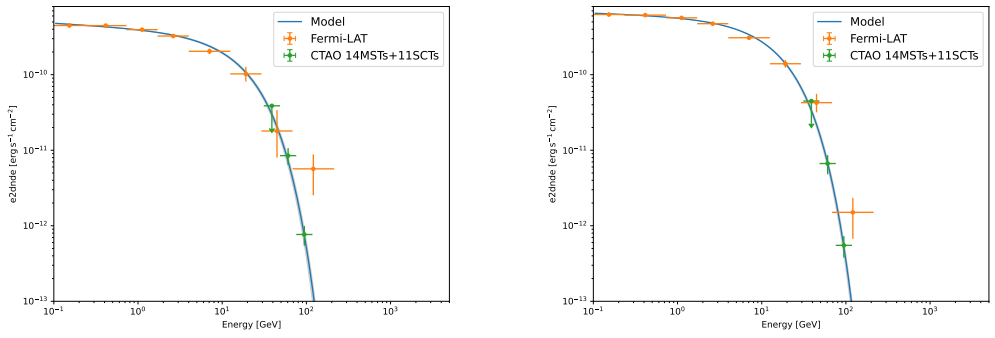

(c)

(d)

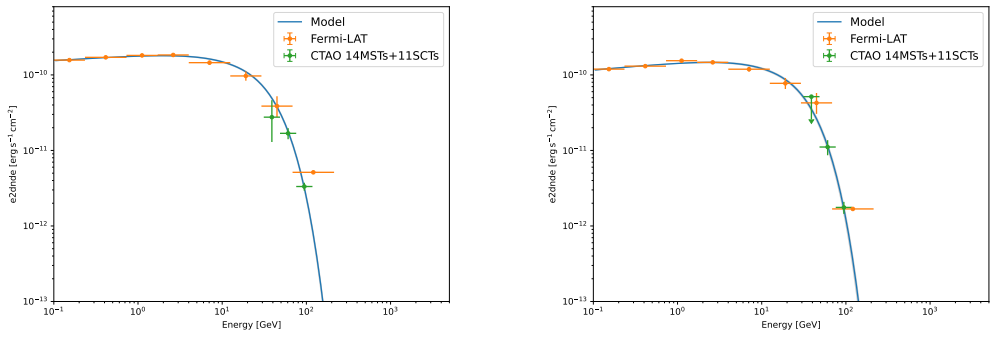

(e)

(f)

Figure 4.12: a) PKS 1510-089's "rising flare" SED with LAT and CTAO flux points. b) PKS 1510-089's "decaying flare" SED with LAT and CTAO flux points. c) 3C 279's "rising flare" SED with LAT and CTAO flux points. d) 3C 279's "decaying flare" SED with LAT and CTAO flux points. e) PKS 0346-27's "rising flare" SED with LAT and CTAO flux points. f) PKS 0346-27's "decaying flare" SED with LAT and CTAO flux points. The model used to fit the LAT and CTAO data is `gammapy`'s `ExpCutoffPowerLaw3FGLSpectralModel`. The IRF used to simulate the CTAO data is the prod3 with 11MSTs and 14SCTs. The solid blue line represents the fit, while the grey area is the butterfly area.

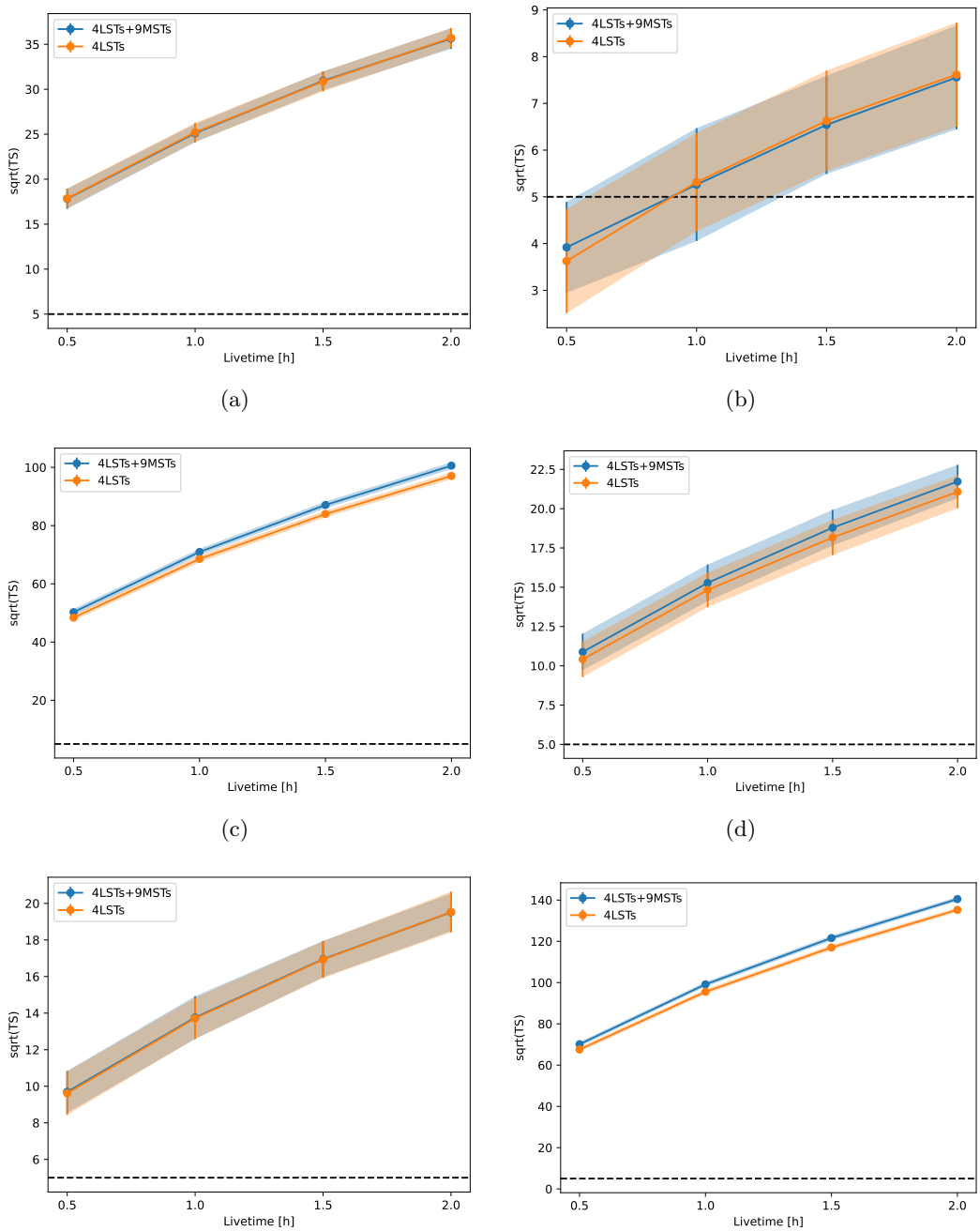

Figure 4.13: a) TS versus livetime of the "rising flare" period of PKS 0736+01. b) TS versus livetime of the "decaying flare" period of PKS 0736+01. c) TS versus livetime of the "rising flare" period of PKS 1222+216. d) TS versus livetime of the "decaying flare" period of PKS 1222+216. e) TS versus livetime of the "rising flare" period of Ton 599. f) TS versus livetime of the "decaying flare" period of Ton 599. The plots are made for 2 different configurations of CTAO: 4LSTs in orange and 4LSTs and 9MSTs in blue. The grey dashed line represents the $\sqrt{TS}$ above which the source is detected.

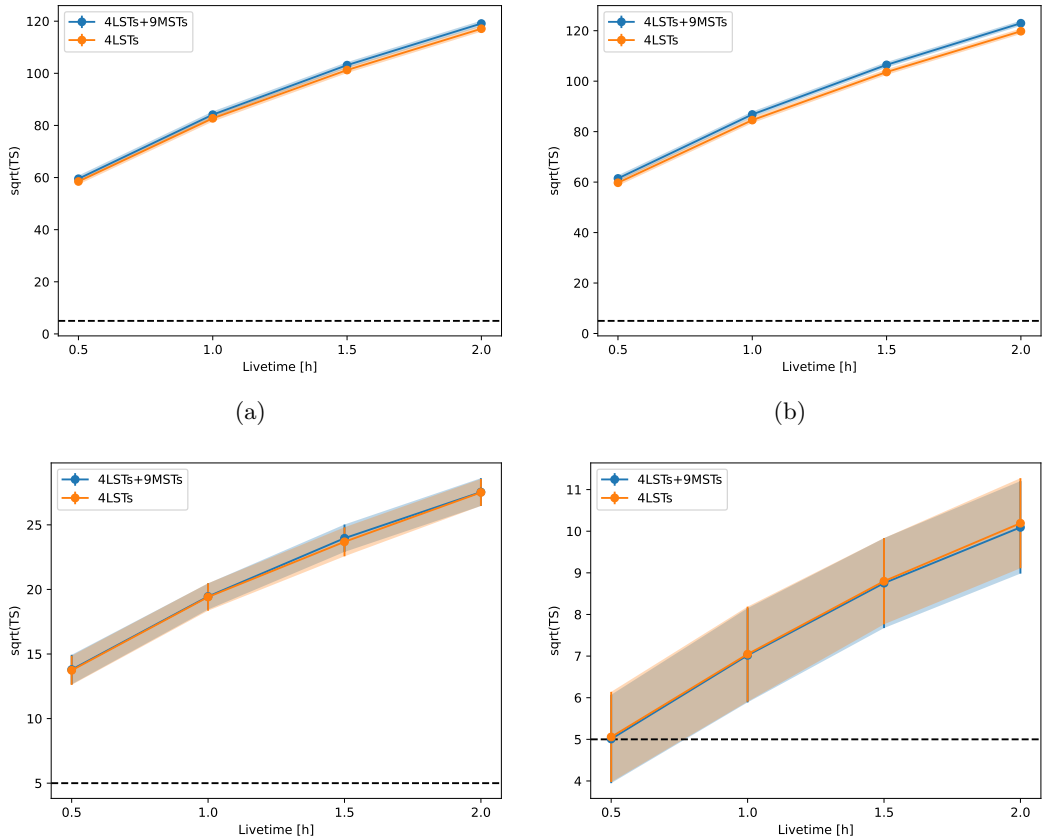

Figure 4.14: a) TS versus livetime of the "rising flare" period of OP 313. b) TS versus livetime of the "decaying flare" period of OP 313. c) TS versus livetime of the "rising flare" period of PKS 1502+106. d) TS versus livetime of the "decaying flare" period of PKS 1502+106. The plots are made for 2 different configurations of CTAO: 4LSTs in orange and 4LSTs and 9MSTs in blue. The grey dashed line represents the $\sqrt{TS}$ above which the source is detected

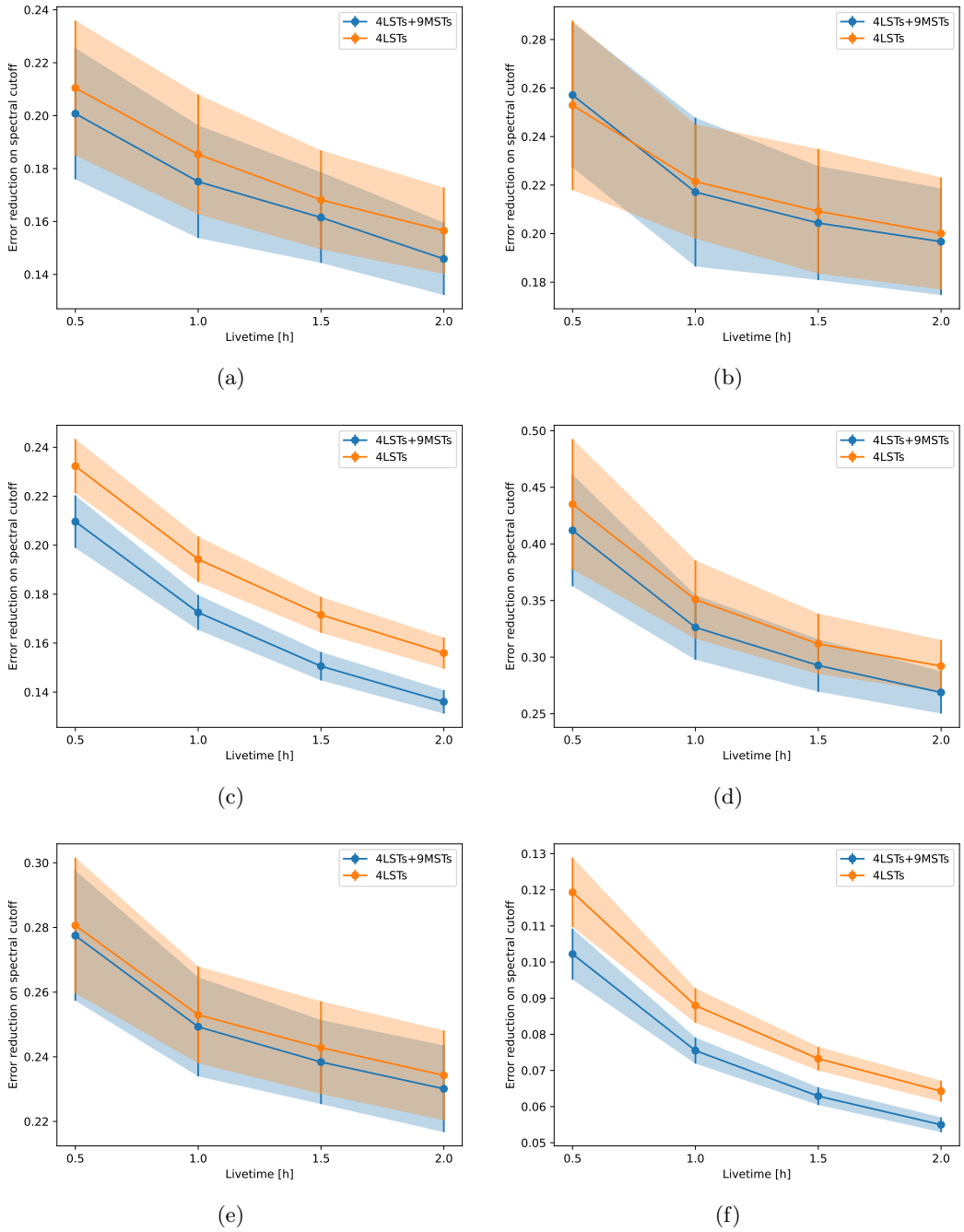

Figure 4.15: a) Error ratio versus livetime of the "rising flare" period of PKS 0736+01. b) Error ratio versus livetime of the "decaying flare" period of PKS 0736+01. c) Error ratio versus livetime of the "rising flare" period of PKS 1222+216. d) Error ratio versus livetime of the "decaying flare" period of PKS 1222+216. e) Error ratio versus livetime of the "rising flare" period of Ton 599. f) Error ratio versus livetime of the "decaying flare" period of Ton 599. The plots are made for 2 different configurations of CTAO: 4LSTs in orange and 4LSTs and 9MSTs in blue.

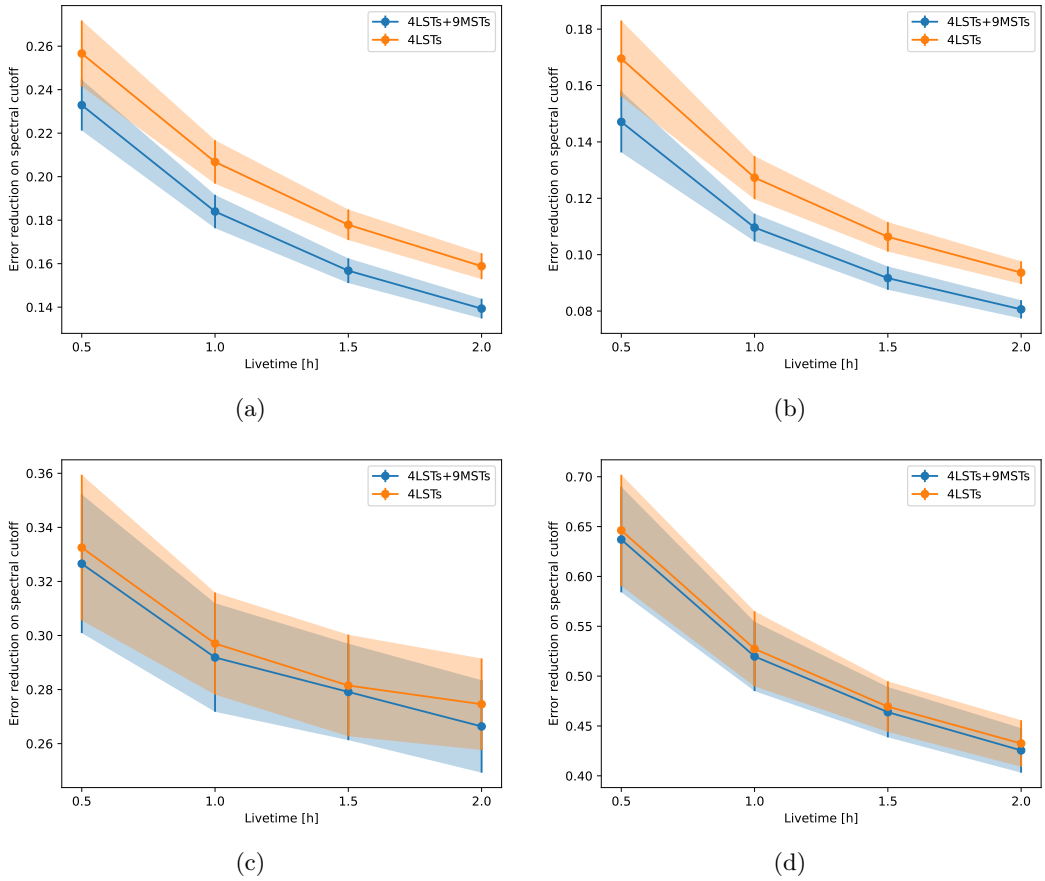

Figure 4.16: a) Error ratio versus livetime of the "rising flare" period of OP 313. b) Error ratio versus livetime of the "decaying flare" period of OP 313. c) Error ratio versus livetime of the "rising flare" period of PKS 1502+106. d) Error ratio versus livetime of the "decaying flare" period of PKS 1502+106. The plots are made for 2 different configurations of CTAO: 4LSTs in orange and 4LSTs and 9MSTs in blue.

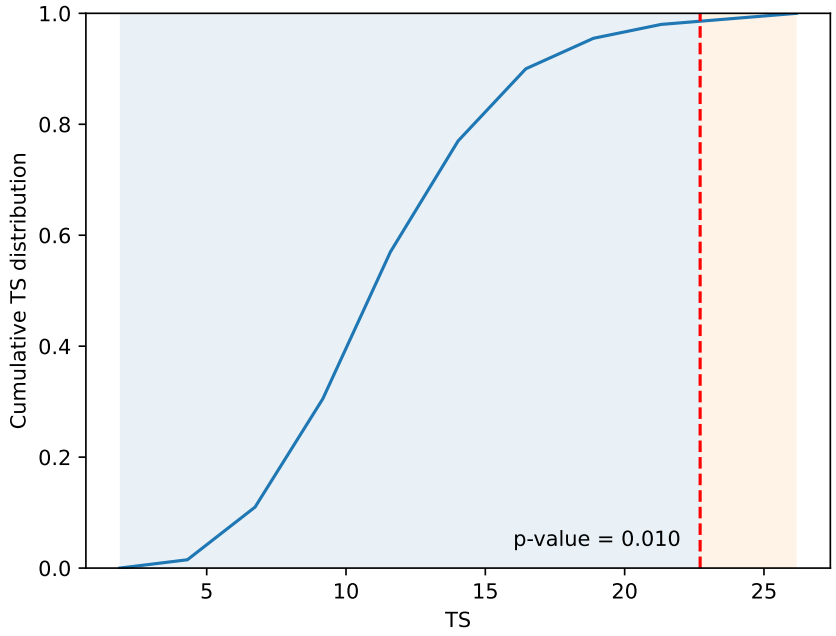

Figure 4.17: Ton 599's "decaying flare" cumulative distribution of the TS in the null-hypothesis case, blue solid line, versus the TS values obtained in the fitting process. The red dashed line shows the average TS value obtained by fitting the flare with an LP model. The blue and red areas help to see where the average red TS line is located with respect to the cumulative TS null-hypothesis distribution.

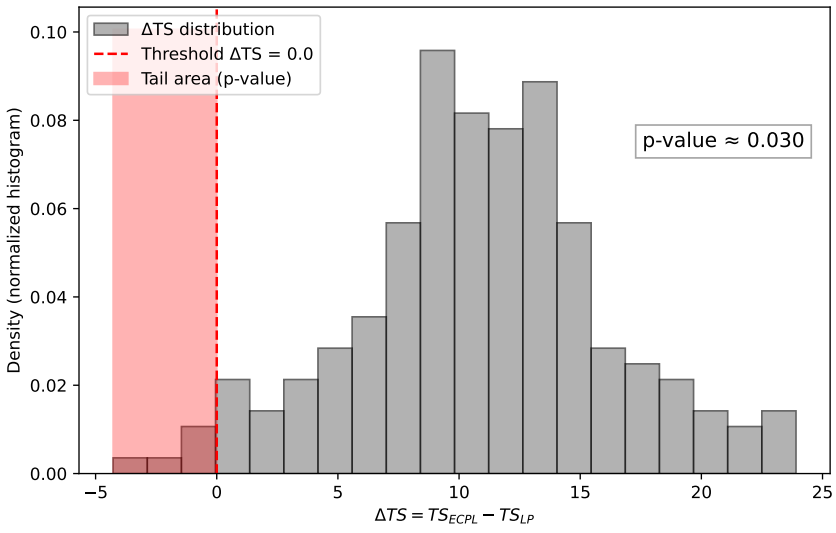

Figure 4.18: Distribution of the test statistic difference ΔTS obtained from $N = 200$ simulations. The shaded red area marks the fraction of realizations with $\Delta TS \leq 0$, which corresponds to the empirical p-value. This histogram is obtained for the "decaying flare" of Ton 599, during the comparison of the LP and ECPL models, after 1hour of observation with 4LSTs.

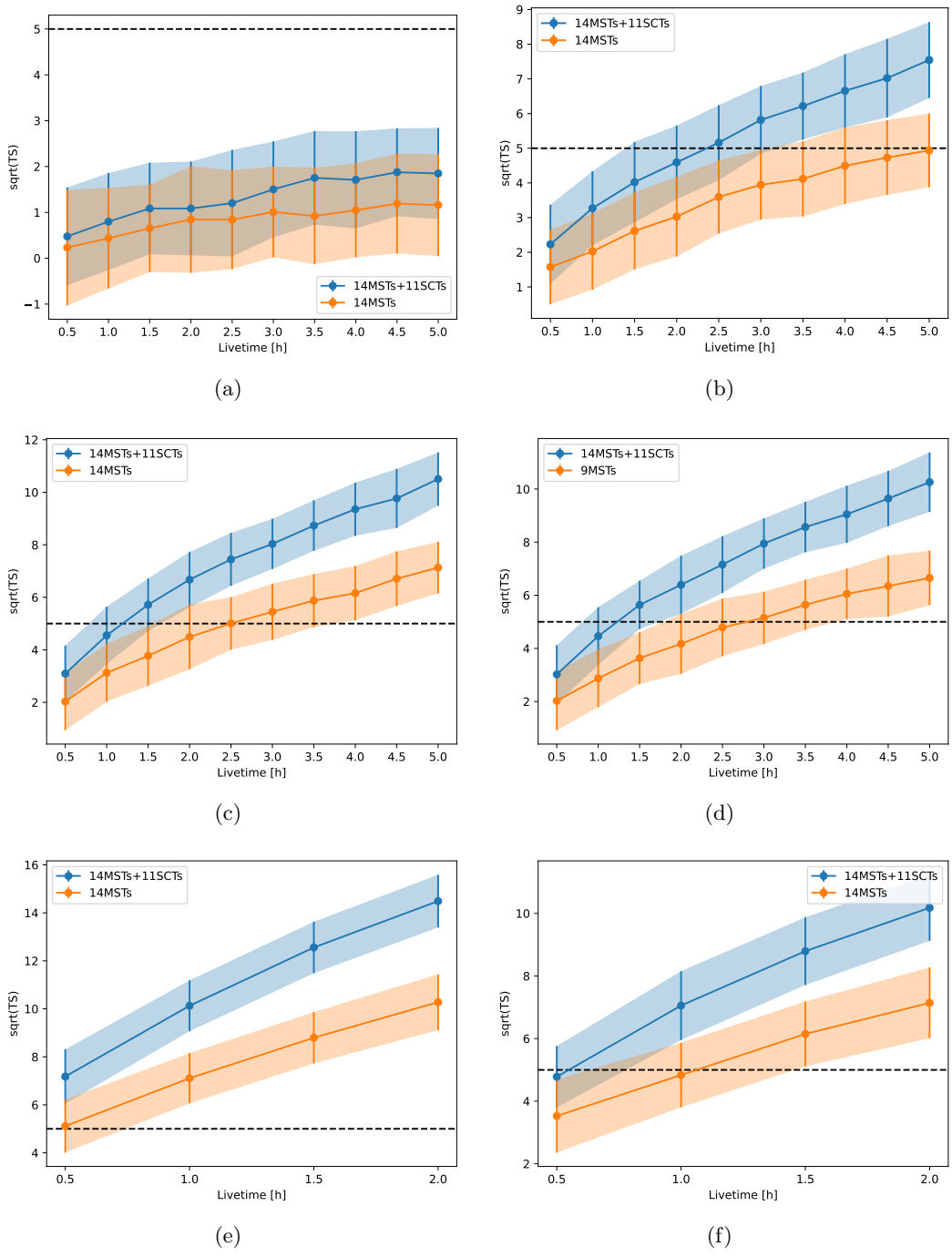

Figure 4.19: a) TS versus livetime of the "rising flare" period of PKS 1510-089. b) TS versus livetime of the "decaying flare" period of PKS 1510-089. c) TS versus livetime of the "rising flare" period of 3C 279. d) TS versus livetime of the "decaying flare" period of 3C 279. e) TS versus livetime of the "rising flare" period of PKS 0346-27. f) TS versus livetime of the "decaying flare" period of PKS0346-27. The plots are made for 2 different configurations of CTAO: 4LSTs in orange and 4LSTs and 9MSTs in blue. The grey dashed line represents the $\sqrt{TS}$ above which the source is detected.

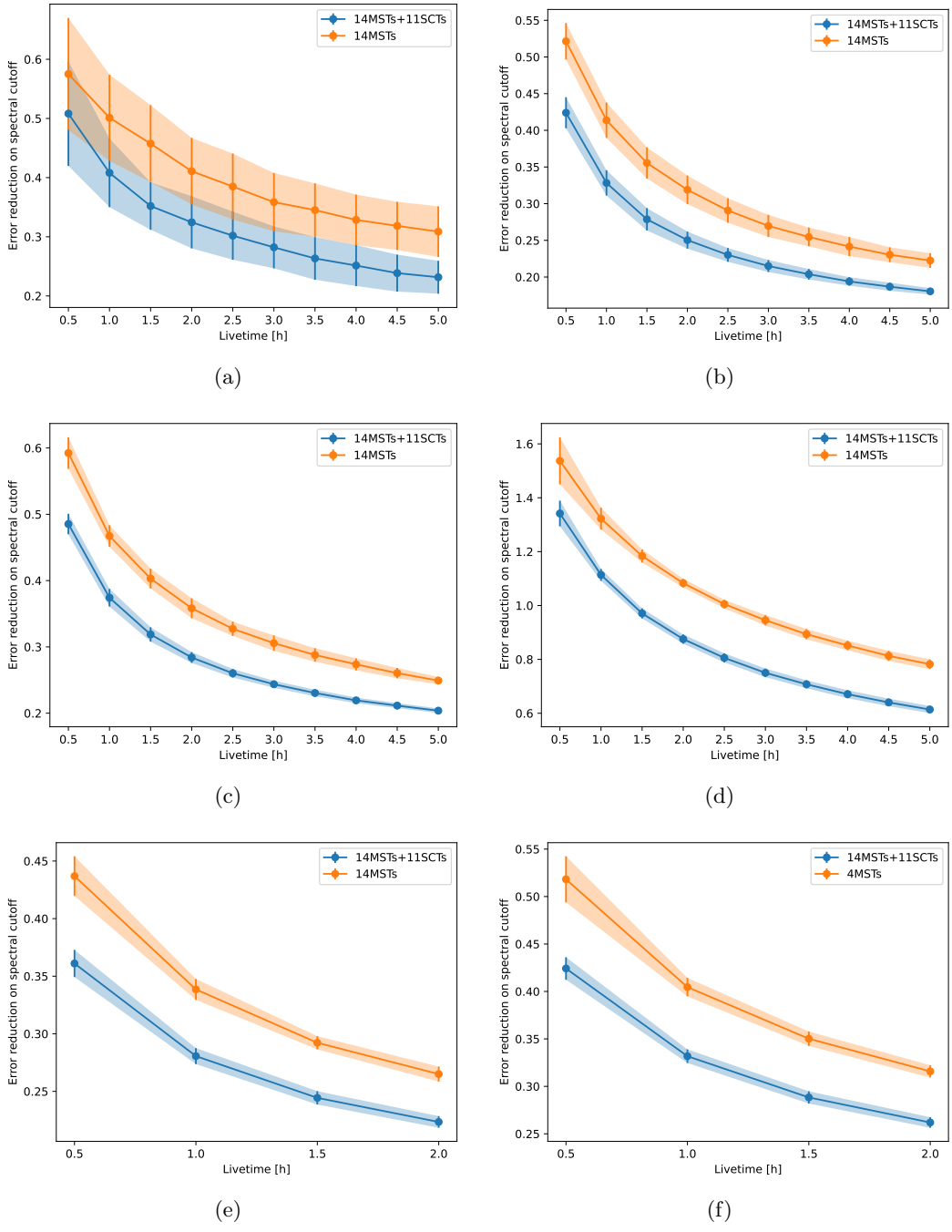

Figure 4.20: a) Error ratio versus livetime of the "rising flare" period of PKS 1510-089. b) Error ratio versus livetime of the "decaying flare" period of PKS 1510-089. c) Error ratio versus livetime of the "rising flare" period of 3C 279. d) Error ratio versus livetime of the "decaying flare" period of 3C 279. e) Error ratio versus livetime of the "rising flare" period of PKS 0346-27. f) Error ratio versus livetime of the "decaying flare" period of PKS 0346-27. The plots are made for 2 different configurations of CTAO: 14MSTs in orange and 14MSTs and 11SCTs in blue.

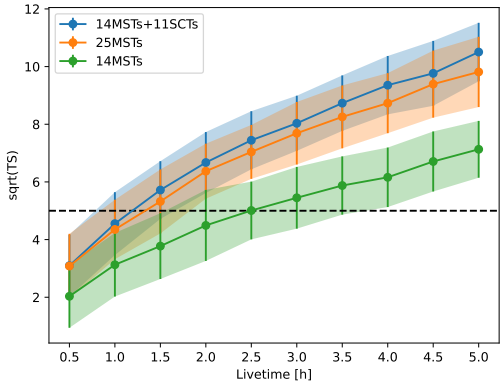

(a)

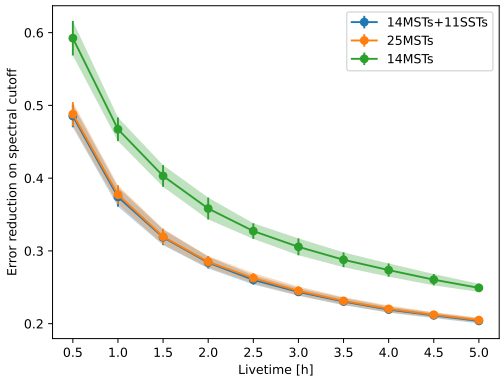

(b)

Figure 4.21: a) 3C 279 "rising flare" $\sqrt{TS}$ vs livetime comparison between 14MSTs, in green, 14MSTs+11SCTs, in blue, and 25MSTs, in orange. The grey dashed line represents the $\sqrt{TS}$ above which there is detection of the source. b) 3C 279 "rising flare" error ratios vs livetime comparison between 14MSTs, in green, 14MSTs+11SCTs, in blue, and 25MSTs, in orange.

Chapter 5

Fermi-LAT follow-up observations in seven years of real-time high-energy neutrino alerts

This Chapter presents the LAT strategy for following up high-energy neutrino alerts applied to seven years of IceCube data (see Section 2.6.1). Right after receiving an alert, a search is performed in order to identify γ-ray activity from known and newly detected sources that are positionally consistent with the neutrino localization. The population of blazars found in coincidence with high-energy neutrinos is studied and compared to the full population of γ-ray blazars detected by LAT.

The neutrino's follow-up analysis is part of the FA pipeline (see Section 2.1.1). Interested FA-GSW shifters can join the effort and contribute to the analysis. I joined the effort of the neutrino group when the idea of writing a paper on the pipeline and on the results started to circulate in the LAT collaboration. I contributed to testing the pipeline, writing the results of the pipeline, publishing them in GCNs Circulars, and doing more follow-ups when needed.

Thanks to the efforts of the neutrino group over the last year, the neutrino pipeline has been improved, and it is completely automatic. This means that the neutrino shifter has to check the results of the pipeline, do more follow-up if needed, write, and publish the GCN circular. The structure of the new automatic pipeline will be part of a future paper, but will not be part of this thesis.

The content of this Chapter has only been slightly modified and will focus mainly on the pipeline; more details and results of this study can be seen in the original publication by [142], published in 2023.

The results presented in this chapter should be interpreted within the broader and still debated framework of neutrino–blazar associations.

5.1 Introduction

Multimessenger astronomy is in a new era with the identification of several candidate neutrino sources. Dedicated observing campaigns have targeted promising

candidates of various types, such as blazars [181], nearby active galaxies [183], and tidal disruption events (TDE; [292], [270]), thanks to the improvements of neutrino telescopes and the multiwavelength programs. The major boost in the association of astrophysical sources with high-energy (> 100 TeV) neutrinos was given by the introduction of a real-time program of alerts by the IceCube South Pole Neutrino Observatory in 2016 [296].

The major challenge in the identification of the neutrino's sources comes from the limited angular resolution of neutrino detectors and from the uneven coverage of the sky of the majority of observing facilities. Furthermore, observational signatures for the identification of hadronic interactions in the spectra of sources are still highly debated (see Section 1.2.8).

LAT observations were crucial for the identification of the most statistically significant coincidence between a high-energy neutrino and an astrophysical source. On 22 September 2017, a $\sim$ 290 TeV neutrino event with a high probability of being astrophysical was detected in spatial coincidence with the γ-ray blazar TXS 0506+056 [181]. Follow-up analysis by the LAT Collaboration [296] identified the blazar in an exceptional flaring state and triggered a rich multiwavelength campaign that involved 18 observational facilities from radio observatories up to imaging air Cherenkov telescopes. This collective effort unveiled the first compelling evidence for a blazar as a neutrino source.

Blazars have been proposed as candidates of extragalactic neutrino sources in several works [e.g. 34, 72, 99, 223, 244, 245, 271]. Before the introduction of the realtime program, a first neutrino blazar candidate was proposed from a coincidence between an IceCube cascade-type event and the blazar PKS 1424-24 which was flaring in radio and γ-rays [193]. Another candidate counterpart to an archival high-energy neutrino event is the blazar GB6 J1040+0617, which was flaring in the LAT and optical bands at the time of the detection of IceCube-141209A [144]. After IceCube began issuing real-time alerts, another candidate neutrino source, the γ-ray blazar PKS 1502+106 was identified through its spatial coincidence with the event IceCube-190730A[143]. Although the source was not flaring in γ-rays at the time of the detection, multiwavelength observations and modeling provided additional evidence in support of it being considered a plausible neutrino emitter [122, 255, 272].

Recent studies of the broader population of AGN have shown that their cores contribute >27% of the observed diffuse neutrino flux [182]. Evidence of >TeV neutrino emission has been found at a 4.2σ significance from the nearby AGN NGC 1068, making it the brightest neutrino point source detected in the Northern Sky [183].

5.2 Follow-up observations with *Fermi*-LAT

Since the introduction of the IceCube Realtime Alert Stream in 2016, a follow-up strategy was defined for neutrino alerts. It consists of a systematic analysis of the sky region around the neutrino arrival direction, looking for known sources that may be flaring or new gamma-ray emitters. The timescales of interest range from a single day up to the full set of historical observations obtained by the LAT over the entire mission.

During a standard follow-up analysis using LAT data, three different timescales are investigated (defined relative to the neutrino arrival time, T_0):

– 1 day before T_0: sensitive to the detection of fast, bright transients, down to a few hours duration.
– 1 month before T_0: sensitive to the detection of recent transient or variable behavior from the sources of interest.
– Full-mission data up to T_0: study long-term behavior of LAT catalog sources and detect weak gamma-ray emitters not reported by the LAT catalogs.

The choice of these timescales is motivated by a trade-off between the instrument sensitivity and the expected time lag between gamma-ray and neutrino emission from time-dependent studies of blazars (see [127] for an application to the gamma-ray flare of TXS 0506+056 in 2017).

After receiving the first GCN Notice with the preliminary localization of the neutrino event from the Astrophysical Multimessenger Observatory Network (AMON)/GCN stream, the first checks were performed on the available data in the region at the 1-day and 1-month timescales. When the refined neutrino localization is released via GCN Circulars by IceCube, the analysis is repeated for the new position at all standard timescales with data up to the neutrino arrival time T_0. This delay between the two GCN revisions is comparable to the typical delay needed by the Fermi Science Support Center (FSSC) servers to have the most recent data up to T_0 available.

When significant detections are found at short timescales within the 90% neutrino uncertainty region, a light curve analysis starting from one year prior to T_0 is performed to characterize the temporal evolution of the source in the short and medium term. In the case of no significant detection at the neutrino best-fit position, a 95% confidence level upper limit is reported corresponding to the detection of a point source with a power-law spectrum with index 2.0.

For typical configurations of the LAT follow-up analysis, photons from the event class developed for point-source analyses were selected in the energy range from 100 MeV up to 1 TeV binned into 10 logarithmically spaced energy intervals per decade, a region of interest (ROI) of at least 15×15 degrees was selected centered on the neutrino best-fit position (or larger for neutrino alerts with wide error contours), binned in 0.1 deg size pixels. Standard data-quality cuts were used to select alerts observed when the detector was in a normal operation mode and remove time periods with the Sun within 15 deg of the ROI center. A maximum-likelihood analysis was performed using the LAT ScienceTools package, along with the latest IRFs and diffuse models, from the FSSC and the `fermipy` package.

5.3 Follow-up observations and results

5.3.1 IceCube Realtime Alert System 1.0

In this section, neutrino track alerts issued between the start of the Realtime System 1.0 in 2016 up to May 31, 2019, are considered. LAT observed 21 alerts issued via GCN Notices. Real-time neutrino alerts were issued via one of two streams - high-energy starting events (HESE) or through-going, extreme high-energy events (EHE) - with neutrino events being classified according to their topology [4]. In the three years of this program, 12 alerts were classified as HESE and 9 as EHE. The all-sky

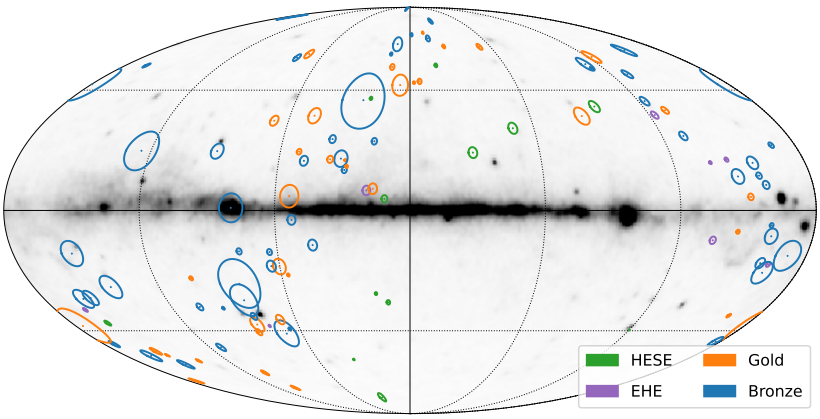

Figure 5.1: All-sky map showing the best-fit positions and 90% containment regions (approximated as circles with the same areas) of the IceCube Realtime Alert stream in galactic coordinates. Gold alerts are shown in orange, Bronze alerts in blue, HESE alerts in green, and EHE in purple (see text for the definitions of the various alert classes). The underlying map in gray scale shows the photon counts in each Healpix pixel from one year of LAT data.

map in Figure 5.1 shows the best-fit localizations and 90% error contours of these alerts with HESE events in green and EHE events in purple.

For 13 of the 21 alerts, there are no coincident sources from the third data release of the Fourth LAT Gamma-ray Source Catalog (4FGL-DR3; [10]). Three of the alerts are each coincident with a single 4FGL-DR3 candidate, which is classified as a blazar. The remaining five alerts are coincident with several 4FGL-DR3 sources.

5.3.2 IceCube Realtime Alert System 2.0

In June 2019, the IceCube Realtime Alert System was updated to its 2.0 version [51]. In this new stream, alerts are classified according to their average probability of being of astrophysical origin, called signalness (s). In the period between June 2019 and May 2023, the LAT observed all 101 alerts issued by IceCube. Among these, 37 were classified as Gold ($s > 50\%$) and 64 as Bronze ($s > 30\%$).

Of the 101 alerts, 44 are not coincident with any 4FGL-DR3 sources, while 17 are each coincident with a single 4FGL-DR3 candidate. The remaining 40 have several source candidates.

5.3.3 Newly detected gamma-ray sources

During the follow-up analysis of high-energy neutrino alerts, new γ-ray sources that do not already appear in the LAT catalogs are occasionally found and reported to the community. These sources are not necessarily causally connected to the neutrinos,

and none of them were exhibiting increased γ-ray activity at the time of the neutrino observations.

Nineteen new sources with a detection significance $> 4\sigma$ have been reported, of which only 7 had a candidate associated counterpart. A general selection criterion for candidate counterparts is to have, within the 90% localization error of the LAT source, a blazar candidate detected in different catalogs. Table 5.1 lists these new sources along with the corresponding IceCube alert name and the tentative association. Only 4 of these sources have been reported in subsequent versions of the 4FGL-DR3 catalog (shown in boldface in Table 5.1).

Table 5.1: New gamma-ray sources detected at $> 4\sigma$ that are in coincidence with IceCube alerts during realtime follow-up observations with LAT data. Sources in boldface are included in the latest version of the LAT 4FGL catalog used in this work.

Alert Name	***Fermi*-LAT Name**	**Association**	**ATel/GCN**
IC190704A	**Fermi J1045.3+2751**	1WHSP J104516.2+275133	ATel#12906 [128]
IC191119A	**Fermi J1511.0+0550**	NVSS J151100+054916	ATel#13306 [143]
IC200109A	**Fermi J1055.8+1034**	-	ATel#13402 [138]
IC200523A	Fermi J2231.0+0034	WISEA J223133.89+003312.8	GCN#27816 [62]
IC200530A	Fermi J1707.0+2528	-	GCN#27879 [63]
IC200614A	**Fermi J0202.8+3132**	NVSS J020242+313212	ATel#13811 [132]
IC200911A	Fermi J0330.1+3743	-	ATel#14010 [133]
IC200921A	Fermi J1256.9+2630	-	ATel#14038 [137]
IC201021A	Fermi J1725.5+1312	1RXS 172314.4+142103	ATel#14111 [61]
IC201114A	Fermi J0703.5+0505	-	ATel#14188 [134]
IC210503A	Fermi J0931.9+3633	SDSS J093209.60+363002.6	ATel#14611 [129]
IC210516A	Fermi J0610.5+0946	-	ATel#14639 [130]
IC220115A	Fermi J2350.2+2620	-	ATel#15166 [140]
IC220205A	Fermi J1420.7+1653	-	ATel#15211 [131]
IC220624A	Fermi J1458.0+4119	-	ATel#15478 [135]
IC220822A	Fermi J1810.1+2154	-	ATel#15570 [136]
IC220918A	Fermi J0502.5+0037	-	ATel#15620 [141]
IC230401A	Fermi J0030.2+0005	5BZB J0030-0000	ATel#15977 [146]
IC230506A	Fermi J0320.2+2243	-	GCN#33745 [139]

5.3.4 Multiplet neutrino sources

As the number of neutrino alerts has increased, there has been a steady increase in the number of 4FGL-DR3 sources that are coincident with the localizations of more than one event. In this study, 14 sources were found coincident with the 90% localization regions of 2 neutrino alerts. Of these sources, 11 are associated with blazars, one is associated with the radio galaxy TXS 1516+064, and three are unassociated. All multiplet coincidences are listed in Table 5.2. The last column of Table 5.2 shows the extensions in deg^2 of the alerts coincident with the listed sources. Several sources are coincident with pairs of poorly reconstructed alerts, such as IC210608A and IC221210A.

The most significant candidate blazar counterpart to a high-energy neutrino thus far, TXS 0506+056 (also known as 4FGL J0509.4+0542), belongs to that list of multiplet sources.

Table 5.2: Sources that are spatially coincident with multiple high-energy neutrino alerts. The listed multiwavelength associations and source classes are those reported in the 4LAC-DR3 catalog.

4FGL Name	Association	Class	IceCube names	Area (deg^2)
J2306.6+0940	-	-	IC190619A, IC220424A	28, 5
J2308.9+1111	MG1 J230850+1112	bcu	IC190619A, IC230201A	28, 18
J1518.6+0614	TXS 1516+064	rdg	IC191119A, IC200410A	60, 380
J1523.2+0533	NVSS J152312+053357	bll	IC191119A, IC200410A	60, 380
J0258.1+2030	MG3 J025805+2029	bll	IC191231A, IC211125A	38, 24
J1747.6+0324	-	-	IC210510A, IC220205B	4, 1
J2149.7+1917	TXS 2147+191	bcu	IC210608A, IC221210A	110, 250
J2200.1+2138	TXS 2157+213	bll	IC210608A, IC221210A	110, 250
J2218.6+1941	GALEXASC J221854.64+193841.6	bcu	IC210608A, IC221210A	110, 250
J2225.6+2120	PKS 2223+21	fsrq	IC210608A, IC221210A	110, 250
J2236.9+1839	-	-	IC210608A, IC221210A	110, 250
J2243.9+2021	RGB J2243+203	bll	IC210608A, IC221210A	110, 250
J2248.9+2107	PKS 2246+208	fsrq	IC210608A, IC221210A	110, 250
J0509.4+0542	TXS 0506+056	bll	IC170922A, IC220918A	1, 51

5.3.5 Estimating expected random coincidences

Given the observed coincidences between 4FGL-DR3 sources and multiple neutrino alerts, it is essential to estimate the expected rate of such coincidences occurring by chance. To do so, 10^4 samples of neutrino alerts were simulated starting from the catalogs described above. By repeating the search for coincident 4FGL-DR3 sources for each of the simulated catalogs, it is possible to determine the probability for a source to be coincident with one or multiple neutrino alerts.

Starting from the sample of 122 alerts issued in the realtime programs (see Sections 5.3.1 and 5.3.2), the probability for a 4FGL-DR3 source to be randomly coincident with two or more alerts is $p(N \geq 2) = 3{\times}10^{-2}$. This gives a total expected number of 21 random coincidences. The 14 4FGL-DR3 sources coincident with two neutrino alerts and listed in Table 5.2 are therefore consistent with the expected number of random coincidences.

5.4 Summary

In this Chapter, the LAT follow-up strategy for high-energy neutrino real-time alerts and the γ-ray results from the past 7 years of activity in these searches were presented. The spatial resolution of current neutrino detectors is a strong limit on the searches for astrophysical counterparts, and the tentative associations with astrophysical sources suffer from high chance coincidence probabilities (see also [213]). With the increase in the number of real-time alerts, a growing sample of γ-ray sources that are coincident with multiple neutrinos is emerging. Most of these coincidences are caused by large positional uncertainties in the arrival directions of the neutrinos. Therefore, detailed multi-wavelength studies are necessary to select possible source candidates.

After the outstanding coincidence between the flaring γ-ray blazar TXS 0506+056 and the realtime event IC170922A [181], the only realtime event pinpointing a single, powerful γ-ray blazar is IC190730A, which is coincident with PKS 1502+106 [122].

In this case, the source was not observed to be flaring at the time of the neutrino detection.

The possible association between high-energy neutrinos and blazars has been one of the most debated topics in multi-messenger astrophysics. While some studies have reported evidence in favor of a correlation between IceCube neutrinos and γ-ray–bright blazars, through stacking analyses or population studies [e.g. 2, 3], other works have found results compatible with random associations, and neutrino positional uncertainties are taken into account [e.g. 201, 213, 265]. The results presented in this chapter support the latter scenario. Apart from the well-known case of TXS 0506+056 and the single-source association proposed for PKS 1502+106, the majority of γ-ray sources spatially coincident with IceCube real-time alerts are consistent with chance coincidences driven by the large angular uncertainties of the neutrino events. The absence of systematic γ-ray flaring activity at the time of most neutrino detections further weakens the case for a blazar–neutrino connection.

These results do not rule out the possibility that a small subset of blazars can produce high-energy neutrinos during specific episodes, but they suggest that blazars are unlikely to dominate the diffuse astrophysical neutrino flux. Instead, neutrino production may be shared among different classes of astrophysical objects. In this sense, the results of this chapter are fully consistent with recent population-based studies and highlight the importance of continued real-time follow-up programs combined with detailed multi-wavelength analyses to identify the most promising neutrino source candidates.

In fact, the LAT follow-up program for real-time neutrino alerts is ongoing, and the strategy is constantly improved and synergies with multi-wavelength facilities. Follow-up observations of these real-time alerts with the LAT are crucial for the prompt identification of interesting neutrino source candidates.

Chapter 6

Conclusions

In this thesis, a different set of techniques to investigate blazars' jets was presented, in particular, the one of FSRQs. The combination of mechanisms behind cosmic rays' acceleration in blazars' jets is still unknown, as it seems that during their flaring activity, every blazar exhibits different phenomena in action than the others. It is still debated if blazars' jets can accelerate only leptons or both leptons and hadrons, and this thesis offered both points of view with the analysis of the FSRQ OP 313, in which only the leptonic scenario is considered, and the LAT follow-up strategy for high-energy neutrino real-time alerts, which consider blazars' jets as the origin of the astrophysical neutrinos population detected by IceCube. The hadronic scenario is supported by the fact that the second hump of the SED of blazars may also be produced by hadronic particles. Hence, blazars' jets are candidates for the UHECR population. Another question that this thesis questioned was whether CTAO's different configuration will be sensitive enough to reconstruct the second hump of the SED of the blazars to help the scientific community discriminate between different spectral models, which include leptons and hadrons in the near future.

In Chapter 3, a 15-year-long multi-wavelength analysis of the FSRQ OP 313 was shown. OP 313 was characterized by intense flaring activity from November 2023 until March 2024 and was remarkably observed by LST-1 and MAGIC. Since the goal of the project was not to analyze the VHE emission from the flaring state of OP 313, it focused on the source's behavior in 15 years of *Fermi*-LAT observations. From the light curves comparison, strong variability has been observed from optical to γ-rays, while a different behavior has been observed in radio. Because of this, the analysis focused on the VLBA data, which gives information on the location of the γ-ray emission region in the jet (in the case of OP 313 this was already found in [204]) and on the presence of new knots arising in the jet before or during the γ-ray flaring emission. As a result, the arising of new knots can be responsible for the flaring emission that was detected by *Fermi*-LAT. Furthermore, to test if the constraints obtained from the multi-wavelength analyses would also result in an acceptable description of the SED in different states, two flares were selected in terms of their very different Compton dominance. This is relevant because such significant changes in Compton dominance also mean that the source of the seed photons changed. The two selected SEDs were modeled using a SSC and EC single-zone leptonic model (see [93] for the hadronic modeling). The result of the SED modeling highlights how much the DT's photon fields are important to describe the γ-ray emission of OP 313. The whole analysis of OP 313 is pretty standard;

nevertheless, the quantity of data to analyze from γ-ray to radio was not standard. This is not always the case with high-redshift blazars, and it highlights how peculiar the activity of this source is. Having so much data allowed to focus attention on what phenomena can be responsible for the intense γ-ray flaring emission. In this case, the hypothesis that was brought is further shock acceleration in the jet. However, the results and the parameters obtained in the SED modeling are not unique, opening the opportunity to consider turbulence, kink instabilities, and magnetic reconnection to explain the incredible flaring activity.

This project could be a milestone for a bigger project on FSRQ. Lots of FSRQs observed by LAT show the same intense flaring activity, and a study linking γ-ray data, radio data, and polarization (to consider the role of magnetic fields in the jets) of a large sample of sources could be performed in the future to find a common mechanism able to explain their flaring emission.

To link this idea to the VHE emission of blazars and the curvature in the blazar's SEDs, simulations of CTAO data of eight FSRQs using `gammapy` were performed in Chapter 4. The main goal of the project was to assess how CTAO observations can constrain the curvature of the spectral energy distribution, improve spectral parameters estimation compared to LAT, and help to discriminate between scenarios with or without a spectral cutoff. The SED's curvature provides insight into the physical processes shaping the high-energy emission of blazars. With a better reconstruction of the SED shape, we could obtain information about the distribution of the primary particles, which could be leptons and hadrons or only leptons. In this project, we still considered only electrons as primary particles.

For the five Northern sources' flaring periods, it was shown that the addition of 9MSTs to the 4LSTs will not improve either the detection of the FSRQs nor the spectral parameter estimation nor the model discrimination. The performances of the LSTs are enough to perform spectral studies of the FSRQs.

This result is fundamental in the specific context of this work, as it indicates that, for the purpose of constraining the spectral curvature and possible exponential cutoffs of flaring FSRQs, the performance of the LSTs alone is sufficient in the Northern Hemisphere. In this scenario, the addition of MSTs does not significantly improve the detection significance, spectral parameter estimation, or model discrimination. However, this conclusion is strictly limited to the specific scientific goal addressed here. CTAO has a broad and diverse science program, and MSTs play a fundamental role in many other studies, including the study of γ-ray propagation effects and constraints on the extragalactic background light (EBL). Even for FSRQs, different scientific objectives may benefit from the combined use of LSTs and MSTs to enhance sensitivity at the highest energies.

For the three Southern sources, it was shown that adding 11SCTs contributes to larger TS and better spectral parameter estimations. Regarding the model discrimination, it was shown that it is not always possible to discriminate between different spectral models, but CTAO simulated data will improve their discrimination thanks to the higher sensitivity above tens of GeV.

The results of this project open a future possibility: an analogous study of these sources, or on a larger sample, with the addition of LSTs in the Southern Hemisphere, could be done when the prod6 IRFs will be available. Furthermore, more spectral models can be added. The Klein-Nishina regime and the γ-γ absorption, which are important mechanisms in blazars' jets, were not considered and could be added,

together with models that consider hadron acceleration. Another goal will be to consider LAT and CTAO simultaneous datasets to see how much CTAO's different configurations are sensitive to lower fluxes and short observing time.

Finally, in Chapter 5, blazars' jets were considered the origin of the neutrinos observed by IceCube. With the increase in the number of real-time alerts, a growing sample of γ-ray sources that are coincident with neutrinos is emerging. Most of these events have large positional uncertainties in the arrival directions of the neutrinos. Therefore, detailed multi-wavelength studies are necessary to select possible source candidates.

For this reason, the LAT follow-up program for real-time neutrino alerts is still ongoing, and still focuses on synergies with multi-wavelength facilities. Follow-up observations of these real-time alerts with the LAT are crucial for the prompt identification of interesting neutrino source candidates.

The work shown in this thesis opens up a lot of different projects that could be led in the near future to solve the mysteries of blazars' jets.

Appendix A

Simulations of Supernova Remnants with CTAO's SCTs

During the first year of the Ph.D., I started a sensitivity project on the SCTs. The main goal was to learn how to perform simulations in the CTAO context and show how the addition of SCTs in the Southern Hemisphere will improve the detection of extended sources and the discrimination between different spatial models. The extended sources chosen were SNRs located in the Southern Hemisphere.

The simulations were performed using the `ctools`[1] v. 2.0.0, but since they are not the official CTAO python package, they were performed again using `gammapy` v.1.3. In this Appendix, the results obtained using `gammapy` are reported.

These simulations and their results will be part of a future publication in collaboration with the CTAO SCT-simulation group.

A.1 Supernova Remnants

In this Section, the author of this thesis describes the main characteristics of the supernova (SN) and the SNRs.

A.1.1 Supernova

SN are stars that end their evolution with a large-scale cataclysmic explosive phenomenon, which is due to the gravitational collapse of the iron core of the star itself and which ends with the formation of a Neutron Star or a Black Hole, or leads to its thermonuclear explosion and complete destruction. Supernova explosions are among the most energetic events in the Universe since the Big Bang, releasing more energy ($\sim 10^{51} - 10^{53}$ ergs) than the Sun will release over its entire lifetime [38].

SN are classified based on their optical characteristics for historical reasons. They are divided into two categories:

– Type I supernova have no hydrogen optical lines in the spectrum [211]. They have a further sub-division made according to a strong silicon line that is seen in Type Ia objects, known also as thermonuclear supernova, which are about

[1] `http://cta.irap.omp.eu/ctools/`

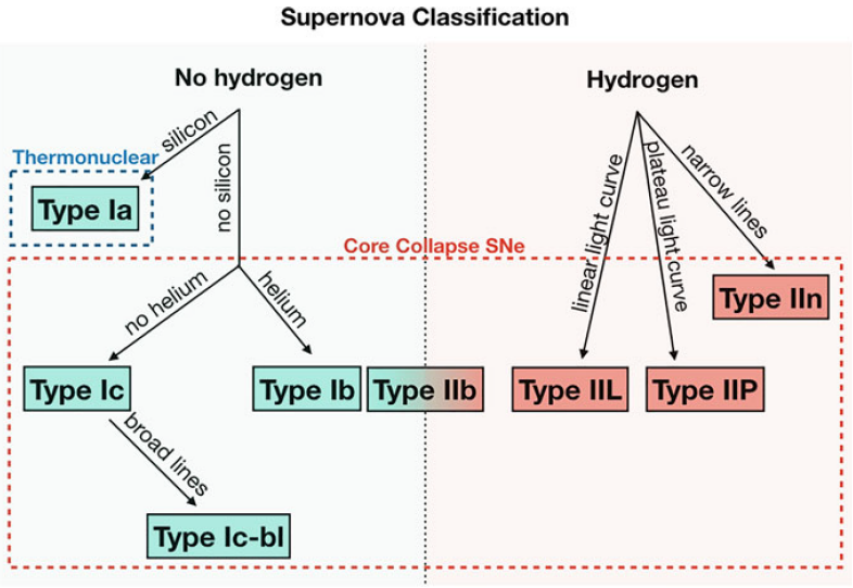

Figure A.1: Schematic view of the classification of SN. Courtesy of [311].

24% of all supernova [211], but is absent in Type Ib/c, which are about 19% of all supernova [211]);

– Type II supernova, known also as core-collapse supernova, which are more or less the 57% of all the supernova population, have strong hydrogen features.

A plot summarizing this classification is shown in Figure A.1. These two classes of supernova have different progenitors and different physical explosion mechanisms [178]:

– Type Ia supernova are produced by the explosion of a carbon–oxygen white dwarf. The reason why white dwarfs are the most promising candidates is that neither hydrogen nor helium is observed in the spectra of these objects [274].

– Type Ib, Ic supernova are core collapse as Type II supernova, but they have shed or been stripped of their outer envelope of hydrogen due to strong stellar winds, and, when compared to the spectrum of Type Ia supernova, they lack the absorption line of silicon. Type Ic have lost most of their helium too.

– Type II supernova occur when a star with a mass larger than $8M_{\odot}$ ends its life with the gravitational collapse of its own iron core.

A.1.2 Supernova Remnants

A SNR is a cloud of expanding material ejected from the star, rich in heavy elements like O, Si, and Fe, that drives a shock wave into the Interstellar Medium (ISM). The shock wave heats the interstellar gas, creating a highly-ionized plasma. SNRs remain visible for thousands, often tens or hundreds of thousands of years before dissipating their energy into the ISM [38]. The life of an SNR consists of four phases:

– Free expansion phase. In this phase, the pressure of the ISM is negligible in comparison to the pressure of the ejected material, so it expands without decelerating. Furthermore, the ejected mass M_{ej} dominates over the swept-up

mass M_{sw}. The radiation emitted is the non-thermal synchrotron radiation emitted by relativistic electrons accelerated, up to GeV energies, in the shock.

- Adiabatic expansion phase or Sedov phase. In this phase, the expansion begins to decelerate due to the forward shock sweeping up a non-negligible amount of material in the ISM ($M_{sw} > M_{ej}$). This phase of deceleration of the forward shock wave also leads to the formation of a "reverse shock," which propagates back into the ejecta towards the center of the SNR [165, 166]. Remnants in the adiabatic or Sedov expansion phase are typically bright at X-ray wavelengths, showing both the hot ISM gas shocked by the forward shock and the hot ejecta shocked by the reverse shock.
- Snowplow phase. This phase happens when the shock velocity has decelerated to $\sim 200\,\mathrm{km\,s^{-1}}$, the temperature of the gas drops below $\sim 10^6\,\mathrm{K}$, and radiative cooling begins to affect the dynamics of the shock evolution. The more the gas cools, the more the cooling rate increases. The density of the shock front becomes highest where the timescale of radiative cooling becomes shortest. A cool, dense shell is formed just behind the shock front as a result, whereas the inner gas still has high temperature and high pressure due to the low density. It is during this phase that the remnant becomes bright in optical emission from recombining atoms [38].
- Dissipation phase. As the SNR gets even older, the expansion velocity becomes smaller. When the shock slows down to a velocity comparable to the sound velocity, the SNR blends into the ISM. The typical SNR's lifetime is around $10^6\,\mathrm{yr}$, during which they will expand to radii of dozens to hundreds of parsecs, filling a volume large enough to encompass hundreds to thousands of star systems [38].

Morphology of Supernova Remnants

Most of the population of SNRs are classified as *shell-type* SNRs. *Shell-type* SNRs emits radiation into the forward shock across the electro-magnetic spectrum. In the radio regime, the emission is dominated by synchrotron emission from energetic electrons (accelerated by the shock wave to GeV energies) spiraling around the turbulent magnetic field at the shock front. At infrared wavelengths, young SNRs are generally dominated by thermal emission from warm dust grains [108]. Dust grains do not feel the passage of the shock wave, but are suddenly immersed in the hot plasma behind the shock, where ion and electron temperatures can be tens of millions of degrees. Hence, the infrared emission results from warmed interstellar grains. At optical wavelengths, if there is partially neutral material present ahead of the shock, charge exchange can take place in the post-shock environment, giving rise to a strong Hα component [77]. At X-ray wavelengths, *shell-type* SNRs show emission from the forward-shocked ISM and the reverse-shocked ejecta, depending on the evolutionary state of the remnant. The X-ray thermal emission is a combination of both Bremmsstrahlung continuum produced when hot ions and electrons interact, as well as line emission from highly-ionized atoms of various metals. Non-thermal emission arises from synchrotron emission identical to that seen in radio waves, but from much more energetic ($\sim 10 - 100\,\mathrm{TeV}$) electrons [38]. In Figure A.2, there are three pictures of the same *shell-type* SNR DEM L71 seen in three different energy bands: radio on the left, infrared in the center, and X-ray on the right.

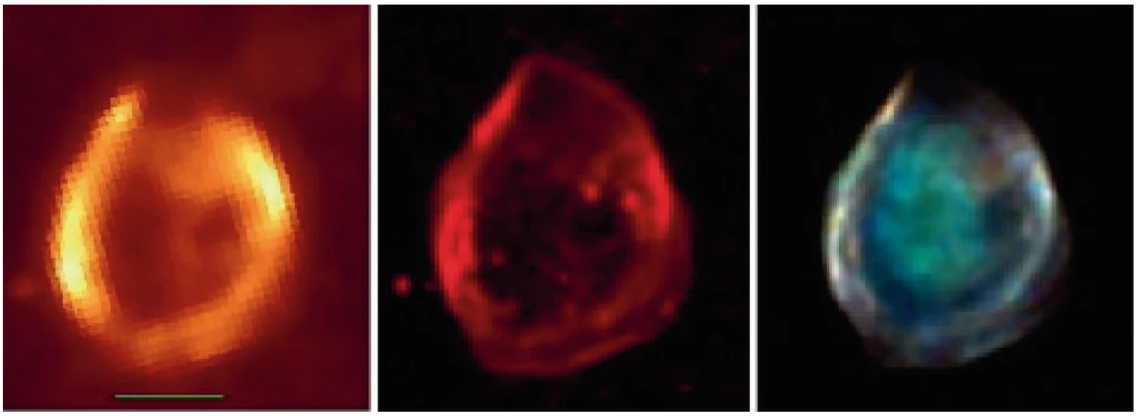

Figure A.2: Left: the Spitzer 24 μm emission from DEM L71. Middle: the remnant in Hα. Right: the remnant in X-rays. Courtesy of [54].

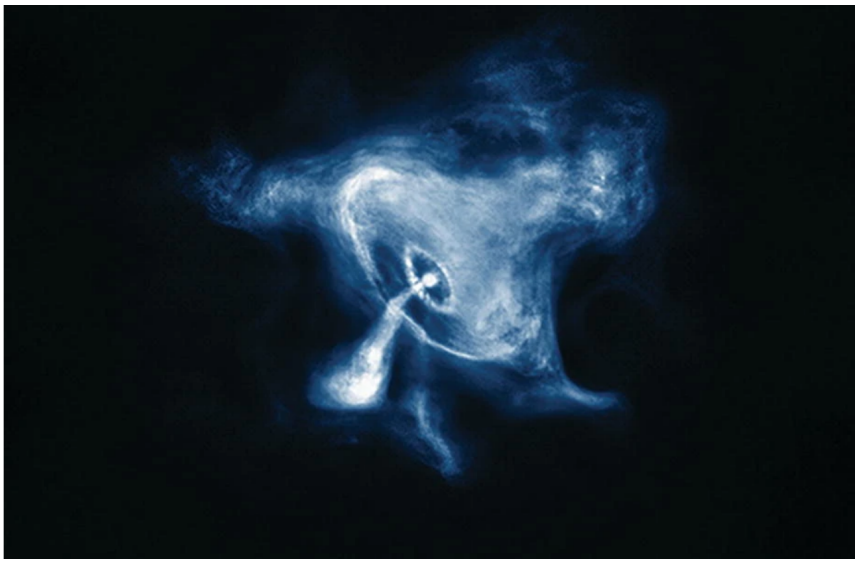

Figure A.3: X-ray image of the Crab nebula taken with Chandra. Courtesy of NASA/CXC/SAO

Plerion-type SNRs are pulsar wind nebulae produced when a core collapse SN produce a neutron star. Pulsar wind nebulae emit bright non-thermal emission from radio to very high energy γ-rays, via synchrotron or inverse Compton processes [321]. The Crab, in Figure A.3, is an example of a *plerion-type* SNR. Some *plerion-type* SNRs are surrounded by shells of emission resulting from the forward shock interacting with the surrounding medium. Such remnants are often called *composite type* SNRs.

Some old SNRs show different morphology in the radio and X-ray bands: the shell structure is seen in radio, while the inner part of the remnants is seen in X-ray. This kind of SNRs is called *mixed morphology-type* SNR. There is still no clear mechanism that can explain this morphology. One hypothesis is that the outer shell cools down due to the expansion and radiative cooling. As a result, the shock temperature becomes too low to emit thermal X-rays. Synchrotron emission from the accelerated electrons in the shock disappears due to synchrotron cooling. Hence, the shell emitting synchrotron disappears within a few thousand years in the X-

Figure A.4: X-ray image of the *plerion-type* SNR, G21.5-0.9 taken with Chandra. Courtesy of: Heather Matheson Samar Safi-Harb (Univ. Manitoba), CXC, NASA

ray band, whereas it remains for more than ten thousand years in the radio band. Another hypothesis is the so-called *evaporated cloud*. The enhanced X-ray emission inside the shell could arise from gas evaporated from clouds [324] in the cases that shocks of SNRs propagate through a cloudy ISM. An example of composite SNR is shown in Figure A.4.

A.1.3 Acceleration of cosmic rays in supernova Remnants

Supernova remnants are recognized as candidates for the acceleration of galactic CRs with energy below the knee. The CR sources are uniformly distributed throughout the Galaxy, and the CRs are trapped by the galactic magnetic fields. According to the observations, the total kinetic energy of CRs is:

$$\rho_{CR} \times \mathcal{V}_G = 8 \times 10^{54}\text{erg} \tag{A.1}$$

where $\rho_{CR} \simeq 1\,\text{eV/cm}^3$ is the energy density of CRs and $\mathcal{V}_G \sim 5 \times 10^{66}\,\text{cm}^3$ is the galactic volume. If the CRs are confined inside the galactic volume, ρ_{CR} should increase with time in the presence of new galactic core-collapse supernova explosions. An effect that induces a decrease in ρ_{CR} is the escape of CRs from the Galaxy after an escape time $\tau_{esc} \simeq 10^7\,\text{yr} = 3 \times 10^{14}\,\text{s}$. Assuming the energy density being constant, the energy loss rate due to the escape of CRs from the Galaxy is:

$$P_{CR} \simeq \frac{\rho_{CR} \times \mathcal{V}_G}{\tau_{esc}} = 3 \times 10^{40}\text{erg/s} \tag{A.2}$$

Then, the power required by cosmic accelerators, like the SNRs, to refill the galaxy volume is equal to P_{CR}. A supernova explosion of 10 solar masses releases about $10^{51}\,\text{erg}$, in the form of kinetic energy of a shock wave. If the SNRs can accelerate charge particles, they transfer the kinetic energy of the shock wave to the CRs with an efficiency η:

$$P_{SN} \simeq \eta \times f_{SN} \times 10^{51}\text{erg/s} \tag{A.3}$$

Where $f_{SN} \sim 10^{-9}\,\text{s}$ is the fraction of supernova explosions in our Galaxy. By requiring that $P_{CR} = P_{SN}$, the quantity η must be on the order of a few percent.

In this case, the shock waves from supernova explosions can refurbish the Galaxy with new accelerated particles. Two transfer mechanisms are the *diffusive shock acceleration* or *first-order Fermi acceleration mechanism* and the *second-order Fermi acceleration mechanism.*

Second order Fermi acceleration

This mechanism was proposed by Enrico Fermi in 1949 [115] and explains the acceleration of relativistic particles by means of their collision with interstellar clouds [64]. These clouds move randomly and act as *magnetic mirrors.* The collisions could be *heads-on*, which increases the particle's energy, or *overtaking* collisions, which decrease it. However, the average energy gain per collision is:

$$\left\langle \frac{\Delta E}{E} \right\rangle \approx \frac{8}{3} \left(\frac{v}{c} \right)^2 \tag{A.4}$$

where v is the velocity of the cloud and c is the speed of light. From Equation A.4, the energy rate is given by:

$$\frac{dE}{dt} = \frac{4}{3} \left(\frac{v^2}{cL} \right) E = \alpha E \tag{A.5}$$

where L is the mean free path between clouds, along the field lines. It is possible to find the energy spectrum *N(E)* by solving a diffusion-loss equation in the steady state and considering this energy rate, using also the assumption that τ_{esc} is the characteristic time for a particle to remain in the accelerating region [64]. One finds that:

$$N(E)dE = const \times E^{1+\frac{1}{\alpha \tau_{esc}}} dE \tag{A.6}$$

Even though second-order acceleration succeeds in generating a power-law spectrum, it is not a completely satisfactory mechanism. The energy gain is very slow, and the mechanism fails to explain the observed value of 2.7 for the exponent in the power-law spectrum (see Section 1.1.1).

First-order Fermi acceleration mechanism

The mechanism thought to explain the acceleration of CRs in SNRs supernova remnants is the *first-order Fermi acceleration*, also known as *diffusive shock acceleration.* In this process, charged particles scatter elastically off magnetic field irregularities on both sides of a shock front and repeatedly cross the shock due to diffusion. In each crossing, the particles gain an average energy:

$$\left\langle \frac{\Delta E}{E} \right\rangle \approx \frac{4}{3} \frac{u_s}{c} \tag{A.7}$$

where u_s is the shock velocity. Because the probability of escape after each cycle is finite, the combination of systematic energy gain and escape leads to a power-law energy distribution for the accelerated particles. The differential energy spectrum takes the form:

$$N(E)dE \propto E^{-p} dE, \quad p = \frac{r+2}{r-1} \tag{A.8}$$

where $r = u_1/u_2$ is the compression ratio between upstream (u_1) and downstream (u_2) plasma velocities in the shock frame. For a strong, non-relativistic shock in an ideal gas with adiabatic index $\gamma = 5/3$, $r \sim 4$, leading to $p \sim 2$. Hence, the differential energy spectrum is:

$$N(E)dE \propto E^{-2}dE \tag{A.9}$$

This is not perfectly equal to the observed exponent of 2.7, but the first-order mechanism is very promising, being the most effective and probable one, since shock waves are expected to be present in different astrophysical environments [64].

A.2 Set up of the simulations

The two SNRs chosen for this study are:

- RCW 86 ($R.A. = 220.72\,\mathrm{deg}$, $dec. = -62.43\,\mathrm{deg}$) is a *shell-type* SNR seen by H.E.S.S.. It is located at a 2.5 kpc from the Earth, and it has a radius of $R = 0.3 \pm 0.020\,\mathrm{deg}$ [163]. The integral flux of this source above 1 TeV is $F(> 1\,\mathrm{TeV}) = (2.44 \pm 0.67) \times 10^{-12}\,\mathrm{cm}^{-2}\mathrm{s}^{-1}$ equal to 10% of the Crab's integral flux [$F(> 1\,\mathrm{TeV}) = (2.26 \pm 0.08) \times 10^{-11}\,\mathrm{cm}^{-2}\mathrm{s}^{-1}$, 22] and the spectral index is $\Gamma = 1.59 \pm 0.22$ [163].
- RX J0852.0-4266 ($R.A. = 133.00\,\mathrm{deg}$, $dec. = -46.37\,\mathrm{deg}$), also known as Vela Junior, is a *shell-type* SNRseen by H.E.S.S. and by the CANGAROO experiment [109]. It is located at 0.2 kpc from the Earth, and it has a radius of 1 deg [163]. The integral flux of this source above 1 TeV is $F(> 1\,\mathrm{TeV}) = (23.4 \pm 0.7_{stat} \pm 4.9_{syst}) \times 10^{-12}\,\mathrm{cm}^{-2}\mathrm{s}^{-1}$ equal to 103% the Crab's integral flux and the spectral index is $\Gamma = 1.81 \pm 0.08_{stat} \pm 0.20_{syst}$[162].

Both SNRs are located in the Southern Hemisphere, since SCTs are part of a scenario beyond the "Alpha Configuration" in the South.

To perform the simulations, `gammapy` v 1.3 was used. As explained in 4.5.1, to simulate CTAO datasets, the necessary observational parameters must be defined. In this project, a 3D map of each of the SNRs was created using `gammapy`'s class `MapDatasetMaker`. The necessary parameters to create the 3D maps and perform the simulations are:

- The duration of the observation. In this project, the author of this thesis decided to start simulating from 2 hours of observation, adding two hours until 20 hours of livetime was reached, to see the evolution of the TS with time.
- The prod3 version v3.0.0, 20 deg zenith angle, azimuth-averaged pointing, optimized for 50 hours of observation time IRFs. The tested configurations are:
  - the F4 configuration with 14 MSTs, which is part of the Alpha configuration.
  - the C0 configuration with 25 MSTs.
  - the M2 configuration with 14 MSTs and 11 SCTs.
  - the F2 configuration with 25 SCTs.
- The reconstructed energy range, from 350 GeV to 10 TeV.
- The true energy range, from 300 GeV to 15 TeV.

– The background, which was set to a field of view background model. The background model holds the correction parameters applied to the instrumental background.
– The spectral model which was `ExpCutoffPowerLawSpectralModel`. The parameters were set to the values reported in [163] for RCW 86 and in [162] for RX J0852.0-4266. Furthermore, the simulations for RCW 86 were done with a flux equal to 1% of the Crab and 100% of the Crab, and for RX J0852.0-4266 with 13% of the Crab to see if the different configurations of CTAO can detect the same extended sources at different fluxes.
– The spatial model, which is set to the `TemplateSpatialModel` provided by `gammapy` and which are shown in Figure A.5(a) and A.5(b). The other spatial models considered to evaluate the capacity of the different CTAO's configuration to discriminate between different spatial models are:
  * A shell spatial model where the outer radius was fixed at the value reported in [163] for RCW 86 and [162] for RX J0852.0-4266, and the width to 0.2 deg for RCW 86 and 0.1 deg for RX J0852.0-4266.
  * A disk spatial model where the radius was fixed at the value reported in [163] for RCW 86 and [162] for RX J0852.0-4266, the eccentricity was equal to $e = 0.6$ for both of them, the rotation angle was equal to $\phi = 0\,\text{deg}$ for both of them, and the width to 0.2 deg for RCW 86 and 0.1 deg for RX J0852.0-4266.
  * A gaussian spatial model where the radius was fixed at the value reported in [163] for RCW 86 and [162] for RX J0852.0-4266, the eccentricity was equal to $e = 0.6$ for both of them, and the rotation angle was equal to $\phi = 0\,\text{deg}$ for both of them.

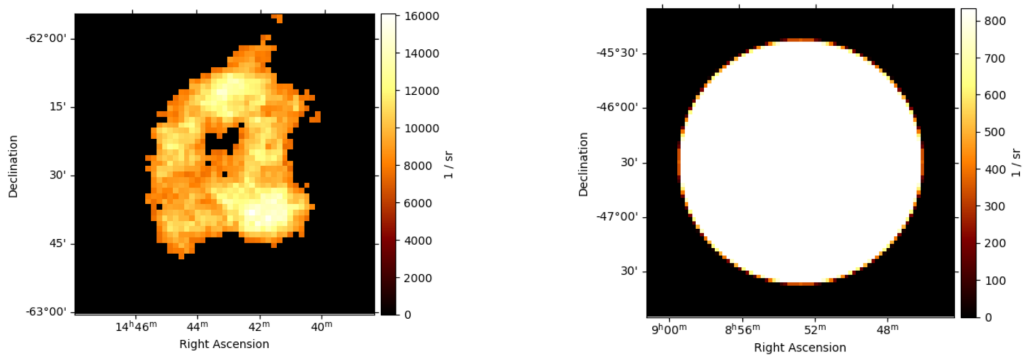

(a) (b)

Figure A.5: a) RCW 86's `TemplateSpatialModel` provided by `gammapy` b) RX J0852.0-4266's `TemplateSpatialModel` provided by `gammapy`.

Once the 3D map was simulated, the source was fitted with the template itself, with the shell spatial model, with the disk spatial model, and with the Gaussian spatial model. From fitting the extended sources with the template model, the $\sqrt{TS}$ and the Bayesian Information Criterion (BIC) [283] were saved. From each fit with the other spatial models, the BIC was saved. The BIC is a criterion for model selection among a finite set of models and the models with lower BIC are generally preferred. The BIC is defined as:

$$BIC = k\ln(n) - 2\ln(\hat{\mathcal{L}}) \tag{A.10}$$

where k is the number of parameters estimated by the model, n is the number of counts in the 3D map, and $\hat{\mathcal{L}}$ is the maximized likelihood. The BIC value were used to perform the spatial models discrimination as the spectral model discrimination was done in and 4.6.3 and 4.6.4.

The simulations were performed 100 times for each livetime, for each CTAO's configuration, for each flux's value, and for each spatial model.

A.3 Results

In this section, the results of the simulations are listed. The main goal of this project was to show how the sensitivity of SCTs improves the detection of extended sources on the Galactic Plane and their spatial model discrimination. To reach this goal, different observation times were set to clearly show the improvement in time.

A.3.1 RCW 86 results using 1% of Crab's flux

RCW 86 was simulated using 1% of Crab flux to see if the different configuration of CTAO can detect the source at this low flux, how many hours of observations are needed to detect it and in how many hours of observation CTAO can discriminate between different spatial models, considering that the best spatial model that fit RCW 86 is the template itself.

Figure A.6 shows the $\sqrt{TS}$ values, in function of the livetime, obtained for the four CTAO's configurations. Each $\sqrt{TS}$ value is the mean of 100 values. In this case, the source is not detected ($\sqrt{TS} < 5$) by none of the four configurations, and no configuration seems to perform better than the others due to the huge error bars. Since there is no detection of the source in 20 hours of observation, the author of this thesis decided to not perform the simulations for RX J0852.0-4266 with 1% of Crab flux.

Figure A.7 shows the *BIC* values, in function of the livetime, obtained for the four CTAO's configurations. Each *BIC* value is the mean of 100 values. Also in this case, it is not possible to determine which configuration is discriminating the spatial models better than the others due to the large error bars.

A.3.2 RCW 86 results using 10% of Crab's flux

RCW 86 was simulated using its true flux with the same goals as the ones shown in A.3.1.

Figure A.8 shows the $\sqrt{TS}$ values, as a function of the livetime, obtained for the four CTAO's configurations. Also in this case, the source is not detected ($\sqrt{TS} < 5$) by none of the four configurations, but the F2 configuration is performing better than the others. In particular, after 20 hours of observation, the TS values of F2 is 14% larger than those of C0 and M2, while M2's value is 1% larger than C0's one. F4, as expected, since it has the smallest number of telescopes, is the one performing worst. In a future project, more hours of observations will be added to see when the different configurations hit the $\sqrt{TS} > 5$ threshold.

Figure A.9 shows the *BIC* values, in function of the livetime, obtained for the four CTAO's configurations. Figure A.9(a) shows that it is not possible to determine

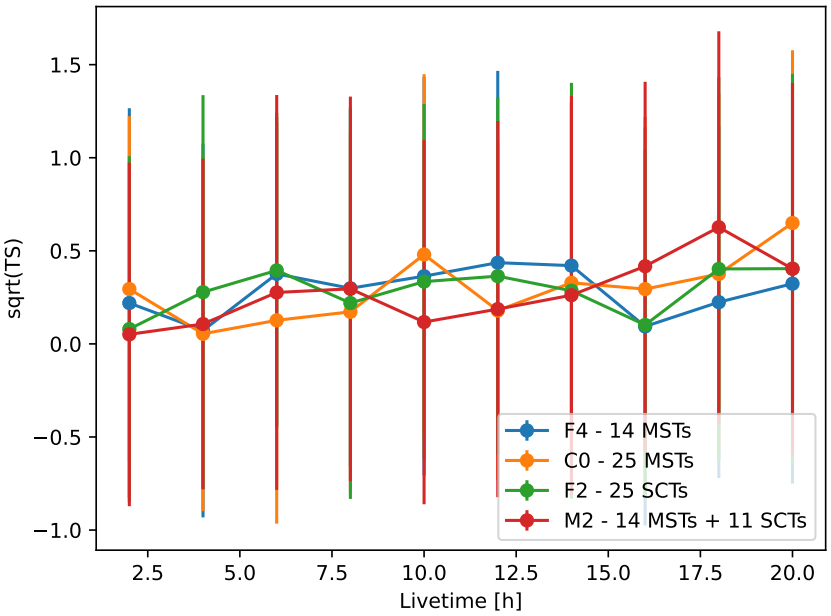

Figure A.6: RCW 86 1% Crab's flux $\sqrt{TS}$ versus livetime for four different CTAO configurations. The values of $\sqrt{TS}$ are the mean value obtained from 100 simulation for each livetime and each configuration of CTAO.

which configuration is discriminating the spatial model due to the large error bars. Figure A.9(b) and Figure A.9(c) show that F2 and M2 are the configurations that perform better. In particular, after 20 hours of observation, and fitting the extended source with a disk, F2 has a BIC value 34% larger than C0, and 26% larger than M2. M2 has a BIC value 8% larger than C0. After 20 hours of observation, and fitting the extended source with a Gaussian spatial model, F2 has a BIC value 41% larger than C0, and 30% larger than M2. M2 has a BIC value 11% larger than C0. Furthermore, the BIC's value in the disk case are smaller than the one in the Gaussian case meaning that the disk spatial model is favorite than the Gaussian spatial model. This result was expected since the Gaussian spatial model fits better Pulsar Wind Nebulae of *plerion-type* SNRs than the *shell-type* ones.

A.3.3 RCW 86 results using 100% of Crab's flux

RCW 86 was simulated using 100% of Crab's flux with the same goals as the ones shown in A.3.1.

Figure A.10 shows the $\sqrt{TS}$ values, in function of the livetime, obtained for the four CTAO's configurations. The source is detected ($\sqrt{TS} > 5$) by all the four configurations in 2 hours of observation and the F2 configuration is performing better than the others. In particular, after 20 hours of observation the TS values of F2 is 9% larger than the one of C0, 10% larger than M2, while M2's value is 1% larger than C0's one. F4 is the one performing worst.

Figure A.11 shows the *BIC* values, in function of the livetime, obtained for the four CTAO's configurations. Figure A.9(a) shows that it is not possible to determine which configuration is discriminating the spatial model due to the large error bars. Figure A.11(b) and Figure A.11(c) show that F2 and M2 are the configurations that

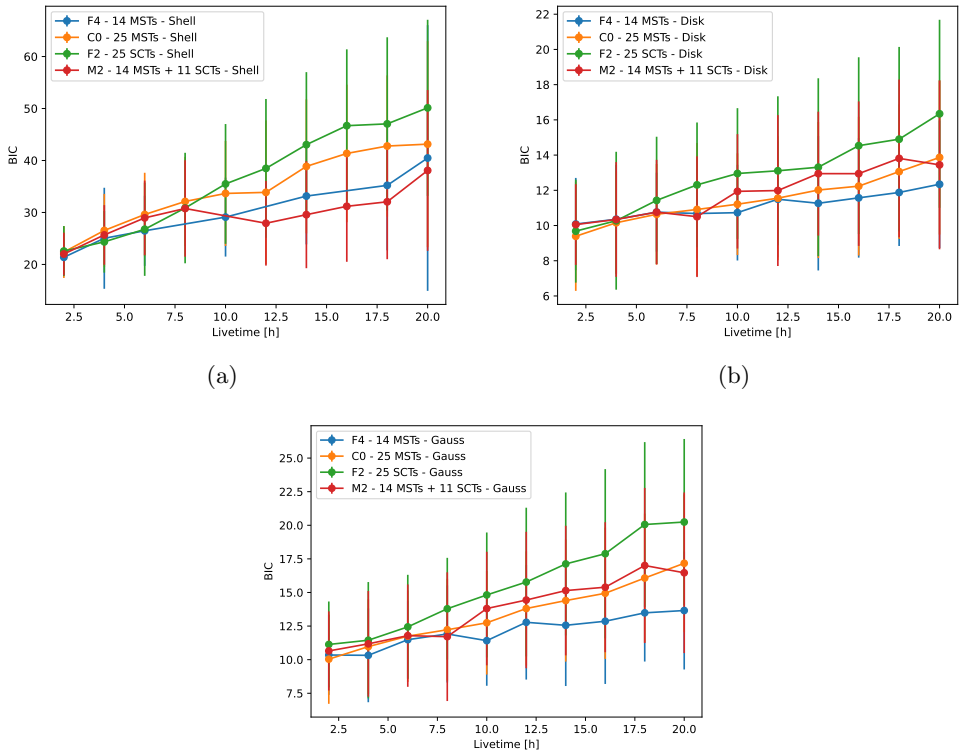

(a) (b)

(c)

Figure A.7: a) RCW 86 1% Crab's flux *BIC* versus livetime for four different CTAO configurations obtained fitting the extended source with a shell spatial model. b) RCW 86 1% Crab's flux *BIC* versus livetime for four different CTAO configurations obtained fitting the extended source with a disk spatial model. c) RCW 86 1% Crab's flux *BIC* versus livetime for four different CTAO configurations obtained fitting the extended source with a Gaussian spatial model. The values of *BIC* are the mean value obtained from 100 simulation for each livetime and each configuration of CTAO.

perform better. In particular, after 20 hours of observation, and fitting the extended source with a disk, F2 has a BIC value 27% larger than C0, and 22% larger than M2. M2 has a BIC value 5% larger than C0. After 20 hours of observation, and fitting the extended source with a Gaussian spatial model, F2 has a BIC value 37% larger than C0, and 30% larger than M2. M2 has a BIC value 7% larger than C0. As expected, the BIC's value in the disk case are smaller than the one in the Gaussian case.

A.3.4 RX J0852.0-4266 results using 13% of Crab's flux

RX J0852.0-4266 SNR was simulated using 13% of Crab's flux with the same goals as the ones shown in A.3.1.

Figure A.12 shows the $\sqrt{TS}$ values, in function of the livetime, obtained for the four CTAO's configurations. The source is detected ($\sqrt{TS} > 5$) by all the four configurations in 2 hours of observation and the F2 configuration is performing better than the others. In particular, after 20 hours of observation the TS values of F2 is

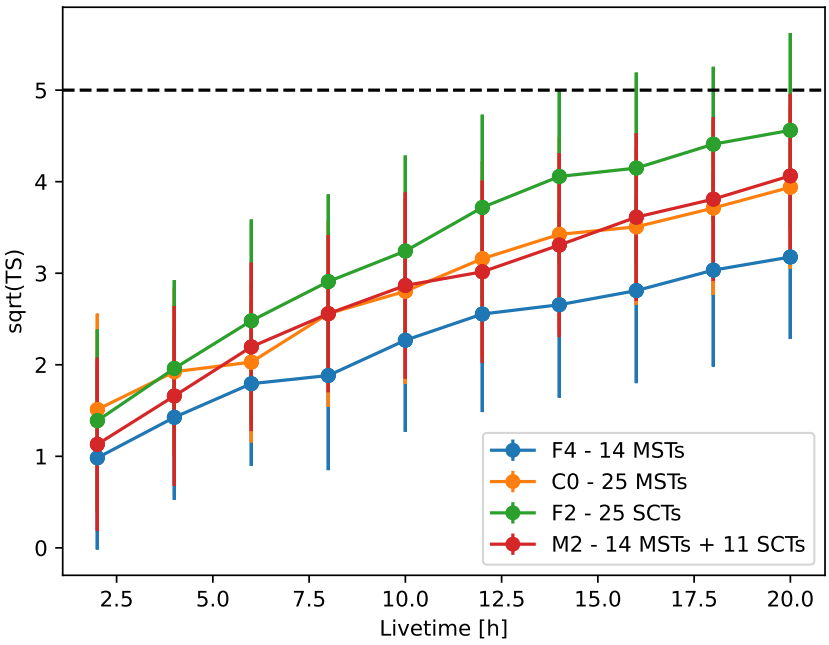

Figure A.8: RCW 86 true flux $\sqrt{TS}$ versus livetime for four different CTAO configurations. The values of $\sqrt{TS}$ are the mean value obtained from 100 simulations for each livetime and each configuration of CTAO.

9% larger than the one of C0, 10% larger than M2, while M2's value is 1% larger than C0's one. F4 is the one performing worst.

Figure A.13 shows the *BIC* values, as a function of the livetime, obtained for the four CTAO's configurations. Figure A.13(a) shows that it is not possible to determine which configuration is discriminating the spatial model due to the large error bars. Figure A.13(b) and Figure A.13(c) show that F2 and M2 are the configurations that perform better. In particular, after 20 hours of observation, and fitting the extended source with a disk, F2 has a BIC value 17% larger than C0, and 12% larger than M2. M2 has a BIC value 5% larger than C0. After 20 hours of observation, and fitting the extended source with a Gaussian spatial model, F2 has a BIC value 17% larger than C0, and 12% larger than M2. M2 has a BIC value 5% larger than C0. As expected, the BIC's value in the disk case are smaller than the one in the Gaussian case.

A.3.5 RX J0852.0-4266 results using 103% of Crab's flux

RX J0852.0-4266 SNR was simulated using its true flux with the same goals as the ones shown in A.3.1.

Figure A.14 shows the $\sqrt{TS}$ values, in function of the livetime, obtained for the four CTAO's configurations. The source is detected ($\sqrt{TS} > 5$) by all the four configurations in 2 hours of observation and the F2 configuration is performing better than the others. In particular, after 20 hours of observation the TS values of F2 is 5% larger than the one of C0, 6% larger than M2, while M2's value is 1% larger than C0's one. F4 is the one performing worst.

Figure A.15 shows the *BIC* values, in function of the livetime, obtained for the four

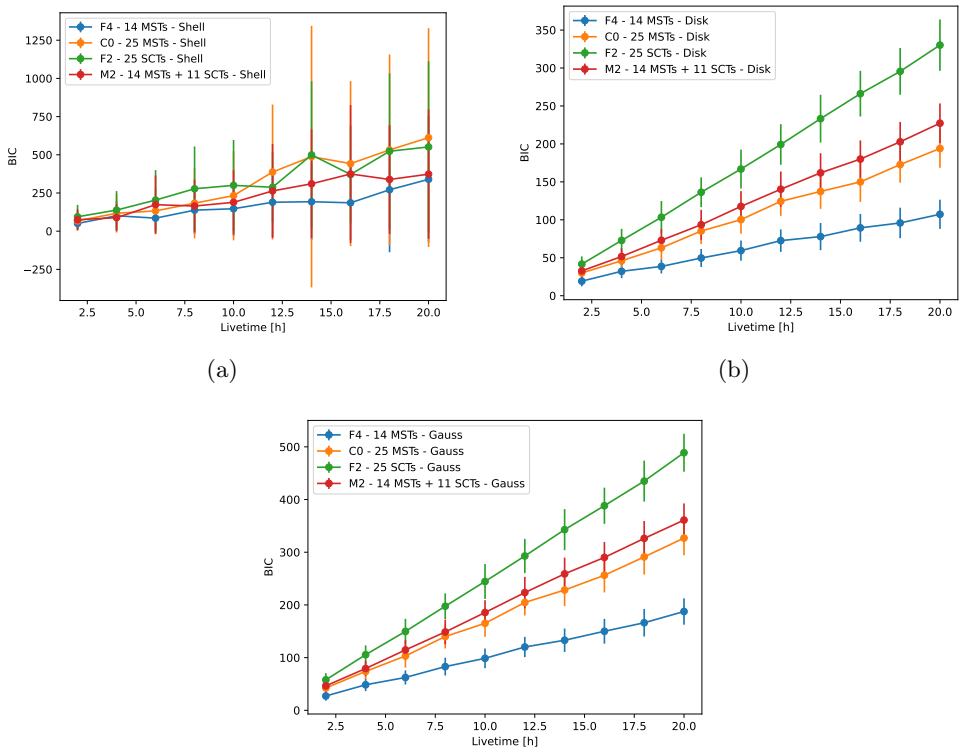

Figure A.9: a) RCW 86 10% Crab's flux *BIC* versus livetime for four different CTAO configurations obtained fitting the extended source with a shell spatial model. b) RCW 86 10% Crab's flux *BIC* versus livetime for four different CTAO configurations obtained fitting the extended source with a disk spatial model. c) RCW 86 10% Crab's flux *BIC* versus livetime for four different CTAO configurations obtained fitting the extended source with a Gaussian spatial model. The values of *BIC* are the mean value obtained from 100 simulation for each livetime and each configuration of CTAO.

CTAO's configurations. Figure A.15(a) shows that it is not possible to determine which configuration is discriminating the spatial model due to the large error bars. Figure A.15(b) and Figure A.15(c) show that F2, C0 and M2 are the configurations that perform better. In particular, after 20 hours of observation, and fitting the extended source with a disk, F2, M2 and C0 has BIC values almost equal. In the Gaussian spatial model case, M2 has BIC values 1% larger than the F2 one. As expected, the BIC's value in the disk case are smaller than the one in the Gaussian case.

A.3.6 The shell spatial model

The shell spatial model was expected to be the spatial model, after the template one, fitting the sources better than the disk and the Gaussian spatial models, because both SNRs are *shell-type*. However, from all the simulations, the shell spatial model does not reproduce the data well. This is mainly due to the fact that the analytical shell available in `gammapy` assumes a perfectly circular and symmetric structure with constant thickness. Real SNRs, on the other hand, are far more complex, showing

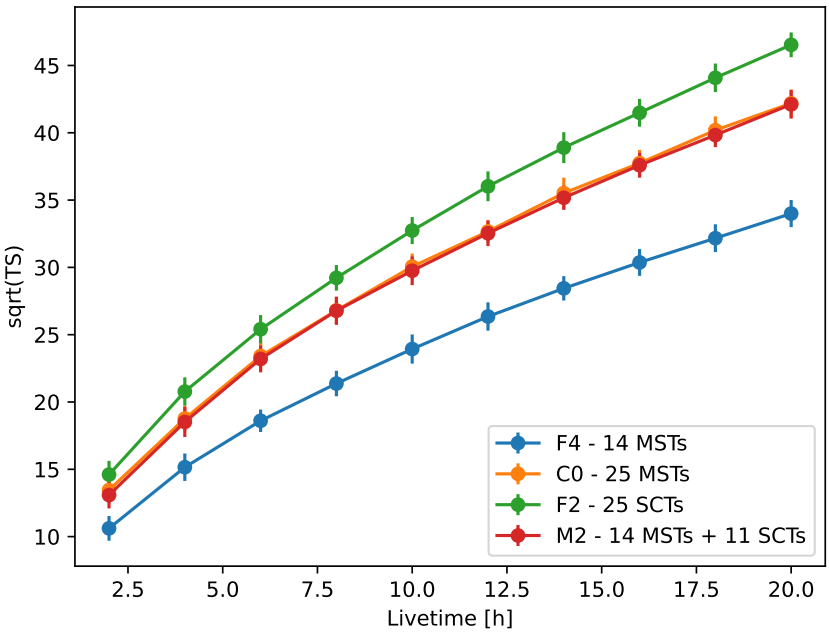

Figure A.10: RCW 86 true flux $\sqrt{TS}$ versus livetime for four different CTAO configurations. The values of $\sqrt{TS}$ are the mean value obtained from 100 simulation for each livetime and each configuration of CTAO.

irregular shapes, asymmetries, and variations in brightness that deviate significantly from such a simple model. As a result, even when adopting physical parameters consistent with the measured extension and thickness of the sources, the shell model cannot properly adapt to their true morphology. The templates include these irregularities, therefore remain the most accurate representation of their morphology. The disk model, despite being even simpler than a shell from a physical point of view, provides a better fit because it is not constrained to reproduce the bright morphology of a shell. Instead, it can approximate the emission as a smooth, extended source with a uniform profile, which adapts more easily to the irregular and asymmetric features present in the data. An example of `gammapy`'s `ShellSpatialModel` is shown in Figure A.16.

A.4 Summary

This project illustrates that the addition of SCTs in CTAO's Southern Hemisphere site will improve the detection and the spatial model discrimination of SNRs. Unfortunately, if the flux of the source is as small as 1% of the Crab's flux, none of the tested configurations can detect the SNRs in 20 hours of observation, and the model discrimination is not possible. On the other hand, sources with larger fluxes, from $10 - 13\%$ of Crab's flux, can be detected by all configurations. In these cases, the model discrimination is possible, with the disk model as the second-best spatial model and the Gaussian one after it. In particular, the configurations that showed better performances are F2, composed of 25SCTs, and M2, which is composed of both MSTs and SCTs. The configuration made by only 25MSTs shows similar performances to M2, but configurations including SCTs are still better thanks to the

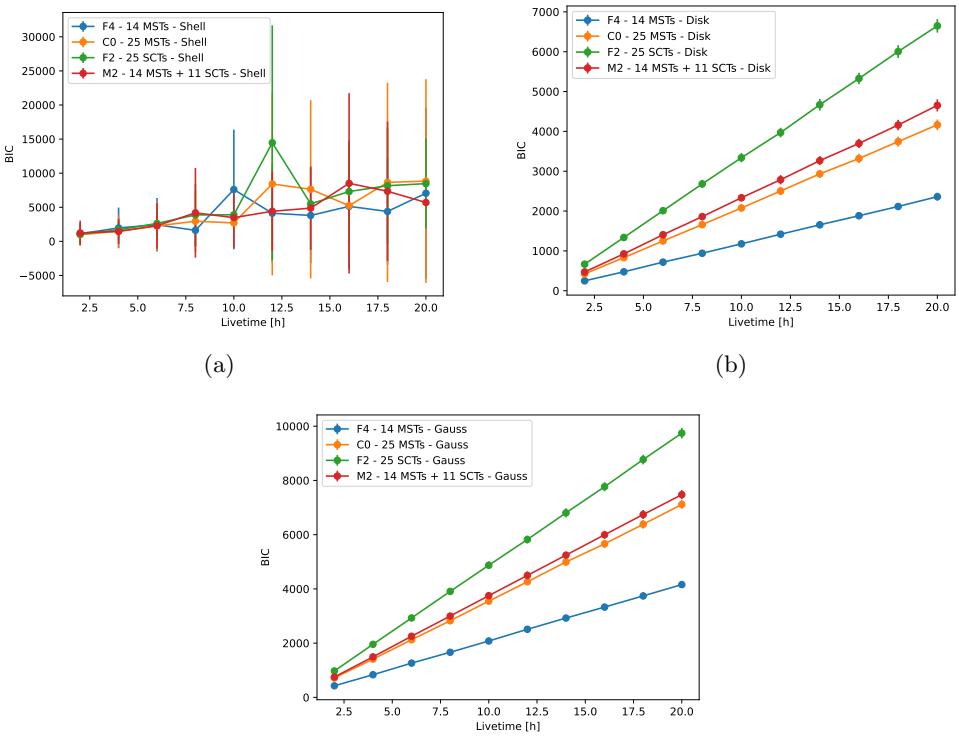

Figure A.11: a) RCW 86 100% Crab's flux *BIC* versus livetime for four different CTAO configurations obtained fitting the extended source with a shell spatial model. b) RCW 86 100% Crab's flux *BIC* versus livetime for four different CTAO configurations obtained fitting the extended source with a disk spatial model. c) RCW 86 100% Crab's flux *BIC* versus livetime for four different CTAO configurations obtained fitting the extended source with a Gaussian spatial model. The values of *BIC* are the mean value obtained from 100 simulation for each livetime and each configuration of CTAO.

better angular resolution due to their dual-optic system.

When prod6 IRFs will be published, this study will be performed again to see if the difference between M2 and C0 is still small and to confirm the goodness of the addition of SCTs to the CTAO's Southern Hemisphere site.

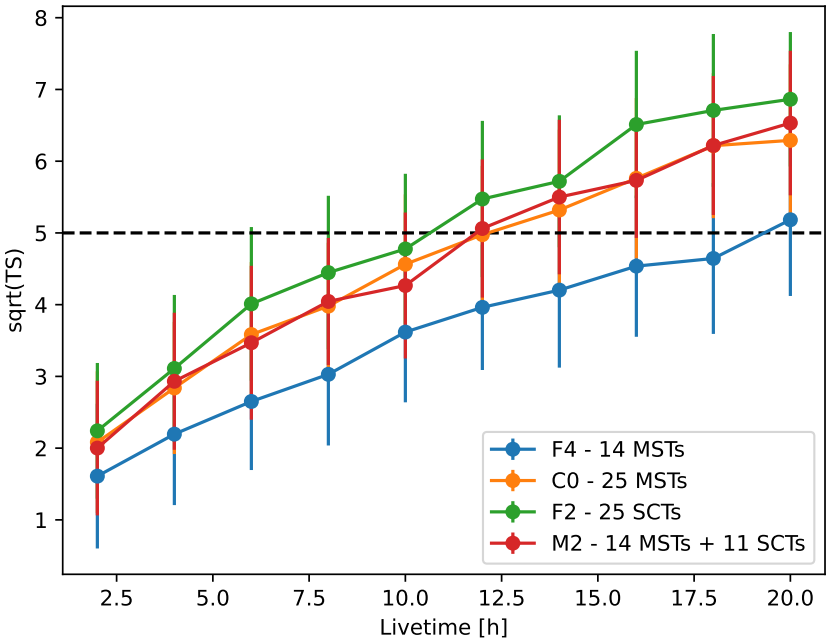

Figure A.12: RX J0852.0-4266 13% of Crab's flux $\sqrt{TS}$ versus livetime for four different CTAO configurations. The values of $\sqrt{TS}$ are the mean value obtained from 100 simulations for each livetime and each configuration of CTAO.

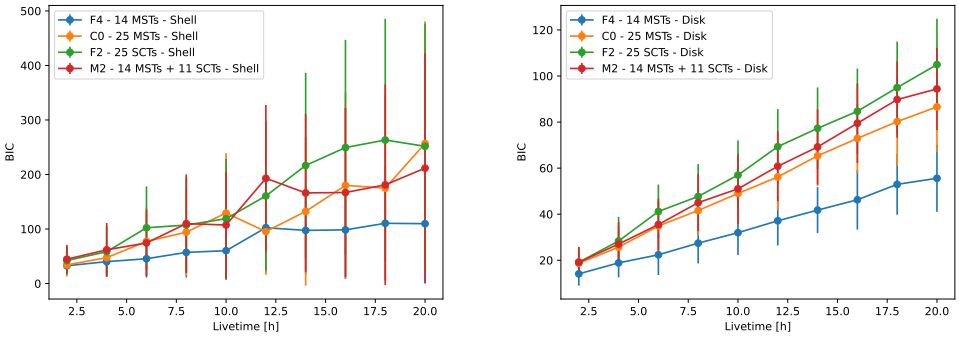

(a)

(b)

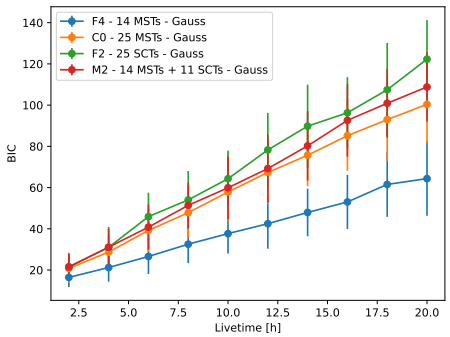

(c)

Figure A.13: a) RX J0852.0-4266 10% Crab's flux *BIC* versus livetime for four different CTAO configurations obtained fitting the extended source with a shell spatial model. b) RX J0852.0-4266 10% Crab's flux *BIC* versus livetime for four different CTAO configurations obtained fitting the extended source with a disk spatial model. c) RX J0852.0-4266 10% Crab's flux *BIC* versus livetime for four different CTAO configurations obtained fitting the extended source with a Gaussian spatial model. The values of *BIC* are the mean value obtained from 100 simulation for each livetime and each configuration of CTAO.

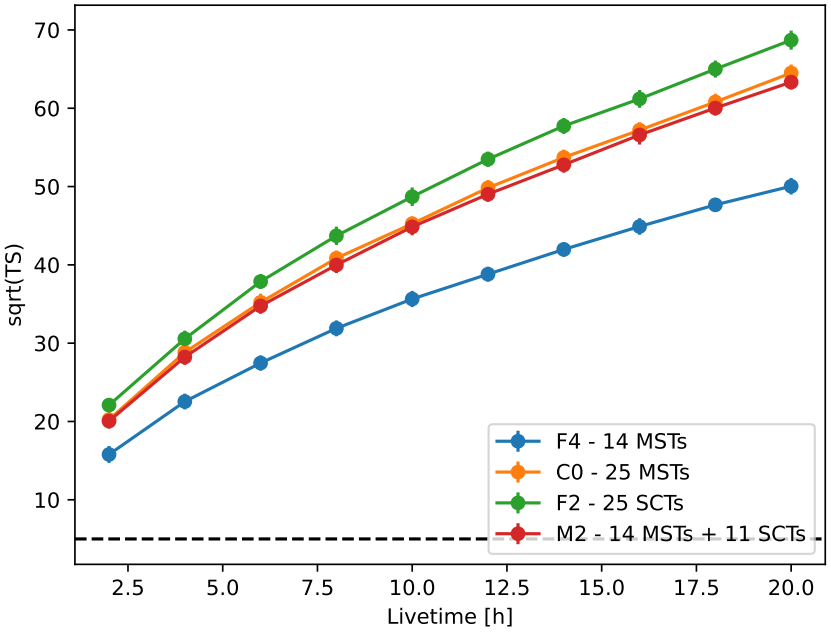

Figure A.14: RX J0852.0-4266 true flux $\sqrt{TS}$ versus livetime for four different CTAO configurations. The values of $\sqrt{TS}$ are the mean value obtained from 100 simulation for each livetime and each configuration of CTAO.

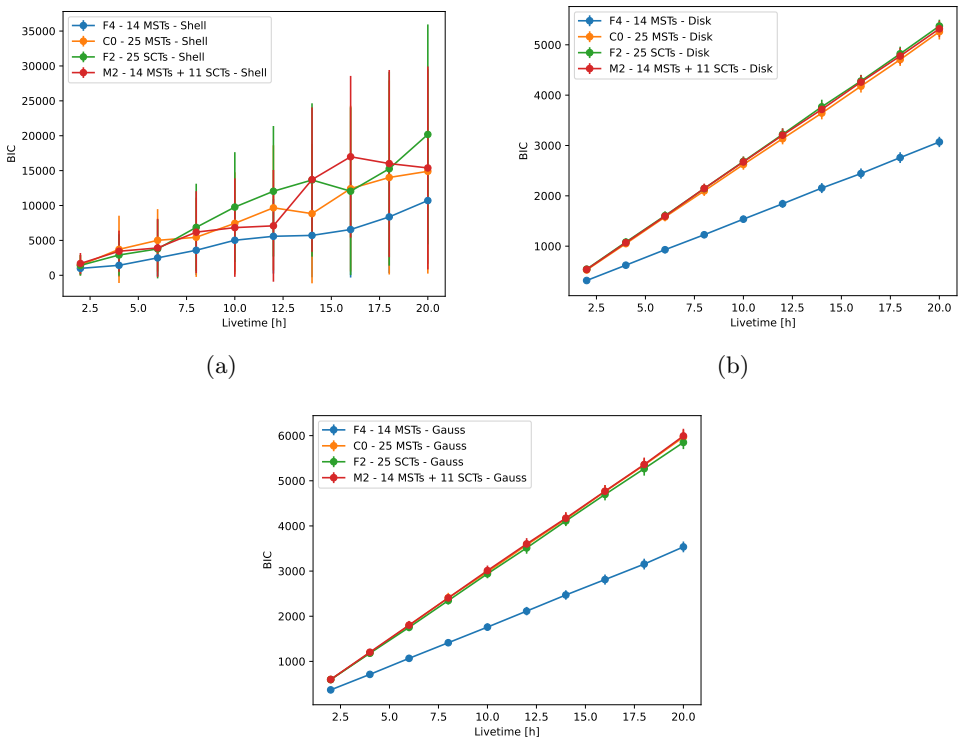

Figure A.15: a) RX J0852.0-4266 true flux *BIC* versus livetime for four different CTAO configurations obtained fitting the extended source with a shell spatial model. b) RX J0852.0-4266 true flux *BIC* versus livetime for four different CTAO configurations obtained fitting the extended source with a disk spatial model. c) RX J0852.0-4266 true flux *BIC* versus livetime for four different CTAO configurations obtained fitting the extended source with a Gaussian spatial model. The values of *BIC* are the mean value obtained from 100 simulation for each livetime and each configuration of CTAO.

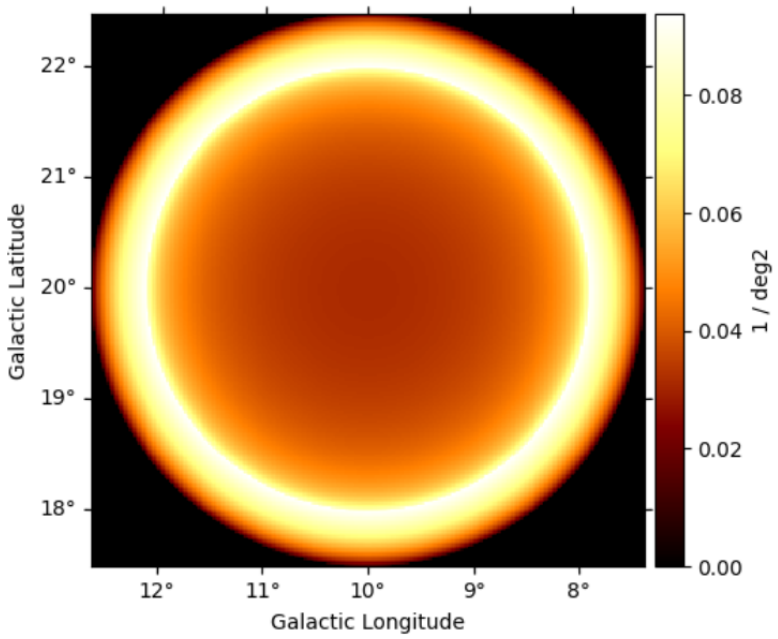

Figure A.16: `Gammapy`'s `ShellSpatialModel` obtained using 2 deg as radius and 0.5 deg as width.

Acknowledgments

The *Fermi* LAT Collaboration acknowledges generous ongoing support from a number of agencies and institutes that have supported both the development and the operation of the LAT as well as scientific data analysis. These include the National Aeronautics and Space Administration and the Department of Energy in the United States, the Commissariat à l'Energie Atomique and the Centre National de la Recherche Scientifique / Institut National de Physique Nucléaire et de Physique des Particules in France, the Agenzia Spaziale Italiana and the Istituto Nazionale di Fisica Nucleare in Italy, the Ministry of Education, Culture, Sports, Science and Technology (MEXT), High Energy Accelerator Research Organization (KEK) and Japan Aerospace Exploration Agency (JAXA) in Japan, and the K. A. Wallenberg Foundation, the Swedish Research Council and the Swedish National Space Board in Sweden.

This thesis was conducted in the context of the CTAO EGAL working group. CTAO gratefully acknowledges financial support from the agencies and organizations listed at https://www.ctao.org/for-scientists/library/acknowledgments/. We would like to thank the computing centers that provided resources for the IRF generation, listed at `https://zenodo.org/records/5499840`.

This thesis has made use of the NASA/IPAC Infrared Science Archive, which is funded by the National Aeronautics and Space Administration and operated by the California Institute of Technology.

This thesis makes use of data obtained at Metsähovi Radio Observatory, operated by Aalto University in Finland.

This thesis makes use of data based on observations with the 100 m telescope of the MPIfR (Max-Planck-Institut für Radioastronomie). I.M., I.N. and V.K. were funded by the International Max Planck Research School (IMPRS) for Astronomy and Astrophysics at the Universities of Bonn and Cologne.

This thesis has made use of data from the MOJAVE database that is maintained by the MOJAVE team [216].

This thesis makes use of VLBA data from the VLBA-BU Blazar Monitoring Program (BEAM-ME and VLBA-BU-BLAZAR; `http://www.bu.edu/blazars/BEAM-ME.html`), funded by NASA through the Fermi Guest Investigator Program. The VLBA is an instrument of the National Radio Astronomy Observatory. The National Radio Astronomy Observatory is a facility of the National Science Foundation operated by Associated Universities, Inc.

This thesis has made use of data from the MOJAVE database that is maintained by the MOJAVE team [216].

Partly based on observations with the 100-m telescope of the MPIfR (Max-Planck-Institut für Radioastronomie) at Effelsberg. Observations with the 100-m radio telescope at Effelsberg have received funding from the European Union's Horizon 2020 research and innovation programme under grant agreement No 101004719 (ORP).

The Submillimeter Array is a joint project between the Smithsonian Astrophysical Observatory and the Academia Sinica Institute of Astronomy and Astrophysics and is funded by the Smithsonian Institution and the Academia Sinica. Maunakea, the location of the SMA, is a culturally important site for the indigenous Hawaiian people; we are privileged to study the cosmos from its summit.

This thesis has made use of data from the Joan Oró Telescope (TJO) of the Montsec Observatory (OdM), which is owned by the Catalan Government and operated by the Institute for Space Studies of Catalonia (IEEC). Based on observations obtained with the Samuel Oschin Telescope 48-inch and the 60-inch Telescope at the Palomar Observatory as part of the Zwicky Transient Facility project. ZTF is supported by the National Science Foundation under Grant No. AST-2034437 and a collaboration including Caltech, IPAC, the Weizmann Institute for Science, the Oskar Klein Center at Stockholm University, the University of Maryland, Deutsches Elektronen-Synchrotron and Humboldt University, the TANGO Consortium of Taiwan, the University of Wisconsin at Milwaukee, Trinity College Dublin, Lawrence Livermore National Laboratories, and IN2P3, France. Operations are conducted by COO, IPAC, and UW. The ZTF forced-photometry service was funded under the Heising-Simons Foundation grant #12540303 (PI: M.J.Graham). This work has made use of data from the Asteroid Terrestrialimpact Last Alert System (ATLAS) project. The Asteroid Terrestrial-impact Last Alert System (ATLAS) project is primarily funded to search for near earth asteroids through NASA grants NN12AR55G, 80NSSC18K0284, and 80NSSC18K1575; byproducts of the NEO smarch include images and catalogs from the survey area. This work was partially funded by Kepler/K2 grant J1944/80NSSC19K0112 and HST GO-15889, and STFC grants ST/T000198/1 and ST/S006109/1. The ATLAS science products have been made possible through the contributions of the University of Hawaii Institute for Astronomy, the Queen's University Belfast, the Space Telescope Science Institute, the South African Astronomical Observatory, and The Millennium Institute of Astrophysics (MAS), Chile.

Bibliography

[1] M. G. Aartsen et al., "Energy reconstruction methods in the IceCube neutrino telescope", en, Journal of Instrumentation **9**, P03009 (2014).

[2] M. G. Aartsen et al., "All-sky Search for Time-integrated Neutrino Emission from Astrophysical Sources with 7 yr of IceCube Data", en, The Astrophysical Journal **835**, Publisher: The American Astronomical Society, 151 (2017).

[3] M. G. Aartsen et al., "Search for Astrophysical Sources of Neutrinos Using Cascade Events in IceCube", en, The Astrophysical Journal **846**, Publisher: The American Astronomical Society, 136 (2017).

[4] M. G. Aartsen et al., "The IceCube realtime alert system", Astroparticle Physics **92**, Publisher: Elsevier ADS Bibcode: 2017APh....92...30A, 30–41 (2017).

[5] B. P. Abbott et al., "Gravitational Waves and Gamma-Rays from a Binary Neutron Star Merger: GW170817 and GRB 170817A", The Astrophysical Journal **848**, ADS Bibcode: 2017ApJ...848L..13A, L13 (2017).

[6] B. P. Abbott et al., "GW170817: Observation of Gravitational Waves from a Binary Neutron Star Inspiral", en, Physical Review Letters **119**, 161101 (2017).

[7] A. A. Abdo et al., "THE SPECTRAL ENERGY DISTRIBUTION OF FERMI BRIGHT BLAZARS", en, The Astrophysical Journal **716**, Publisher: The American Astronomical Society, 30 (2010).

[8] A. A. Abdo et al., "THE SECOND FERMI LARGE AREA TELESCOPE CATALOG OF GAMMA-RAY PULSARS", en, The Astrophysical Journal Supplement Series **208**, Publisher: The American Astronomical Society, 17 (2013).

[9] S. Abdollahi et al., "Fermi Large Area Telescope Fourth Source Catalog", en, The Astrophysical Journal Supplement Series **247**, Publisher: The American Astronomical Society, 33 (2020).

[10] S. Abdollahi et al., "Incremental Fermi Large Area Telescope Fourth Source Catalog", en, The Astrophysical Journal Supplement Series **260**, Publisher: The American Astronomical Society, 53 (2022).

[11] S. Abdollahi et al., "The Fermi-LAT Lightcurve Repository*", en, The Astrophysical Journal Supplement Series **265**, Publisher: The American Astronomical Society, 31 (2023).

[12] A. U. Abeysekara et al., "Multiwavelength observations of the blazar BL Lacertae: a new fast TeV gamma-ray flare", en, The Astrophysical Journal **856**, arXiv:1802.10113 [astro-ph], 95 (2018).

[13] F. Acero et al., “FERMI LARGE AREA TELESCOPE THIRD SOURCE CATALOG”, en, The Astrophysical Journal Supplement Series **218**, Publisher: The American Astronomical Society, 23 (2015).

[14] A. Acharyya and A. C. Sadun, “Investigating Possible Correlations between Gamma-Ray and Optical Lightcurves for TeV-Detected Northern Blazars over 8 Years of Observations”, en, Galaxies **11**, Number: 4 Publisher: Multidisciplinary Digital Publishing Institute, 81 (2023).

[15] M. Ackermann et al., “FERMI-LAT OBSERVATIONS OF THE DIFFUSE GAMMA-RAY EMISSION: IMPLICATIONS FOR COSMIC RAYS AND THE INTERSTELLAR MEDIUM”, en, The Astrophysical Journal **750**, Publisher: The American Astronomical Society, 3 (2012).

[16] M. Ackermann et al., “The Fermi All-sky Variability Analysis: A List of Flaring Gamma-Ray Sources and the Search for Transients in Our Galaxy”, The Astrophysical Journal **771**, ADS Bibcode: 2013ApJ...771...57A, 57 (2013).

[17] M. Ackermann et al., “THE SPECTRUM OF ISOTROPIC DIFFUSE GAMMA-RAY EMISSION BETWEEN 100 MeV AND 820 GeV”, en, The Astrophysical Journal **799**, Publisher: The American Astronomical Society, 86 (2015).

[18] M. Ackermann et al., “Fermi Large Area Telescope Detection of Extended Gamma-Ray Emission from the Radio Galaxy Fornax A”, The Astrophysical Journal **826**, ADS Bibcode: 2016ApJ...826....1A, 1 (2016).

[19] M. Ackermann et al., “MINUTE-TIMESCALE ¿100 MeV -RAY VARIABILITY DURING THE GIANT OUTBURST OF QUASAR 3C 279 OBSERVED BY FERMI-LAT IN 2015 JUNE”, en, The Astrophysical Journal Letters **824**, Publisher: The American Astronomical Society, L20 (2016).

[20] C. B. Adams et al., “Variability and Spectral Characteristics of Three Flaring Gamma-Ray Quasars Observed by VERITAS and Fermi-LAT”, en, The Astrophysical Journal **924**, Publisher: The American Astronomical Society, 95 (2022).

[21] I. Agudo, A. Marscher, S. G. Jorstad, and J. L. Gómez, *Discerning the location of the gamma-ray emission region in blazars from multi-messenger observations*, Conference Name: Highlights of Spanish Astrophysics VII ADS Bibcode: 2013hsa7.conf..152A, eprint: arXiv:1210.2234, May 2013.

[22] F. Aharonian et al., “Observations of the Crab nebula with HESS”, en, Astronomy & Astrophysics **457**, Publisher: EDP Sciences, 899–915 (2006).

[23] F. Aharonian et al., “An Exceptional Very High Energy Gamma-Ray Flare of PKS 2155–304”, en, The Astrophysical Journal **664**, Publisher: IOP Publishing, L71 (2007).

[24] F. A. Aharonian, “TeV gamma rays from BL Lac objects due to synchrotron radiation of extremely high energy protons”, New Astronomy **5**, ADS Bibcode: 2000NewA....5..377A, 377–395 (2000).

[25] S. Aiello et al., “Observation of an ultra-high-energy cosmic neutrino with KM3NeT”, en, Nature **638**, Publisher: Nature Publishing Group, 376–382 (2025).

[26] G. B. Airy, “On the Diffraction of an Object-glass with Circular Aperture”, Transactions of the Cambridge Philosophical Society **5**, ADS Bibcode: 1835TCaPS...5..283A, 283 (1835).

[27] F. D. Albareti et al., "The 13th Data Release of the Sloan Digital Sky Survey: First Spectroscopic Data from the SDSS-IV Survey Mapping Nearby Galaxies at Apache Point Observatory", The Astrophysical Journal Supplement Series **233**, ADS Bibcode: 2017ApJS..233...25A, 25 (2017).

[28] J. Aleksić et al., "The major upgrade of the MAGIC telescopes, Part II: A performance study using observations of the Crab Nebula", Astroparticle Physics **72**, 76–94 (2016).

[29] T. Alexander, "Is AGN Variability Correlated with Other AGN Properties?—ZDCF Analysis of Small Samples of Sparse Light Curves", en, in Astronomical Time Series, edited by D. Maoz, A. Sternberg, and E. M. Leibowitz (1997), pp. 163–166.

[30] T. Alexander, *Improved AGN light curve analysis with the z-transformed discrete correlation function*, en, arXiv:1302.1508 [astro-ph], Feb. 2013.

[31] R. R. J. Antonucci and J. S. Miller, "Spectropolarimetry and the nature of NGC 1068.", The Astrophysical Journal **297**, Publisher: IOP ADS Bibcode: 1985ApJ...297..621A, 621–632 (1985).

[32] K. A. Arnaud, "XSPEC: The First Ten Years", **101**, Conference Name: Astronomical Data Analysis Software and Systems V ADS Bibcode: 1996ASPC..101...17A, 17 (1996).

[33] B. Aschenbach, "X-ray telescopes", en, Reports on Progress in Physics **48**, 579 (1985).

[34] A. Atoyan and C. D. Dermer, "High-Energy Neutrinos from Photomeson Processes in Blazars", Physical Review Letters **87**, Publisher: American Physical Society, 221102 (2001).

[35] W. Atwood et al., *Pass 8: Toward the Full Realization of the Fermi-LAT Scientific Potential*, ADS Bibcode: 2013arXiv1303.3514A, Mar. 2013.

[36] W. B. Atwood et al., "THE LARGE AREA TELESCOPE ON THE FERMI GAMMA-RAY SPACE TELESCOPE MISSION", en, The Astrophysical Journal **697**, Publisher: The American Astronomical Society, 1071 (2009).

[37] J. Ballet, P. Bruel, T. H. Burnett, B. Lott, and T. F.-L. collaboration, *Fermi Large Area Telescope Fourth Source Catalog Data Release 4 (4FGL-DR4)*, arXiv:2307.12546 [astro-ph], July 2024.

[38] A. Bamba and B. J. Williams, "Supernova remnants: Types and evolution", en, in , arXiv:2211.02217 [astro-ph] (2022), pp. 1–12.

[39] C. Bartolini, *ATel #16497: Fermi-LAT detection of renewed gamma-ray activity from the FSRQ OP 313*, Jan. 2024.

[40] C. Bartolini, F. Giacchino, D. Elenterio, and M. S. Gisonna, *ATel #16356: Fermi-LAT detection of renewed gamma-ray activity from the FSRQ OP 313, and enhanced gamma-ray activity from the FSRQ ON 393*, Jan. 2023.

[41] R. Barvainis, "Hot Dust and the Near-Infrared Bump in the Continuum Spectra of Quasars and Active Galactic Nuclei", The Astrophysical Journal **320**, Publisher: IOP ADS Bibcode: 1987ApJ...320..537B, 537 (1987).

[42] V. Beckmann and C. R. Shrader, *Active Galactic Nuclei*, Publication Title: Active Galactic Nuclei ADS Bibcode: 2012agn..book.....B (Aug. 2012).

[43] M. C. Begelman, “Can a spherically accreting black hole radiate very near the Eddington limit”, Monthly Notices of the Royal Astronomical Society **187**, 237–251 (1979).

[44] M. C. Begelman, R. D. Blandford, and M. J. Rees, “Theory of extragalactic radio sources”, Reviews of Modern Physics **56**, Publisher: American Physical Society, 255–351 (1984).

[45] A. R. Bell, A. T. Araudo, J. H. Matthews, and K. M. Blundell, “Cosmic-ray acceleration by relativistic shocks: limits and estimates”, Monthly Notices of the Royal Astronomical Society **473**, 2364–2371 (2018).

[46] E. C. Bellm et al., “The Zwicky Transient Facility: System Overview, Performance, and First Results”, en, Publications of the Astronomical Society of the Pacific **131**, Publisher: The Astronomical Society of the Pacific, 018002 (2018).

[47] G. F. Bignami et al., “The COS-B experiment for gamma-ray astronomy.”, Space Science Instrumentation **1**, ADS Bibcode: 1975SSI.....1..245B, 245–268 (1975).

[48] R. D. Blandford and A. Königl, “Relativistic jets as compact radio sources.”, The Astrophysical Journal **232**, Publisher: IOP ADS Bibcode: 1979ApJ...232...34B, 34–48 (1979).

[49] R. Blandford, D. Meier, and A. Readhead, “Relativistic Jets from Active Galactic Nuclei”, en, Annual Review of Astronomy and Astrophysics **57**, Publisher: Annual Reviews, 467–509 (2019).

[50] P. Blasi, “The origin of galactic cosmic rays”, en, The Astronomy and Astrophysics Review **21**, 70 (2013).

[51] E. Blaufuss, T. Kintscher, L. Lu, and C. F. Tung, “The Next Generation of IceCube Real-time Neutrino Alerts”, in , Vol. 36, ADS Bibcode: 2019ICRC...36.1021B (July 2019), p. 1021.

[52] M. Błażejowski, M. Sikora, R. Moderski, and G. M. Madejski, “Comptonization of Infrared Radiation from Hot Dust by RelativisticJets inQuasars”, en, The Astrophysical Journal **545**, Publisher: IOP Publishing, 107 (2000).

[53] M. Boettcher, D. E. Harris, and H. Krawczynski, *Relativistic Jets from Active Galactic Nuclei*, Publication Title: Relativistic Jets from Active Galactic Nuclei ADS Bibcode: 2012rjag.book.....B (Jan. 2012).

[54] K. J. Borkowski et al., “Dust Destruction in Type Ia Supernova Remnants in the Large Magellanic Cloud”, en, The Astrophysical Journal **642**, Publisher: IOP Publishing, L141 (2006).

[55] M. Böttcher, A. Reimer, K. Sweeney, and A. Prakash, “LEPTONIC AND HADRONIC MODELING OF FERMI-DETECTED BLAZARS”, en, The Astrophysical Journal **768**, Publisher: The American Astronomical Society, 54 (2013).

[56] M. Böttcher and P. Els, “GAMMA–GAMMA ABSORPTION IN THE BROAD LINE REGION RADIATION FIELDS OF GAMMA-RAY BLAZARS”, en, The Astrophysical Journal **821**, Publisher: The American Astronomical Society, 102 (2016).

[57] A. A. Breeveld, W. Landsman, S. T. Holland, P. Roming, N. P. M. Kuin, and M. J. Page, "An Updated Ultraviolet Calibration for the Swift/UVOT", in , Vol. 1358, ADS Bibcode: 2011AIPC.1358..373B (Aug. 2011), pp. 373–376.

[58] S. Britzen et al., "A swirling jet in the quasar 1308+326", Astronomy and Astrophysics **602**, Publisher: EDP ADS Bibcode: 2017A&A...602A..29B, A29 (2017).

[59] A. M. Brown, "Locating the -ray emission region of the flat spectrum radio quasar PKS 1510089", Monthly Notices of the Royal Astronomical Society **431**, 824–835 (2013).

[60] Buson, *ATel #6068: Fermi LAT Detection of a GeV Flare from OP 313 (B2 1308+32)*, 2014.

[61] S. Buson, S. Garrappa, C. C. Cheung, and M. Ajell, "Fermi-LAT Gamma-ray Observations of IceCube-201021A and detection of a new gamma-ray source, Fermi J1725.5+1312", The Astronomer's Telegram **14111**, ADS Bibcode: 2020ATel14111....1B, 1 (2020).

[62] S. Buson, S. Garrappa, and Fermi-LAT Collaboration, "Fermi-LAT Gamma-ray Observations of IceCube-190523A", GRB Coordinates Network **27816**, ADS Bibcode: 2020GCN.27816....1B, 1 (2020).

[63] S. Buson, S. Garrappa, and Fermi-LAT Collaboration, "Fermi-LAT Gamma-ray Observations of IceCube-200530A", GRB Coordinates Network **27879**, ADS Bibcode: 2020GCN.27879....1B, 1 (2020).

[64] M. Bustamante et al., "High-energy cosmic-ray acceleration", en,

[65] Z. Cao et al., "Introduction to Large High Altitude Air Shower Observatory (LHAASO)", Acta Astronomica Sinica **60**, ADS Bibcode: 2019AcASn..60...19C, 19 (2019).

[66] Z. Cao et al., "Discovery of the Ultrahigh-energy Gamma-Ray Source LHAASO J2108+5157", en, The Astrophysical Journal Letters **919**, Publisher: The American Astronomical Society, L22 (2021).

[67] Z. Cao et al., "Ultrahigh-energy photons up to 1.4 petaelectronvolts from 12 -ray Galactic sources", Nature **594**, ADS Bibcode: 2021Natur.594...33C, 33–36 (2021).

[68] C. Casadio, J. L. Gómez, P. Grandi, S. G. Jorstad, A. P. Marscher, M. L. Lister, Y. Y. Kovalev, T. Savolainen, and A. B. Pushkarev, "THE CONNECTION BETWEEN THE RADIO JET AND THE GAMMA-RAY EMISSION IN THE RADIO GALAXY 3C 120", en, The Astrophysical Journal **808**, Publisher: The American Astronomical Society, 162 (2015).

[69] C. Casadio et al., "A MULTI-WAVELENGTH POLARIMETRIC STUDY OF THE BLAZAR CTA 102 DURING A GAMMA-RAY FLARE IN 2012", en, The Astrophysical Journal **813**, Publisher: The American Astronomical Society, 51 (2015).

[70] W. Cash, "Parameter estimation in astronomy through application of the likelihood ratio.", The Astrophysical Journal **228**, ADS Bibcode: 1979ApJ...228..939C, 939–947 (1979).

[71] A. Celotti and G. Ghisellini, "The power of blazar jets: The power of blazar jets", en, Monthly Notices of the Royal Astronomical Society **385**, 283–300 (2008).

[72] M. Cerruti, A. Zech, C. Boisson, and S. Inoue, "A hadronic origin for ultra-high-frequency-peaked BL Lac objects", Monthly Notices of the Royal Astronomical Society **448**, 910–927 (2015).

[73] M. Cerruti et al., "Target of opportunity observations of blazars with H.E.S.S.", AIP Conference Proceedings **1792**, 050029 (2017).

[74] K. C. Chambers et al., *The Pan-STARRS1 Surveys*, arXiv:1612.05560 [astro-ph], Jan. 2019.

[75] C. C. Cheung, D. Gasparrini, and S. Buson, "Fermi LAT detection of GeV flaring activity from blazar Ton 599 (4C +29.45)", The Astronomer's Telegram **10931**, ADS Bibcode: 2017ATel10931....1C, 1 (2017).

[76] C. C. Cheung, D. E. Harris, and Ł. Stawarz, "Superluminal Radio Features in the M87 Jet and the Site of Flaring TeV Gamma-Ray Emission", en, The Astrophysical Journal **663**, Publisher: IOP Publishing, L65 (2007).

[77] R. A. Chevalier, R. P. Kirshner, and J. C. Raymond, "The optical emission from a fast shock wave with application to supernova remnants.", The Astrophysical Journal **235**, Publisher: IOP ADS Bibcode: 1980ApJ...235..186C, 186–195 (1980).

[78] T. Chiarusi and M. Spurio, "High-energy astrophysics with neutrino telescopes", en, The European Physical Journal C **65**, 649–701 (2010).

[79] S. Ciprini, "Fermi LAT confirmation of a strong GeV flare from 4C 21.35 (PKS 1222+21)", The Astronomer's Telegram **2349**, ADS Bibcode: 2009ATel.2349....1C, 1 (2009).

[80] S. Ciprini, *ATel #7801: Fermi-LAT detection of hard spectrum and highest-level gamma-ray outburst from the distant blazar PKS 1502+106*, July 2015.

[81] K. Cleary, C. R. Lawrence, J. A. Marshall, L. Hao, and D. Meier, "Spitzer Observations of 3C Quasars and Radio Galaxies: Mid-Infrared Properties of Powerful Radio Sources", en, The Astrophysical Journal **660**, Publisher: IOP Publishing, 117 (2007).

[82] T. E. H. T. Collaboration et al., "First M87 Event Horizon Telescope Results. I. The Shadow of the Supermassive Black Hole", en, The Astrophysical Journal Letters **875**, Publisher: The American Astronomical Society, L1 (2019).

[83] T. K.-G. Collaboration et al., "KASCADE-Grande measurements of energy spectra for elemental groups of cosmic rays", en, Astroparticle Physics **47**, arXiv:1306.6283 [astro-ph], 54–66 (2013).

[84] T. L. S. Collaboration and t. V. Collaboration, "GW150914: Implications for the stochastic gravitational wave background from binary black holes", en, Physical Review Letters **116**, arXiv:1602.03847 [gr-qc], 131102 (2016).

[85] T. P. A. Collaboration et al., "Constraining the sources of ultra-high-energy cosmic rays across and above the ankle with the spectrum and composition data measured at the Pierre Auger Observatory", Journal of Cosmology and Astroparticle Physics **2023**, arXiv:2211.02857 [astro-ph], 024 (2023).

[86] S. D. Connolly, *ASCL.net - DELightcurveSimulation: Light curve simulation code*, 2016.

[87] J. Cortina, *ATel #16381: First detection of VHE gamma-ray emission from FSRQ OP 313 with LST-1*, 2023.

[88] L. Costamante, S. Cutini, G. Tosti, E. Antolini, and A. Tramacere, "On the origin of gamma-rays in Fermi blazars: beyondthe broad-line region", Monthly Notices of the Royal Astronomical Society **477**, 4749–4767 (2018).

[89] *CTAO-North*, en-US.

[90] *CTAO-South*, en-US.

[91] F. D'Ammando, *ATel #3473: Fermi LAT detection of a very intense and rapid gamma-ray flare from the blazar PKS 1510-089*, July 2011.

[92] F. D'Ammando, *ATel #6731: Fermi LAT detection of increased gamma-ray emission from PKS 0736+01*, Nov. 2014.

[93] A. A. Dar, Z. shah, S. Sahayanathan, N. Iqbal, S. Bhattacharyya, and D. Bose, *Signature of hadronic emission in gamma-ray spectrum of B2 1308+326*, arXiv:2503.01583 [astro-ph], Mar. 2025.

[94] A. De Angelis, G. Galanti, and M. Roncadelli, "Transparency of the Universe to gamma-rays", Monthly Notices of the Royal Astronomical Society **432**, 3245–3249 (2013).

[95] A. De Angelis and M. Pimenta, *Introduction to Particle and Astroparticle Physics*, en, Undergraduate Lecture Notes in Physics (Springer International Publishing, Cham, 2018).

[96] H. Dembinski, P. Ongmongkolkul, and C. Deil, *Scikit-hep/iminuit at v2.2.1*, en, 2020.

[97] C. Dermer, R. Schlickeiser, and A. Mastichiadis, aap (1992).

[98] C. D. Dermer, *High Energy Radiation from Black Holes — Princeton University Press*, en, ISBN: 9780691144085, Oct. 2009.

[99] C. D. Dermer, J. D. Finke, H. Krug, and M. Böttcher, "GAMMA-RAY STUDIES OF BLAZARS: SYNCHRO-COMPTON ANALYSIS OF FLAT SPECTRUM RADIO QUASARS", en, The Astrophysical Journal **692**, Publisher: The American Astronomical Society, 32 (2009).

[100] C. D. Dermer and R. Schlickeiser, "Model for the High-Energy Emission from Blazars", The Astrophysical Journal **416**, Publisher: IOP ADS Bibcode: 1993ApJ...416..458D, 458 (1993).

[101] L. Di Venere, "The prototype Schwarzschild–Couder Telescope: A medium-sized telescope for the Cherenkov Telescope Array", Nuclear Instruments and Methods in Physics Research Section A: Accelerators, Spectrometers, Detectors and Associated Equipment **1056**, 168432 (2023).

[102] A. Donath et al., "Gammapy: A Python package for gamma-ray astronomy", en, Astronomy & Astrophysics **678**, arXiv:2308.13584 [astro-ph], A157 (2023).

[103] D. Donato, "Fermi LAT observed another strong GeV flare from 4C 21.35 (PKS 1222+21)", The Astronomer's Telegram **2584**, ADS Bibcode: 2010ATel.2584....1D, 1 (2010).

[104] D. Donato, G. Ghisellini, G. Tagliaferri, and G. Fossati, "Hard X-ray properties of blazars", en, Astronomy & Astrophysics **375**, Number: 3 Publisher: EDP Sciences, 739–751 (2001).

[105] A. J. Drake et al., "FIRST RESULTS FROM THE CATALINA REAL-TIME TRANSIENT SURVEY", en, The Astrophysical Journal **696**, Publisher: The American Astronomical Society, 870 (2009).

[106] P. Drake and C. Adams, "VERITAS follow-up observation of the BL Lac blazar B2 1811+31 2020 Flare", en, in Proceedings of 38th International Cosmic Ray Conference — PoS(ICRC2023), arXiv:2309.12920 [astro-ph] (Aug. 2023), p. 701.

[107] L. O. Drury, "An introduction to the theory of diffusive shock acceleration of energetic particles in tenuous plasmas", en, Reports on Progress in Physics **46**, 973 (1983).

[108] E. Dwek and R. G. Arendt, "Dust-gas interactions and the infrared emission from hot astrophysical plasmas.", Annual Review of Astronomy and Astrophysics **30**, ADS Bibcode: 1992ARA&A..30...11D, 11–50 (1992).

[109] S. Ebisuzaki et al., "The CANGAROO Project 3.8m Telescope", in , Vol. 2, ADS Bibcode: 1991ICRC....2..607E (Aug. 1991), p. 607.

[110] R. A. Edelson, "THE DISCRETE CORRELATION FUNCTION: A NEW METHOD FOR ANALYZING UNEVENLY SAMPLED VARIABILITY DATA", en, ApJ. . . (1988).

[111] D. J. Eisenstein and P. Hut, "HOP: A New Group-finding Algorithm for N-Body Simulations", en, The Astrophysical Journal **498**, Publisher: IOP Publishing, 137 (1998).

[112] D. Emmanoulopoulos, *Generating artificial light curves: revisited and updated — Monthly Notices of the Royal Astronomical Society — Oxford Academic*, 2013.

[113] P. A. Evans et al., "Methods and results of an automatic analysis of a complete sample of Swift-XRT observations of GRBs", Monthly Notices of the Royal Astronomical Society **397**, 1177–1201 (2009).

[114] A. C. Fabian, "Observational Evidence of Active Galactic Nuclei Feedback", en, Annual Review of Astronomy and Astrophysics **50**, Publisher: Annual Reviews, 455–489 (2012).

[115] E. Fermi, "On the Origin of the Cosmic Radiation", Physical Review **75**, Publisher: American Physical Society, 1169–1174 (1949).

[116] A. V. Filippenko, W. D. Li, R. R. Treffers, and M. Modjaz, "The Lick Observatory Supernova Search with the Katzman Automatic Imaging Telescope", **246**, Conference Name: IAU Colloq. 183: Small Telescope Astronomy on Global Scales ADS Bibcode: 2001ASPC..246..121F, 121 (2001).

[117] J. D. Finke, "COMPTON DOMINANCE AND THE BLAZAR SEQUENCE", en, The Astrophysical Journal **763**, Publisher: The American Astronomical Society, 134 (2013).

[118] J. D. Finke, "EXTERNAL COMPTON SCATTERING IN BLAZAR JETS AND THE LOCATION OF THE GAMMA-RAY EMITTING REGION", en, The Astrophysical Journal **830**, Publisher: The American Astronomical Society, 94 (2016).

[119] D. Foreman-Mackey, D. W. Hogg, D. Lang, and J. Goodman, "Emcee: The MCMC Hammer", en, Publications of the Astronomical Society of the Pacific **125**, arXiv:1202.3665 [astro-ph], 306–312 (2013).

[120] G. Fossati, L. Maraschi, A. Celotti, A. Comastri, and G. Ghisellini, "A unifying view of the spectral energy distributions of blazars", en, Monthly Notices of the Royal Astronomical Society **299**, 433–448 (1998).

[121] A. Franceschini, G. Rodighiero, and M. Vaccari, "Extragalactic optical-infrared background radiation, its time evolution and the cosmic photon-photon opacity", Astronomy and Astrophysics **487**, ADS Bibcode: 2008A&A...487..837F, 837–852 (2008).

[122] A. Franckowiak et al., "Patterns in the Multiwavelength Behavior of Candidate Neutrino Blazars", en, The Astrophysical Journal **893**, Publisher: The American Astronomical Society, 162 (2020).

[123] L. Fuhrmann et al., "Detection of significant cm to sub-mm band radio and gamma-ray correlated variability in Fermi bright blazars", Monthly Notices of the Royal Astronomical Society **441**, 1899–1909 (2014).

[124] L. Fuhrmann et al., "The F-GAMMA programme: multi-frequency study of active galactic nuclei in the Fermi era - Programme description and the first 2.5 years of monitoring", en, Astronomy & Astrophysics **596**, Publisher: EDP Sciences, A45 (2016).

[125] D. C. Gabuzda, R. I. Kollgaard, D. H. Roberts, and J. F. C. Wardle, "Is 1308+326 a BL Lacertae Object or a Quasar?", The Astrophysical Journal **410**, Publisher: IOP ADS Bibcode: 1993ApJ...410...39G, 39 (1993).

[126] T. K. Gaisser, R. Engel, and E. Resconi, *Cosmic Rays and Particle Physics*, 2nd ed. (Cambridge University Press, Cambridge, 2016).

[127] S. Gao, A. Fedynitch, W. Winter, and M. Pohl, "Modelling the coincident observation of a high-energy neutrino and a bright blazar flare", Nature Astronomy **3**, ADS Bibcode: 2019NatAs...3...88G, 88–92 (2019).

[128] S. Garrappa and S. Buson, "Fermi-LAT detection of the new gamma-ray source Fermi J1511+0550, positionally consistent with the high-energy neutrino IC191119A", The Astronomer's Telegram **13306**, ADS Bibcode: 2019ATel13306....1G, 1 (2019).

[129] S. Garrappa, S. Buson, and C. C. Cheung, "Fermi-LAT Gamma-ray Observations of IceCube-210503A and detection of a new gamma-ray source, Fermi J0931.9+3633", The Astronomer's Telegram **14611**, ADS Bibcode: 2021ATel14611....1G, 1 (2021).

[130] S. Garrappa, S. Buson, and C. C. Cheung, "Fermi-LAT Gamma-ray Observations of IceCube-210516A", The Astronomer's Telegram **14639**, ADS Bibcode: 2021ATel14639....1G, 1 (2021).

[131] S. Garrappa, S. Buson, C. C. Cheung, J. Sinapius, and Fermi-LAT Collaboration, "Fermi-LAT Gamma-ray Observations of IceCube-220205A", GRB Coordinates Network **31557**, ADS Bibcode: 2022GCN.31557....1G, 1 (2022).

[132] S. Garrappa, S. Buson, and Fermi-LAT Collaboration, "Fermi-LAT Gamma-ray Observations of IceCube-200614A and detection of a new gamma-ray source, Fermi J0202.8+3132", GRB Coordinates Network **27966**, ADS Bibcode: 2020GCN.27966....1G, 1 (2020).

[133] S. Garrappa, S. Buson, and Fermi-LAT Collaboration, "Fermi-LAT Gamma-ray Observations of IceCube-200911A and detection of a new gamma-ray source, Fermi J0330.1+3743", GRB Coordinates Network **28421**, ADS Bibcode: 2020GCN.28421....1G, 1 (2020).

[134] S. Garrappa, S. Buson, and Fermi-LAT Collaboration, "Fermi-LAT Gamma-ray Observations of IceCube-201114A", GRB Coordinates Network **28918**, ADS Bibcode: 2020GCN.28918....1G, 1 (2020).

[135] S. Garrappa, S. Buson, and Fermi-LAT Collaboration, "Fermi-LAT Gamma-ray Observations of IceCube-220624A and and detection of a new gamma-ray source, Fermi J1458.0+4119", GRB Coordinates Network **32285**, ADS Bibcode: 2022GCN.32285....1G, 1 (2022).

[136] S. Garrappa, S. Buson, and Fermi-LAT Collaboration, "Fermi-LAT gamma-ray observations of IceCube-220822A and detection of a new gamma-ray source, Fermi J1810.1+2154", GRB Coordinates Network **32478**, ADS Bibcode: 2022GCN.32478....1G, 1 (2022).

[137] S. Garrappa, S. Buson, D. Gasparrini, and Fermi-LAT Collaboration, "Fermi-LAT Gamma-ray Observations of IceCube-190730A", GRB Coordinates Network **25239**, ADS Bibcode: 2019GCN.25239....1G, 1 (2019).

[138] S. Garrappa, S. Buson, V. Paliya, and Fermi-LAT Collaboration, "Fermi-LAT Gamma-ray Observations of IceCube-200109A and detection of a possible new gamma-ray source, Fermi J1055.8+1034", The Astronomer's Telegram **13402**, ADS Bibcode: 2020ATel13402....1G, 1 (2020).

[139] S. Garrappa, S. Buson, J. Sinapius, D. Bernard, and Fermi-LAT Collaboration, "Fermi-LAT gamma-ray observations of IceCube-230506A", GRB Coordinates Network **33745**, ADS Bibcode: 2023GCN.33745....1G, 1 (2023).

[140] S. Garrappa, S. Buson, J. Sinapius, and Fermi-LAT Collaboration, "Fermi-LAT Gamma-ray Observations of IceCube-220115A and detection of a new gamma-ray source, Fermi J2350.2+2620", GRB Coordinates Network **31479**, ADS Bibcode: 2022GCN.31479....1G, 1 (2022).

[141] S. Garrappa, S. Buson, J. Sinapius, and Fermi-LAT Collaboration, "Fermi-LAT gamma-ray observations of IceCube-220918A and detection of a new gamma-ray source, Fermi J0502.5+0037", The Astronomer's Telegram **15620**, ADS Bibcode: 2022ATel15620....1G, 1 (2022).

[142] S. Garrappa, S. Buson, J. Sinapius, A. Franckowiak, I. Liodakis, C. Bartolini, M. Giroletti, C. Nanci, G. Principe, and T. M. Venters, "Fermi-LAT follow-up observations in seven years of real-time high-energy neutrino alerts", en, Astronomy & Astrophysics **687**, Publisher: EDP Sciences, A59 (2024).

[143] S. Garrappa, S. Buson, T. Venters, and Fermi-LAT Collaboration, "Fermi-LAT Gamma-ray Observations of IceCube-190704A and detection of the new gamma-ray source 1WHSP J104516.2+275133", GRB Coordinates Network **24989**, ADS Bibcode: 2019GCN.24989....1G, 1 (2019).

[144] S. Garrappa et al., "Investigation of Two Fermi-LAT Gamma-Ray Blazars Coincident with High-energy Neutrinos Detected by IceCube", en, The Astrophysical Journal **880**, Publisher: The American Astronomical Society, 103 (2019).

[145] S. Garrappa, *ATel #15483: Fermi-LAT detection of enhanced gamma-ray activity from the FSRQ OP 313 (B2 1308+32)*, 2022.

[146] S. Garrappa and J. Valverde, "Fermi-LAT detection of record flaring activity from the blazar Ton 599 (4C +29.45)", The Astronomer's Telegram **15859**, ADS Bibcode: 2023ATel15859....1G, 1 (2023).

[147] D. Gasparrini, "Fermi-LAT detection of renewed flaring activity from the blazar Ton 599 (4C +29.45)", The Astronomer's Telegram **14897**, ADS Bibcode: 2021ATel14897....1G, 1 (2021).

[148] N. Gehrels et al., "The Swift Gamma-Ray Burst Mission", en, The Astrophysical Journal **611**, Publisher: IOP Publishing, 1005 (2004).

[149] G. Ghisellini, C. Righi, L. Costamante, and F. Tavecchio, "The Fermi blazar sequence", Monthly Notices of the Royal Astronomical Society **469**, 255–266 (2017).

[150] G. Ghisellini and F. Tavecchio, "The blazar sequence: a new perspective", en, Monthly Notices of the Royal Astronomical Society **387**, 1669–1680 (2008).

[151] G. Ghisellini and F. Tavecchio, "Fermi/LAT broad emission line blazars", Monthly Notices of the Royal Astronomical Society **448**, 1060–1077 (2015).

[152] G. Ghisellini, F. Tavecchio, L. Maraschi, A. Celotti, and T. Sbarrato, "The power of relativistic jets is larger than the luminosity of their accretion disks", Nature **515**, arXiv:1411.5368 [astro-ph], 376–378 (2014).

[153] G. Ghisellini, *Radiative Processes in High Energy Astrophysics*, en, Vol. 873, arXiv:1202.5949 [astro-ph] (2013).

[154] D. Giannios, D. A. Uzdensky, and M. C. Begelman, "Fast TeV variability in blazars: jets in a jet", Monthly Notices of the Royal Astronomical Society **395**, Publisher: OUP ADS Bibcode: 2009MNRAS.395L..29G, L29–L33 (2009).

[155] R. C. Gilmore, A. Bouvier, V. Connaughton, A. Goldstein, N. Otte, J. R. Primack, and D. A. Williams, "IACT observations of gamma-ray bursts: prospects for the Cherenkov Telescope Array", en, Experimental Astronomy **35**, 413–457 (2013).

[156] P. Giommi, P. Padovani, G. Polenta, S. Turriziani, V. D'Elia, and S. Piranomonte, "A simplified view of blazars: clearing the fog around long-standing selection effects", Monthly Notices of the Royal Astronomical Society **420**, 2899–2911 (2012).

[157] S. L. Glashow, "Resonant Scattering of Antineutrinos", Physical Review **118**, Publisher: American Physical Society, 316–317 (1960).

[158] P. Good, *Permutation, Parametric and Bootstrap Tests of Hypotheses*, en, Springer Series in Statistics (Springer-Verlag, New York, 2005).

[159] K. Grasha, J. Darling, A. Bolatto, A. K. Leroy, and J. T. Stocke, "A Search for Intrinsic H I 21 cm and OH 18 cm Absorption toward Compact Radio Sources", The Astrophysical Journal Supplement Series **245**, ADS Bibcode: 2019ApJS..245....3G, 3 (2019).

[160] K. Greisen, "End to the Cosmic-Ray Spectrum?", Physical Review Letters **16**, Publisher: American Physical Society, 748–750 (1966).

[161] M. A. Gurwell, A. B. Peck, S. R. Hostler, M. R. Darrah, and C. A. Katz, "Monitoring Phase Calibrators at Submillimeter Wavelengths", in From Z-Machines to ALMA: (Sub)Millimeter Spectroscopy of Galaxies, Vol. 375, ADS Bibcode: 2007ASPC..375..234G (Oct. 2007), p. 234.

[162] H. E. S. S. Collaboration et al., "Deeper H.E.S.S. observations of Vela Junior (RX J0852.0-4622): Morphology studies and resolved spectroscopy", Astronomy and Astrophysics **612**, Publisher: EDP ADS Bibcode: 2018A&A...612A...7H, A7 (2018).

[163] H. E. S. S. Collaboration et al., "The H.E.S.S. Galactic plane survey", Astronomy and Astrophysics **612**, Publisher: EDP ADS Bibcode: 2018A&A...612A...1H, A1 (2018).

[164] F. Haardt and L. Maraschi, "A Two-Phase Model for the X-Ray Emission from Seyfert Galaxies", The Astrophysical Journal **380**, Publisher: IOP ADS Bibcode: 1991ApJ...380L..51H, L51 (1991).

[165] A. J. S. Hamilton and C. L. Sarazin, "A new similarity solution for reverse shocks in supernova remnants.", The Astrophysical Journal **281**, Publisher: IOP ADS Bibcode: 1984ApJ...281..682H, 682–689 (1984).

[166] A. J. S. Hamilton and C. L. Sarazin, "Heating and cooling in reverse shocks into pure heavy-element supernova ejecta", en, The Astrophysical Journal **287**, 282 (1984).

[167] R. G. Harrington, "The 48-inch Schmidt-type Telescope at Palomar Observatory", Publications of the Astronomical Society of the Pacific **64**, ADS Bibcode: 1952PASP...64..275H, 275 (1952).

[168] R. C. Hartman et al., "The Third EGRET Catalog of High-Energy Gamma-Ray Sources", The Astrophysical Journal Supplement Series **123**, ADS Bibcode: 1999ApJS..123...79H, 79–202 (1999).

[169] A. M. Hillas, "The Origin of Ultra-High-Energy Cosmic Rays", en, Annual Review of Astronomy and Astrophysics **22**, Publisher: Annual Reviews, 425–444 (1984).

[170] J. A. Hinton, "The status of the HESS project", New Astronomy Reviews, 2nd VERITAS Symposium on the Astrophysics of Extragalactic Sources **48**, 331–337 (2004).

[171] P. T. P. Ho, J. M. Moran, and K. Y. Lo, "The Submillimeter Array", en, The Astrophysical Journal **616**, Publisher: IOP Publishing, L1 (2004).

[172] J. R. Hoerandel, "On the knee in the energy spectrum of cosmic rays", en, Astroparticle Physics **19**, arXiv:astro-ph/0210453, 193–220 (2003).

[173] J. A. Högbom, "Aperture Synthesis with a Non-Regular Distribution of Interferometer Baselines", Astronomy and Astrophysics Supplement Series **15**, ADS Bibcode: 1974A&AS...15..417H, 417 (1974).

[174] J. Holder et al., "The first VERITAS telescope", Astroparticle Physics **25**, 391–401 (2006).

[175] D. Horan, *ATel #1905: Fermi-LAT detection of renewed activity from the blazar PKS 1502+106*, Jan. 2009.

[176] T. Hovatta, E. Valtaoja, M. Tornikoski, and A. Lähteenmäki, "Doppler factors, Lorentz factors and viewing angles for quasars, BL Lacertae objects and radio galaxies", en, Astronomy & Astrophysics **494**, Number: 2 Publisher: EDP Sciences, 527–537 (2009).

[177] T. Hovatta et al., "Connection between optical and -ray variability in blazars", Monthly Notices of the Royal Astronomical Society **439**, 690–702 (2014).

[178] F. Hoyle and W. A. Fowler, "Nucleosynthesis in Supernovae.", The Astrophysical Journal **132**, Publisher: IOP ADS Bibcode: 1960ApJ...132..565H, 565 (1960).

[179] F. Hungwe, *ATel #3694: Record gamma-ray flux level detected from PKS 1510-089 by Fermi/LAT*, Oct. 2011.

[180] G. Iafrate, F. Longo, and F. D'Ammando, "Fermi LAT detection of a very intense GeV flare from 4C +21.35 (PKS 1222+21)", The Astronomer's Telegram **2687**, ADS Bibcode: 2010ATel.2687....1I, 1 (2010).

[181] IceCube Collaboration et al., "Multimessenger observations of a flaring blazar coincident with high-energy neutrino IceCube-170922A", Science **361**, ADS Bibcode: 2018Sci...361.1378I, eaat1378 (2018).

[182] IceCube Collaboration et al., "Search for neutrino emission from cores of active galactic nuclei", Physical Review D **106**, Publisher: American Physical Society, 022005 (2022).

[183] Icecube collaboration et al., "Evidence for neutrino emission from the nearby active galaxy NGC 1068", Science **378**, Publisher: American Association for the Advancement of Science, 538–543 (2022).

[184] S. Inoue and F. Takahara, "Electron Acceleration and Gamma-Ray Emission from Blazars", The Astrophysical Journal **463**, Publisher: IOP ADS Bibcode: 1996ApJ...463..555I, 555 (1996).

[185] M. Janiak, M. Sikora, and R. Moderski, "Magnetization of jets in luminous blazars", Monthly Notices of the Royal Astronomical Society **449**, 431–439 (2015).

[186] I. Jankov, A. B. Kovačević, D. Ilić, P. Sánchez-Sáez, and R. Nikutta, *pyZDCF: Initial Release*, Oct. 2022.

[187] D. Jones, *1968ASPL...10..145J Page 145.*

[188] S. Jorstad and A. Marscher, "The VLBA-BU-BLAZAR Multi-Wavelength Monitoring Program", en, Galaxies **4**, Publisher: Multidisciplinary Digital Publishing Institute, 47 (2016).

[189] S. G. Jorstad, A. P. Marscher, J. R. Mattox, A. E. Wehrle, S. D. Bloom, and A. V. Yurchenko, "Multiepoch Very Long Baseline Array Observations ofEGRET-detectedQuasars and BL LacertaeObjects: Superluminal Motion of Gamma-Ray BrightBlazars", en, The Astrophysical Journal Supplement Series **134**, Publisher: IOP Publishing, 181 (2001).

[190] S. G. Jorstad et al., "Polarimetric Observations of 15 Active Galactic Nuclei at High Frequencies: Jet Kinematics from Bimonthly Monitoring with the Very Long Baseline Array", en, The Astronomical Journal **130**, Publisher: IOP Publishing, 1418 (2005).

[191] S. G. Jorstad et al., "A TIGHT CONNECTION BETWEEN GAMMA-RAY OUTBURSTS AND PARSEC-SCALE JET ACTIVITY IN THE QUASAR 3C 454.3", en, The Astrophysical Journal **773**, Publisher: The American Astronomical Society, 147 (2013).

[192] S. G. Jorstad et al., "Kinematics of Parsec-scale Jets of Gamma-Ray Blazars at 43 GHz within the VLBA-BU-BLAZAR Program", en, The Astrophysical Journal **846**, Publisher: The American Astronomical Society, 98 (2017).

[193] M. Kadler et al., "Coincidence of a high-fluence blazar outburst with a PeV-energy neutrino event", Nature Physics **12**, ADS Bibcode: 2016NatPh..12..807K, 807–814 (2016).

[194] S. Kankkunen, M. Tornikoski, T. Hovatta, and A. Lähteenmäki, "Long-term radio variability of active galactic nuclei at 37 GHz", en, Astronomy & Astrophysics **693**, Publisher: EDP Sciences, A318 (2025).

[195] S. Kaspi, W. N. Brandt, D. Maoz, H. Netzer, D. P. Schneider, and O. Shemmer, "Reverberation Mapping of High-Luminosity Quasars: First Results", en, The Astrophysical Journal **659**, Publisher: IOP Publishing, 997 (2007).

[196] E. Y. Khachikian and D. W. Weedman, "An atlas of Seyfert galaxies.", The Astrophysical Journal **192**, Publisher: IOP ADS Bibcode: 1974ApJ...192..581K, 581–589 (1974).

[197] J.-Y. Kim, T. P. Krichbaum, R.-S. Lu, E. Ros, U. Bach, M. Bremer, P. d. Vicente, M. Lindqvist, and J. A. Zensus, "The limb-brightened jet of M87 down to the 7 Schwarzschild radii scale", en, Astronomy & Astrophysics **616**, Publisher: EDP Sciences, A188 (2018).

[198] J. G. Kirk, F. M. Rieger, and A. Mastichiadis, "Particle acceleration and synchrotron emission in blazar jets", en, (1998).

[199] J. G. Kirk and A. F. Heavens, "Particle acceleration at oblique shock fronts", en, Monthly Notices of the Royal Astronomical Society **239**, 995–1011 (1989).

[200] K. Kotera and A. V. Olinto, "The Astrophysics of Ultrahigh Energy Cosmic Rays", en, Annual Review of Astronomy and Astrophysics **49**, arXiv:1101.4256 [astro-ph], 119–153 (2011).

[201] P. M. Kouch, E. Lindfors, T. Hovatta, I. Liodakis, K. I. I. Koljonen, K. Nilsson, J. Jormanainen, V. F. Ramazani, and M. J. Graham, "Optimizing the hunt for extraterrestrial high-energy neutrino counterparts", Astronomy & Astrophysics **696**, arXiv:2502.17567 [astro-ph], A73 (2025).

[202] P. M. Kouch et al., "Association of the IceCube neutrinos with blazars in the CGRaBS sample", en, Astronomy & Astrophysics **690**, Publisher: EDP Sciences, A111 (2024).

[203] P. M. Kouch et al., *CAZ catalog and optical light curves of 7918 blazar-selected AGN*, arXiv:2510.16584 [astro-ph], Oct. 2025.

[204] I. G. Kramarenko, A. B. Pushkarev, Y. Y. Kovalev, M. L. Lister, T. Hovatta, and T. Savolainen, "A decade of joint MOJAVE–Fermi AGN monitoring: localization of the gamma-ray emission region", Monthly Notices of the Royal Astronomical Society **510**, 469–480 (2022).

[205] A. Kraus et al., "Intraday variability in compact extragalactic radio sources: II. Observations with the Effelsberg 100 m radio telescope", en, Astronomy & Astrophysics **401**, 161–172 (2003).

[206] W. Kraushaar, G. W. Clark, G. Garmire, H. Helmken, P. Higbie, and M. Agogino, "Explorer XI Experiment on Cosmic Gamma Rays.", The Astrophysical Journal **141**, ADS Bibcode: 1965ApJ...141..845K, 845 (1965).

[207] J. H. Krolik and M. C. Begelman, "Molecular Tori in Seyfert Galaxies: Feeding the Monster and Hiding It", The Astrophysical Journal **329**, Publisher: IOP ADS Bibcode: 1988ApJ...329..702K, 702 (1988).

[208] K. Le Bail et al., "IVS Observation of ICRF2-Gaia Transfer Sources", The Astronomical Journal **151**, ADS Bibcode: 2016AJ....151...79L, 79 (2016).

[209] A. Letessier-Selvon and T. Stanev, "Ultrahigh Energy Cosmic Rays", Reviews of Modern Physics **83**, 10.1103/RevModPhys.83.907 (2011).

[210] LHAASO Collaboration et al., "Measurement of Ultra-High-Energy Diffuse Gamma-Ray Emission of the Galactic Plane from 10 TeV to 1 PeV with LHAASO-KM2A", Physical Review Letters **131**, Publisher: American Physical Society, 151001 (2023).

[211] W. Li et al., "Nearby Supernova Rates from the Lick Observatory Supernova Search. II. The Observed Luminosity Functions and Fractions of Supernovae in a Complete Sample", Monthly Notices of the Royal Astronomical Society **412**, arXiv:1006.4612 [astro-ph], 1441–1472 (2011).

[212] I. Liodakis, T. Hovatta, M. F. Aller, H. D. Aller, M. A. Gurwell, A. Lähteenmäki, and M. Tornikoski, "Identifying changing jets through their radio variability", en, Astronomy & Astrophysics **654**, Publisher: EDP Sciences, A169 (2021).

[213] I. Liodakis, T. Hovatta, V. Pavlidou, A. C. S. Readhead, R. D. Blandford, S. Kiehlmann, E. Lindfors, W. Max-Moerbeck, T. J. Pearson, and M. Petropoulou, "The hunt for extraterrestrial high-energy neutrino counterparts", Astronomy and Astrophysics **666**, Publisher: EDP ADS Bibcode: 2022A&A...666A..36L, A36 (2022).

[214] I. Liodakis, T. Hovatta, D. Huppenkothen, S. Kiehlmann, W. Max-Moerbeck, and A. C. S. Readhead, "Constraining the Limiting Brightness Temperature and Doppler Factors for the Largest Sample of Radio-bright Blazars", en, The Astrophysical Journal **866**, Publisher: The American Astronomical Society, 137 (2018).

[215] I. Liodakis, R. W. Romani, A. V. Filippenko, D. Kocevski, and W. Zheng, "Probing Blazar Emission Processes with Optical/Gamma-Ray Flare Correlations", en, The Astrophysical Journal **880**, Publisher: The American Astronomical Society, 32 (2019).

[216] M. L. Lister, M. F. Aller, H. D. Aller, M. A. Hodge, D. C. Homan, Y. Y. Kovalev, A. B. Pushkarev, and T. Savolainen, "MOJAVE. XV. VLBA 15 GHz Total Intensity and Polarization Maps of 437 Parsec-scale AGN Jets from 1996 to 2017", en, The Astrophysical Journal Supplement Series **234**, Publisher: The American Astronomical Society, 12 (2018).

[217] M. L. Lister, D. C. Homan, K. I. Kellermann, Y. Y. Kovalev, A. B. Pushkarev, E. Ros, and T. Savolainen, "Monitoring Of Jets in Active Galactic Nuclei with VLBA Experiments. XVIII. Kinematics and Inner Jet Evolution of Bright Radio-loud Active Galaxies", en, The Astrophysical Journal **923**, Publisher: The American Astronomical Society, 30 (2021).

[218] M. L. Lister et al., "MOJAVE: MONITORING OF JETS IN ACTIVE GALACTIC NUCLEI WITH VLBA EXPERIMENTS. V. MULTI-EPOCH VLBA IMAGES", en, The Astronomical Journal **137**, 3718–3729 (2009).

[219] M. L. Lister et al., "MOJAVE. XVII. Jet Kinematics and Parent Population Properties of Relativistically Beamed Radio-loud Blazars", en, The Astrophysical Journal **874**, Publisher: The American Astronomical Society, 43 (2019).

[220] F. Longo, M. Giroletti, and G. Iafrate, "Fermi LAT detection of increasing gamma-ray activity of blazar PKS 1222+216", The Astronomer's Telegram **2021**, ADS Bibcode: 2009ATel.2021....1L, 1 (2009).

[221] B. Lott, L. Escande, S. Larsson, and J. Ballet, "An adaptive-binning method for generating constant-uncertainty/constant-significance light curves with Fermi-LAT data", en, Astronomy & Astrophysics **544**, Publisher: EDP Sciences, A6 (2012).

[222] H. Mangal, *ATel #14404: Fermi/LAT detection of enhanced gamma-ray activity from the blazars OP 313 and 4C +01.02*, 2021.

[223] K. Mannheim, *The proton blazar.* ISSN: 0004-6361 Volume: 269 ADS Bibcode: 1993A&A...269...67M, Mar. 1993.

[224] K. Mannheim and P. L. Biermann, "Gamma-ray flaring of 3C 279 : a proton-initiated cascade in the jet ?", Astronomy and Astrophysics **253**, ADS Bibcode: 1992A&A...253L..21M, L21–L24 (1992).

[225] M. Mariotti, *ATel #2684: MAGIC detects a VHE flare from 4C +21.35 (PKS 1222+21)*, June 2019.

[226] A. P. Marscher and S. G. Jorstad, "THE MEGAPARSEC-SCALE X-RAY JET OF THE BL Lac OBJECT OJ287", en, The Astrophysical Journal **729**, Publisher: The American Astronomical Society, 26 (2011).

[227] A. P. Marscher et al., "The inner jet of an active galactic nucleus as revealed by a radio-to--ray outburst", en, Nature **452**, Publisher: Nature Publishing Group, 966–969 (2008).

[228] P. Marziani, J. W. Sulentic, D. Dultzin-Hacyan, M. Calvani, and M. Moles, "Comparative Analysis of the High- and Low-Ionization Lines in the Broad-Line Region of Active Galactic Nuclei", The Astrophysical Journal Supplement Series **104**, ADS Bibcode: 1996ApJS..104...37M, 37 (1996).

[229] E. Massaro, M. Perri, P. Giommi, and R. Nesci, "Log-parabolic spectra and particle acceleration in the BL Lac object Mkn 421: Spectral analysis of the complete BeppoSAX wide band X-ray data set", en, Astronomy & Astrophysics **413**, 489–503 (2004).

[230] E. Massaro, A. Tramacere, M. Perri, P. Giommi, and G. Tosti, "Log-parabolic spectra and particle acceleration in blazars: III. SSC emission in the TeV band from Mkn 501", en, Astronomy & Astrophysics **448**, 861–871 (2006).

[231] F. Massaro, D. J. Thompson, and E. C. Ferrara, "The extragalactic gamma-ray sky in the Fermi era", en, The Astronomy and Astrophysics Review **24**, 2 (2015).

[232] D. Maurin, M. Ahlers, H. Dembinski, A. Haungs, P.-S. Mangeard, F. Melot, P. Mertsch, D. Wochele, and J. Wochele, "A cosmic-ray database update: CRDB v4.1", en, The European Physical Journal C **83**, 971 (2023).

[233] J. M. Mehlhaff, "Magnetic Reconnection and the Extreme Plasmas of Blazar Jets", ADS Bibcode: 2021PhDT.....6M, Ph.D. thesis (Jan. 2021).

[234] M. Meyer and J. Conrad, "Sensitivity of the Cherenkov Telescope Array to the detection of axion-like particles at high gamma-ray opacities", en, Journal of Cosmology and Astroparticle Physics **2014**, arXiv:1410.1556 [astro-ph], 016–016 (2014).

[235] M. Meyer, D. Montanino, and J. Conrad, "On detecting oscillations of gamma rays into axion-like particles in turbulent and coherent magnetic fields", en, Journal of Cosmology and Astroparticle Physics **2014**, 003 (2014).

[236] M. Meyer, M. Petropoulou, and I. M. Christie, "The Observability of Plasmoid-powered Gamma-Ray Flares with the Fermi Large Area Telescope", en, The Astrophysical Journal **912**, Publisher: The American Astronomical Society, 40 (2021).

[237] M. Meyer, J. D. Scargle, and R. D. Blandford, "Characterizing the Gamma-Ray Variability of the Brightest Flat Spectrum Radio Quasars Observed with the Fermi LAT", en, The Astrophysical Journal **877**, Publisher: The American Astronomical Society, 39 (2019).

[238] Mirzoyan, *ATel #9105: Title: MAGIC detects exceptionally high activity from PKS 1510-089 at very high energy gamma-rays*, June 2016.

[239] R. Mirzoyan, *ATel #11545: MAGIC detection of increased activity from FSRQ 3C 279 at very-high-energy gamma rays*, Apr. 2018.

[240] K. Mohana A et al., "Multiband cross-correlated radio variability of the blazar 3C279", Monthly Notices of the Royal Astronomical Society **527**, 6970–6980 (2024).

[241] A. Mücke and R. J. Protheroe, "A proton synchrotron blazar model for flaring in Markarian 501", Astroparticle Physics **15**, ADS Bibcode: 2001APh....15..121M, 121–136 (2001).

[242] A. Mücke, R. J. Protheroe, R. Engel, J. P. Rachen, and T. Stanev, "BL Lac objects in the synchrotron proton blazar model", Astroparticle Physics **18**, ADS Bibcode: 2003APh....18..593M, 593–613 (2003).

[243] R. Mukherjee, *ATel #11075: VERITAS Detection of VHE Emission from Ton 599*, Dec. 2017.

[244] K. Murase, C. D. Dermer, H. Takami, and G. Migliori, "BLAZARS AS ULTRA-HIGH-ENERGY COSMIC-RAY SOURCES: IMPLICATIONS FOR TeV GAMMA-RAY OBSERVATIONS", en, The Astrophysical Journal **749**, Publisher: The American Astronomical Society, 63 (2012).

[245] K. Murase and F. W. Stecker, "High-Energy Neutrinos from Active Galactic Nuclei", in *The Encyclopedia of Cosmology. Set 2: Frontiers in Cosmology. Volume 2: Neutrino Physics and Astrophysics*, ADS Bibcode: 2023ecnp.book..483M (Nov. 2023), pp. 483–540.

[246] I. Myserlis et al., "Full-Stokes polarimetry with circularly polarized feeds - Sources with stable linear and circular polarization in the GHz regime", en, Astronomy & Astrophysics **609**, Publisher: EDP Sciences, A68 (2018).

[247] R. Naab et al., "Measurement of the astrophysical diffuse neutrino flux in a combined fit of IceCube's high energy neutrino data", en, in *Proceedings of 38th International Cosmic Ray Conference — PoS(ICRC2023)*, Vol. 444, Conference Name: 38th International Cosmic Ray Conference (SISSA Medialab, Sept. 2024), p. 1064.

[248] K. Nalewajko and M. Gupta, "The sequence of Compton dominance in blazars based on data from WISE and Fermi-LAT", en, Astronomy & Astrophysics **606**, Publisher: EDP Sciences, A44 (2017).

[249] de Naurois, *ATel #9102: Increased VHE activity from PKS 1510-089 detected with H.E.S.S.* May 2016.

[250] M. de Naurois, *ATel #11239: H.E.S.S. detection of a strong VHE activity from the blazar 3C 279*, Jan. 2018.

[251] M. de Naurois and D. Mazin, "Ground-based detectors in very-high-energy gamma-ray astronomy", Comptes Rendus Physique, Gamma-ray astronomy / Astronomie des rayons gamma **16**, 610–627 (2015).

[252] A. Neronov, "Introduction to multi-messenger astronomy", en, Journal of Physics: Conference Series **1263**, Publisher: IOP Publishing, 012001 (2019).

[253] E. Nieppola, E. Valtaoja, M. Tornikoski, T. Hovatta, and M. Kotiranta, "Blazar sequence – an artefact of Doppler boosting", en, Astronomy & Astrophysics **488**, 867–872 (2008).

[254] K. Nilsson et al., "Long-term optical monitoring of TeV emitting blazars - I. Data analysis", en, Astronomy & Astrophysics **620**, Publisher: EDP Sciences, A185 (2018).

[255] F. Oikonomou, M. Petropoulou, K. Murase, A. Tohuvavohu, G. Vasilopoulos, S. Buson, and M. Santander, "Multi-messenger emission from the parsec-scale jet of the flat-spectrum radio quasar PKS 1502+106 coincident with high-energy neutrino IceCube-190730A", en, Journal of Cosmology and Astroparticle Physics **2021**, Publisher: IOP Publishing, 082 (2021).

[256] R. Ojha, *ATel #11542: Fermi LAT detection of renewed strong GeV activity from the FSRQ 3C 279*, Apr. 2018.

[257] P. Padovani et al., "Active galactic nuclei: what's in a name?", en, The Astronomy and Astrophysics Review **25**, 2 (2017).

[258] P. Padovani, "The microjansky and nanojansky radio sky: source population and multiwavelength properties: The microjansky and nanojansky radio sky", en, Monthly Notices of the Royal Astronomical Society **411**, 1547–1561 (2011).

[259] P. Padovani, "The faint radio sky: radio astronomy becomes mainstream", en, The Astronomy and Astrophysics Review **24**, 13 (2016).

[260] A. Pandey, P. Kushwaha, P. J. Wiita, R. Prince, B. Czerny, and C. S. Stalin, "Origin of the broadband emission from the transition blazar B2 1308+326", en, Astronomy & Astrophysics **681**, Publisher: EDP Sciences, A116 (2024).

[261] K. Pearson, "X. On the criterion that a given system of deviations from the probable in the case of a correlated system of variables is such that it can be reasonably supposed to have arisen from random sampling", The London, Edinburgh, and Dublin Philosophical Magazine and Journal of Science **50**, Publisher: Taylor & Francis _eprint: https://doi.org/10.1080/14786440009463897, 157–175 (1900).

[262] B. M. Peterson, *An Introduction to Active Galactic Nuclei*, Publication Title: An introduction to active galactic nuclei ADS Bibcode: 1997iagn.book.....P (Feb. 1997).

[263] M. Petropoulou, D. Giannios, and L. Sironi, "Blazar flares powered by plasmoids in relativistic reconnection", Monthly Notices of the Royal Astronomical Society **462**, Publisher: OUP ADS Bibcode: 2016MNRAS.462.3325P, 3325–3343 (2016).

[264] E. A. Pier and J. H. Krolik, "Infrared Spectra of Obscuring Dust Tori around Active Galactic Nuclei. II. Comparison with Observations", The Astrophysical Journal **418**, Publisher: IOP ADS Bibcode: 1993ApJ...418..673P, 673 (1993).

[265] A. V. Plavin, Y. Y. Kovalev, Y. A. Kovalev, and S. V. Troitsky, "Directional Association of TeV to PeV Astrophysical Neutrinos with Radio Blazars", en, The Astrophysical Journal **908**, Publisher: The American Astronomical Society, 157 (2021).

[266] W. J. Potter and G. Cotter, "Synchrotron and inverse-Compton emission from blazar jets – III. Compton-dominant blazars", Monthly Notices of the Royal Astronomical Society **431**, 1840–1852 (2013).

[267] G. Principe, "Fermi-LAT detection of renewed flaring activity from the blazar Ton 599 (4C +29.45)", The Astronomer's Telegram **14722**, ADS Bibcode: 2021ATel14722....1P, 1 (2021).

[268] A. C. S. Readhead, "On the Possible Non-Isotropy of the Radio Emission from Compact Extragalactic Objects", en, Physica Scripta **21**, 662 (1980).

[269] A. C. S. Readhead, M. H. Cohen, T. J. Pearson, and P. N. Wilkinson, "Bent beams and the overall size of extragalactic radio sources", en, Nature **276**, Publisher: Nature Publishing Group, 768–771 (1978).

[270] S. Reusch et al., "Candidate Tidal Disruption Event AT2019fdr Coincident with a High-Energy Neutrino", Physical Review Letters **128**, Publisher: APS ADS Bibcode: 2022PhRvL.128v1101R, 221101 (2022).

[271] X. Rodrigues, A. Fedynitch, S. Gao, D. Boncioli, and W. Winter, "Neutrinos and Ultra-high-energy Cosmic-ray Nuclei from Blazars", The Astrophysical Journal **854**, Publisher: IOP ADS Bibcode: 2018ApJ...854...54R, 54 (2018).

[272] X. Rodrigues, S. Garrappa, S. Gao, V. S. Paliya, A. Franckowiak, and W. Winter, "Multiwavelength and Neutrino Emission from Blazar PKS 1502 + 106", en, The Astrophysical Journal **912**, Publisher: The American Astronomical Society, 54 (2021).

[273] P. W. A. Roming et al., "The Swift Ultra-Violet/Optical Telescope", en, Space Science Reviews **120**, 95–142 (2005).

[274] F. K. Röpke, I. R. Seitenzahl, S. Benitez, M. Fink, R. Pakmor, M. Kromer, S. A. Sim, F. Ciaraldi-Schoolmann, and W. Hillebrandt, "Modeling Type Ia supernova explosions", Progress in Particle and Nuclear Physics, Particle and Nuclear Astrophysics **66**, 309–318 (2011).

[275] M. N. Rosillo, F. Acero, J. Otero-Santos, M. V. Acosta, R. Terrier, and A. Arbet-Engels, *A Unified Multi-Wavelength Data Analysis Workflow with gammapy. Constraining the Broadband Emission of FSRQ OP 313*, en, arXiv:2409.20487 [astro-ph], Sept. 2024.

[276] G. B. Rybicki and A. P. Lightman, *Radiative processes in astrophysics*, en (Wiley-VCH Verlag GmbH & Co. KGaA, Weinheim, [Germany], 2004).

[277] A. Saldana-Lopez, A. Domínguez, P. G. Pérez-González, J. Finke, M. Ajello, J. R. Primack, V. S. Paliya, and A. Desai, "An observational determination of the evolving extragalactic background light from the multiwavelength HST/CANDELS survey in the Fermi and CTA era", Monthly Notices of the Royal Astronomical Society **507**, 5144–5160 (2021).

[278] E. E. Salpeter, "Accretion of Interstellar Matter by Massive Objects.", The Astrophysical Journal **140**, Publisher: IOP ADS Bibcode: 1964ApJ...140..796S, 796–800 (1964).

[279] J. D. Scargle, J. P. Norris, B. Jackson, and J. Chiang, "STUDIES IN ASTRONOMICAL TIME SERIES ANALYSIS. VI. BAYESIAN BLOCK REPRESENTATIONS", en, The Astrophysical Journal **764**, Publisher: The American Astronomical Society, 167 (2013).

[280] E. F. Schlafly and D. P. Finkbeiner, "MEASURING REDDENING WITH SLOAN DIGITAL SKY SURVEY STELLAR SPECTRA AND RECALIBRATING SFD", en, The Astrophysical Journal **737**, Publisher: The American Astronomical Society, 103 (2011).

[281] J. L. Schmitt, "BL Lac identified as a Radio Source", en, Nature **218**, Publisher: Nature Publishing Group, 663–663 (1968).

[282] D. P. Schneider et al., "THE SLOAN DIGITAL SKY SURVEY QUASAR CATALOG. V. SEVENTH DATA RELEASE", en, The Astronomical Journal **139**, Publisher: The American Astronomical Society, 2360 (2010).

[283] G. Schwarz, "Estimating the Dimension of a Model", The Annals of Statistics **6**, Publisher: Institute of Mathematical Statistics, 461–464 (1978).

[284] S. Seabold and J. Perktold, "Statsmodels: Econometric and Statistical Modeling with Python", en, scipy, 10.25080/Majora-92bf1922-011 (2010).

[285] N. I. Shakura and R. A. Sunyaev, "Black holes in binary systems. Observational appearance.", Astronomy and Astrophysics **24**, ADS Bibcode: 1973A&A....24..337S, 337–355 (1973).

[286] M. C. Shepherd, "Difmap: an Interactive Program for Synthesis Imaging", **125**, Conference Name: Astronomical Data Analysis Software and Systems VI ADS Bibcode: 1997ASPC..125...77S, 77 (1997).

[287] M. C. Shepherd, T. J. Pearson, and G. B. Taylor, *1994BAAS...26..987S Page 987*, 1994.

[288] A. Shukla and K. Mannheim, "Gamma-ray flares from relativistic magnetic reconnection in the jet of the quasar 3C 279", en, Nature Communications **11**, Publisher: Nature Publishing Group, 4176 (2020).

[289] M. Sikora, M. Begelman, and M. Rees, "Comptonization of Diffuse Ambient Radiation by a Relativistic Jet: The Source of Gamma Rays from Blazars?", ApJ, 10.1086/173633 (1994).

[290] L. Sironi, A. Spitkovsky, and J. Arons, "THE MAXIMUM ENERGY OF ACCELERATED PARTICLES IN RELATIVISTIC COLLISIONLESS SHOCKS", en, The Astrophysical Journal **771**, Publisher: The American Astronomical Society, 54 (2013).

[291] M. Spurio, "An Overview of Multimessenger Astrophysics", en, in *Probes of Multimessenger Astrophysics: Charged cosmic rays, neutrinos, gamma-rays and gravitational waves*, edited by M. Spurio (Springer International Publishing, Cham, 2018), pp. 1–27.

[292] R. Stein et al., "A tidal disruption event coincident with a high-energy neutrino", Nature Astronomy **5**, ADS Bibcode: 2021NatAs...5..510S, 510–518 (2021).

[293] M. Stickel, P. Padovani, and C. M. Urry, "1991ApJ...374..431S Page 431", ApJ **374**, 431 (1991).

[294] E. J. Summerlin and M. G. Baring, "DIFFUSIVE ACCELERATION OF PARTICLES AT OBLIQUE, RELATIVISTIC, MAGNETOHYDRODYNAMIC SHOCKS", en, The Astrophysical Journal **745**, Publisher: The American Astronomical Society, 63 (2011).

[295] *Swift: About Swift - UVOT Instrument Description.*

[296] Y. T. Tanaka, S. Buson, and D. Kocevski, "Fermi-LAT detection of increased gamma-ray activity of TXS 0506+056, located inside the IceCube-170922A error region.", The Astronomer's Telegram **10791**, ADS Bibcode: 2017ATel10791....1T, 1 (2017).

[297] M. Tarnopolski, N. Żywucka, V. Marchenko, and J. Pascual-Granado, "A Comprehensive Power Spectral Density Analysis of Astronomical Time Series. I. The Fermi-LAT Gamma-Ray Light Curves of Selected Blazars", en, The Astrophysical Journal Supplement Series **250**, Publisher: The American Astronomical Society, 1 (2020).

[298] M. Tashiro and K. Makishima, *1995PASJ...47..131T Page 131*, 1995.

[299] F. Tavecchio and G. Ghisellini, *On the magnetization of BL Lac jets*, en, Sept. 2015.

[300] F. Tavecchio and G. Ghisellini, "On the magnetization of BL Lac jets", Monthly Notices of the Royal Astronomical Society **456**, 2374–2382 (2016).

[301] H. Teräsranta et al., "Fifteen years monitoring of extragalactic radio sources at 22, 37 and 87 GHz", en, Astronomy and Astrophysics Supplement Series **132**, 305–331 (1998).

[302] D. J. Thompson, S. Djorgovski, and R. de Carvalho, "Spectroscopy of Radio Sources from the Parkes 2700 MHz Survey", Publications of the Astronomical Society of the Pacific **102**, ADS Bibcode: 1990PASP..102.1235T, 1235 (1990).

[303] J. Timmer and M. König, "On generating power law noise.", Astronomy and Astrophysics **300**, ADS Bibcode: 1995A&A...300..707T, 707 (1995).

[304] A. Tramacere, P. Giommi, M. Perri, F. Verrecchia, and G. Tosti, "Swift observations of the very intense flaring activity of Mrk 421 during 2006. I. Phenomenological picture of electron acceleration and predictions for MeV/GeV emission", en, Astronomy & Astrophysics **501**, Number: 3 Publisher: EDP Sciences, 879–898 (2009).

[305] A. Tramacere, E. Massaro, and A. M. Taylor, "STOCHASTIC ACCELERATION AND THE EVOLUTION OF SPECTRAL DISTRIBUTIONS IN SYNCHRO-SELF-COMPTON SOURCES: A SELF-CONSISTENT MODELING OF BLAZARS' FLARES", en, The Astrophysical Journal **739**, Publisher: The American Astronomical Society, 66 (2011).

[306] A. Tramacere, V. Sliusar, R. Walter, J. Jurysek, and M. Balbo, "Radio- -ray response in blazars as a signature of adiabatic blob expansion", en, Astronomy & Astrophysics **658**, A173 (2022).

[307] A. Tramacere, "JetSeT: Numerical modeling and SED fitting tool for relativistic jets", Astrophysics Source Code Library, ADS Bibcode: 2020ascl.soft09001T, ascl:2009.001 (2020).

[308] E. Treister, C. M. Urry, and P. Lira, *AGN Unification and the X-ray Background*, Conference Name: The X-ray Universe 2005 Volume: 604 ADS Bibcode: 2006ESASP.604..845T, eprint: arXiv:astro-ph/0505300, Jan. 2006.

[309] C. M. Urry and P. Padovani, "Unified Schemes for Radio-Loud Active Galactic Nuclei", Publications of the Astronomical Society of the Pacific **107**, Publisher: IOP ADS Bibcode: 1995PASP..107..803U, 803 (1995).

[310] J. P. v. d. Van den Berg, M. Boettcher, A. Dominguez, and M. Lopez-Moya, "Systematic Physical Characterization of the Gamma-Ray Spectra of 2FHL Blazars", en, The Astrophysical Journal **874**, arXiv:1901.03494 [astro-ph], 47 (2019).

[311] J. Vink, *Physics and Evolution of Supernova Remnants*, Publication Title: Physics and Evolution of Supernova Remnants ADS Bibcode: 2020pesr.book.....V (Jan. 2020).

[312] J. J. P. Virtanen and R. Vainio, "Stochastic Acceleration in Relativistic Parallel Shocks", en, The Astrophysical Journal **621**, arXiv:astro-ph/0411184, 313–323 (2005).

[313] K. Wachter, R. Leach, and E. Kellogg, "Parameter estimation in X-ray astronomy using maximum likelihood.", The Astrophysical Journal **230**, ADS Bibcode: 1979ApJ...230..274W, 274–287 (1979).

[314] S. Wagner, *ATel #15020: Enhanced HE and VHE gamma-ray activity from the FSRQ PKS 0346-27*, Nov. 2021.

[315] S. M. Wagner et al., "Statistical properties of flux variations in blazar light curves at GeV and TeV energies", en, in Proceedings of 37th International Cosmic Ray Conference — PoS(ICRC2021) (July 2021), p. 868.

[316] S. P. Wakely and D. Horan, "TeVCat: An online catalog for Very High Energy Gamma-Ray Astronomy", en, (2008).

[317] R. C. Walker, P. E. Hardee, F. B. Davies, C. Ly, and W. Junor, "The Structure and Dynamics of the Subparsec Jet in M87 Based on 50 VLBA Observations over 17 Years at 43 GHz", en, The Astrophysical Journal **855**, Publisher: The American Astronomical Society, 128 (2018).

[318] A. A. Watson, "High-energy cosmic rays and the Greisen–Zatsepin–Kuz'min effect", en, Reports on Progress in Physics **77**, Publisher: IOP Publishing, 036901 (2014).

[319] D. Watson et al., "ASCA and other contemporaneous observations { } of the blazar B2 1308+326", Astronomy and Astrophysics **364**, ADS Bibcode: 2000A&A...364...43W, 43–52 (2000).

[320] Z. R. Weaver, S. G. Jorstad, A. P. Marscher, D. A. Morozova, I. S. Troitsky, I. Agudo, J. L. Gómez, A. Lähteenmäki, J. Tammi, and M. Tornikoski, "Kinematics of Parsec-scale Jets of Gamma-Ray Blazars at 43 GHz during 10 yr of the VLBA-BU-BLAZAR Program", en, The Astrophysical Journal Supplement Series **260**, Publisher: The American Astronomical Society, 12 (2022).

[321] K. W. Weiler and N. Panagia, "Are Crab-type Supernova Remnants (Plerions) Short-lived?", Astronomy and Astrophysics **70**, Publisher: EDP ADS Bibcode: 1978A&A....70..419W, 419 (1978).

[322] M. C. Weisskopf, "The Chandra X-Ray Observatory: An overview", Advances in Space Research **32**, 2005–2011 (2003).

[323] G. L. White, D. L. Jauncey, A. Savage, A. E. Wright, M. J. Batty, B. A. Peterson, and S. Gulkis, "Redshifts of Southern Radio Sources. VII.", The Astrophysical Journal **327**, ADS Bibcode: 1988ApJ...327..561W, 561 (1988).

[324] R. L. White and K. S. Long, "Supernova Remnant Evolution in an Interstellar Medium with Evaporating Clouds", The Astrophysical Journal **373**, Publisher: IOP ADS Bibcode: 1991ApJ...373..543W, 543 (1991).

[325] P. N. Wilkinson, A. C. S. Readhead, G. H. Purcell, and B. Anderson, "Radio structure of 3C147 determined by multi-element very long baseline interferometry", en, Nature **269**, Publisher: Nature Publishing Group, 764–768 (1977).

[326] B. J. Wills and D. Wills, "Spectroscopy of 125 QSO candidates and radio galaxies.", The Astrophysical Journal Supplement Series **41**, Publisher: IOP ADS Bibcode: 1979ApJS...41..689W, 689–700 (1979).

[327] J.-H. Woo and C. M. Urry, "Active Galactic Nucleus Black Hole Masses and Bolometric Luminosities", en, The Astrophysical Journal **579**, Publisher: IOP Publishing, 530 (2002).

[328] M. Wood, R. Caputo, E. Charles, M. Di Mauro, J. Magill, J. S. Perkins, and on behalf of the Fermi-LAT Collaboration, "Fermipy: An open-source Python package for analysis of Fermi-LAT Data", en, in *Proceedings of 35th International Cosmic Ray Conference — PoS(ICRC2017)*, Vol. 301, Conference Name: 35th International Cosmic Ray Conference (SISSA Medialab, Aug. 2018), p. 824.

[329] J. M. Wrobel, R. C. Walker, and H. Fu, "Evidence from the Very Long Baseline Array that J1502SE/SW are Double Hotspots, not a Supermassive Binary Black Hole", The Astrophysical Journal **792**, ADS Bibcode: 2014ApJ...792L...8W, L8 (2014).

[330] S. Wu, S. Chen, and LHAASO Collaboration, "Highlight of LHAASO science results on PeVatrons", en, in Proceedings of 38th International Cosmic Ray Conference — PoS(ICRC2023) (Sept. 2023), p. 010.

[331] M. H. Xu, J. M. Anderson, R. Heinkelmann, S. Lunz, H. Schuh, and G. L. Wang, "Structure Effects for 3417 Celestial Reference Frame Radio Sources", en, The Astrophysical Journal Supplement Series **242**, Publisher: The American Astronomical Society, 5 (2019).

[332] K. Yoshida, M. Petropoulou, K. Murase, and F. Oikonomou, "Flare Duty Cycle of Gamma-Ray Blazars and Implications for High-energy Neutrino Emission", en, The Astrophysical Journal **954**, Publisher: The American Astronomical Society, 194 (2023).

[333] G. T. Zatsepin and V. A. Kuz'min, "Upper Limit of the Spectrum of Cosmic Rays", Soviet Journal of Experimental and Theoretical Physics Letters **4**, Publisher: Springer ADS Bibcode: 1966JETPL...4...78Z, 78 (1966).

[334] J. A. Zensus and T. J. Pearson, "Superluminal radio sources", Superluminal Radio Sources, ADS Bibcode: 1987slrs.work.....Z (1987).

[335] X. Zhang, Z. Sun, X. Chen, L. Pan, and Y. Zhong, "Summary of Lunar Constellation Navigation and Orbit Determination Technology", en, Aerospace **11**, Publisher: Multidisciplinary Digital Publishing Institute, 497 (2024).

[336] P. van Zyl, *ATel #11189: Fermi LAT detection of strong GeV activity from the blazar 3C 279*, Jan. 2018.